

# **ELIMINATION OF SKIN-STRETCH INDUCED MOTION ARTEFACTS FROM ELECTROCARDIOGRAM SIGNALS**

**Anubha Kalra**

A thesis submitted to

Auckland University of Technology

in fulfilment of the requirements for the degree of

Doctor of Philosophy (PhD.)



**Institute of Biomedical Technologies**

**School of Engineering**

**Faculty of Design and Creative Technologies**

Supervisors: Dr. Andrew Lowe, Prof Ahmed Al-Jumaily

© Anubha Kalra

June 2017

## ABSTRACT

Electrocardiography (ECG) is widely used in clinical practice, for example to diagnose coronary artery disease or the cause of chest pain during a stress test, while the patient is running on a treadmill. Ambulatory ECG monitoring is used for long term recording of ECG signals, while the patient carries out his/her daily activities. Artefacts in ECG are caused by the patient's movement, moving cables, interference from outside sources, electromyography (EMG) interference and electrical contact from elsewhere on the body. Most of these artefacts can be minimised by using proper electrode design and ECG circuitry. However, artefacts due to subject's movement are hard to identify and eliminate and can be easily mistaken for symptoms of arrhythmia and the physiological effects of exercise, leading to misdiagnosis and false alarms.

Skin stretch has been identified as a major source of motion artefacts in ECG signals, which arise due to the flow of current, called the 'injury current' across the epidermis. Thus, the skin is generally abraded or punctured to minimize variations in injury current. This is unpleasant and not useful for long term monitoring, as the skin regrows after 24 hours. Present motion sensing approaches to artefact reduction in ECG do not measure motion in terms of skin stretch.

The main goal of this study is to quantify and eliminate motion artefacts from ECG pertaining to skin stretch. A polymer patch electrode with Young's modulus lower than of skin has been developed to simultaneously measure ECG and skin stretch using an optical sensing technique. These signals were combined with infinitesimal strain theory to quantify skin stretch as two dimensional strains. Principal component analysis (PCA) and independent component analysis (ICA) were utilised for motion artefact removal from ECG signals.

A motion Artefact Rejection (AR) system has been developed to validate the approach implemented in this study. As this study mainly focuses on skin stretch induced artefacts, a plastic tube has been used to stretch the forearm skin of 7 subjects across the following age groups: 18–35 years (3 subjects), 36–55 years (2 subjects), and 56 years and above (2 subjects). ECG with motion artefacts were measured using CNT/PDMS electrodes and dry Ag electrodes. The reference ECG (ECG at rest) was measured from the chest using conventional Ag/AgCl electrodes. The average improvements in SNRs using PCA and ICA algorithms were found to be 4.249 dB and 9.586 dB respectively, while the average

of maximum deviation from rest/reference ECG was 0.0843 for ECG with motion artefacts, 0.0702 for ECG after PCA and 0.0442 for ECG after ICA.

Both PCA and ICA algorithms also aided in removing baseline wander and high frequency noises in the cases of less or no motion artefact. The system performed well in removing artefacts generated due to EMG interference and stretching the skin perpendicular, diagonal and parallel to Langer's lines. Higher SNRs were achieved when PCA and ICA were performed by using 2D strains as motion information than when no motion information was used. In conclusion, ICA used for motion artefact reduction in ECG signals shows better performance than other techniques employing adaptive filtering, PCA and ICA.

A novel, state-of-the-art technique to identify and eliminate motion artefacts from ECG signals has been developed through this study which is feasible for practical implementations.

## ACKNOWLEDGEMENTS

This journey would not have been possible without the love and support of my family. They have instilled in me a deep sense of value of education and have motivated me to be ambitious and to strive for my aspirations.

I would like to sincerely thank my primary supervisor Dr. Andrew Lowe for giving me the opportunity to do research on this interesting topic and for mentoring me throughout the PhD. I am deeply thankful for his efforts in proofreading my thesis and for helping me in organizing my research findings. He has provided me with his invaluable suggestions and has motivated me to think about new and alternate ways to improve my thesis. He is a great listener and has always encouraged me to express my ideas and discuss my problems with him. This has been a long and daunting journey and there were times when I lost path, but he always showed confidence in my ability to complete this PhD.

I would also like to express my deepest gratitude to my secondary supervisor Professor Ahmed Al-Jumaily for his insightful comments and for helping me understand the strength and weaknesses of my thesis. I would like to thank him for providing me with adequate funding throughout my PhD tenure which has been a huge relief to me and has allowed me to focus on my research.

I would like to acknowledge my teaching supervisor Jeff Kilby for keeping my spirits high and for making me laugh in tense situations.

I am sincerely thankful to my close friend Dipanjan Das for taking care of me and cooking delicious meals for me when I was busy working before the deadlines. In particular, I am thankful to Gautam Anand for boosting my confidence and helping me stay calm and focussed throughout the PhD.

Also I thank my friends Parn and Yasir for helping me with my experiments during my PhD and for being so supportive and caring.

I am also thankful to my friends and colleagues at IBtec for the stimulating discussions, and for all the fun we have had in the last three years.

Finally, I would like to dedicate this thesis to my sweet grandma (I call her Biji) who jumped with excitement on knowing about my enrollment into PhD program. She is very proud of me and has always been there for me in my tough times.

# TABLE OF CONTENTS

<b>Abstract</b> .....	<b>i</b>
<b>Acknowledgements</b> .....	<b>iii</b>
<b>List of Figures</b> .....	<b>ix</b>
<b>List of Tables</b> .....	<b>xvii</b>
<b>Attestation of Authorship</b> .....	<b>xviii</b>
<b>List of Units, Symbols and Abbreviations</b> .....	<b>xix</b>
<b>Chapter 1      Background</b> .....	<b>22</b>
1.1      Generation and Significance of the Electrocardiogram (ECG) .....	22
1.2      Modern Forms of ECG Measurement Systems .....	26
1.2.1 <i>Holter Monitors</i> .....	27
1.2.2 <i>Event Monitors</i> .....	28
1.2.3 <i>Implantable Loop Recorders</i> .....	28
1.2.4 <i>Patch Sensors</i> .....	29
1.2.5 <i>Other Systems</i> .....	32
1.3      Design of ECG Circuitry in Ambulatory Devices.....	34
1.4      Electrode Topologies for ECG Sensing.....	39
1.5      Carbon Nano Tubes for ECG and Stretch Sensing.....	43
1.6      Sources of Noise in Ambulatory ECG Systems .....	44
1.7      Motion Tracking .....	46
1.7.1 <i>Accelerometers</i> .....	46
1.7.2 <i>Linear Variable Differential Transformers (LVDTs)</i> .....	47
1.7.3 <i>Gradiometers</i> .....	48
1.7.4 <i>Optical Sensors</i> .....	49
1.8      PCA And ICA for Motion Artefact Rejection.....	52
1.9      Other Motion Artefact Rejection Algorithms.....	55
1.10     Effect of Padding on Motion Artefact Reduction.....	57
1.11     Summary.....	59
<b>Chapter 2      Literature Review</b> .....	<b>61</b>
2.1      Introduction .....	61
2.2      Skin Stretch: A Major Source of Motion Artefact.....	61
2.3      Young’s Modulus of the Skin.....	63
2.4      Significance of Young’s Modulus .....	64
2.5      Methods Employed for Mechanical Testing of the Skin.....	65

2.5.1	<i>Tensile Test</i> .....	66
2.5.2	<i>Indentation Test</i> .....	67
2.5.3	<i>Suction Test</i> .....	70
2.5.4	<i>Torsion Test</i> .....	71
2.6	Factors Affecting the Young’s Modulus of the Skin.....	73
2.6.1	<i>Langer’s Lines</i> .....	73
2.6.2	<i>Age, Gender and Skin’s Thickness</i> .....	75
2.6.3	<i>Hydration</i> .....	78
2.7	Summary.....	80
<b>Chapter 3</b>	<b>Research Gap and Objectives</b> .....	<b>81</b>
3.1	Summary of Previous Studies.....	81
3.2	Research Gap and Research Questions.....	82
3.3	Research and Thesis Outline.....	83
<b>Chapter 4</b>	<b>Development of Stretchable Polymer Electrodes</b> .....	<b>85</b>
4.1	Introduction.....	85
4.2	PDMS Preparation.....	85
4.3	Young’s Modulus of PDMS Films.....	87
4.4	Preparation of CNT/ PDMS Electrodes.....	90
4.5	Young’s Modulus of CNT/ PDMS Electrodes.....	92
4.6	Conductance of the Electrodes.....	93
4.7	Summary.....	97
<b>Chapter 5</b>	<b>Optical Strain Measurement System</b> .....	<b>99</b>
5.1	Introduction.....	99
5.2	Mathematical Approach to Quantify Skin Stretch.....	99
5.3	PDMS Stretch Simulation in Solidworks®.....	105
5.4	Experimental Validation.....	112
5.5	Results.....	114
5.6	Discussion.....	118
5.7	Summary.....	119
<b>Chapter 6</b>	<b>A Pilot Study on ECG Motion Artefact Rejection</b> .....	<b>120</b>
6.1	Introduction.....	120
6.2	Materials and Methods.....	120
6.3	Motion Artefact Rejection using PCA in Matlab.....	122
6.4	Motion Artefact Rejection using ICA in Matlab.....	128
6.5	Results and Discussion.....	134

6.6	Summary.....	142
<b>Chapter 7</b>	<b>Validation of Artefact Rejection System .....</b>	<b>144</b>
7.1	Introduction .....	144
7.2	Materials and Methods .....	146
7.3	Performance Parameters .....	147
7.3.1	<i>Improvement in SNRs.....</i>	<i>148</i>
7.3.2	<i>Infinity Norm (<math>\infty</math>-Norm).....</i>	<i>148</i>
7.3.3	<i>Student's t-Test.....</i>	<i>149</i>
7.4	Evaluating System Performance Under Different Conditions.....	149
7.4.1	<i>EMG induced Artefact Rejection Efficiency.....</i>	<i>149</i>
7.4.2	<i>Intra-Test Repeatability.....</i>	<i>149</i>
7.4.3	<i>PCA With and Without Beat Segmentation .....</i>	<i>150</i>
7.4.4	<i>Effect of Langer's Lines .....</i>	<i>150</i>
7.4.4.1	<i>Effect of Stretching the Skin Perpendicular to Langer's Lines .....</i>	<i>151</i>
7.4.4.2	<i>Effect of Stretching the Skin Parallel to Langer's Lines .....</i>	<i>151</i>
7.4.4.3	<i>Effect of Stretching the Skin Diagonal to Langer's Lines .....</i>	<i>151</i>
7.4.5	<i>Alternative Methods of calculating Strain Signals.....</i>	<i>152</i>
7.4.6	<i>Metrics used for Comparison with Other Research.....</i>	<i>157</i>
7.4.7	<i>Comparison between CNT/PDMS and Dry Ag Electrodes .....</i>	<i>158</i>
7.5	Results .....	159
7.5.1	<i>Skin Stretch induced Artefact Rejection.....</i>	<i>159</i>
7.5.2	<i>Evaluating System Performance under Different Conditions .....</i>	<i>165</i>
7.5.2.1	<i>EMG induced Artefact Rejection Efficiency.....</i>	<i>165</i>
7.5.2.2	<i>Intra-Test Repeatability.....</i>	<i>166</i>
7.5.2.3	<i>PCA With and Without Beat Segmentation .....</i>	<i>167</i>
7.5.2.4	<i>Effect of Langer's Lines.....</i>	<i>169</i>
7.5.3	<i>Strain Contribution in Skin Stretch Quantification.....</i>	<i>172</i>
7.5.4	<i>Comparison of this Study with Other Research .....</i>	<i>178</i>
7.5.5	<i>Comparison between CNT/PDMS and Dry Ag Electrodes .....</i>	<i>179</i>
7.6	Discussion.....	180
7.7	Summary.....	186
<b>Chapter 8</b>	<b>Conclusions and Future Works.....</b>	<b>189</b>
8.1	Conclusions .....	189
8.2	Future Directions .....	190
8.2.1	<i>Future Sensor Development.....</i>	<i>190</i>
8.2.2	<i>Further Development of Algorithms .....</i>	<i>191</i>
8.2.3	<i>Further Validation .....</i>	<i>191</i>

<b>References.....</b>	<b>191</b>
<b>Appendices.....</b>	<b>208</b>
Appendix A: List of Publications .....	208
Appendix B: Acceptance Letter from Ethics Committee at Auckland University of Technology for ECG Data Collection .....	209
Appendix C: Safety data sheet of Materials used in this study: .....	212
<i>Sylgard® 184</i> .....	213
<i>Ten 20 ® Conductive Paste</i> .....	214
<i>Multi Walled Carbon Nanotubes</i> .....	215
Appendix D: Device Specifications.....	216
<i>Ta.Xt Plus</i> .....	216
<i>Lcr Meter E4980a</i> .....	217
<i>Physioflow</i> .....	218
<i>G-Usbamp 3.0</i> .....	219

## LIST OF FIGURES

Figure 1.1: Representation of Einthoven’s triangle. ....	23
Figure 1.2: Depolarization and repolarization resulting in cardiac activity.....	24
Figure 1.3: Common examples of abnormal ECGs [11].....	25
Figure 1.4: 5 lead and 3 lead cable hook up in Holter monitor and Event Monitor [30].....	28
Figure 1.5: Cardiac diagnostic landscape of various ambulatory ECG monitors [44].....	30
Figure 1.6: Multipurpose vest shirt. ....	33
Figure 1.7: Generalized ECG block diagram.....	35
Figure 1.8: Use of a driven right leg circuit to reduce common mode voltage [54]. ....	37
Figure 1.9: Schematic diagram of an isolated biomedical circuit [55]. ....	38
Figure 1.10: Various Electrode Topologies [61].....	39
Figure 1.11: Fabrication of active electrodes [64]. ....	41
Figure 1.12: A: ECG with motion artefacts, B: ECG without motion artefacts. ....	45
Figure 1.13: Diagrammatic representation of the coordinate system in a 3-axis accelerometer. ....	47
Figure 1.14: Single Inductive Linear Variable Differential Transformers.....	48
Figure 1.15: Parameters affecting the source capacitance of the gradiometer (quad configuration). .....	49
Figure 1.16: : Optical Components integrated in an electrode [108]. ....	50
Figure 1.17: Placement of electrodes and optical sensor [108]. ....	52
Figure 1.18: Signal processing using adaptive filtering. ....	56
Figure 1.19: Depiction of electrode locations [144]. ....	58
Figure 1.20: Effect of increasing pressure on electrode-skin impedance, EKG and motion artefact [144]. ....	59
Figure 2.1: Schematic Diagram of the skin [108]. ....	62
Figure 2.2: Structure of Collagen Fibre in different phases [161]. ....	64
Figure 2.3: Young’s modulus at different indentation depths for cylindrical  and spherical indenters.....	69

Figure 2.4: Twisting of skin for measuring elasticity in the Torsion Test.....	71
Figure 2.5: Variation in Young's modulus with the orientation of Langer's lines.....	74
Figure 2.6: Variation of Young's modulus with age and gender, measured using different testing techniques.....	76
Figure 2.7: Variation in Young's modulus with humidity: ♦ Papir (tensile test on stratum corneum), ■ Park and Baddiel (tensile test), ▲ Wildnauer (tensile test on human upper back).....	79
Figure 4.1: Laurell Spin Coater WS-650Mz-23NPP used to fabricate thin PDMS films.....	86
Figure 4.2: Texture Analyser.....	87
Figure 4.3: Stress-strain curve obtained from the texture analyser for tension-relaxation test of PDMS substrate with a B: CA ratio of 10:1.....	88
Figure 4.4: Comparison of stress-strain plots for PDMS mixtures with different B:CA ratios..	89
Figure 4.5: Mixing of CNT and DMF in controlled environment using ultrasonic mixer.....	91
Figure 4.6: Use of SEM to observe the dispersion of CNTs in PDMS; a: using DMF, b: without using DMF.....	92
Figure 4.7: Stress-strain curve obtained from texture analyser for tension-relaxation test of CNT/PDMS substrate with a B: CA ratio of 10:1.....	93
Figure 4.8: Measurement of conductance of CNT/DMF electrodes at different frequencies using LCR meter.....	94
Figure 4.9: Measurement of conductance across the CNT/DMF electrodes.....	94
Figure 4.10: Variation in conductance with frequency for different electrodes.....	95
Figure 4.11: Variation in conductance with frequency for CNT/PDMS samples with different thickness.....	96
Figure 4.12: Variation in conductance with frequency for CNT/PDMS samples at different stretch percentages.....	97
Figure 5.1: A body undergoing infinitesimal deformation [242].....	100
Figure 5.2: Mohr's circle for plane strain.....	103
Figure 5.3: Set of points A, B and C on skin undergoing deformation, displaced at A', B' and C'.....	104
Figure 5.4: Stretch simulation using curved and rectangular clamps.....	107

Figure 5.5: Solid mesh geometries [251].	108
Figure 5.6: Meshing of PDMS using high quality solid meshing.	109
Figure 5.7: PDMS stretch application on a circular region at the bottom left corner in SolidWorks.	111
Figure 5.8: Use of rectangular and curved clamps to conduct tensile tests.	112
Figure 5.9: Motion tracking from first frame using Euclidean distance mapping.	114
Figure 5.10: Delaunay triangulation using the checkerboard corner points.	114
Figure 5.11: Strain distribution in $\epsilon_x$ for PDMS stretch simulation in SolidWorks (left) and PDMS translation by texture analyser (right) using rectangular clamps	115
Figure 5.12: Strain distribution in $\epsilon_y$ for PDMS stretch simulation in SolidWorks (left) and PDMS translation by texture analyser (right) using rectangular clamps	115
Figure 5.13: Strain distribution in $\epsilon_{xy}$ for PDMS stretch simulation in SolidWorks (left) and PDMS translation by texture analyser (right) using rectangular clamps	116
Figure 5.14: Strain distribution in $\epsilon_x$ for PDMS stretch simulation in SolidWorks (left) and PDMS translation by texture analyser (right) using curved clamps	116
Figure 5.15: Strain distribution in $\epsilon_y$ for PDMS stretch simulation in SolidWorks (left) and PDMS translation by texture analyser (right) using curved clamps	117
Figure 5.16: Strain distribution in $\epsilon_{xy}$ for PDMS stretch simulation in SolidWorks (left) and PDMS translation by texture analyser (right) using curved clamps	117
Figure 5.17: Strain differences/errors ( $\epsilon_x$ , $\epsilon_y$ & $\epsilon_{xy}$ ) as a function of thickness.	118
Figure 6.1: Movements induced in arm by back and forth movement, opening and closing fist and rotating wrist clockwise and anticlockwise	121
Figure 6.2: Flowchart representing the quantification of ECG motion artefact.	122
Figure 6.3: Acquired ECG signal (in green) and ECG after baseline removal (in red).	123
Figure 6.4: R peak detection and ECG beat segregation.	124
Figure 6.5: Flow chart representing the steps employed in the working of PCA	126

Figure 6.6: (A) Original ECG signal with motion artefacts; (B) PCA filtering of (A) through beat segmentation without using strains; (C) PCA filtering of (A) through beat segmentation by using strains $\epsilon_x$ , $\epsilon_y$ and $\epsilon_{xy}$ (in red) .....	127
Figure 6.7: Flowchart representing the procedure involved in ICA .....	128
Figure 6.8: Steps involved in the JADE algorithm. ....	133
Figure 6.9: Plots of normal and shear strain components against time.....	134
Figure 6.10: PDMS patch adhered to the arm and displacement vectors from the first frame. ....	135
Figure 6.11: Contour plots showing change in normal strain $\epsilon_x$ with change in displacement .....	136
Figure 6.12: Contour plots showing change in normal strain $\epsilon_y$ with change in displacement .....	136
Figure 6.13: Contour plots showing change in shear strain $\epsilon_{xy}$ with change in displacement. ....	137
Figure 6.14: (a) ECG without motion artefacts; (b) ECG with motion artefacts (induced by back and forth movement); (c) bandpass filtering of ECG signal (a); (d) bandpass filtering of ECG signal (b) .....	138
Figure 6.15: (A) ECG with motion artefacts due to back and forward arm movement; (B) PCA filtering of ECG using beat segmentation; (C) ICA filtering of ECG using the JADE algorithm .....	139
Figure 6.16: (A) ECG with motion artefacts caused by closing fist and opening hand continuously, B. PCA filtering of ECG using beat segmentation, C. ICA filtering of ECG using JADE algorithm .....	140
Figure 6.17: (A) ECG with motion due to clockwise and anticlockwise rotation of the wrist; (B) PCA filtering of ECG using beat segmentation; (C) ICA filtering of ECG using the JADE algorithm.....	141
Figure 7.1: Flow chart describing the layout of the experimental validation of the system. ....	145
Figure 7.2: ECG measurement set up .....	146
Figure 7.3: Generating motion artefact by stretching forearm using a plastic tube .....	147
Figure 7.4: Orientation of Langer's lines on human forearm .....	150
Figure 7.5: Introducing motion artefacts by stretching the skin parallel to Langer's lines.....	151
Figure 7.6: Introducing motion artefacts by stretching the skin diagonal to Langer's lines.....	152

Figure 7.7: Detecting the patch's boundary in each frame .....	153
Figure 7.8: Detecting and tracking the corner points of the checker boxes within the patch ...	153
Figure 7.9: Strains obtained from different regions of the CNT/PDMS patch. ....	154
Figure 7.10: Arrangement of data matrix by taking normal and shear strains ( $\epsilon_x$ , $\epsilon_y$ and $\epsilon_{xy}$ ) as motion information in PCA and ICA .....	155
Figure 7.11: Arrangement of data matrix by taking principal strains ( $\epsilon_1$ , $\epsilon_2$ ) as motion information in PCA and ICA. ....	155
Figure 7.12: Arrangement of data matrix by taking maximum principal strain ( $\epsilon_1$ ) as motion information in PCA and ICA. ....	156
Figure 7.13: Arrangement of data matrix by taking minimum principal strain ( $\epsilon_2$ ) as motion information in PCA and ICA. ....	156
Figure 7.14: Arrangement of data matrix by taking normal and shear strains ( $\epsilon_x$ , $\epsilon_y$ and $\epsilon_{xy}$ ) from 4 checkerboard regions as motion information in PCA and ICA. ....	157
Figure 7.15: Case with least improvement in SNR (1.7337 dB) using PCA. A: ECG with motion artefact induced in Subject 4 by opening hand and closing fist continuously (in red); B: Signal filtered using PCA (in green); C: Reference signal (in blue).....	161
Figure 7.16: Case with most improvement in SNR (6.0291 dB) using PCA. A: ECG with motion artefact induced in Subject 7, by opening hand and closing fist continuously (in red); B: Signal filtered using PCA (in green); C: Reference signal (in blue).....	161
Figure 7.17: Case with least improvement in SNR (5.872 dB) using ICA. A: ECG with motion artefact induced in Subject 2, by stretching the forearm skin using a glass slide (in red), B: Signal filtered using ICA (in green), C: Reference signal (in blue).....	162
Figure 7.18: Case with most improvement in SNR (12.74 dB) using ICA. A: ECG with motion artefact induced in Subject 6, by stretching the forearm skin using a glass slide (in red), B: Signal filtered using ICA (in green), C: Reference signal (in blue).....	162
Figure 7.19 : A: ECG (in mV) with motion artefact induced in Subject 4 for the first time sequence (0–15 seconds), SNR= 3.5171(in green); B: Corresponding strain $\epsilon_x$ (in red); C: Corresponding strain $\epsilon_y$ (in blue); D: Corresponding strain $\epsilon_{xy}$ (in black) .....	163

Figure 7.20: A: ECG (in mV) with motion artefact induced in Subject 4 for the second time sequence (15–30 seconds), SNR= -3.4925 (in green); B: Corresponding strain $\epsilon_x$ (in red); C: Corresponding strain $\epsilon_y$ (in blue); D: Corresponding strain $\epsilon_{xy}$ (in black).....	163
Figure 7.21: A: ECG (in mV) with motion artefact induced in Subject 4 for the third time sequence (30–45 seconds), SNR= -0.8761(in green); B: Corresponding strain $\epsilon_x$ (in red); C: Corresponding strain $\epsilon_y$ (in blue); D: Corresponding strain $\epsilon_{xy}$ (in black) .....	164
Figure 7.22: A: ECG (in mV) with motion artefact induced in Subject 4 for the fourth time sequence (45-60 seconds), SNR= -0.3916 (in green); B: Corresponding strain $\epsilon_x$ (in red); C: Corresponding strain $\epsilon_y$ (in blue); D: Corresponding strain $\epsilon_{xy}$ (in black). .....	164
Figure 7.23: Comparison of SNRs calculated for ECG with motion artefact and ECG filtered using PCA and ICA (represented by MA, PCA and ICA respectively) by inducing motion artefacts in 2 subjects, at different time intervals.....	166
Figure 7.24: Comparison of $\infty$ -norms (represented by MA, PCA and ICA respectively) by inducing motion artefacts in 2 subjects, at different time intervals .....	167
Figure 7.25: Comparison of SNRs on application of PCA with and without peak detection/beat segmentation (represented as PCA peaks and PCA respectively) .....	168
Figure 7.26: A: Recorded ECG signal with motion artefact (in Subject 2 by stretching the skin using a plastic tube); B: PCA filtering on ECG without beat segmentation; C: PCA filtering on ECG with beat segmentation; D: Reference ECG signal.....	169
Figure 7.27: Comparison of SNRs calculated for ECG with motion artefact and ECG filtered using PCA and ICA (represented by MA, PCA and ICA respectively) by stretching the skin parallel, diagonal and perpendicular to Langer’s lines .....	169
Figure 7.28: A: ECG with motion artefact in Subject 1 on stretching the skin parallel to Langer’s lines, SNR= 9.58 dB (in red); B: ECG after PCA filtering, SNR= 11.02 dB (in black); C: ICA after ICA filtering, SNR=12.601 dB (in green); D: Reference ECG signal (in blue).....	170
Figure 7.29: A: ECG with motion artefact in Subject 1 on stretching the skin diagonal to Langer’s lines, SNR= -2.021 dB (in red); B: ECG after PCA filtering, SNR= 4.15 dB (in black); C: ICA after ICA filtering, SNR=10.86 dB (in green); D: Reference ECG signal (in blue).....	170

Figure 7.30: A: ECG with motion artefact in Subject 1 on stretching the skin perpendicular to Langer’s lines, SNR=1.7657 dB (in red); B: ECG after PCA filtering, SNR= 4.9587 dB (in black); C: ECG after ICA filtering, SNR=11.445 dB (in green); D: Reference ECG signal (in blue) .	171
Figure 7.31: Strain plots ( $\epsilon_x, \epsilon_y, \epsilon_{xy}$ ) corresponding to ECG signals acquired by stretching the skin parallel (in green), diagonal (in red) and perpendicular (in blue) to Langer’s lines.....	171
Figure 7.32: Evaluation of SNRs using PCA and taking mean and median values of strains as motion information .....	173
Figure 7.33: Evaluation of SNRs using ICA and taking mean and median values of strains as motion information .....	173
Figure 7.34: Evaluation of $\infty$ -norm using PCA and taking mean and median values of strains as motion information. ....	174
Figure 7.35: Evaluation of $\infty$ -norm using ICA and taking mean and median values of strains as motion information. ....	174
Figure 7.36: Mean and median strains (for all points in Figure 7.8) corresponding to ECG measurement in Subject 1 (age group: 18–35 years) for 60 seconds.....	175
Figure 7.37: Mean and median strains (for corner points in Figure 7.7) corresponding to ECG measurement in Subject 1 (age group: 18–35 years) for 60 seconds.....	175
Figure 7.38: Mean and median strains (for points in region 1 in Figure 7.9) corresponding to ECG measurement in Subject 1 (age group: 18–35 years) for 60 seconds.....	176
Figure 7.39: Mean and median strains (for points in region 4 in Figure 7.9) corresponding to ECG measurement in Subject 1 (age group: 18–35 years) for 60 seconds.....	176
Figure 7.40: A: ECG with motion artefact, filtered using ICA with data set arrangement in Case 1 (Figure 7.10); B: On taking motion information from all points (Figure 7.8); C: On taking motion information from corner points (Figure 7.7); D: On taking motion information from points in region 4 (Figure 7.9) E: Reference ECG from shoulders .....	177
Figure 7.41: ECG measurement for 10 seconds at rest using: A: Dry Ag electrodes on wrist with SNR= 9.029 dB; B: CNT/PDMS electrodes on wrist with SNR= 15.27 dB; C: Ag/AgCl electrodes on chest .....	180

Figure 7.42: Small and large displacements (blue arrows) of checkerboard corner points (in green circles) from the points in initial frame (in red circles) ..... 183

Figure 7.43: Displacements (blue arrows) of checkerboard corner points (in green circles) in Regions A and B from the points in the initial frame (in red circles)..... 184

Figure 7.44: Representation of position of each region of the checkerboard from the ECG sensing site..... 185

Figure 7.45: A comparison of performance of the AR system under different conditions..... 188

## LIST OF TABLES

Table 1.1: Features and diagnostic efficacy of various ambulatory ECG monitors .....	31
Table 1.2: Advantages and disadvantages of commercial ambulatory ECG sensors. ....	34
Table 1.3: Comparison between wet, dry and capacitive electrodes for long-term bio sensing. ....	42
Table 2.1: Values of Young's modulus at quasistatic and dynamic speeds using tensile test. ...	67
Table 2.2: Values of Young's modulus at quasistatic and dynamic speeds using indentation. ..	68
Table 2.3: Young's modulus using suction at different deformations & aperture sizes. ....	71
Table 2.4: Young's modulus obtained through torsion for different guard ring parameters. ....	72
Table 4.1: Parameters used in the mechanical testing of the CNT/PDMS film using texture analyser. ....	88
Table 4.2: Average Young's modulus for PDMS with different B: CA ratios.....	90
Table 5.1: Approximate material properties used to emulate PDMS. ....	106
Table 5.2: Meshing parameters for PDMS stretch simulation.....	110
Table 7.1: Comparison of various performance parameters for ECG with motion artefacts (MA) and ECG filtered using PCA and ICA for 60 seconds. ....	160
Table 7.2: Performance of PCA and ICA in eliminating EMG induced artefacts.....	165
Table 7.3: Comparison of PCA and ICA performance for Case 5, average displacements and without motion information against Case 1 .....	178
Table 7.4: Comparison between performances in related research with those in the current study .....	179

## ATTESTATION OF AUTHORSHIP

“I hereby declare that this submission is my own work and that, to the best of my knowledge and belief, it contains no material previously published or written by another person (except where explicitly defined in the acknowledgements), nor material which to a substantial extent has been submitted for the award of any other degree or diploma of a university or other institution of higher learning.”

..... (signed)

04/10/2017

..... (date)

# LIST OF UNITS, SYMBOLS AND ABBREVIATIONS

## UNITS

SYMBOL	UNIT
dB	decibels
Hz	hertz
kPa	kilo-pascal
mA	milli-ampere
mbar	milli-bar
Mpa	mega-pascal
mV	milli-volt
Nm <sup>-1</sup>	newton per meter
s <sup>-1</sup>	per-second
μS	micro-siemens
Ω	ohm

## SYMBOLS

SYMBOL	QUANTITY	UNIT
E	Young's Modulus	N m <sup>-2</sup>
G	Conductance	S
I	Current	A or mA
Kc	Stiffness	N m <sup>-1</sup>
L <sub>2</sub>	Euclidian norm	
V	Voltage	V or mV

Z

Impedance

$\Omega$

## ABBREVIATIONS

$\infty$ -norm

Infinity Norm

AR

Artefact Rejection

CNT

Carbon Nano Tubes

DMF

N-N Dimethylformamide

DRL

Driven Right Leg

ECG

Electrocardiogram

EEG

Electroencephalogram

EFICA

Efficient Fast Independent Component Analysis

EKF

Extended Kalman Filter

EMG

Electromyogram

EPIC

Electric Potential Integrated Circuit

IAFEs

Integrated Analogue Front End solutions

ICA

Independent Component Analysis

ILR

Implantable Loop Recorder

IPG

Impedance-Plethysmography

JADE

Joint Approximation Diagonalization of Eigen Matrices

KLT

Kanade Lucas-Tomasi

LMS

Least Mean Square

NLMS

Normalized Least mean Square

RLMS

Recursive Least Mean Square

LVDT	Linear Variable Differential Transformer
MA	Motion Artefacts
MCT	Mobile Cardiac Telemetry
MWCNT	Multi-Walled Carbon Nano Tubes
NMP	N-Methyl-2-pyrrolidone
PCA	Principal Component Analysis
PDMS	Polydimethylsiloxane
PPG	Photo-Plethysmography
RMS	Recursive Mean Square
SNR	Signal to Noise Ratio
SWCNT	Single-Walled Carbon Nano Tubes
VF	Ventricular Fibrillation
VT	Ventricular Tachycardia

# CHAPTER 1 BACKGROUND

## 1.1 GENERATION AND SIGNIFICANCE OF THE ELECTROCARDIOGRAM (ECG)

Biopotentials are the electrical signals that are produced inside the body due to various biochemical processes that form a part of living metabolism. The monitoring/recording of these signals are essential in the analysis of various physiological parameters and diagnosis. Electrocardiogram (ECG), electromyogram (EMG) and electroencephalogram (EEG) are biopotential signals from the heart, muscles and brain, respectively. The ECG gives a measurement of the electrical activity of the heart over time. It is an important clinical diagnostic measure which is widely known and practiced. It can be used to diagnose conditions such as cardiac arrhythmias, murmurs, pulmonary embolism and left ventricular hypertrophy [1]. Other than medical applications, ECG monitoring finds use in sports, for example optimising his or her performance during training [2].

Previous studies date back to 1838 when Carlo Mateucci demonstrated the electrical signal accompanying each heartbeat with his experiment on ‘rheoscopic frog’ [3]. The first human ECG was obtained by Waller (1887) [4], using saline sensors connected to crude galvanometers. Einthoven (1901) [5] developed a string galvanometer and devised an improvement over Waller’s method. He used buckets filled with saline as the sensors, one for each hand and one for the left leg. Through his work, in 1912, his method became known for ‘Einthoven’s Triangle’ and is an important basis for all forms of ECG measurements [6]. The shape of Einthoven’s triangle represents an inverted equilateral triangle with its centre at the heart. The branches of the triangle sum as vectors to a zero voltage (Figure 1.1) and represent potential differences measured by ECG.

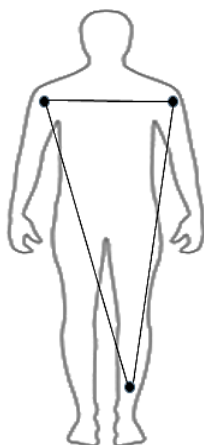


*Figure 1.1: Representation of Einthoven's triangle.*

The electrical conduction in heart is carried out by special cells responsible for the flow of current from one cell to another. A normal heart beat starts in in the sino-atrial node (S-A node), located in the right atrium. The S-A node is connected to the left atrium through an electrical path. This makes both the atria contract at the same time when the S-A node fires. There is a slight delay in the conduction while the electrical signal travels down to the ventricles through the atrio-ventricular node (A-V node). The action potentials generated by different cells in the myocardium leads to the formation of an ECG signal. This action potential causes the muscle tissue to contract by the flow of ions from cell to cell. This ionic flow causes a change in potential which is known as depolarization and restoring back the original potential is called repolarization as shown in Figure 1.2 [7].

An action potential arises when there is a difference in ionic concentration on the two sides of the cell membrane. Ion channels made up of large proteins are prevalent in the cell membrane. These channels have discrete biophysical properties that might cause channels to:

- I. Open and close quickly.
- II. Open quickly, close over long periods.
- III. Open and close after long periods.
- IV. Permit ions to flow only in one direction.
- V. Open all the time.

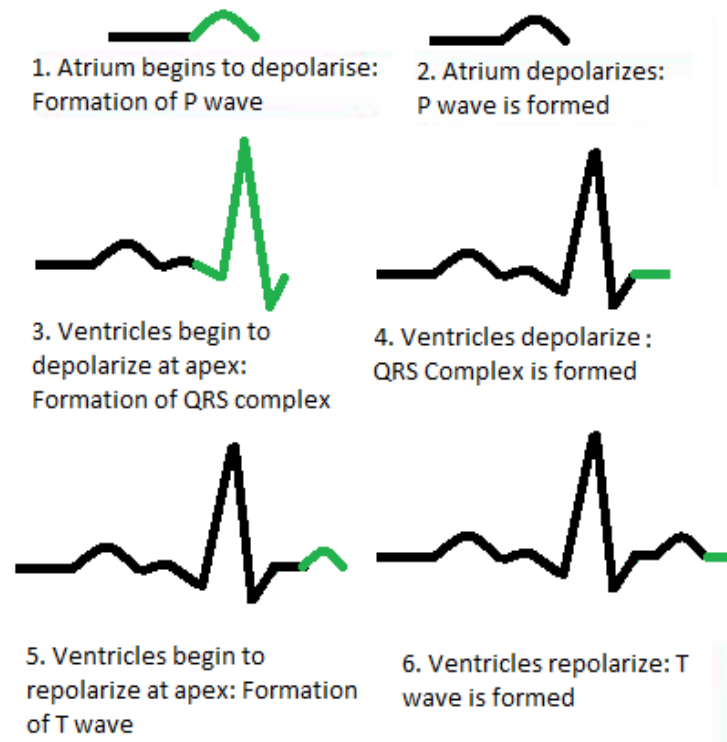


Figure 1.2: Depolarization and repolarization resulting in cardiac activity.

In the human body, these ion channels control the heart beat rate, the perception of sound or sight, or storage of a memory [8]. The cardiac action potential involves the exchange of Sodium ( $\text{Na}^+$ ), Potassium ( $\text{K}^+$ ), Chloride ( $\text{Cl}^-$ ), and Calcium ( $\text{Ca}^{2+}$ ) ions across the cell membranes of the heart [9].  $\text{Na}^+$  and  $\text{Cl}^-$  are found outside the cell at rest, while  $\text{K}^+$  is found inside the cell.  $\text{Ca}^{2+}$  ions can be found both inside and outside the cells in a calcium store known as the sarcoplasmic reticulum. During depolarization, the  $\text{Na}^+$  ions enter the cell membranes, making the voltage positive. The  $\text{K}^+$  ions leave the cell membrane during repolarization. The intracellular concentration during the whole process is kept constant by the ion transporters or pumps, which maintain the leakage or the flow of ions across the cell membrane. The automatic nervous system affects, but does not control, the speed of action potential in the pacemaker cells.

An ECG test is generally used by the doctors to analyse if the electrical activity is slow, fast or irregular. It is also used by cardiologists to measure the amount of electrical activity in the heart, to make sure that the heart muscles aren't overworked [10]. Some common examples of abnormal ECGs can be seen in Figure 1.3.

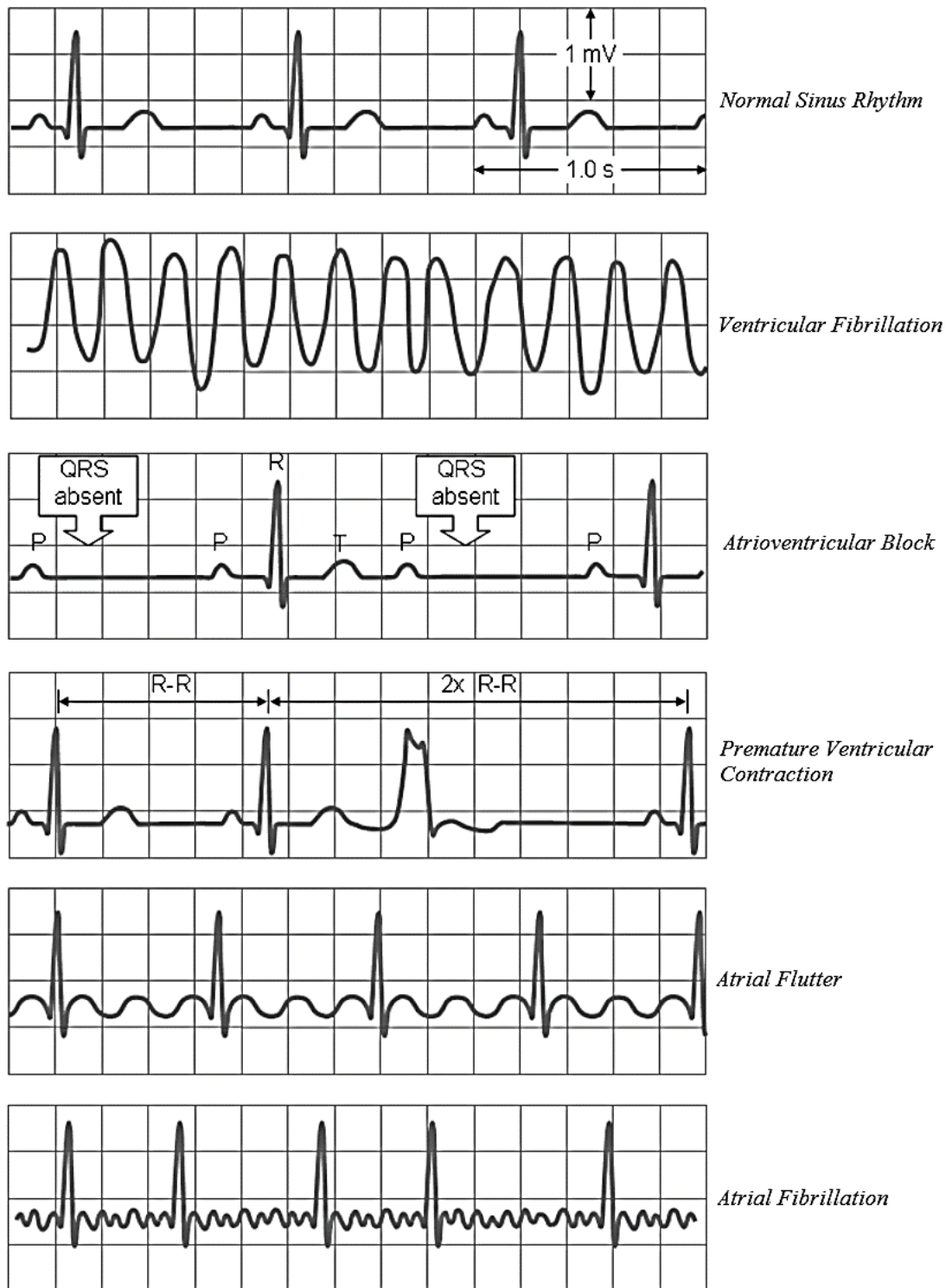


Figure 1.3: Common examples of abnormal ECGs [11].

The ECG is also important in protecting and guiding the health of the athletes [12]. In a recent survey by Harmon and Asif (2011) [13], all cases of sudden deaths were identified using the National Collegiate Athletic Association (NCCA) database. During

the 5-year period, there were 273 sudden deaths in a total of 1 969 663 patients. Cardiovascular-related sudden death was the leading cause of death in medical cases (56%), accounting for 75% of sudden deaths during exertion. Male athletes were more than twice as likely as female athletes to die suddenly. The inclusion of a 12-lead ECG in screening tests of all the athletes was recommended by the European Society of Cardiology (ESC) [14]. However, it is difficult to distinguish the abnormal patterns from the physiological effects of training. Many clinical findings that may cause a concern in the general population are normal for athletes.

An ECG can be used by the cardiologists to approximate the electrical axis of the heart, by observing the deflection in the QRS complex [11, Ch. 19]. Deviation of the electrical axis to the left can be due to hypertension, aortic stenosis, ischemic heart disease etc., while the deviation to the right is a consequence of chronic obstructive lung disease, pulmonary emboli, congenital heart disease etc. [11]. An ECG test can be used to find the heart beat frequency, to distinguish between normal sinus rhythms (60-100 beats per minute), sinus bradycardia (less than 60 beats per minute) and sinus tachycardia (higher than 100 beats per minute). Chaotic and irregular fluctuations in the ECG baseline can be due to atrial fibrillation, while the presence of saw-toothed flutter waves instead of P waves can indicate the condition of atrial flutter.

## **1.2 MODERN FORMS OF ECG MEASUREMENT SYSTEMS**

Having established the importance of the ECG as a one-off measure, it is also recognised that long term monitoring of the ECG is clinically important. There is worldwide demand for a continuous health monitoring system that can detect heart rate variability through which cardiovascular diseases (accounting for 48% of non-communicable disease deaths, as per 2012 WHO Statistics [15]) can be diagnosed and managed at an early stage. Although standard clinical devices are employed with sensing techniques for blood perfusion, cardiac sound and vascular blood velocity; ambulatory ECG and blood pressure monitoring are considered the most mature techniques [16]. Cardiac arrhythmia events can be life threatening, therefore regular monitoring and recording of ECG is valuable and can be used by a physician to achieve timely and accurate diagnosis or to determine the cause of the symptoms on patients [17].

The ambulatory ECG device provides a continuous monitoring of the heart for longer periods of time, while the patient is performing his or her daily activities. Ambulatory ECG systems aim to achieve patient comfort and ease of use as well as efficient signal acquisition. Ambulatory systems are used to identify infrequent and highly variable cardiac arrhythmias which normally pass undetected in clinical situations [18] [19]. Ambulatory ECG monitoring, in conjunction with clinical findings can be useful in investigating heart conditions such as palpitations, light-headedness or syncope [20].

### ***1.2.1 Holter monitors***

The first ambulatory cardiac monitoring device, now known as a Holter monitor was built by a famous American biophysicist Norman J. Holter (1914-1983) [21]. Modern Holter monitors are battery-operated, portable devices which can measure the ECG continuously for 24-48 hours [22], and are worn by the patients with suspected, frequent palpitations having slow, fast or an uneven heartbeat. They may also be used if a person has a pacemaker to ensure its proper functioning. 12 channel Holter monitors obtain ECG signals in the same representation as during common rest ECG and/or stress test measurement using the Mason-Likar lead system. However, the resolution of recordings using 12 channel Holter monitors is significantly lower than standard 12-lead ECG. Modern Holter monitors employ two or three channel ECG [22].

The clinical importance of arrhythmia detected using ambulatory ECG monitoring can be determined by finding its correlation with the simultaneous occurrence of suggestive symptoms. The symptoms of cardiac arrhythmia occur more frequently in outpatients than in hospitalized patients. Surawicz et al. [23] through his experiments found that the symptoms of cardiac arrhythmia in outpatients and inpatients were 55% and 6% respectively. However, the correlation of symptoms with detected arrhythmia in inpatients (95%) was higher than in outpatients (44%). In another study performed by Zeldis et al. in 1980 [24], the concurrence of the symptoms with an associated arrhythmia was found only in 50 of 371 patients (13%) using Holter monitors. Cardiac diagnosis obtained using Holter monitor by Drake (in 1984) [25], showed no significant relevance with associated arrhythmias. Thus, it can be inferred that Holter monitors employing 24-hour ECG monitoring exhibit a low diagnostic efficacy. Continuous long term monitoring is necessary for the correct diagnosis of the arrhythmia detected by an ambulatory device. When the monitoring time of the Holter monitor was increased from 24 to 72 hours in 95 patients with syncope [26], the occurrence of symptomatic events

increased from 15% to 27%. Therefore, 24 hour ambulatory monitoring might not be enough to identify potentially important arrhythmias [27].

### **1.2.2 Event monitors**

In cases where patients experience intermittent or rare symptoms of palpitations, event monitors are used for ambulatory monitoring of the ECG. Event monitors, also known as loop monitors, are small and light-weight devices which can be triggered by the patient when they feel symptoms arise. The latest event recorders employ real-time continuous cardiac monitoring, where the arrhythmic event data is automatically transferred to the monitoring station [28] [29]. In comparison to Holter monitors, event monitors are smaller in size and can record cardiac activities for longer periods of time [17]. Lead placement in modern Holter and event monitors can be seen in Figure 1.4.

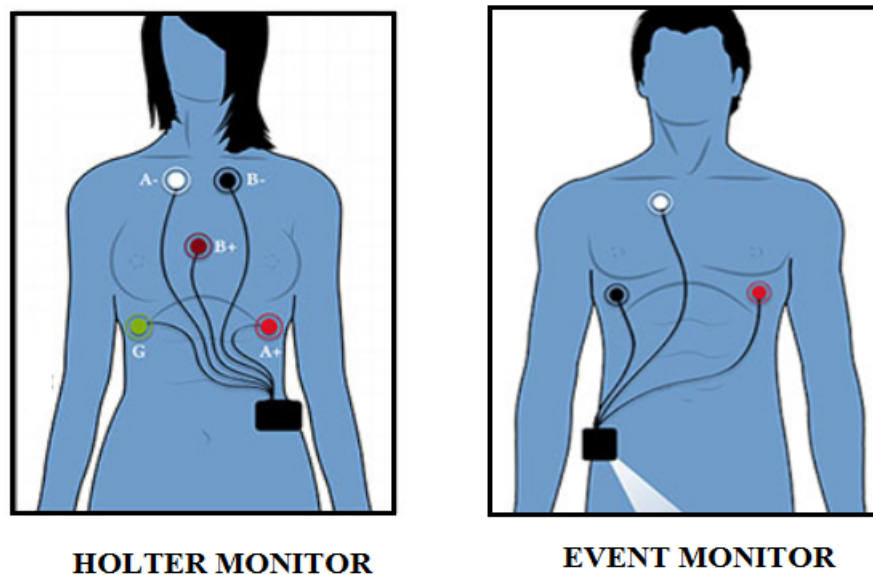


*Figure 1.4: 5 lead and 3 lead cable hook up in Holter monitor and Event Monitor [30].*

### **1.2.3 Implantable loop recorders**

Implantable loop recorders (ILRs) or insertable cardiac monitors (ICM) are used for the detection of infrequent arrhythmias or in the cases where other ambulatory devices are indeterminate. They are used for cardiac monitoring for prolonged periods of months to up to 3 years [31] [32]. ILR devices are placed under the skin and can automatically record continuous long-term signals.

#### ***1.2.4 Patch sensors***

In recent years, innovative engineering has led to the development of non-invasive thin patch electrodes for long-term ECG monitoring. Two examples of adhesive patch electrodes available in the market are Zio Patch (iRhythm, CA, USA) and SEEQ Mobile Cardiac Telemetry (Medtronic, Minneapolis, USA). The Zio patch device can measure one-lead ECG using a small adhesive patch. It can record cardiac activity for up to 14 days continuously without requiring any leads, wires or batteries [33] [34]. SEEQ Mobile Cardiac Telemetry (MCT) sensors can be used for 30 day ECG monitoring, are water resistant and can be worn during showering [35]. Devices such as this are a convenient type of ECG monitor and can be used to obtain the average, maximum and minimum heart rate, number of premature beats, longest R-R intervals and ECG recordings for patient triggered events [27].

Another patch type ECG device is the Netguard, developed by Mindray [36]. The device is composed of two custom electrodes worn on the chest. A drawback of the product was that it was limited to operating within range of its base station.

A similar device, V patch was developed by Intelesens [37]. The device performed in a similar way to Netguard, offering advantages of portability and a battery life of a week after a full charge. The shortcoming was the addition of a bulky base station, to be worn along with the device.

The integration of the sensing electrodes in a patch to form a Band-Aid adds to the list of existing smart devices to sense bio signals. It provides very convenient way ambulatory cardiac monitoring along with features like real time analysis and wireless ECG telemetry. Also, the monitoring can be complemented with functions like auto-trigger event handling and recurring event handling.

A glass bottle cap has also been implemented as a reusable, compact ECG patch electrode. Engineering World Health's ECG pads do not have to be thrown away after use; they can be boiled to sterilize them [38]. The conductive gel required to fix the pad on the chest can be made of water, flour or salt. There are several commercial research groups and companies that have developed variants of wearable patches as biomedical sensors [39].

The main advantage of using patch sensors is that they are easy to use, can be used for long-term ECG monitoring, require less maintenance, are less intrusive to daily activities and water-resistant [40]. In 2014, Barret et al. [34] conducted a study in which both Zio patch and SEEQ MCT systems were well accepted by the subjects, where 93.7% of them found the former more comfortable and 81% preferred them over Holter monitor. However, their disadvantages include high cumulative consumer costs and dependence on the device's company for accurate generation of a summary report. In one study by Shinbane et al. (in 2013) [41], the average time to diagnose a clinically relevant arrhythmia was found to be  $5.8 \pm 6.1$  days, therefore patch electrodes have a higher diagnostic efficacy than Holter and Event monitors. In another study conducted by Rosenberg et al. (2013) in 75 subjects [42], the use of Zio patch for  $\sim 10.8$  days resulted in the determination of 81% more arrhythmias compared with 24-hour Holter monitoring. The diagnostic yield efficiency using Zio patch increased from 43.9 to 62.2% when the duration of ECG monitoring was increased from 48 hours to  $7.6 \pm 3.6$  days [33].

Figure 1.5 shows the number of people using Holter monitors, event monitors, ILRs and patch sensors (MCT) annually [43]. A comparison of their features has been illustrated in Table 1.1.



Figure 1.5: Cardiac diagnostic landscape of various ambulatory ECG monitors [43].

Table 1.1: Features and diagnostic efficacy of various ambulatory ECG monitors

<b>Ambulatory ECG Monitors</b>	<b>Features [27]</b>	<b>Diagnostic Efficacy [43]</b>
Holter Monitors	<p>Are used in patients with daily or nearly daily symptoms. A Holter monitor report includes:</p> <ul style="list-style-type: none"> <li>• Total heart beats</li> <li>• Average heart rate</li> <li>• Maximum and minimum heart rates</li> <li>• Number of premature beats</li> <li>• Episodes of tachyarrhythmia and the etiology of the arrhythmias</li> <li>• Longest R-R interval</li> <li>• ST segment changes</li> <li>• Patient-triggered symptoms and any associated ECG findings</li> <li>• Hourly samples of the ECG tracing (eg. hourly samples).</li> </ul>	5 % to 13 %
Event Monitors	<p>Are used in patients with weekly to monthly symptoms. An Event monitor report includes:</p> <ul style="list-style-type: none"> <li>• Patient triggered ECG recordings.</li> <li>• Technician’s interpretation of the tracings.</li> <li>• Reported symptoms and their duration.</li> </ul>	<p>Syncope 6 % - 25 %</p> <p>Palpitations 39 % - 68 %</p>
Implantable Loop Recorders	<p>Are used in patients with infrequent symptoms (less than monthly). An implantable loop recorder report includes:</p> <ul style="list-style-type: none"> <li>• ECG tracings for each patient-triggered or auto-triggered event.</li> <li>• Technician's interpretation of the tracing.</li> <li>• Reported symptoms and their duration.</li> </ul>	45 % - 88 %

*Table 1.1: Features and diagnostic efficacy of various ambulatory ECG monitors (continued..)*

Zio Patch	<p>Are used for long-term non-invasive ECG recording. Zio patch report includes:</p> <ul style="list-style-type: none"> <li>• Average heart rate</li> <li>• Maximum and minimum heart rates</li> <li>• Number of premature beats</li> <li>• Episodes of tachyarrhythmia and the etiology of the arrhythmias</li> <li>• Longest R-R interval</li> </ul>	88 %
-----------	--	------

It should be noted that Zio patch exhibited a higher diagnostic efficacy than Holter monitors due to its extended monitoring duration. Cheung et al. (2014) [44] pointed out that 17% more reportable arrhythmia events were reported by Holter monitor than Zio patch on 24 hours of monitoring. This could be due to the single-channel system in the Zio patch as compared to multi-channel in Holter monitors. The differences in detection algorithms can also be responsible for the variation in diagnostic efficacy [40].

### **1.2.5 Other systems**

Other types of commercially available ambulatory ECG devices include EPIC sensors [45] [46], chest harnesses [47] and multi-purpose vest shirts [48].

An unconventional approach of using EPIC (Electric Potential Integrated Circuit) sensors was designed to track the heart and respiration rates for vehicle drivers. These sensors were mounted on the back side of the chair and operate by capacitively sensing the ECG. To ensure proper safety conditions, the person touches both the sensor and some metal at ground potential. A steady ECG signal can be obtained after a settling time of tens of seconds due to large time constants pertaining to large impedance parameters.

An ambulatory ECG chest harness was developed by Cleveland based Orbital Research, which can measure ECG up to 48 hours. No skin preparation or use of any conductive gel is required as dry electrodes are embedded in the chest harness. A direct contact with skin is made and the electrodes are held in place so as to reduce the effect of motion artefacts and improve the signal-to-noise ratio of Orbital's dry electrodes.

A vest shirt allows medical professionals to perform frequent and less costly fitness and ECG monitoring. The body temperature, motion and ECG can be measured through this shirt. Motion detection is evaluated using an accelerometer. A multipurpose shirt of this type can be seen in Figure 1.6.

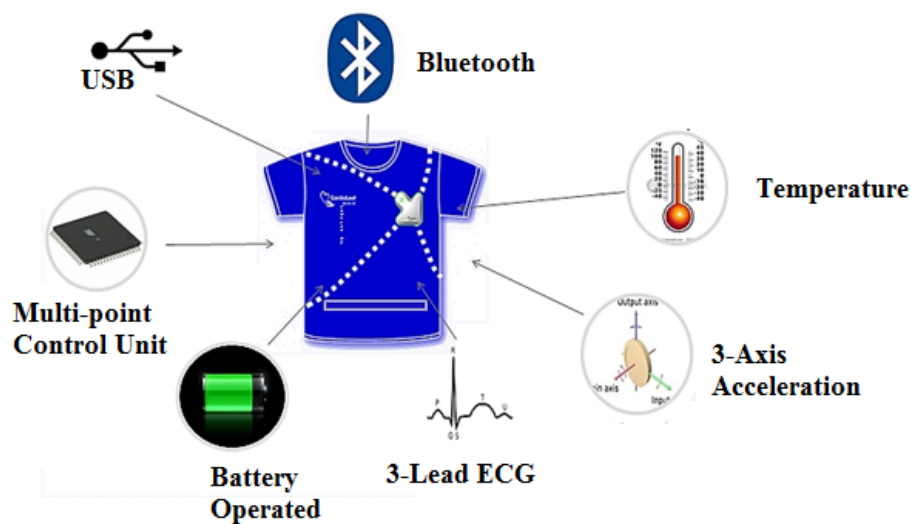


*Figure 1.6: Multipurpose vest shirt.*

Another proposition by IMEC (Belgium) for a wearable ECG device comprises of three leads along with a 3 axis accelerometer and Bluetooth radio for wireless transmission. It has a battery life of up to a month. However, the limitation of the device is that it doesn't transmit raw ECG data, but derived waveform information like heart rate, offset of P, QRS and T waves, etc. [49].

A comparison of Epic sensors, chest harness and multipurpose vest shirts has been presented in Table 1.2.

*Table 1.2: Advantages and disadvantages of commercial ambulatory ECG sensors.*

<b>Commercial ECG Sensors</b>	<b>Advantages</b>	<b>Disadvantages</b>
<b>Epic Sensors</b>	<ol style="list-style-type: none"> <li>1. Can monitor patient's alertness while driving.</li> </ol>	<ol style="list-style-type: none"> <li>1. Patient needs to sit still on the seat for a considerable amount of time to allow the circuit to settle.</li> <li>2. Very user specific, therefore can't be used when person is performing his/her daily activities.</li> </ol>
<b>Chest Harness</b>	<ol style="list-style-type: none"> <li>1. Can monitor ECG of the patient for up to 48 hours without using any adhesive or conductive paste.</li> </ol>	<ol style="list-style-type: none"> <li>1. Provide low electrical conduction.</li> <li>2. Their performance depends on the presence of sweat on the chest of the patient.</li> <li>3. Not comfortable for long time ECG monitoring.</li> </ol>
<b>Multipurpose Vest Shirts</b>	<ol style="list-style-type: none"> <li>1. Very comfortable to wear.</li> <li>2. Can monitor temperature, acceleration and ECG of the patient.</li> </ol>	<ol style="list-style-type: none"> <li>1. Prone to signal distortions due to the varying amount of skin-sensor gap.</li> </ol>

### **1.3 DESIGN OF ECG CIRCUITRY IN AMBULATORY DEVICES**

The earliest machines used to record ECG were large, cumbersome devices that required patients to immerse their limbs into bucket electrodes filled with saline solution.

Improvements in electrodes and instrumentation electronics, as well as the development of analogue to digital converters and digital computers have revolutionised the ECG. Many modern ECG's are small enough for a single person to easily carry and often include digital filtering techniques and computerised interpretation methods.

In a typical modern device using skin contact or non-contact electrodes, the differential voltages caused by the depolarisation and polarisation of the heart muscle can be detected. These signals are then amplified using an instrumentation amplifier. At this stage analogue filtering and further amplification takes place before the signal is digitised by an analogue to digital Converters (ADC). This digital signal can then undergo digital signal processing (DSP) such as filtering. Lastly the signal can be displayed, stored, and transmitted as required. A patient protection circuit protects the patient from potential electrical shocks or burns [50] [51]. A generalised ECG block diagram is shown in Figure 1.7.

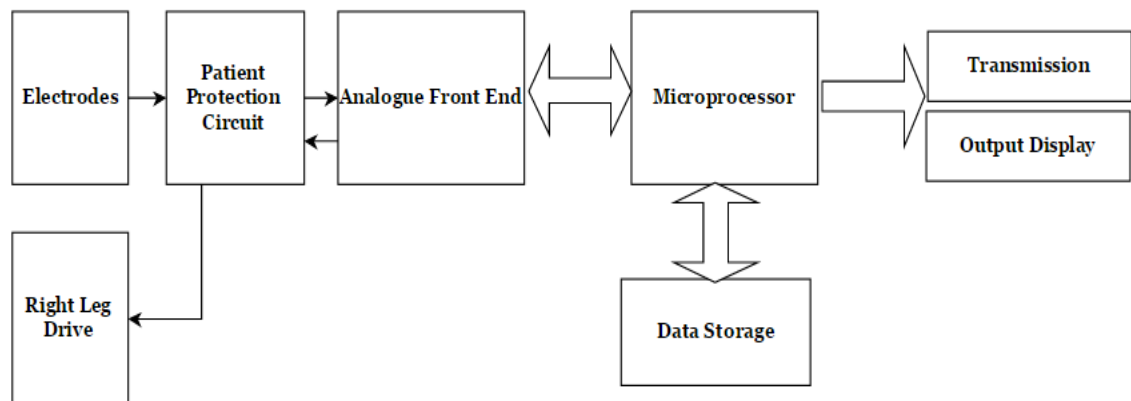


*Figure 1.7: Generalized ECG block diagram*

The first stage of ECG circuit consists of an instrumentation amplifier that amplifies the weak ECG signal, which has a typical amplitude of 0.5 mV and eliminates the high frequency noise received by the antenna (the leads connecting the electrodes to the amplifier) [52].

The instrumentation amplifier is essentially a combination of two buffer stages, which eliminates the need for input impedance matching. Chi et al. (2009) [53] integrated an instrumentation amplifier with an additional bootstrapping amplifier. Bootstrapping is

a method through which an operational amplifier restores its losses by increasing the input impedance and a part of the output of the instrumentation amplifier is used to drive the input. Integrated analogue front end solutions (IAFEs) available today have made it possible to produce high quality ECG recordings with very small, portable, low power devices. These IAFEs include a range of different features and, compared to discrete components, have excellent electrical characteristics and very high resolution ADCs at a relatively low cost in extremely small packages.

Another elementary aspect of the ECG circuit is the introduction of a band pass filter network with a lower cut-off frequency of 0.5 Hz and a higher cut-off frequency of 100 Hz, which corresponds to the typical frequency bandwidth of the ECG signal. A notch filter with a cut-off frequency of 50 Hz (or 60 Hz) can be used to remove interference due to mains power [52]. An inverter can correct negative QRS in the ECG. The introduction of a DC-offset stage with the band pass filter adjusts the offset of the recorded ECG waveform from the reference voltage, thereby making Analogue to Digital Conversion easier [52].

The main purpose of adding a driven right leg circuit to an ECG circuit is to reduce the common mode voltage in isolated and non-isolated measurements [54]. For a three lead configuration, the voltage ( $V_{cm}$ ) between the right leg and amplifier common (due to right leg impedance  $Z_{rl}$ ) is countered by the output of the driven right leg amplifier as shown in Figure 1.8.

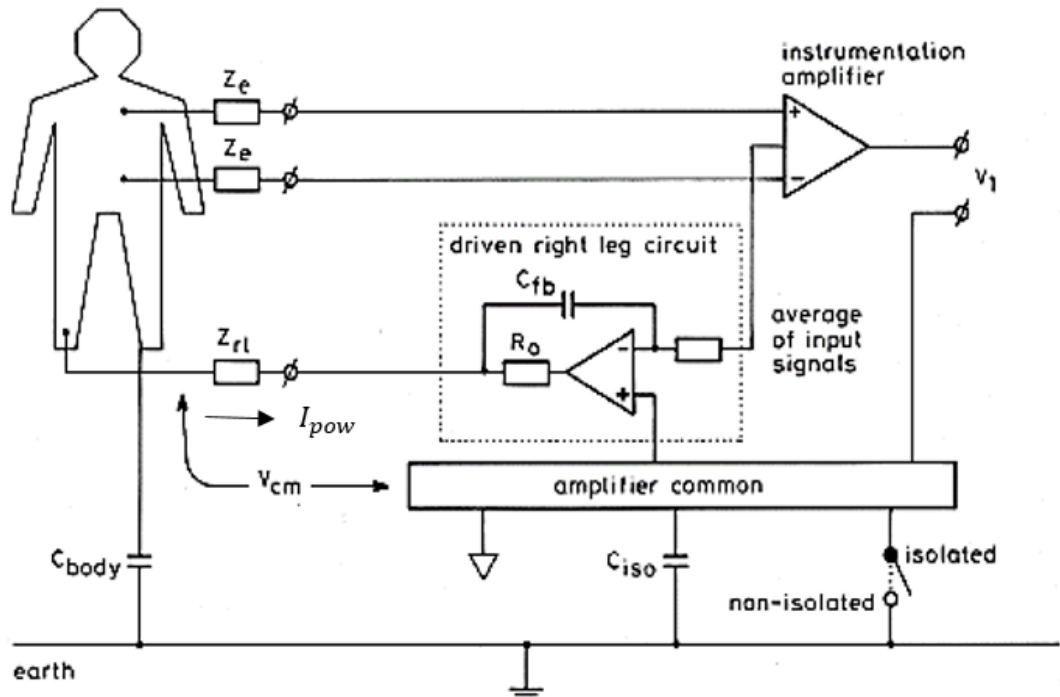


Figure 1.8: Use of a driven right leg circuit to reduce common mode voltage [54].

A sufficient galvanic isolation is necessary to ensure the safety of the patient if he or she contacts the mains line voltage, which is typically 220V, 50Hz [55],[56]–[58]. Bio-signals are distorted due to the presence of high levels of interference through the mains power supply. A basic model illustrating the purpose of an isolation mode amplifier can be seen in Figure 1.9.  $C_{body}$  is the capacitance between body and ground &  $C_{pow}$  is the capacitance between body and mains power causing the interference current  $I_{pow}$  to flow through  $Z_{rl}$ .

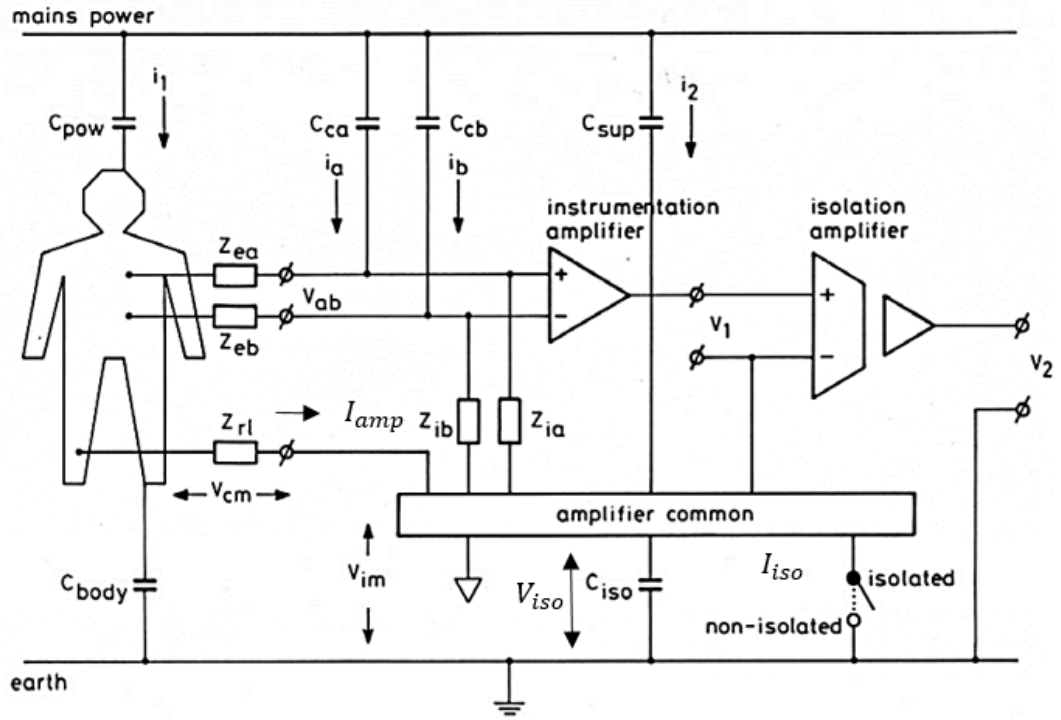


Figure 1.9: Schematic diagram of an isolated biomedical circuit [55].

In Figure 1.9,  $I_{amp}$  flows through  $Z_{rl}$  to the isolated common of the amplifier and via the isolated capacitance  $C_{iso}$  to the ground. The isolation amplifier gives an output voltage  $V_2$  which serves the purpose of suppressing the isolation mode voltage  $V_{im}$ . With the switch closed, the value of  $I_{iso}$  is reduced to a great extent, which in-turn reduces  $V_{iso}$ .

According to the International Electrotechnical Commission (IEC 60601) medical standards [59], the maximum allowable leakage current a patient should experience under the normal operating conditions is between  $10\mu\text{A}$  and  $50\mu\text{A}$ . Using this as the patient protection goal, the resistance necessary to limit the current can be calculated by:

$$\text{Resistance} = \frac{\text{Supply Voltage}}{\text{Leakage current}} \quad (1.1)$$

It is obligatory to shield the measuring cables to reduce the interference currents in the wire. The capacitance of the shielded cables can reduce the input impedance of the

amplifier. Thus, the shield is driven with the signal at the inner wire [60]. This mechanism is known as guarding.

#### 1.4 ELECTRODE TOPOLOGIES FOR ECG SENSING

A diagram representing four ways in which electrodes are used to measure biopotentials (electrode topologies) is given in Figure 1.10.

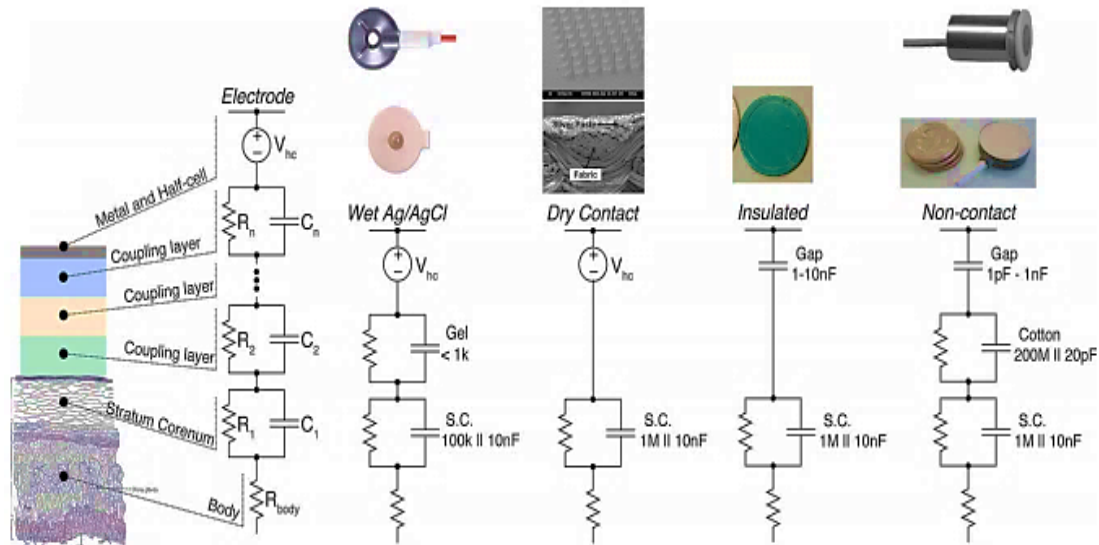


Figure 1.10: Various Electrode Topologies [61].

In ECG monitoring, conventional silver-silver chloride (Ag/AgCl) electrodes are widely used. These electrodes use a conductive paste to maintain good electrical contact between the electrode and the skin and typically incorporate an electrolyte gel or solution that buffers the electrolytic composition through the outer and inner layers of the skin. This poses problems for long term ECG monitoring, mainly because the gel might dry out over time [62]. Also, the use of electrolyte benefits from the region of application being as stationary as possible so that the electrode-skin impedance doesn't change if the electrolyte egresses due to movement of the patient. Moreover, the gel can cause allergic reactions for some patients' skin. Despite decades of research in non-contact electrodes, conventional wet Ag/AgCl electrodes are still used universally for clinical and research applications [63].

Dry electrodes make electrical contact with the skin but do not employ paste or gel media. Some flexible dry electrodes made of rubber, fabric or foam are considered to be quite appealing in terms of comfort of the patient and reducing motion artefacts by conforming to the body during motion. Although the use of dry electrodes is advantageous in terms of comfort for the patient, its use is limited as dry electrodes tend to fail to adhere to the skin for long times. The electrode-skin interface structure for dry and non-contact electrodes is much more variable than for wet electrodes. The skin-electrode interface can be described as a layered capacitive and conductive structure, with a series combination of parallel RC elements [64]. The performance of dry electrodes depends on the presence of sweat on the skin. The conventional notion that low resistance (high conductance) is essential for electrode performance could be misleading. There is a trade-off between the performance of dry and wet electrodes in the transient and stability periods. The wet electrodes perform well allowing for a short time to stabilize the electrochemical interface, whereas dry electrodes take a comparatively longer time to achieve a stable trace.

Conventionally, dry and wet electrodes are operated through direct physical contact with the skin. Capacitive sensing provides a non-contact mode of operation. The capacitive electrodes sense the signals with a significant gap between the sensor and the skin. The signal is essentially coupled through an insulation media such as hair, clothing or air. Electrostatic frictional effects also contribute to the input voltage noise. A coupling capacitance is formed between the skin and the electrode. The thickness of the dielectric between the skin and the electrode, and the surface area of the plates decides the value of coupling capacitance [65]. Conductive threads when integrated into garments can act as a capacitive sensor and are also classified as textile-based sensors or textile electrodes. They have become a desirable form of ambulatory ECG monitoring. Although they provide comfort to the patient, their use is limited as they provide high skin contact impedance due to their asymmetrical surfaces [62], [66]–[70].

Knitting or embroidering of conductive yarns has been commonly used for textile ECG measurements. Active electrodes were fabricated by Chi et al. (2010) [64], in the form of a layered structure with a single non-woven substrate sandwiched between two layers as shown in Figure 1.11.

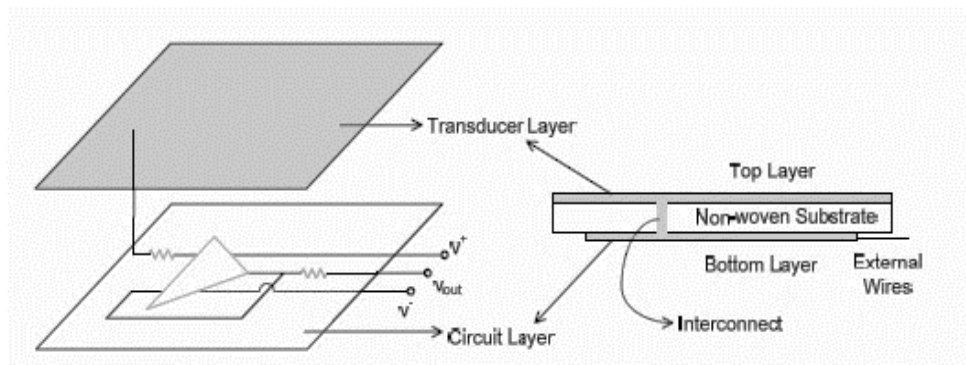


Figure 1.11: Fabrication of active electrodes [64].

The basic purpose of active electrodes was to eliminate the variation effect of skin electrode contact impedance arising from movement of the patient. The use of active electrodes in place of passive electrodes successfully reduced the motion artefacts induced in ECG while performing vigorous activities like jogging [62].

A comparison illustrating the advantages and limitations of three types of widely used electrodes: wet, dry and capacitive has been provided in Table 1.3.

Table 1.3: Comparison between wet, dry and capacitive electrodes for long-term bio sensing.

Electrode types	Benefits	Disadvantages
Wet	Makes best electrical contact with skin due to presence of electrolyte.	<ul style="list-style-type: none"> <li>• Gel might dry over time.</li> <li>• Gel might cause an allergic reaction on patient's skin.</li> </ul>
Dry	No adhesive required.	<ul style="list-style-type: none"> <li>• Low electrical conduction.</li> <li>• The performance depends on the presence of sweat on the skin.</li> </ul>
Capacitive	<ul style="list-style-type: none"> <li>• Comfortable for the patient.</li> <li>• Easy to be woven or embedded into a fabric.</li> <li>• Biocompatible</li> </ul>	<ul style="list-style-type: none"> <li>• The resistance offered by the fabric decreases the signal quality.</li> <li>• A coupling capacitance is formed between the skin and the electrode.</li> <li>• Provide high skin contact impedance.</li> </ul>

The rate of electrochemical processes occurring between the electrode and the skin surface is directly proportional to the area of their interface. For this reason, porous polymer wet electrodes that provide an immensely high electrode/electrolyte interaction area are favourable to implement in an ambulatory ECG system [71]. Conformal polymer electrodes stuck onto the chest of the patient using an adhesive can reduce inaccuracies due to change in subject-sensor gap in capacitive electrodes. Also, they provide a better electrical conduction than dry and capacitive electrodes. Lee (2014) [72] developed thin flexible polymer electrodes using carbon nano tubes (CNTs) and polydimethylsiloxane (PDMS) with similar mechanical properties to the skin. The

advantage of using CNT based electrodes is that they penetrate the wrinkles of the skin and maintain a steady contact. This leads to an increase in the contact area, thereby reducing the contact impedance. CNT polymer electrodes are discussed further in the next section.

The choice of electrodes for biomedical applications, especially ECG monitoring, depends not only on the comfort that they offer to the patient, but also on the quality of the signal obtained. The skin-electrode interface decides the operational characteristics of any electrode system in conjunction with the properties of the electrode material.

## **1.5 CARBON NANO TUBES FOR ECG AND STRETCH SENSING**

Carbon nano tubes (CNTs) are an allotrope of carbon which are cylindrical in shape and are potentially useful in a variety of applications like optics, nanotechnology etc. There are two main kinds of CNTs: single-walled CNTs (SWCNTs) and multi-walled CNTs (MWCNTs). They are cost effective and good conductors of electricity [73]. The CNTs are tangled and assembled randomly, therefore, they exhibit good electrical contact if embedded in a polymer electrode when the polymer is stretched or bent [72].

Cai et al (2013) [74] employed stretchable CNT/PDMS elastomers for human motion detection. One of the methods proposed to fabricate CNT/PDMS electrodes is by dispersing the CNT in PDMS by mechanical force as explained by Jung et al. (2012) [75]. In order to ensure a homogeneous dispersion of CNT in PDMS, the mechanical force must be greater than the van der Waals forces of attraction between CNTs.

Different concentrations of CNTs were dispersed in PDMS by Jung et al (2012) [75], and qualitatively comparable ECG signals were obtained on adding 4.5 wt% of CNT in PDMS. The CNT/PDMS composites of different concentrations (1 wt%, 1.5 wt%, 2 wt% and 4.5 wt %) were stretched from 5 % to 45 % at constant extension velocity; and least change in conductivity with stretching was observed for composites with 4.5 wt% CNT in PDMS.

Electrodes made of CNT, graphene and PDMS fabricated for wearable ECG monitoring by Wang et al. [76] exhibited good electrical performance with a concentration of 6% CNT and graphene in PDMS with a mixing ratio of 9:1 (CNT:graphene).

Lee (2012) [77], fabricated ECG sensing electrodes by wetting the CNTs before mixing them with PDMS. This was done to detangle the CNTs to improve the electrical conductivity. Strong forces of attraction between the CNTs lead to CNT clumping. These agglomerates disturb the formative electrical networking in the electrodes. An effective way to disperse CNTs in PDMS was performed by sonication of CNTs in an organic solvent N-methyl-2-pyrrolidone (NMP) [78]. The ultrasonic agitation or mixing of up to 4 vol. % of CNTs with NMP prior to its dispersion in PDMS showed a good homogeneity of CNTs in the elastomer [78].

A controlled deposition of SWCNTs in N-N dimethylformamide (DMF) was performed by Liu (1999) [79]. The suspensions of CNTs in DMF were found to be stable and could be stored at room temperature for several months. From various reports [80]–[82], it can be observed that the CNTs can be detangled in both DMF and NMP solvents to a significant degree [83]. Both DMF and NMP are hygroscopic solvents [84], however DMF is cheaper and tends to spontaneously break down over time [85].

## **1.6 SOURCES OF NOISE IN AMBULATORY ECG SYSTEMS**

Several noise sources having different frequency ranges are associated with ambulatory ECG monitoring. The low frequency noise is called the baseline wander, medium frequency noise includes power frequency interference and high frequency noise can be substantially due to electromyography (EMG) signals. The non-physiological sources of artefact such as external electromagnetic signals and power line frequency can be successfully removed with the use of a driven right leg (DRL) circuit, as discussed in section 1.3. In modern ECG devices, digital filters are typically used to eliminate baseline wander from ECG waveforms. Artefacts in ECG are also generated due to the contraction of the muscles in the vicinity of the electrodes [86], which can be reduced to some extent by proper electrode design and placement [87].

Holter monitors have electrodes attached with tape or adhesives, which might cause skin irritation and discomfort to the patient. Moreover, the moist inner pad of the Ag/AgCl electrodes used with Holter monitors can dry up over time, leading to a poor connection.

Cable movements during exercise can introduce noise, which can be reduced by using a unity gain buffer amplifier (voltage follower) at each electrode [88]. The capacitive

mismatch in active non-contact electrodes can be significantly reduced by bootstrapping [53]. Other sources of noise include contact noises, which are introduced in ECG signals due to disturbances in electrode-skin impedance caused by poor adhesion and conductance of the electrodes [89].

Artefacts due to motion in all ambulatory devices is inevitable. Motion artefacts refer to the noise generated in the ECG due to movement of the electrodes. Ambulatory devices can mistake motion artefact for fatal arrhythmias such as ventricular fibrillation (VF) or ventricular tachycardia (VT) and may trigger a false alarm [90]. An example showing the effect of motion artefacts on ECG is illustrated in Figure 1.12.

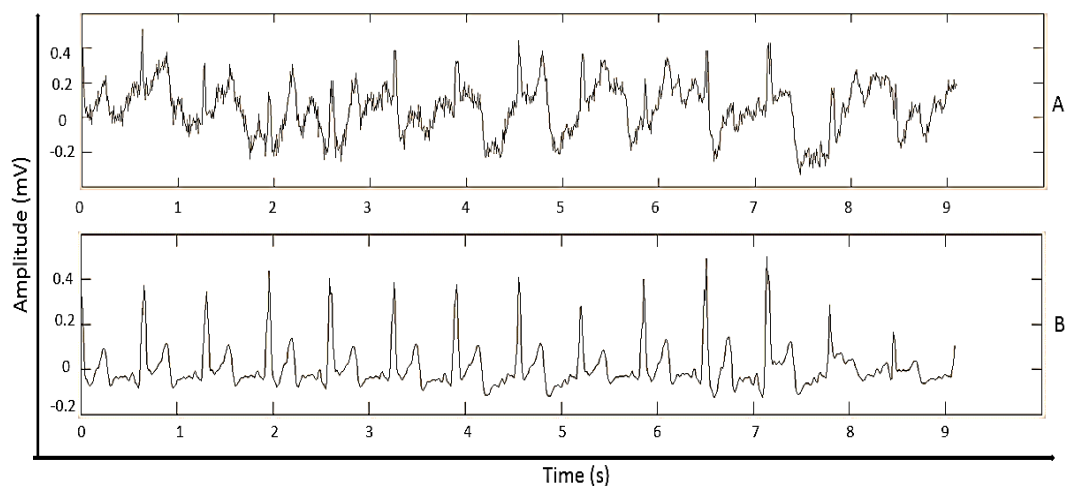


*Figure 1.12: A: ECG with motion artefacts, B: ECG without motion artefacts.*

ECG motion artefacts are generated due to such things as tremor or shivering, exercising and heavy breathing. In addition to measurement artefacts such as electrode-skin interface changes, physiological artefacts resulting from this motion also occur and are generated through the skin; therefore different measures such as skin abrasion and mechanical stabilization are adopted to minimise motion artefacts [86]. However, skin abrasion may cause skin irritation or skin infection in some patients. Motion artefacts strongly affect the ECG morphology and remain one of the major problems in short-term and long-term ECG monitoring.

Although many ambulatory ECG monitoring biosensors have been commercialised to date, a major problem is still faced due to patients performing motion related activities

that introduce unwanted signal noise and makes monitoring less effective [91]. The frequency spectrum of the motion artefact overlaps the ECG, therefore, it is the most difficult form of noise to be removed from the ECG signals [92]. Beyond skin abrasion, various motion biosensors used to date to remove motion related noise don't respond well in cases where the patient is performing vigorous exercises [93].

Approaches to motion artefact reduction include modification of materials involved in the skin electrode interface and by implementing models and algorithms for reducing motion artefact contribution [94], as discussed in the following sections. While much research has been conducted to remove time invariant noise, the removal of motion induced artifacts remains an unsolved problem [95]. The latest motion artefact rejection techniques employ motion tracking devices to identify motion and incorporate their use into adaptive algorithms like neural networks [96, p.] and fuzzy-rule-based adaptive nonlinear filters [97] to adjust digital filter coefficients. Various motion sensing and signal processing techniques employed to eliminate motion artefacts from ECG signals have been discussed in sections 1.7 and 1.8 respectively.

## **1.7 MOTION TRACKING**

Motion tracking finds use in diverse applications such as head tracking, in the sports industry for measuring the performance of athletes, in the entertainment industry for movie-making and in development of video games [101]. Motion tracking can be employed to eliminate motion artefacts in ambulatory ECG measurements. The currently used motion tracking devices for this application are described in this section.

### ***1.7.1 Accelerometers***

Several studies identify motion artefacts in ECG by employing external devices such as accelerometers. The accelerometers are used predominantly to measure motion parameters in a mechanical model of a system. For the accurate detection of motion, 3-D spatial measurements are taken to consider the effects in each orthogonal plane. This can be achieved by using 3-axis accelerometers and have been proposed to realize adaptive motion artefact reduction. In 2008, Yoon and Min [100] implemented an adaptive filtering technique to estimate the subject's movement using a 3D accelerometer. The motion information was then subtracted from the ECG signal to

derive a refined ECG output. In Figure 1.13, the 3 orthogonal axes-  $U$ ,  $V$  and  $W$  constitute the acceleration coordinates, while  $U'$ ,  $V'$  and  $W'$  account for global Cartesian coordinates. The chest of the subject is aligned in the  $V'$ - $W'$  plane, and it was presumed that ECG was generated in the  $U'$  axis. The motion artefact will be aligned along  $V'$ -axis when the subject is walking or jumping.

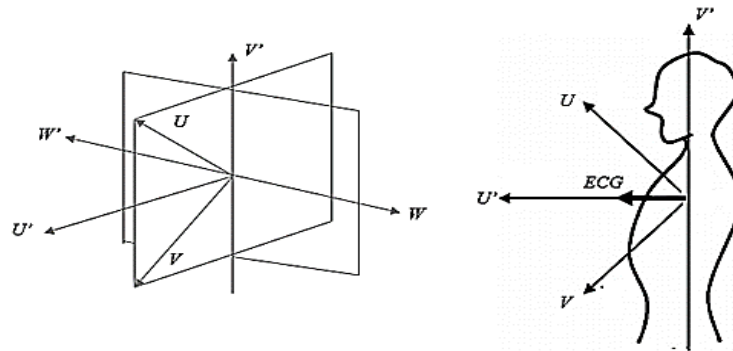


Figure 1.13: Diagrammatic representation of the coordinate system in a 3-axis accelerometer.

A tri-axial accelerometer offering the measurement of both dynamic and static acceleration was used by Kishimoto and Kutsana (in 2007) [101] to sense the motion artefact in ECG during sleep. In 2011, Liu [102] used the signals from an accelerometer to cancel the motion artefacts through adaptive filtering in a portable ECG recorder with Bluetooth technology. From experiments conducted by Raya and Sison [103], it was inferred that the use of a single axis accelerometer (particularly vertical axis) was sufficient for motion artefact cancellation. This was supported by the fact that the major kinematic acceleration in humans was found in vertical direction.

### 1.7.2 Linear variable differential transformers (LVDTs)

Kang (2007) [62] made use of linear variable differential transformers (LVDTs) for the estimation of changing position and deformations due to stretching while measuring ECG. A double substrate sensor structure with stretchable and non-stretchable textiles was implemented, as seen in Figure 1.14. Fine magnetic wires were stitched on the stretchable area. The convention has been to employ piezoelectric films due to their flexibility; however, their use is limited only to detection of micro displacements. As

the sensor stretches, two rectangular spirals slide over each other changing the mutual inductance between them.

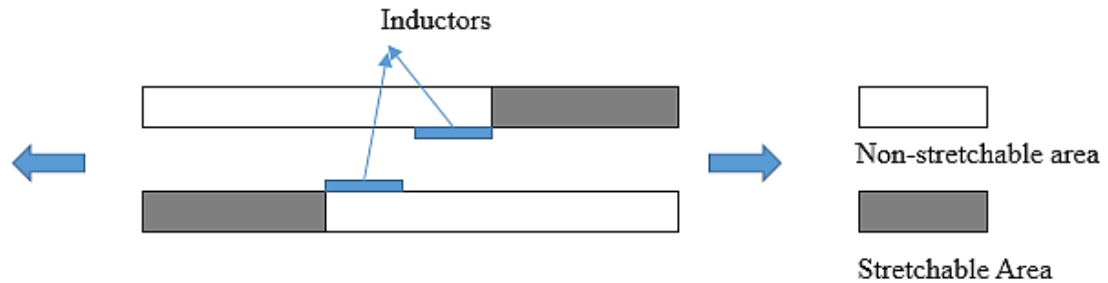


*Figure 1.14: Single Inductive Linear Variable Differential Transformers.*

Non-washable fabric active electrodes were employed for long term monitoring of respiratory and ECG signals, therefore electrode sensors may malfunction due to sweat and other water sources. Screen printing technology was implemented to incorporate the sensors into textiles, which may dramatically reduce the inductance due to geometric limitations of screen printed lines on rough textile substrates.

### **1.7.3 Gradiometers**

Non-contact electrodes with a polymer over-layer of thickness 0.18 mm were fabricated from a copper printed circuit board for measurement of ECG signals by Peng (in 2014) [104]. Dual and quad gradiometer electrode configurations were devised to account for a subject's activity or ambient modulation. The output of dual electrode gradiometers was taken as the difference between the positive and the negative voltages. Whereas for quad electrodes, the output was measured by calculating the difference between the diagonal summations.

The obtained signal depended upon certain parameters like the distance between the subject and the sensor 'h', and the angles  $\theta_x$  and  $\theta_y$ , as observed in Figure 1.15. Change in these parameters modulated the source capacitance by changing the subject-sensor gap. The source capacitance was a series combination of the capacitance from the polymer over-layer, air gap and the subject's clothing.

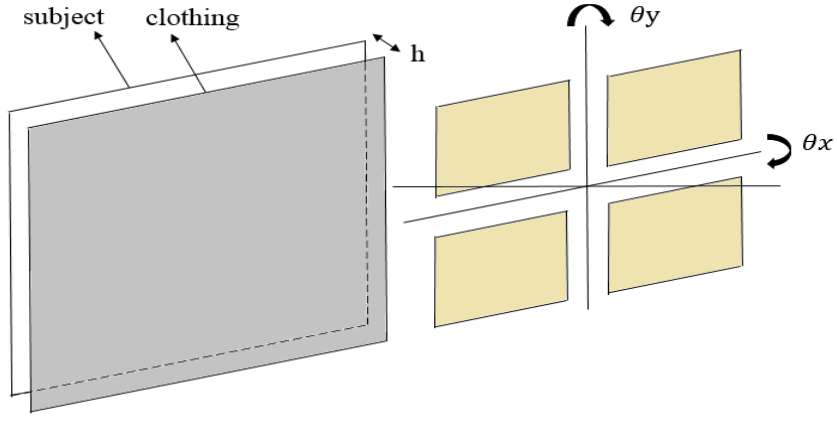


Figure 1.15: Parameters affecting the source capacitance of the gradiometer (quad configuration).

The ECG signals were obtained from two gradiometer electrodes and conventional Ag/AgCl electrodes. Using the measured R-R intervals, the average beats per minute (bpm) were determined along with its standard deviation. The performances of dual and quad gradiometer configurations ( $\Delta D$  and  $\Delta Q$ ) were calculated using:

$$\Delta D (\%) = \frac{bpm_{dual} - bpm_{Ag/AgCl}}{bpm_{Ag/AgCl}} 100 \quad (1.2)$$

$$\Delta Q (\%) = \frac{bpm_{quad} - bpm_{Ag/AgCl}}{bpm_{Ag/AgCl}} 100 \quad (1.3)$$

The performance of dual and quad electrode configurations were evaluated at subject-sensor gaps of 5, 15, 21 & 28 mm. The average values of  $\Delta D$  and  $\Delta Q$  were found to be 0.38% and 0.345% respectively. The downside of this study was that bpm was used as a performance evaluation index instead of SNR.

#### 1.7.4 Optical sensors

Image-based motion tracking techniques involve feature selection for tracking objects in consecutive frames using colour based comparison, edge detection, optical flow methods or texture intensity methods [105]. Several point detection techniques in

*MATLAB*<sup>®</sup> employ feature tracking algorithms like Kanade Lucas-Tomasi (KLT) and surface feature detection. Another popular technique ‘estimate geometric transform’ returns a 2D geometric transformed image and employ M-estimator Sample Consensus (MSAC) algorithm to map the initial image to the final image [106], [107].

A sensor to estimate skin stretch simultaneously with ECG was developed by Liu in 2007 [108], as seen in Figure 1.16.

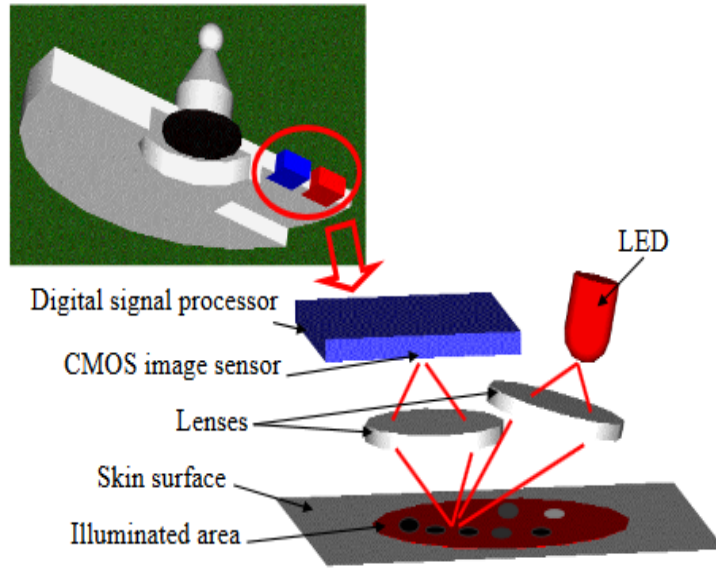


Figure 1.16: : Optical Components integrated in an electrode [108].

The surface underneath the sensor was illuminated using a light emitting diode (LED), and the displacement of the skin from the reference was measured using a CMOS image sensor. Assuming  $L$  as the distance between the fixed edge and the imaging area, the optical sensor output was calculated by:

$$L = \sqrt{(x - x_0)^2 + (y - y_0)^2} \quad (1.4)$$

where  $x$  and  $y$  are the optical sensor outputs and  $x_0$  and  $y_0$  are initial optical sensor outputs.

These uniaxial displacements were used to adjust the filter coefficients of an adaptive filter employing a least mean squares algorithm (LMS), first devised by Widrow and Hoff in 1960 [109]. The LMS algorithm was used to minimize the difference between

the noisy ECG and the output of the optical sensor. This can be explained through the following set of equations.

Considering  $s$  as the clean ECG signal,  $a$  as the movement artefact and  $L$  as the optical sensor output, the noisy ECG signal  $d$  can be given as:

$$d = s + a \quad (1.5)$$

The adaptive filter error can be given as:

$$e = s + a - L \quad (1.6)$$

The objective of the filter was to minimize  $a - L$ , which can be achieved by minimizing the statistical expectation (E) of the square of the error [110].

The expectation of square of the adaptive filter error can be represented by  $E(e)^2$  as shown in equation (1.7)

$$\begin{aligned} E(e)^2 &= E(s + a - L)^2 \\ &= E(s)^2 + E(a)^2 + 2E(sa) - 2E(sL) + E(a - L)^2 \end{aligned} \quad (1.7)$$

As ECG and noise are assumed to be uncorrelated, therefore, the equation (1.7) can be re-written as:

$$E(e)^2 = E(s)^2 + E(a - L)^2 \quad (1.8)$$

Thus, reduction in motion artefacts can be achieved by minimizing the filter's error  $E(e)^2$ . The ECG signals were acquired from the chest of the subject as shown in Figure 1.17. The optical sensor was attached by double-sided adhesive in the vicinity of the electrode on the left forearm.

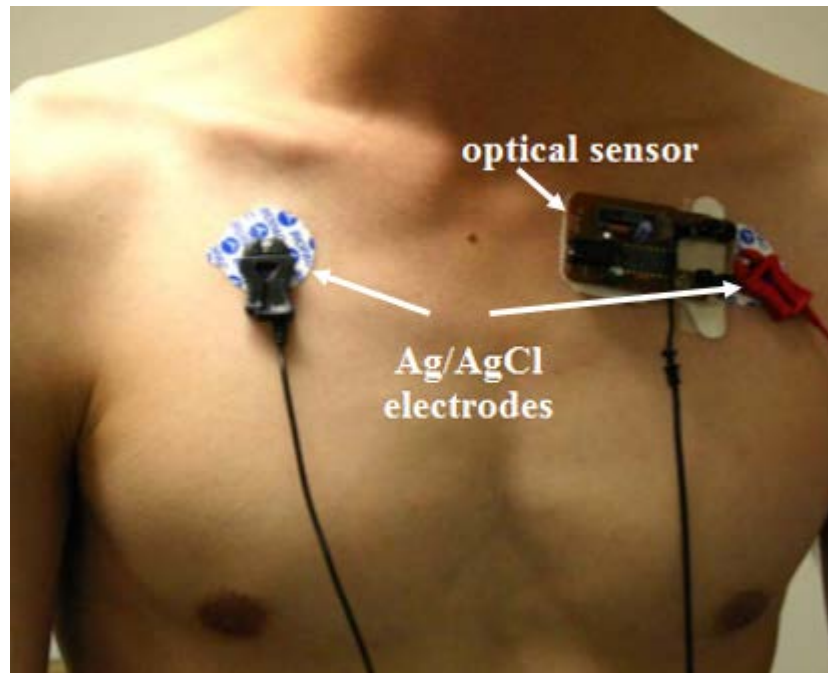


*Figure 1.17: Placement of electrodes and optical sensor [108].*

## **1.8 PCA AND ICA FOR MOTION ARTEFACT REJECTION**

In addition to measurement hardware, software techniques have also been employed for motion artefact rejection in several studies and are discussed in this section.

PCA and ICA are widely used for noise cancellation in ECG signals. In PCA, the data matrix is decomposed into a set of orthogonal components arranged in the order of their importance. In other words, if the first component of PCA is the best representation of the data set, then the second component will be the second best representation and will be orthogonal to the first component. In ICA, uncorrelated components of the data are generated. ICA aims at producing such non-Gaussian transformations which assure that the output signals are statistically independent [111]. The basic concept involved in the working of PCA and ICA has been explained in the following chapters. The main difference between PCA and ICA is that the former decomposes the data into a set of uncorrelated components, whereas the later provides a set of statistically independent components.

Ramaswamy (2004) [112], implemented PCA by adaptively segmenting uni-channel ECG signals. A higher increase in SNR was observed when the signal was corrupted with more noise.

Romero (2010) [111], implemented PCA on noisy ECG signals (8-channel) obtained from 5 healthy subjects. The three most significant principal components showing the highest correlation with the clean ECG were chosen. The performance of PCA was better when more principal components were retained in cases of highly corrupted signals. A reduction in signal to noise ratio (SNR) was observed on reducing the ECG channels from 8 to 2. Therefore, the performance of PCA was found to be dependent on the number of ECG measurements in the input data set.

Romero (2011) [114], investigated the performance of PCA and ICA in the context of motion artefact rejection from ECG signals acquired for 10 seconds. It was observed that both PCA and ICA showed similar performances when the SNR of the noisy ECG was up to 2dB, while ICA outperformed PCA for SNRs below that value.

In another study [39], 37 sets of 10 seconds of ECG signals were obtained from healthy subjects using a 3-lead ECG system. Two motion rejection algorithms were explored: multi-lead ECG de-noising based on ICA, and adaptive filtering using electrode-tissue impedance (ETI). The signal quality was measured by using two parameters: correlation coefficient and positive predictivity. A significant noise reduction with a 10% increase in correlation with clean ECG was reported on implementation of ICA. The statistical significance or the positive predictivity of the proposed beat detection algorithm was increased from 93% to 100%.

Alkhidir and Sluzek (2015) [115], measured ECG signals by placing textile electrodes on the wrists of a subject. The motion artefact was generated in the wrist by performing some random hand movements. Two additional electrodes were placed on the left wrist near the ECG sensing electrode to estimate the bio potential difference across the electrodes due to hand movement. The motion artefact removal was conducted by performing adaptive filtering and ICA. The motion information acquired by the additional electrodes was used to adjust the filter coefficients of the adaptive filter. Adaptive filtering and ICA were implemented by using a normalized LMS error cancellation algorithm and Fast ICA package in *MATLAB* respectively. To assess the performance of adaptive filtering and ICA, SNRs were computed before and after filtering. The SNR achieved after adaptive filtering (3.87dB) was higher than ICA (0.394dB).

A comparative analysis of ICA and adaptive filtering was performed by Rehman and Khan in 2016 [116]. Due to its non-iterative nature, ICA performed better than the three iterative gradient based algorithms employing LMS, normalized LMS (NLMS) and recursive LMS (RLMS). NLMS is generally used to normalize the LMS filter's input to attain better filter stability, whereas RLMS (also known as RLS) recursively finds the coefficients to minimize the linear least squares cost function related to the input signals.

Two ICA algorithms: Efficient Fast ICA (EFICA) and Joint Approximation Diagonalization of Eigen Matrices (JADE) were used for motion artefact removal from emergency ECG signals by Granegger and Werther (2011) [117]. The sensitivity of both the algorithms was found to be above 99.5%.

The Fast ICA algorithm was applied by Jain and Shakya (2014) [118] to denoise baseline wander noise from ECG signals. The de-noising baseline wander noise was simulated in *MATLAB*. An average improvement of 1.26dB in SNR was estimated.

For bio-signals such as ECG, ICA has been found to be increasingly used since it does not require any prior knowledge of the system [119] [120]. In one study [121], the performance of various ICA algorithms like Cardoso's joint approximate diagonalization of eigen matrices (JADE), Hyvarinen's fixed point method (Fast ICA) and Comon's algorithm were compared and JADE and Fast ICA were found to perform slightly better than Comon's algorithm. Puntonet and Prieto (2004) [122] performed a comparative study between Fast ICA and JADE on four synthetically generated EMG signals mixed together. The muscle contractions in the EMG signals were simulated from different numbers of motor units (3, 5, 8 and 10). It was observed that JADE performed considerably better than Fast ICA in separating the synthetically generated EMG signals into the contribution from different motor units. Interestingly, the effectiveness of JADE increased on increasing the number of source signals. However through experiments performed by Matic (2009) [123], it was observed that the performance of Fast ICA was marginally better than JADE in QRS wave detection. Both JADE [124]–[126] and Fast ICA [127]–[129] maximise the independence of their components by using a fixed point algorithm and jointly diagonalizing fourth order cumulant tensors respectively [130].

A general model representing the working of JADE algorithm for ECG filtering has been explained in a later chapter.

## 1.9 OTHER MOTION ARTEFACT REJECTION ALGORITHMS

Several techniques other than PCA and ICA have been employed for elimination of motion artefacts from biomedical signals.

The wavelet transform is a proven tool for efficient filtering of signals in bio-signal processing [131]–[133]. It involves the decomposition of the signal, followed by its thresholding and then the proper reconstruction [134]. One study [135] used different wavelets to reduce motion artefacts from corrupted photo-plethysmography (PPG) signals. The wavelets used included the Daubechies, bi-orthogonal, symlet, Coiflet etc. out of which the Daubechies produced the best performance. In a study performed by Foo (2006) [136], the adaptive filtering technique was found to be more efficient in removing motion artefacts from PPG signals as compared to discrete wavelet transformation.

The wavelet transform technique combined with ICA was implemented by Abbaspour (2015) [137] for motion artefact rejection. Motion artefact was added to 30 minutes of simulated ECG signal which was then filtered using wavelet transform. After that, ICA was used on the wavelet transformed signal and a higher SNR of 14.2 dB was achieved compared to 13.85 dB using only wavelet transform.

Adaptive filtering is also a common filtering technique for the treatment of bio signals. Thakur and Zhu, 1991, applied it in foetal ECG recording, cancelling the cardiogenic interference signal from that obtained from impedance plethysmography (IPG), noise reduction from muscles, cancelling the 60 Hz power supply interference and ECG motion artefact reduction [92].

Generally, adaptive filtering is realized by the subtraction of the noise from the received signal in an adaptive manner. The noise essentially is the unwanted component, here being the motion artefacts. The technique employs two inputs, one being the overall ECG signal, and the other being the noise source. As seen in Figure 1.18, the adaptive filter estimates the noise from its source sensor which is then subtracted from the first input [108].

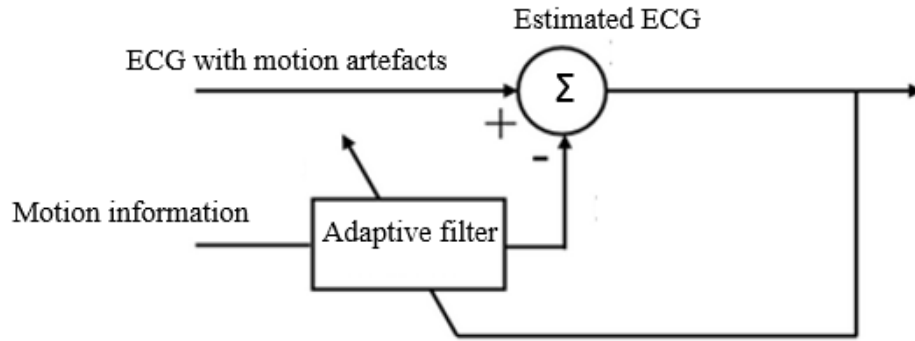


Figure 1.18: Signal processing using adaptive filtering.

Many previous studies have utilised adaptive techniques incorporating adaptive neural networks [96] and fuzzy based adaptive non-linear filters [97] to check the ECG for motion artefacts.

Although the adaptive filters are easy to implement in modern microprocessors, they are more useful for performing rhythm analysis than diagnostic analysis in ambulatory ECG monitoring. It is hard to identify the signal and noise components from an ECG measurement contaminated with large amounts of motion artefact, as it has the same morphology as the QRS complex in the ECG [138]. Kigawa and Oguri [139] implemented a neural network to differentiate between ECG signal and motion artefact.

ECG signal with motion artefacts were modelled by Khambalkar (2012) [140] who then used a Wiener filter for motion artefact cancellation and its performance was compared with an adaptive filter employing LMS. The Wiener filter does not require an additional sensor like an adaptive filter and use the statistics of the signals to determine the filter coefficients. The noise signal was simulated in *MATLAB* using the obtained ambulatory ECG signal. The average improvement in SNR after the implementation of Wiener filter was found to be 13.9 dB.

In another study [141], a discrete time extended Kalman filter (EKF) was implemented to denoise the ECG signal. A set of state space equations in terms of phase ( $\theta$ ) and amplitude ( $z$ ) to model ECG were developed as shown in equations (1.9) and (1.10).

$$\theta_{k+1} = (\theta_k + \delta) \times \text{mod } 2\pi \quad (1.9)$$

$$z_{k+1} = \frac{\sum_i (\delta \alpha_i \omega)}{b_i^2 [\Delta \theta_i \exp\left(-\frac{\Delta \theta_i^2}{2b^2}\right)]} + z_k + \eta \quad (1.10)$$

Here  $z_k$  represents the ECG magnitude at time 'k' at a sampling period  $\delta$ ,  $\Delta \theta_i = \theta_k - \theta_i \text{ mod } (2\pi)$  where  $\theta$  is the phase variable and summation  $i$  is taken over a number of Gaussian functions which can be used to get a desired ECG signal. Here summation  $i$  is taken over P, Q, R, S and T waves of the ECG signal and  $\theta_i$  represents the Gaussian centre,  $\alpha_i$  denotes the Gaussian peak and  $b_i$  represents the Gaussian width. The other parameters  $\omega$  and  $\eta$  represent the process and white Gaussian noise respectively. Both are assumed to be stationary in this equation.  $z_k$  and  $\theta_k$  represent the state space equations of the extended Kalman filter. The dynamic ECG model is linearized continuously by updating the state equations with time. In an extended Kalman filtering approach, *a priori* information about the ECG dynamics is used to extract the ECG signal from the background noise. EKF is a prediction based model which requires the formation of complex state space equations under different circumstances. The limitation of using EKF is that it only works for systems with a unimodal distribution (having a single maximum), which can prove to be a problem in biomedical applications [142].

## 1.10 EFFECT OF PADDING ON MOTION ARTEFACT REDUCTION

The electrode contact pressure with the skin and the surface moisture have been considered as two main factors influencing the skin-electrode impedance [143]–[145]. According to experiments performed by Kim et al. (2008) [146], an improvement in the ECG signal quality was observed when higher contact pressures were applied on the electrodes.

Comert et al. (2013) [147], recorded a two channel ECG from the chest of a subject as shown in Figure 1.19.

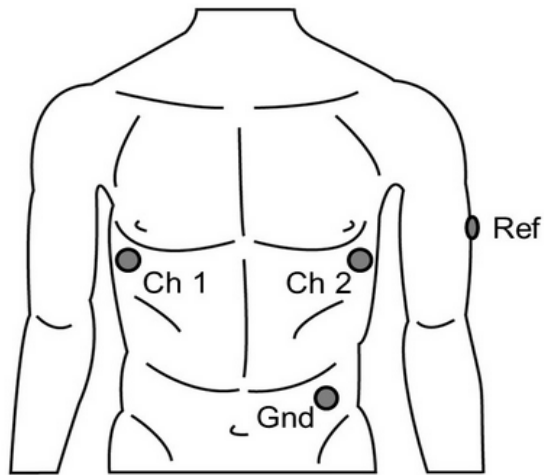


*Figure 1.19: Depiction of electrode locations [147].*

A reference electrode was placed on the lateral upper arm location, where motion artefact was introduced by random arm movements. This was done to simultaneously record ECG signal with motion artefacts (between reference and Ch1) and without motion artefacts (between Ch1 and Ch2). The noise due to motion was estimated by calculating the difference in detected R peaks between both signals. A reduction in noise was observed when a pressure of between 5 and 25 mmHg was applied on the reference electrode using a foam pad. Pressure exerted on the foam pad greatly influenced the motion artefact depending on the foam material and the intensity of pressure exerted. The electrode-skin impedance was also measured to study the change in impedance with change in pressure. The effect of increasing electrode pressure on motion artefact related parameters is illustrated in Figure 1.20.

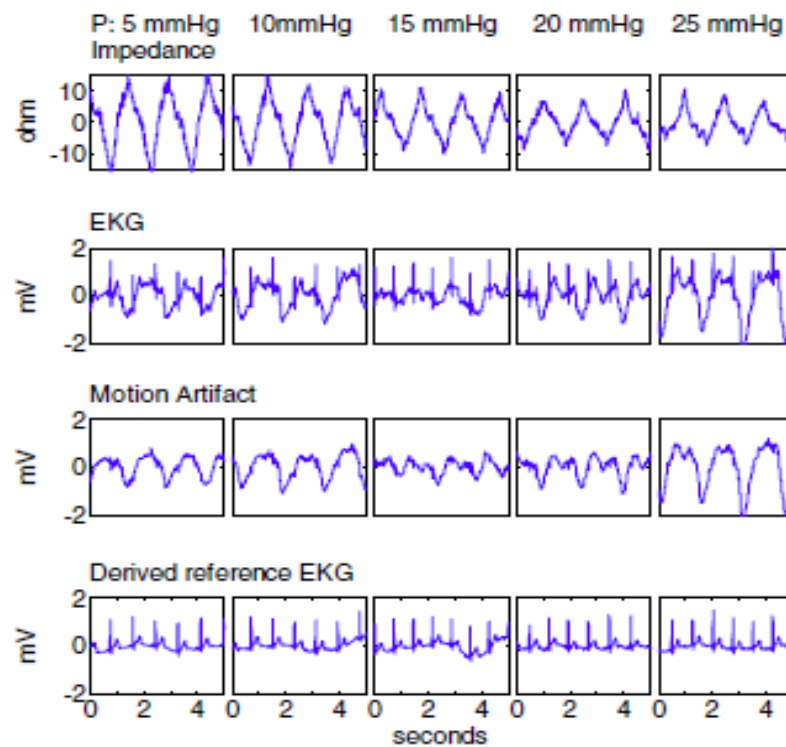


Figure 1.20: Effect of increasing pressure on electrode-skin impedance, EKG and motion artefact [147].

A depression in electrode-skin impedance was observed when the applied pressure was greater than 15mmHg. However, when pressure of more than 20mmHg was exerted, the ECG signal deteriorated.

## 1.11 SUMMARY

The clinical approaches used for cardiac arrhythmia diagnosis only provide a periodic assessment of the disease. The majority of cardiac deaths are sudden, therefore continuous monitoring of the heart is necessary to enable timely detection of any cardiac instability. Many arrhythmias occur paroxysmally and might be hard to record in the doctor's office [148]. Thus, ambulatory ECG monitoring can be useful for short term or long term evaluation of cardiac arrhythmias. Many symptoms arise only while performing certain activities like eating, exercising or sleeping. A continuous ECG recording can help in detection of such events, the type of pattern they produce, how long they last and whether they are related in time.

Ambulatory ECG monitors can be externally worn as Holter monitors, event monitors and patch sensors or implanted in the skin's subcutaneous layer as ILRs. As discussed, the clinical importance of ECG recordings increases if the monitoring duration is increased. Adhesive patch sensors have been demonstrated to be superior to Holter and event monitors, mainly because of their longer study period. However, the episodes of cardiac arrhythmias and congenital heart diseases in patients have mainly been assessed using 12-lead ECG and Holter monitors [149] [150].

The main physiological and non-physiological sources of noise in ambulatory ECG monitoring have been discussed in this chapter. The major problem in ambulatory ECG monitoring is the sensitivity to motion artefacts. This may hinder the cardiac diagnosis and lead to inappropriate treatment decisions. Applying pressure on the electrodes can aid in minimizing these artefacts, however, the ECG signals can deteriorate if more pressure is applied. The contribution of skin stretch in generating motion artefacts has been explained in chapter 2. Several methods employed by various researchers to reduce motion artefacts from ambulatory ECG systems by applying advanced signal processing algorithms were discussed in this chapter. Of all the software filtering techniques, PCA and ICA have proven to be more promising than adaptive filtering, Kalman filtering and filtering using wavelet transforms. Adaptive filters tend to remove important diagnostic information from ECG signals and therefore are mainly used in applications that require rhythm analysis, whereas Kalman filtering requires a prior information of the system unlike PCA and ICA. Wavelet transform is a computationally intensive technique and has proven to be less effective than PCA and ICA in several studies.

The original contributions to knowledge made by this study include showing that skin stretch information is effective in rejecting motion artefacts from ECG signals using novel, modified PCA and ICA algorithms adapted to achieve this purpose. The publications arising from this thesis have been mentioned in the appendices.

## **CHAPTER 2      LITERATURE REVIEW**

### **2.1    INTRODUCTION**

Skin is the largest organ of the body and protects us from microbes and the elements, helps regulate the body temperature, and permits the sensations of touch, heat and cold [151]. This chapter reviews the physiology and mechanical properties of skin as they relate to ECG measurement. The effect of skin stretch in generation of motion artefacts in biomedical signals is explained. Skin stretch which will necessarily depend on the mechanical behaviour of the skin and the factors affecting its Young's modulus and so a thorough review on estimating the Young's modulus through tensile, indentation, torsion and suction tests has been conducted here. The various factors such as Langer's lines, skin thickness, ageing and hydration influencing the skin's Young's modulus have also been considered.

### **2.2    SKIN STRETCH: A MAJOR SOURCE OF MOTION ARTEFACT**

The movement of the patient results in skin stretch; which in turn generates potentials in the epidermis. Skin stretch is considered a major physiological source of motion artefact in the ECG [108].

Odman [152] established a non-linear relationship between motion artefact and the mechanical stress applied on the skin. The skin stretch potentials obtained at different equally spaced time series were found to vary between individuals. In 1981, Odman measured the magnitude of deformation-induced potentials in the skin area beneath the electrodes [153]. Two metal plates were adhered to the skin and the rectangular area of the skin between the plates was stretched. The magnitude of potentials decreased with increasing distance from the rectangular zone. The movement-induced potentials were studied in different electrode configurations by Odman and Oberg in 1982 [154]. The study concluded that only small potential variations occur due to change in conduction caused by electrode electrolyte displacement during motion, while skin deformation is the major source of motion artefact. The origin of skin stretch induced motion artefacts was explained by Talhouet and Webster in 1986 [155]. From their experiments, it was

inferred that both motion artefact and impedance increase logarithmically with skin stretch. In 1989 [156], Odman found that the potential changes due to skin stretch were higher in curved skin surfaces than in flatter skin surfaces.

Skin is composed of three layers: epidermis, dermis, and hypodermis [157] as illustrated in Figure 2.1.

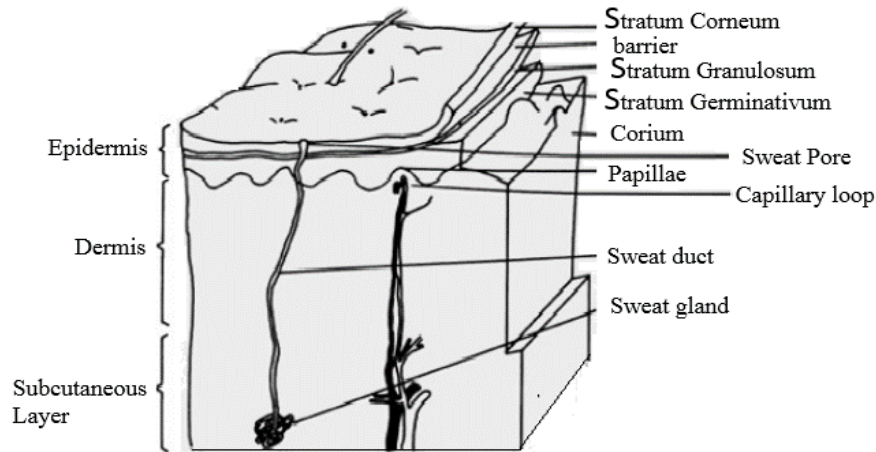


Figure 2.1: Schematic Diagram of the skin [108].

The capillary loops in the corneum nourish the skin. The new cells form in the stratum germinativum and move outward towards the stratum granulosum and the barrier layer [86]. The cells die in the barrier layer, stay on the surface of stratum corneum and fall off after some time. Bioelectric currents are generated due to various biological activities occurring in the body. The bioelectricity in the skin is caused due to the flow of ions between the dead cells on the epidermis and the new cells on the inner skin layers [108]. The epidermis layer is a storage of negative ions (anions) and is permeable to positive ions (cations) [158]. On the other hand, the inner layers of the skin have a positive charge on them due to the accumulation of positive ions (cations). Therefore, the skin behaves like a dc battery where the current is generated due to the flow of positive and negative ions across the barrier layer [158]. The skin's bioelectricity may depend on various factors such as hydration, emotions, stress and disease.

The impedance of the barrier layer is  $50 \text{ k}\Omega/\text{cm}^2$  and the skin potential between the inside and outside of the barrier layer is 30mV. When the skin stretches, the skin potential can drop to 25 mV, and this 5mV change in the potential appears as motion artefact in

biopotential measurements. Thakor and Webster hypothesized that the difference in metabolic activities between stratum corneum and stratum germinativum lead to the flow of ‘injury current’ through the extracellular resistance [159] [108]. The 5mV difference in the skin potential can be reduced by scratching the skin with about 20 strokes of fine sandpaper [160]. The sand paper scratches through the barrier layer and short circuits the skin potential [86]. The use of sandpaper to abrade the skin can cause bleeding, which might lead to skin infection. A skin puncturing technique developed by Burbank and Webster in 1978 showed significant reduction in motion artefacts [161]. The barrier layer provides a protection to the underlying layers of the skin from irritating substances like electrode gels. Therefore, only mild electrode gels should be used after the skin is abraded with sand paper [86]. However, the motion artefact returns as the skin regrows in 24 hours [160].

### **2.3 YOUNG’S MODULUS OF THE SKIN**

The Young’s Modulus of skin is measured as a ratio of the stress applied to the skin *in vitro* or *in vivo* to the skin deformation. Pereira [162] considered skin to be viscoelastic, where there is a dynamic alteration in the stress-strain relationship, until a stable state is attained [106].

The stress-strain behaviour of the skin is typically explained in three phases: When a strain of up to 0.3% is applied, the elastin fibres offer low resistance to the applied strain [163]. The skin exhibits isotropic behaviour and collagen fibres remain tangled and intertwined and do not contribute to the stiffness as seen in Figure 2.2. Phase 1 offers a linear stress-strain relationship and a low Young’s modulus (0.1-2MPa) [164].

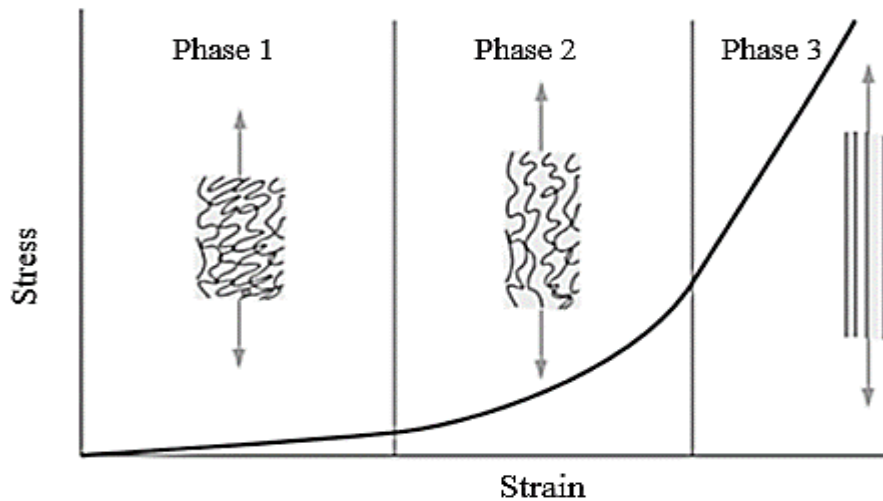


Figure 2.2: Structure of Collagen Fibre in different phases [164].

In Phase 2, the collagen fibres offer some resistance to the deformation [165] and the crimped collagen fibres begin to stretch, thus introducing non-linearity into the stress strain relationship. In the final Phase 3, for applied strain above 0.6%, the crimps begin to disappear and a linear stress-strain relationship can be observed. The collagen fibres break after the application of an ultimate tensile strain of 0.7% [164].

Young's modulus measurements differ with many factors, including the type of test performed (*in vivo* or *in vitro*), method of testing (tensile or indentation), test velocities (in tensile testing) or depth (in indentation techniques) [166]. These factors are discussed in this chapter.

## 2.4 SIGNIFICANCE OF YOUNG'S MODULUS

The Young's modulus of the skin is a vital parameter describing the characteristics of skin. One of the striking features of a healthy skin is its ability to return to normal after being pulled. Cosmetic surgeons use a variety of topical and invasive methods to maintain the skin's elasticity to prevent ageing [167]. The mechanical testing of skin can be useful to determine the mechanical behaviour of skin in the field of dermatology, to determine the course of a disease (Scleroderma, morphea, radio dermatitis etc.) or to

follow a cosmetic application. It can be used in detection of diseases in connective tissues such as mid-dermis elastolysis [168].

UV radiation has been found to induce skin contractions causing photo ageing which can be analysed using Young's modulus through the stress-strain relationship [169]. Quantification of hardness, elasticity and viscosity of the skin can help estimate the skin's thickness which is a significant index for diagnosing patients with systemic sclerosis [170].

In previous reviews, Hendriks [171] discussed several innovative techniques to determine the mechanical and structural properties of the skin such as ultrasound, confocal microscopy, optical coherence tomography and nuclear magnetic resonance. The use of the above methods is however restricted to the measurement of skin's thickness and tomography.

Knowing the Young's modulus of skin can help in calibrating the elasticity of bio-sensors to measure skin-stretch induced motion artifacts. This chapter provides an average range of Young's modulus of the skin by comparing the work of various authors, thereby covering a broad range of factors affecting the Young's Modulus.

## **2.5 METHODS EMPLOYED FOR MECHANICAL TESTING OF THE SKIN**

The mechanical behaviour of the skin is measured by changing the shape of skin by employing different techniques such as stretching (tensile test), applying a perpendicular load on the skin (indentation test), elevating the skin in an aperture (suction test) and rotating the epidermis to different degrees (torsion test). All these tests have been discussed in detail in the following sections.

The mechanical testing of skin can be further classified into *in-vivo* and *in-vitro* tests. *In-vitro* tests provide a simple and easy to model stress-strain relationship under controlled conditions with fewer confounding factors. *In-vitro* tests can also be used to calculate the ultimate tensile stress and strain when the skin ruptures. However, it can be difficult to clamp samples without applying an axial load and structural integrity of the excised skin is altered particularly at the edges of the sample as it is no longer attached to the body [172]. In comparison, *in-vivo* tensile measures are able to include

anatomical and physiological effects on skin properties. For example, skin ageing provides a negative impact on skin's ability to perform functions like body temperature regulation and water loss prevention. Longitudinal studies of Young's modulus values of skin must therefore be done *in-vivo*.

### **2.5.1 Tensile test**

Tensile testing is the most common type of test performed *ex-vivo* under controlled conditions [157]. In tensile tests, the skin is stretched parallel to the plane of the skin. The load can either be uniaxial or biaxial. In early work, Manschot and Brakkee [173] performed uniaxial strain measurements on human skin (calf) and observed a non-linear relationship between stress and applied strain. The minimum and maximum values of the Young's modulus across the tibial axis were found to be 0.32 and 4 MPa respectively and 0.3 and 20 MPa, respectively, along it. Meijer et.al [174] performed uniaxial tensile measurements on the forearm and found the stiffness value (Kc) to be 25 MPa. The work proposed a combined numerical-experimental method based on Lanir's skin model [175] which considers the strain-energy function to be the sum of individual strain-energy values of the tissues.

Several investigations relating to tensile testing of the skin at dynamic [176]–[178] and quasistatic (low level) speeds [179], [180] have been reported and a summary of results is given in Table 2.1.

Table 2.1: Values of Young's modulus at quasistatic and dynamic speeds using tensile test.

References	Skin Source	Speed	~Young's Modulus
Annaidh et.al. [176]	Not Mentioned	Dynamic (14.5m s <sup>-1</sup> to 29 m s <sup>-1</sup> )	100 MPa
Jacquemoud et.al. [177]	Forehead	Dynamic (3 m s <sup>-1</sup> )	14 MPa, 140 MPa and 35 MPa (for longitudinal, transverse and shear strain)
Gallagher et.al. [178]	Back	Dynamic (2 m s <sup>-1</sup> )	83.3 MPa
Ankersen et.al. [179]	Abdomen	Quasistatic (0.83 mm s <sup>-1</sup> )	14.96 MPa
Ottenio et.al. [180]	Abdomen	Quasistatic Speed (0.16 mm s <sup>-1</sup> )	4.02 ± 3.81 MPa

From Table 2.1, it can be inferred that the Young's modulus measured at quasistatic speeds (0.1-0.9 mm/s) varies from 4–15 MPa while for dynamic speeds (2–30 m/s), it varies from 14–100 MPa. Significant fluctuations in these values have been found with different orientations like transverse and shear, however, the overall Young's modulus increased monotonically with speed. Tensile tests at a dynamic speed are generally conducted to investigate skin failure, while quasistatic speed is used to carry out conventional tests to measure the skin stiffness.

### 2.5.2 Indentation test

Indentation is one of the most widely used and accepted means of measurement of skin's bio-mechanical properties-*in vivo*. It employs the use of an indenter which comes into contact with and applies a perpendicular force on a small area of skin. This method

characterizes skin as a monolayer by restricting the indentation amplitude to microns. However, the accurate prediction of Young’s modulus can be done only by considering the effects of underlying layers. Delalleau et.al. [181] proposed a combined numerical-experimental work to estimate the skin elasticity. The skin was assumed to be a linearly elastic semi-infinite layer. Pailler-Mattie et.al. [182] investigated different mechanical models to determine the effects of the underlying tissue layers and developed a two layer elastic model for mechanical analysis. The indentation method ascertained Young’s modulus in the perpendicular direction without any skin pre-stressing [183], [184]. The obtained values for skin’s Young’s modulus varied from 4.5 – 8 kPa.

The value of Poisson’s ratio also contributes to the obtained Young’s modulus calculations using indentation. Choi [185] performed experiments on bovine patellar articular cartilage and estimated the Young’s modulus to be 1.33 – 2.21 MPa for a Poisson’s ratio ranging from 0.45 – 0.47 using single indentation test. Jia [186] in his research, identified the variation of Young’s modulus with indentation depth using finite element analysis. Dynamic analysis was performed on two gel samples with different Young’s moduli between 0 – 500 Hz using the Tissue Resonator Indenter Device (TRID). Some of the studies relating to indentation tests at quasistatic and dynamic speeds are summarized in Table 2.2.

*Table 2.2: Values of Young’s modulus at quasistatic and dynamic speeds using indentation.*

<b>References</b>	<b>Skin Source</b>	<b>Speed</b>	<b>Young’s Modulus</b>
Boyer et.al. [187] (Laser Displacement Method)	Forearm	Dynamic (0.8 mm s <sup>-1</sup> to 42 mm s <sup>-1</sup> )	4.75 – 17.99 MPa
Khaothong [188]	Inner-forearm	Quasistatic (1 mm s <sup>-1</sup> )	0.1-2.4 MPa
Zheng and Mak [189]	Tibia/Fibula	Quasistatic (0.5 - 1 mm s <sup>-1</sup> )	10.4–89.4 kPa

The efficiency of simple indentation measurements in thin films can be compromised by ignoring the combined contributions of the film and indenter to measured properties, as has been analysed in various works [190]–[194]. Jia [186] measured tissue mechanical properties in terms of static stiffness and dynamic stiffness as a function of various indenter depths and found an increasing trend for both. Groves [157] determined the elasticity of the skin at various indenter depths, for spherical and cylindrical indenters.

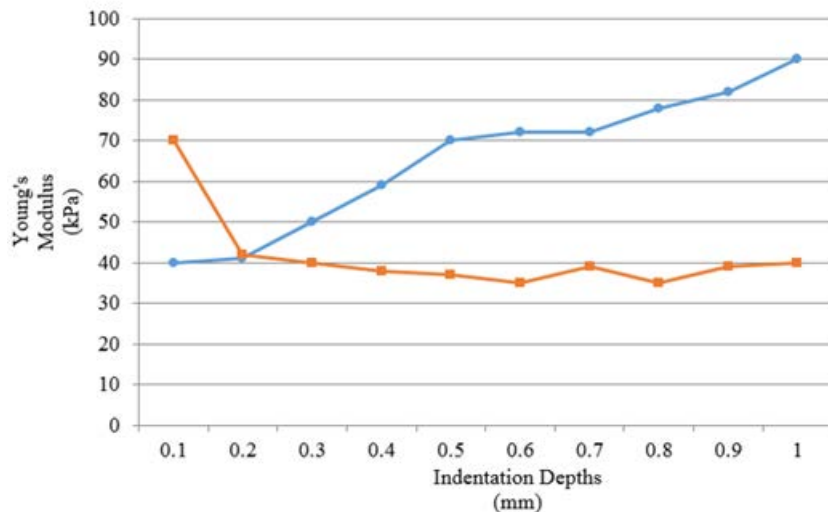


Figure 2.3: Young's modulus at different indentation depths for cylindrical  and spherical  indenters

It can be inferred that the cylindrical indenter measured a higher average value of Young's modulus than the spherical indenter at higher indentation depths. Kuilenburg [195] also investigated the necessity of considering the geometry and size of indenters while considering the measurement of skin's elasticity.

In general, Young's moduli found by indentation are significantly lower than those found by tensile tests, indicating that skin is highly anisotropic when thickness and in-plane directions are considered. A contributing factor may be that Young's modulus values are dependent on contact dimensions and range of fit. The indentation contact is very small whereas the tensile tests are macroscopic. Furthermore, in an indentation test, the Young's modulus depends on the depth of the indenter in contact with the underlying tissues. Therefore, when the depth of the indenter is small; the skin poses lower resistance from the collective effect of the underlying tissues/fibres or matrices. Conversely, these structures play a significant role in resisting tensile deformations.

### 2.5.3 Suction test

The mechanical properties of thin elastic membranes of materials can be determined using diaphragm tests, where the membrane is clamped and inflated in the form of a dome, while the pressure of suction is controlled by a pressure controller.

Early work of Grahame [196], Alexander and Cook [197] adopted a method of suction to stratum corneum considering skin to be isotropic. Following these works, the suction method to investigate anisotropy of skin has evolved to become a common procedure for skin mechanical testing. Generally, it employs the measurement of skin elevation in a circular aperture caused due to vacuum conditions ( $< 500$  mBar) [198] using optical systems like Dermaflex and Cutometer.

Dermaflex is a device with an aperture size of 10 mm, the cup being adhered to the skin to prevent creep. It has been used to measure skin distensibility [199] and to account for mechanical properties of dermis [200] by measuring elasticities as a percentage of skin retraction after the stretch. The Cutometer is a suction device employing probe apertures between 2-8 mm with the application of negative pressure through a vacuum pump [201]. Barel et.al. [202] determined stress-strain and strain-time curves using a Cutometer at 2 mm aperture and found a linear response within 150 – 500 mBar. Skin elevations of 0.1-0.6 mm were observed yielding Young's modulus values between 130-260 kPa at different skin sites. Diridollou et.al. [203] developed a suction system with ultrasound scanning – an echo rheometer capable of measuring thickness of epidermis and dermis. It operated in 3 modes at a frequency of 20 MHz and provided an axial resolution of 0.07 mm.

Table 2.3 represents different values of Young's modulus obtained by the suction method, measuring deformation with different aperture sizes.

Suction tests are a common choice for skin testing, as they are easy to apply *in-vivo* and also allow for additional deformation detection through, for example, imaging ultrasound. However, this technique involves the skin undergoing both in-plane and normal loading and depends on theoretical models to determine elastic properties. Moreover, the value of skin thickness has an effect along with the aperture size and the magnitude of negative suction pressure. According to the models proposed by Siqueira

[204] and Timoschenko [205], the Young's modulus of the skin exhibits an exponential increase with increase in aperture size.

*Table 2.3: Young's modulus using suction at different deformations & aperture sizes.*

<b>References</b>	<b>Skin Source</b>	<b>Deformation measurement/ Aperture Size</b>	<b>Young's Modulus</b>
Diridollou [203]	Forearm	100 mBar suction/ 6 mm	130 kPa
Hendriks [171]	Forearm	350 mBar suction, Ultrasound detection/ 6 mm	56 kPa
Barel [202]	Cheek	150 – 500 mBar suction/ 2 mm	130 – 260 kPa
Liang [206]	Palm, Forearm	450 mBar/ 2 mm	25 kPa, 100 kPa

#### **2.5.4 Torsion test**

Torsion measurements are carried out by applying a constant torque through a guard ring and an intermediary disc and measuring the resultant rotation of skin as seen in Figure 2.4.



*Figure 2.4: Twisting of skin for measuring elasticity in the Torsion Test.*

The method is supposed to reduce the skin anisotropic effects since the underlying layers do not contribute to the readings as postulated by Escoffier et .al. [207]. As the torque is applied, an immediate elastic deformation occurs followed by the occurrence of creeping viscoelastic deformation which is time dependent. The release of torque leads to immediate recovery followed by a slow recovery process which is usually not completed [208]. In torsion, the elongation is replaced by rotation and hence the measurement of elasticity becomes more complex. Early work includes that of Sanders [209], who performed an *in vivo* analysis to determine the extensibility of skin subjected to torsion. A twist of 0.8 mN-m was applied to a disc of diameter 8.7 mm. Young’s modulus was calculated using the formula (Vlasblom, 1967 [210]):

$$Young's\ Modulus = \frac{2M (1 + \mu)}{4eR^2\theta} \quad (2.1)$$

where  $M$  is the applied torque,  $e$  is the skin thickness,  $\mu$  is Poisson’s ratio,  $R$  is disc radius and  $\theta$  is the rotation.

The values of Young’s modulus obtained by using torsion techniques are shown in Table 2.4.

*Table 2.4: Young’s modulus obtained through torsion for different guard ring parameters.*

<b>References</b>	<b>Skin Source</b>	<b>Torque/ Disc diameter/ Guard ring diameter</b>	<b>Young’s Modulus</b>
Sanders [209]	Forearm	0.8 mN-m/ 8.7 mm/ _	0.02 – 0.1 MPa
Agache et.al. [211]	Forearm	28.6 mN-m /25 mm/ 35 mm	0.42 – 0.85 MPa
Escoffier et.al [207]	Forearm	2.3 – 10.4 mN-m /18 mm/ 24 mm	1.12 MPa

Other significant works include the study of Grebenyuk and Uten'kin [212], who worked on different anatomical sites on children resulting in rotations of 7 -10° at an application of a constant torque.

Torsion measurements are an accepted and reproducible means of in-plane skin elasticity analysis. However, they assume an isotropic behaviour of skin layers and a uniform deformation for the entire skin thickness. However, this consequently assumes that the applied force gradient reaches uniformly to the deeper layers of the skin. Also, since the measure of torsion is the rotational angle, it obtains, essentially, the shear modulus of the skin, which is theoretically related to the Young's Modulus.

## **2.6 FACTORS AFFECTING THE YOUNG'S MODULUS OF THE SKIN**

Skin is the outermost layer of the human body which regulates the body temperature and protects the body from abrasion and water loss. Skin is found to be highly anisotropic and Young's modulus is found to be dependent on orientation, where highest value can be twice the perpendicular values. Young's modulus decreases up to three orders of magnitude with hydration. An inverse relationship between skin's thickness and Young's modulus is observed. It can be concluded that the thickness of skin increases with age until 30 years and varies inversely with age after that. The following sections summarise the evidence of correlation of Young's modulus with these intramural and extraneous factors. The effect of various internal and external factors on human and animal skin can be assumed to be comparable due to their similar anatomical and physiological structures [213].

### **2.6.1 Langer's lines**

The epidermis is the outermost layer of the skin and acts as a protective shell. The dermis is the layer between the epidermis and the hypodermis, that protects and cushions the skin from stress and strain, and provides: elasticity to the skin, a sense of touch, and heat [214]. The hypodermis is essentially a fat layer of varying thickness which connects the underlying muscles to the skin [215]. The first two layers have a thickness of around 0.07- 0.12mm and 1mm-4mm respectively [165]. The lower region of the dermis, which

is the reticular dermis, is composed of collagen and elastin fibres (0.3-3.0 $\mu$ m in diameter) which deform as the fibres stretch and re-orientate [216]. Collagen is made up of protein and is cross-linked with covalent bonds. The cross-linking defines the strength of the fibre which varies with age and pathology [164]. With age, the collagen bundles become more compact and provide less room or space between individual bundles, thus increasing the Young's modulus (E) of skin [165].

The direction in which the skin exhibits the least flexibility, due to the alignment of collagen fibres within the dermis, corresponds to the direction of Langer's lines, named after their discoverer Karl Langer (1819-1887) [217]. The understanding of Langer's lines is important in surgery, as the cuts made in the direction of (i.e. parallel to) these lines heal better [218]. These types of cuts are less subject to tensile stress [219]. The directions of Langer's lines change with ageing. Young's modulus of the skin also depends on the orientation of Langer's Lines. Several tensile tests have been carried out by taking the skin samples perpendicular, parallel and at 45° to the Langer's lines [178]. The results have been summarised in Figure 2.5.

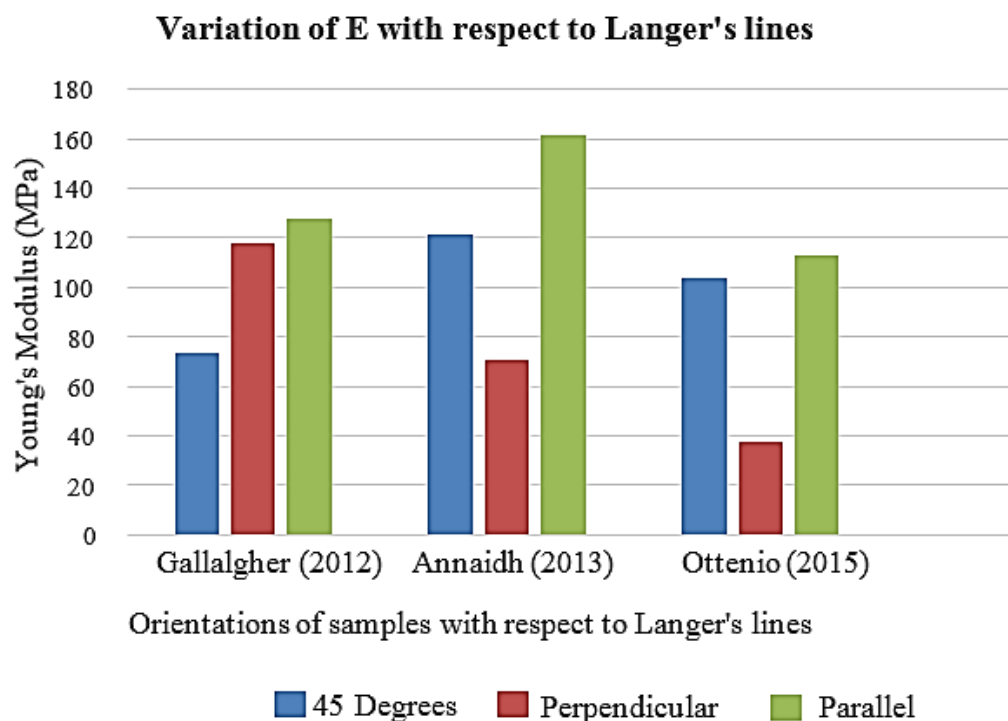


Figure 2.5: Variation in Young's modulus with the orientation of Langer's lines.

Annaidh [172] and Gallagher [178] concluded that Young's modulus measured at 45° and perpendicular to the Langer's lines is lower than that measured at parallel orientations. On the other hand, Ottenio [180] suggested comparable values of Young's moduli at 45° and parallel locations.

Ankersen [179] tested the mechanical properties of a synthetic chamois. He demonstrated that the corresponding strain at 45° is greater than in a direction parallel to Langer's lines.

According to Escoffier [207], the anisotropic effects of the skin can be minimised by applying stress parallel to the plane of the skin, thereby minimizing the contribution of the underlying layers.

Liang [206] proposed a frequency dependent relationship between Langer's lines and Young's Modulus. At a frequency of 50 Hz, the Young's modulus for perpendicular and parallel orientations were found to be comparable (100 kPa and 85 kPa) using dynamic optical coherence elastography, but at a frequency of 600 Hz, Young's modulus for perpendicular configuration was found to be much lower than the parallel configuration (100 kPa and 220 kPa).

### **2.6.2 Age, gender and skin's thickness**

The biomechanical properties of the skin change significantly with age, as it undergoes structural and cellular changes. Several studies pertaining to change in biomechanical properties of skin with ageing have been done in the past and no significant agreement was found amongst them. Young's modulus increases with age according to Diridollou [220] and Alexander [221], but decreases with age according to Boyer [222] and Sanders [223]. Diridollou [220] conducted suction experiments on skin using an echo rheometer which comprised of a cylindrical aperture filled with a coupling liquid placed normal to the skin's surface. The cylinder was integrated with a pressure control circuit used to elevate the skin and an electronic circuit to measure the skin's displacement corresponding to the first echo produced by the coupling liquid. He observed that the skin behaves differently with age for men and women and developed a mathematical equation corresponding to the change in Young's modulus with age. The graph in Figure 2.6 indicates that the Young's modulus increases after 30 and 50 years of age for both men and women. A noticeable difference in the pattern can be observed between men

and women after 80 years of age. The Young's modulus of the skin increases for men and decreases for women after 80 years. This variance in trend can be understood by considering the effect of skin's thickness with age in male and female. It was assumed that the skin's thickness increases between 10-20 years, lowering Young's modulus values and decreases after 50 years. The increasing behaviour of Young's modulus can be explained on the basis of the composition of collagen with age. Alexander [221] observed that Young's modulus of the skin decreases initially up to 30 years until skin reaches a maturity level, and then begins to rise indicating an increase in stiffness.

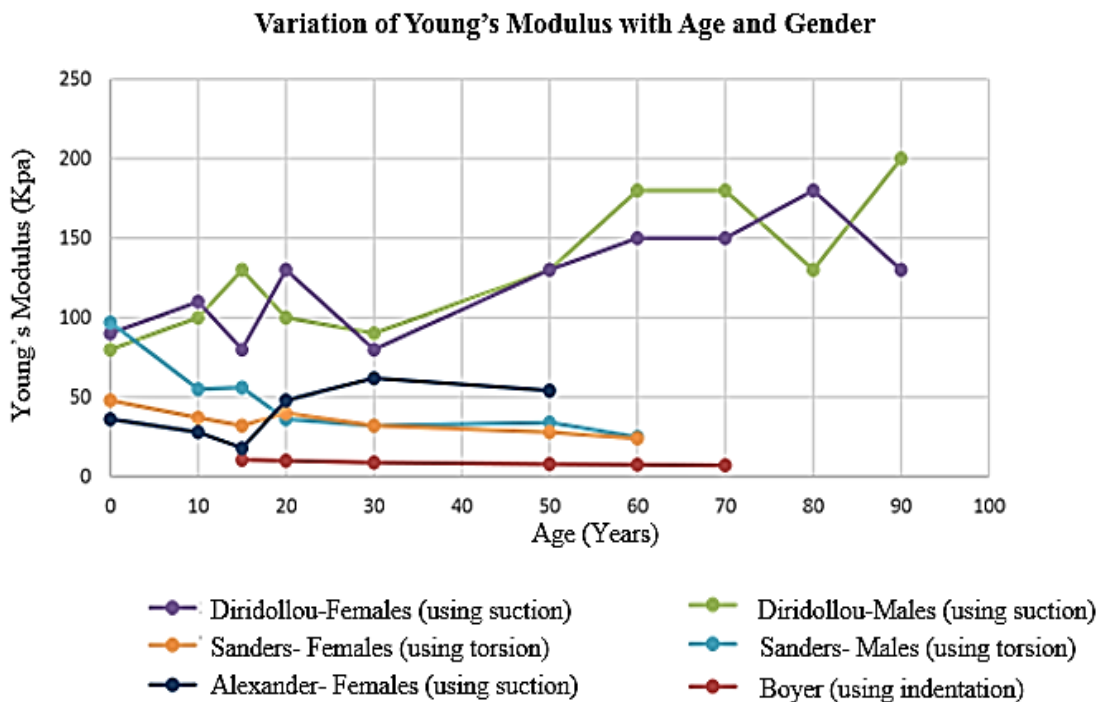


Figure 2.6: Variation of Young's modulus with age and gender, measured using different testing techniques.

In contrast, many studies found that the Young's modulus of skin decreased with age. Boyer [222] assessed the skin's stiffness with age in 46 subjects by using a dynamic indentation method. The values of Young's modulus for the youngest and the oldest group were found to be 10.7 kPa and 7.2 kPa respectively. A possible reason for this type of behaviour is that the skin's age, thereby lowering the Young's modulus measured by an indenter.

Sanders [223] measured the mechanical properties of skin in males and females using the torsion method. A continuous decrease in Young's modulus with age for men and women was observed through (see Figure 2.6). Discontinuity and wear and tear of the collagen network with age can justify the sagging of the skin, which leads to a decline in Young's Modulus.

The anisotropic properties of the skin can be explained due the different orientation of collagen fibres in the dermis, as discussed earlier. Escoffier [207] analysed the variance of thickness of skin with ageing and determined a linear regression equation for men and women, where  $E_p$  is the skin thickness in millimetres. A linear regression equation for men and women up to 30 years [207] can be given as:

$$E_p = 0.7 + (8 \times 10^{-3} \times age) \quad (2.2)$$

Separate relationships were determined for men and women after 30 years:

For women:

$$E_p = 0.89 - (3 \times 10^{-3} \times age) \quad (2.3)$$

For men:

$$E_p = 1.05 - (4 \times 10^{-3} \times age) \quad (2.4)$$

The relation between skin's thickness and age was found to be inverse after 30 years, but men's skin was found to be 16% thicker than women after 30 years. Diridollou [220] used an ultrasonic scanner to measure skin thickness and found the thickness of men's skin to be 5.2% greater than women. Zheng [189] and Hara [224] found an inverse relation between skin's thickness and Young's Modulus. Zheng observed that the average value of Young's modulus for men at different sites and different postures was 40% more than that of females.

The elasticity and viscosity of skin also depends on the site of testing. Comparing the values of Young's modulus from different parts of pig skin using tensile testing, Ankersen [179] found that Young's modulus for pig back and belly were 15 MPa and 7 MPa respectively. Similarly when Liang [206] conducted experiments using Optical Coherence Tomography (OCT), he came to a conclusion that the Young's modulus for different sites *viz.* volar forearm, dorsal forearm and palm were 101.180, 68.678 and 24.910 kPa respectively.

Ishikawa [225] performed experiments on 191 human subjects by using a new suction device and noted that there is no significant relation between skin's elasticity with sex or degree of obesity. Although, when experiments were carried out on different body sites – finger, forearm, hand and chest, then Young's modulus on the chest was significantly lower than that of the other three sites.

### **2.6.3 Hydration**

Stratum corneum, the outermost layer of the epidermis, regulates water flow through the skin and acts as a barrier against the penetration of foreign substances. Many studies have shown the effect of hydration on the mechanical properties of skin. Kuilenburg [195] found that the effective Young's modulus of the stratum corneum decreased significantly with increase in hydration. On the other hand, the other layers of skin showed a minor influence of hydration on the magnitude of Young's Modulus.

According to Blank [226], stratum corneum receives moisture from the fluids which are present in the layers beneath it. Sweat glands become active at temperatures above 30°C. Moreover, unclothed areas tend to lose some water content due to evaporation, reducing the moisture content of stratum corneum to below that for the underneath layers.

Park and Baddiel [227] stated that water behaves as a plasticizer and converts the skin from a glassy state to a rubbery state. At low hydration levels, the elasticity increases due to stretching of bonds, but at higher hydration levels, the hydrogen bonds become hydrated (weak) and the sulphide bonds remain intact, thereby leading to the formation of a lightly cross-linked network of collagen fibres.

Wildnauer [228] reported that under controlled room temperatures, the fracture strain of stratum corneum excised from the human upper back increased from 20% to 190% when the relative humidity was increased from 0 to 100%.

Papir [229] investigated the change in mechanical properties of the stratum corneum in rats pertaining to alterations in hydration and temperature. It was observed that the stratum corneum became more elastic and ductile with increasing moisture content. Additionally, at 22°C and 77% relative humidity, a steep fall in the value of Young's modulus was observed.

Figure 2.7 represents a comparison of different works showing variations in Young's modulus with relative humidity.

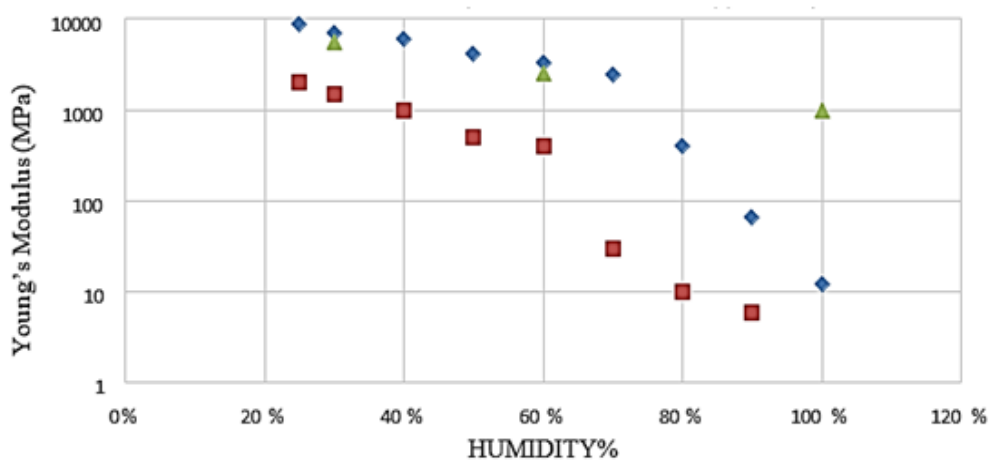


Figure 2.7: Variation in Young's modulus with humidity: ♦ Papir (tensile test on stratum corneum), ■ Park and Baddiel (tensile test), ▲ Wildnauer (tensile test on human upper back).

Uniaxial tensile tests were performed on wet and dry synthetic chamois by Ankersen [179]. High moisture content in the synthetic chamois caused a slight increase in both failure stress and strain, demonstrating the increase in elasticity on increasing the hydration on skin.

Liang [206] investigated Young's modulus at different frequencies for wet, dry and normal skin. The values of Young's modulus obtained at a driving frequency of 50 Hz were the lowest for wet skin and the highest for dry skin. At larger frequencies of around 500 Hz, the wet and normal skin experienced a gain in Young's modulus, though there was a dramatic decline in the Young's modulus of dry skin.

## 2.7 SUMMARY

Four major methods employed for mechanical testing of the skin have been discussed in detail. Young's modulus in the thickness-direction typically measures between 10.4 kPa to 17.99 MPa by indentation tests. However, measured values can depend on indenter geometry and whether quasistatic or dynamic testing is being performed. Values of between 0.02 kPa and 140 MPa are typical for both tensile and torsion tests. Tensile tests indicate higher Young's modulus at higher strain rates, indicating that skin is viscoelastic. Young's modulus measured by suction tests span 25 kPa to 260 kPa, which is between the ranges found from indentation (thickness-mode) and tensile/torsion (in-plane mode). This may be because suction tests involve both in-plane and perpendicular deformations.

In-plane measurements of Young's modulus depend on orientation with respect to Langer's lines, where highest Young's modulus is seen in the parallel orientation, and can be twice the perpendicular values of Young's Modulus.

In addition to anisotropy, and technique-dependent variables, Young's modulus decreases up to three orders of magnitude with hydration, and this effect appears primarily confined to the stratum corneum.

The relationship with demographic features such as age is less clear but is possibly biphasic, with increasing Young's modulus below 30 years, and decreasing values thereafter. No consistent difference between sexes is observed. Several studies showed an inverse relation between the skin's thickness and the Young's Modulus, and skin thickness is also dependent on age, sex and body site. This suggests individual variation is much greater than age and gender effects on their own.

In many applications *in vivo* testing provides more relevant information than *in vitro* testing. Indentation tests are mostly performed *in vivo*, and are relatively easily applied. This study involves the estimation of skin's deformation *in vivo*, therefore, the average range of Young's Modulus has been taken between 7.2 kPa and 17.9 MPa, considering the effect of Langer's lines, age, gender, skin's thickness and hydration.

## CHAPTER 3 RESEARCH GAP AND OBJECTIVES

### 3.1 SUMMARY OF PREVIOUS STUDIES

The phenomena of generation of ECG due to the flow of bioelectric currents in the heart and the importance of ECG monitoring to diagnose various heart abnormalities by the cardiologists have been discussed in chapter 1. A 12-lead ECG system used in hospitals provides a detailed and calibrated analysis of heart rhythm, conduction and repolarization from multiple lead vectors, enabling the detection of cardiac structural, electrophysiological and metabolic abnormalities and drug effects [40]. However, ambulatory ECG monitoring is required to detect cardiac episodes that occur infrequently. Modern trends in ambulatory ECG monitoring aim for the use of patch sensors for long-term monitoring in place of conventional Holter and event monitors. The diagnostic efficacy of patch sensors is higher than Holter or event monitors.

The main sources of noise in ambulatory ECG systems have been mentioned in chapter 1. The use of driven right leg in ECG circuits and proper electrode placement can be implemented to remove noise from power line and EMG interference. It can be inferred that the conventional Ag/AgCl electrodes provide the best electrical contact with the skin, although the electrolyte gel may dry out after sometime or may cause skin irritation in some patients. These electrodes are inconvenient to wear for long durations as compared to dry or capacitive electrodes. However, the electrode-skin impedance offered by dry and capacitive textile electrodes is high and depends on the presence of sweat on the skin and application of pressure. The use of flexible, porous and conductive CNT/PDMS polymer patch electrodes is recommended for long term use to increase comfort. These electrodes can be stuck on the patient's skin using a conductive paste that is biocompatible.

Motion artefacts remain one of the major problems in short-term and long-term ECG monitoring and can lead to wrong diagnosis and trigger false alarms. Motion tracking using accelerometers, inductance in LVDTs, capacitance in gradiometers and displacement in optical sensors has been extensively applied to identify motion artefacts in ECG. Software techniques employing wavelet transform, adaptive filtering, EKF, PCA and ICA have been employed for motion artefact removal. Some of these techniques are reported to provide satisfactory performance.

Skin stretch is a major physiological source of motion artefact in ECG due to the flow of injury current across the barrier layer of the skin. This has resulted in employing techniques to reduce this artefact, such as skin abrasion using sand paper and skin puncturing. Skin abrasion may lead to skin irritation and the motion artefact may return back due to skin regrowth. The amplitude and frequency range of motion artefacts due to skin stretch is comparable to ECG, therefore it is difficult to identify and eliminate them using adaptive software techniques. The magnitude of skin stretch depends on the Young's modulus of the skin, and is affected by orientation in relation to Langer's lines, hydration and age. The average range of Young's modulus of the skin lies between 7.2 kPa and 17.9 MPa.

### **3.2 RESEARCH GAP AND RESEARCH QUESTIONS**

It is apparent from the reviewed literature that existing approaches to reducing motion artefact from ECG do not address a main cause of motion artefact, which is skin stretch. A number of studies have applied algorithms to reduce motion artefact by examining only the ECG signal. Other researchers have made use of a noise signal such as uniaxial displacement, sensor acceleration or other sources which do not directly measure or address skin stretch as a primary cause of motion artefact. The optical sensing technique implemented by Liu (2007) [108] measured absolute displacement of the images in any direction, thereby neglecting to calculate the strain (normal and shear) of the skin.

This work aims to reduce ECG motion artefacts by exploiting the physical principal of injury current due to skin strain as a primary contributor to motion artefacts. It will account for the directions and the orientation of the skin strain field at the electrode to try to achieve a high signal to noise ratio (SNR) while preserving user comfort and biocompatibility.

The major research questions that can be identified are thus:

- I.** How to track and quantify motion artefact in terms of skin stretch at the point of biopotential measurement?
- II.** Can the incorporation of skin stretch information using PCA and ICA aid in eliminating motion artefacts from ECG signals?

Therefore, main objectives of this research are as follows:

- I. To investigate an appropriate method of quantifying motion artefacts in terms of skin stretch while acquiring ECG measurements.
- II. To investigate a technique to incorporate the skin stretch measurements in PCA and ICA and find the best approach to reject motion artefacts from ECG signals.

The research addressing these questions has been presented in the following chapters of this thesis.

### 3.3 RESEARCH AND THESIS OUTLINE

Considering the range of skin's Young's modulus (7.2 kPa and 17.9 MPa), PDMS films with similar elasticity to that of skin have been prepared (discussed in chapter 4); so that they can be used to emulate skin stretch. The Young's modulus of the films was tested and found to lie within the range of skin. Conductive CNT/PDMS and graphene/PDMS electrodes were prepared for measuring ECG signals. The conductance of these electrodes were compared with conventional Ag/AgCl and dry Ag electrodes. The CNT/PDMS electrodes showed a higher conductance over graphene/PDMS electrodes, therefore they were considered appropriate for carrying out ECG measurements. The Young's modulus of the CNT/PDMS electrodes was tested and found to lie within the acceptable range of skin's Young's modulus. Thus, a conductive polymer patch electrode (CNT/PDMS) with similar elasticity to skin was successfully developed to measure ECG and skin stretch under the electrode.

In chapter 5, a PDMS film electrode was printed with a checkerboard pattern to quantify skin stretch. A high speed camera was utilized to track the movement of the film on stretching. The video frames were filtered and processed to identify the checkerboard corners in each frame. Infinitesimal strain theory was used to calculate the 2D strain distribution from point displacements in MATLAB<sup>®</sup>. The derived 2D strain distributions were validated against strains calculated by carrying out stretch simulations in *SolidWorks*<sup>®</sup>. In this way, the optical technique was qualified to measure skin stretch from CNT/PDMS electrodes.

The basic principal behind the working of PCA and ICA has been covered in chapter 6. ECG signals were acquired from a subject's arms and three different kinds of movements were introduced. The strains due to motion were quantified using the

method described in chapter 5. The quantified strains were utilized as motion information in PCA and ICA algorithms to identify and eliminate motion artefacts from ECG signals. The results were compared and a significant reduction in motion artefact from ECG signals was observed after the implementation of PCA and ICA,

The developed motion artefact rejection system has been validated in seven healthy subjects, as described in chapter 7. ECG signals with and without motion artefacts were acquired simultaneously from the arms (by inducing movement) and the chest (at rest). The ECG signals from the chest were obtained using conventional Ag/AgCl electrodes and were considered as reference, whereas noisy ECG signals from the arms were measured using CNT/PDMS electrodes. The performance of the system was evaluated in terms of improvement in SNR and infinity norm ( $\infty$ -norm) and was compared with other related work. The system outperformed systems which do not directly address skin stretch as the main cause of motion artefact. It was also found that CNT/PDMS electrodes exhibited a higher SNR than dry Ag electrodes when used in this system.

In chapter 8, a critical analysis of the thesis has been presented and novel contributions with directions for future work have been highlighted.

## **CHAPTER 4 DEVELOPMENT OF STRETCHABLE POLYMER ELECTRODES**

### **4.1 INTRODUCTION**

This chapter describes the preparation of PDMS films having various Young's moduli. The Young's modulus was evaluated for each film by conducting tension-relaxation tests. The PDMS electrodes were made conductive by mixing them with multi-walled CNTs and graphene using an ultrasonic mixer. The CNTs and graphene were wetted in DMF prior to their dispersion in PDMS. This was done to avoid them clumping in PDMS and to ensure more uniform dispersion. The conductance of the CNT/PDMS and graphene/PDMS electrodes was measured using an LCR meter (E4980A Keysight Technologies, California, USA) and was compared with that of Ag/AgCl and dry Ag electrodes. The Young's modulus of the CNT/PDMS film was evaluated and compared with that of PDMS and human skin. The ECG measurements in this study were carried out using CNT/PDMS electrodes which were glued onto the skin using a conductive adhesive.

### **4.2 PDMS PREPARATION**

PDMS is a silicon-based polymer which belongs to the group of polymeric organosilicon compounds [230]. PDMS is widely used for the fabrication and prototyping of microfluidic chips [231]. It is a bio-compatible, optically clear, inert, non-flammable and non-toxic polymer. PDMS is available in liquid form and its elastic polymer, or elastomer, is prepared by mixing it with a cross-linking or a curing agent. The elastic properties, specifically the Young's modulus, of PDMS can be altered by changing the ratio of base (liquid PDMS) to curing agent. Therefore, PDMS with similar elasticity to that of human skin can be prepared and used to emulate skin stretch. PDMS is not without its shortcomings, however, and these include change in its mechanical properties with time (also known as PDMS ageing), its sensitivity to exposure to some chemicals, and difficulty in managing the liquid due to its highly viscous nature. Two types of PDMS commonly used by researchers are PDMS RTV-615 (Momentive Performance Materials, New York, USA, formerly and GE Silicones) and PDMS

Sylgard 184 (Dow Corning, Michigan, USA). Although PDMS RTV-615 is more robust and convenient for the fabrication of bilayer microfluidic devices, PDMS Sylgard 184 is less prone to contamination, softer and easy to cure [231] [232]. Therefore, PDMS Sylgard 184 consisting of Part A: Base (B) and Part B: Curing Agent (CA) was used in this research.

The time and temperature required to cure PDMS varies with thickness. PDMS samples of different thicknesses were fabricated using spin coating. Spin coating is a procedure which involves the deposition of thin uniform films on a central flat substrate of a spin coater. The coating material (PDMS in this case) is applied on the centre of the substrate which is either spinning at low speed or not spinning at all. The spin coater is then rotated at high speeds to uniformly spread the coating material on the substrate using centrifugal force [233]. The spin coating was performed in this case by using a Laurell Spin Coater (Model WS-650Mz-23NPP, Laurell Technologies Corporation, Paris, France). The thickness of the elastomer was controlled by altering the spinning speed and other parameters of the spin coater, as seen in Figure 4.1.



Figure 4.1: Laurell Spin Coater WS-650Mz-23NPP used to fabricate thin PDMS films

PDMS elastomers with different B:CA ratios were prepared. The process involved in PDMS membrane realization is explained below:

1. B and CA were poured in ratios of 8:1, 10:1, 12:1 and 15:1 in separate Petri dishes and then mixed vigorously for 2 minutes using a wooden spoon.
2. The PDMS mixtures were poured on thin glass slabs of dimensions 30 mm × 30 mm × 5 mm.
3. The PDMS was formed into a membrane using a spin coater at a speed of 500 rpm for 10 seconds.
4. The glass slabs were placed in a desiccator for 45 minutes to degas the PDMS mixtures and to remove air bubbles.
5. The PDMS mixtures were baked in an oven at a temperature of 80°C for 2 hours [234].
6. The PDMS substrates were peeled from the glass slabs using tweezers.

### 4.3 YOUNG'S MODULUS OF PDMS FILMS

After the realization of thin membranes, a PDMS film with dimensions of 30mm × 30mm × 2.5 mm was subjected to tensile testing using a TA.XTPlus texture analyser from Stable Microsystems (Surrey, UK), as seen in Figure 4.2.

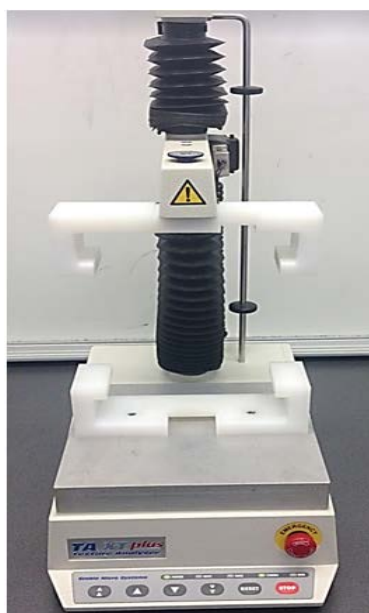


*Figure 4.2: Texture Analyser*

The values assigned to the testing parameters in the texture analyser settings are listed in Table 4.1.

*Table 4.1: Parameters used in the mechanical testing of the CNT/PDMS film using texture analyser.*

Test parameters	Value/Type
Test mode	Tension-Compression
Test speed	0.5mm/sec
Target mode	Strain
Maximum strain percentage	60%

The TA.XTPlus allows data acquisition of force and displacement at up to 500 points per second. The tensile tests were conducted at a speed of 0.5 mm/s and a maximum strain of 60 %. The PDMS samples were subjected to a tension-relaxation test over a time period of 10 seconds. The force and resulting displacement data were used to calculate the stress-strain locus; an example is shown in Figure 4.3. The curve was smoothed by using a Savitzky-Golay smoothing filter in MATLAB.

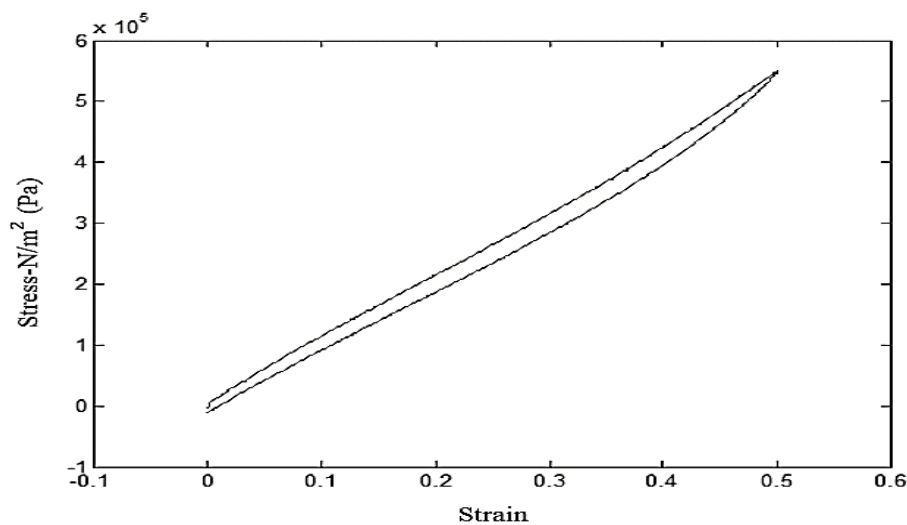


*Figure 4.3: Stress-strain curve obtained from the texture analyser for tension-relaxation test of PDMS substrate with a B: CA ratio of 10:1*

A hysteresis loop can be observed in the stress-strain plot of the PDMS substrate in Figure 4.3. When elastomers are stretched, the polymer molecules become more oriented and less random. This decrease in randomness makes the elastomer hotter. On releasing the polymer, it contracts and gets colder, since the molecules must adsorb heat to become more random. This heat transfer between the elastomer and its surroundings accounts for the hysteresis loop associated with elastomers [235].

The slopes of the stress-strain curves during elongation were evaluated to find the values of Young's modulus for all PDMS samples. The mean values of the slopes were taken as the average Young's modulus for each PDMS substrate. Figure 4.4 shows a comparison between the stress-strain plots of PDMS mixtures with different B:CA ratios.

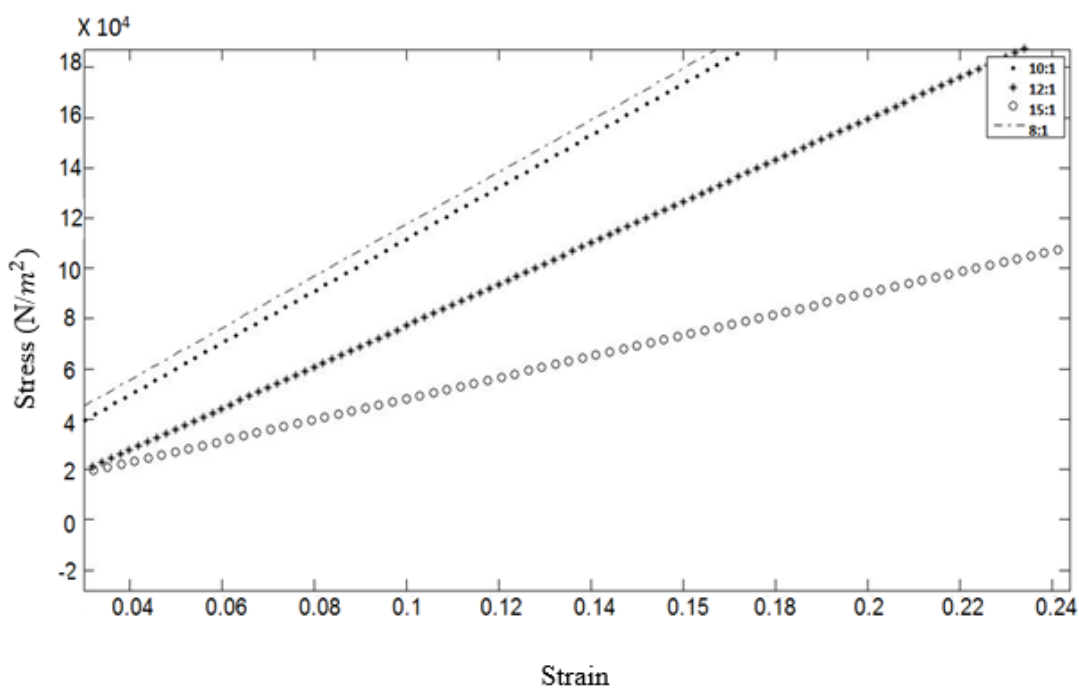


Figure 4.4: Comparison of stress-strain plots for PDMS mixtures with different B:CA ratios

As observed from Figure 4.4, the slope of the curve decreases as the ratio of PDMS B to CA increases. The average Young's modulus values for different PDMS samples are given in Table 4.3.

Table 4.2: Average Young's modulus for PDMS with different B: CA ratios

PDMS Base: Curing Agent	Young's modulus (MPa)
8:1	1.0538
10:1	1.0398
12:1	0.8623
15:1	0.3798

As mentioned in chapter 2, the range of Young's modulus for skin lies between 7.2 kPa and 17.9 MPa. Skin stretch information is used for motion artefact quantification and its removal from ambulatory ECG measurements. The main goal here is to develop a prototype which does not significantly obstruct the skin stretch and has a Young's modulus lower or equal to that of the skin. The Young's modulus of PDMS is lower than the average Young's modulus of the skin and can be modified by altering the B:CA ratio. Therefore, the use of PDMS to emulate skin stretch is an appropriate choice.

#### 4.4 PREPARATION OF CNT/ PDMS ELECTRODES

As discussed in chapter 1, there are two major types of CNTs: single-walled and multi-walled. Multi-walled CNTs have a higher tensile strength [236], better dispersability in polymers [237], and are more electrically conductive [238] than single-walled CNTs. Therefore, multi-walled CNTs with a diameter of 50–85 nm and length of 10–15 micrometres were purchased from Graphene Supermarket (New York, USA) for this study. As mentioned in section 1.5, 4.5 wt% concentration of CNTs in PDMS was considered appropriate for ECG monitoring. The CNT/PDMS-based electrically conductive, stretchable and biocompatible electrodes were prepared using this CNT and PDMS (Sylgard 184).

One gram of CNTs was dispersed in 40 ml of DMF solution and then mixed vigorously using a 750 Watt ultrasonic processor (Sonics & Materials Inc., Connecticut, USA) for 1 hour at a temperature of 40°C, as shown in Figure 4.5.



*Figure 4.5: Mixing of CNT and DMF in controlled environment using ultrasonic mixer.*

After sonication, a visual inspection of the mixture was performed to confirm the debundling of CNT dispersion. The purpose of sonicating CNTs with DMF was to modify the CNTs by detangling them for their homogenous dispersion in PDMS. Figure 4.6 shows images obtained from a scanning electron microscope (SEM) (Hitachi SU-70, Illinois, USA) in which CNTs are dispersed in PDMS with and without prior sonication with DMF. The CNTs (white in colour) in Figure 4.6a are widely spaced and uniformly distributed within the PDMS (grey in colour), while CNT bundling can be seen in Figure 4.6b.

The dispersion was vacuum-filtered using a glass fibre filter of 125  $\mu\text{m}$  porosity. The CNT-DMF mixture was dried to evaporate the remaining DMF using a digital hotplate stirrer (Labnet AccuPlate, Auckland, New Zealand) at 140°C for 2 hours. This was followed by the sonication of 4.5wt% of dried and debundled CNT with PDMS (B:CA ratio = 10:1) at room temperature for 1 hour [78]. The sonication of CNT with PDMS was performed to ensure thorough and uniform mixing.

A part of the mixture was poured on a glass slab with dimensions of 30 mm  $\times$  30 mm  $\times$  5 mm and the slab was then spun using the Laurell Spin Coater. The film was then

cured at room temperature for 24 hours. CNT/PDMS films of various thicknesses were fabricated by altering the speed of the spin coater.

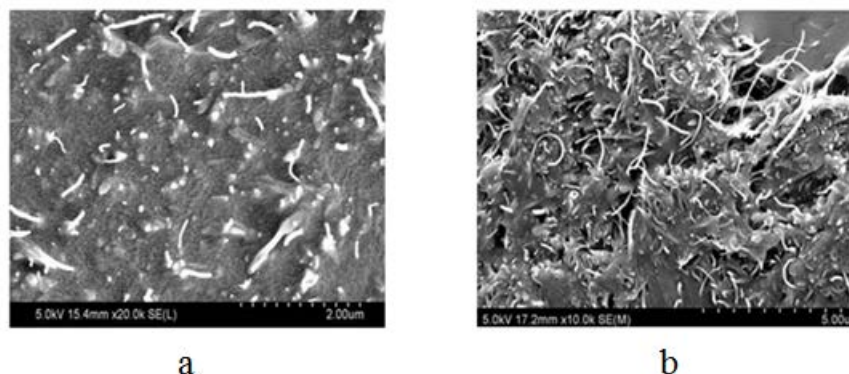


*Figure 4.6: Use of SEM to observe the dispersion of CNTs in PDMS; a: using DMF, b: without using DMF*

As mentioned in section 1.5, some researchers have used graphene to prepare conductive electrodes for bio signal measurements. Therefore, conductive electrodes were prepared by sonication of 4.5wt% graphene (purchased from Graphene Supermarket, New York, USA) with PDMS (B: CA ratio = 10:1). Like CNTs, graphene tends to agglomerate due to the presence of strong van der Waals forces of attraction between them [239]. Hence, the graphene was wetted and sonicated with DMF solution before mixing with PDMS.

#### **4.5 YOUNG'S MODULUS OF CNT/ PDMS ELECTRODES**

Tensile testing was performed on the CNT/PDMS films with dimensions of 30 mm × 30 mm × 2 mm using the texture analyser to find and compare the Young's modulus of these films with the PDMS films fabricated in the section 4.2. The tensile test was carried out under the same boundary conditions used for the PDMS film tensile test.

The CNT/PDMS films were subjected to a tension-relaxation test over a time period of 10 seconds. The force and resulting displacement data were used to calculate the stress-strain loci, an example of which is shown in Figure 4.7.

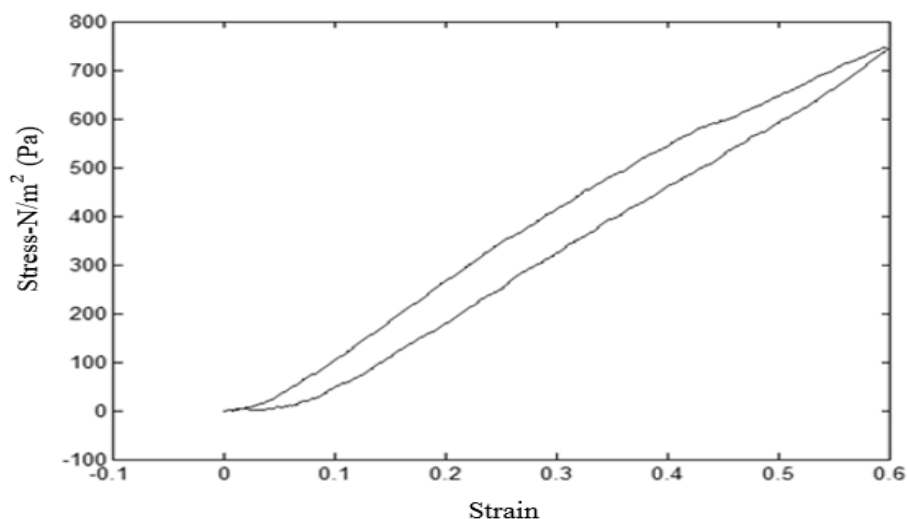


Figure 4.7: Stress-strain curve obtained from texture analyser for tension-relaxation test of CNT/PDMS substrate with a B: CA ratio of 10:1

The slope of the stress-strain curve during elongation was calculated to find the Young's modulus of elasticity for the CNT/PDMS film. The mean value of the slope was found to be 1.3309 kPa, which was considered as the average Young's modulus for the films. The Young's modulus of the CNT/PDMS film was approximately 800 times lower than the PDMS film (B:CA ratio = 10:1) and approximately 5 times lower than the minimum Young's modulus of human skin (7.2 kPa). CNTs are black in colour and liquid PDMS is colourless, therefore the electrodes prepared by adding CNT in PDMS were black.

#### 4.6 CONDUCTANCE OF THE ELECTRODES

The impedance of the CNT/PDMS, graphene/PDMS, dry Ag and commercially purchased foam-padded Ag/AgCl (3M Red Dot, Minnesota, USA) electrodes was measured and compared at frequencies ranging from 20 Hz to 10 KHz using an LCR meter, as seen in Figure 4.8. The dry Ag electrode was prepared by removing the sticky electrolyte gel from the back of the purchased Ag/AgCl electrode using a pair of tweezers. Aluminium snaps were glued using conductive paste Ten 20 (Weaver and Company, Colorado, USA) on both sides of CNT/PDMS and graphene/PDMS electrodes.

The magnitude and phase of the impedance were measured across the surface of the electrodes using Kelvin leads clipped on the aluminium snaps, as shown in Figure 4.9.

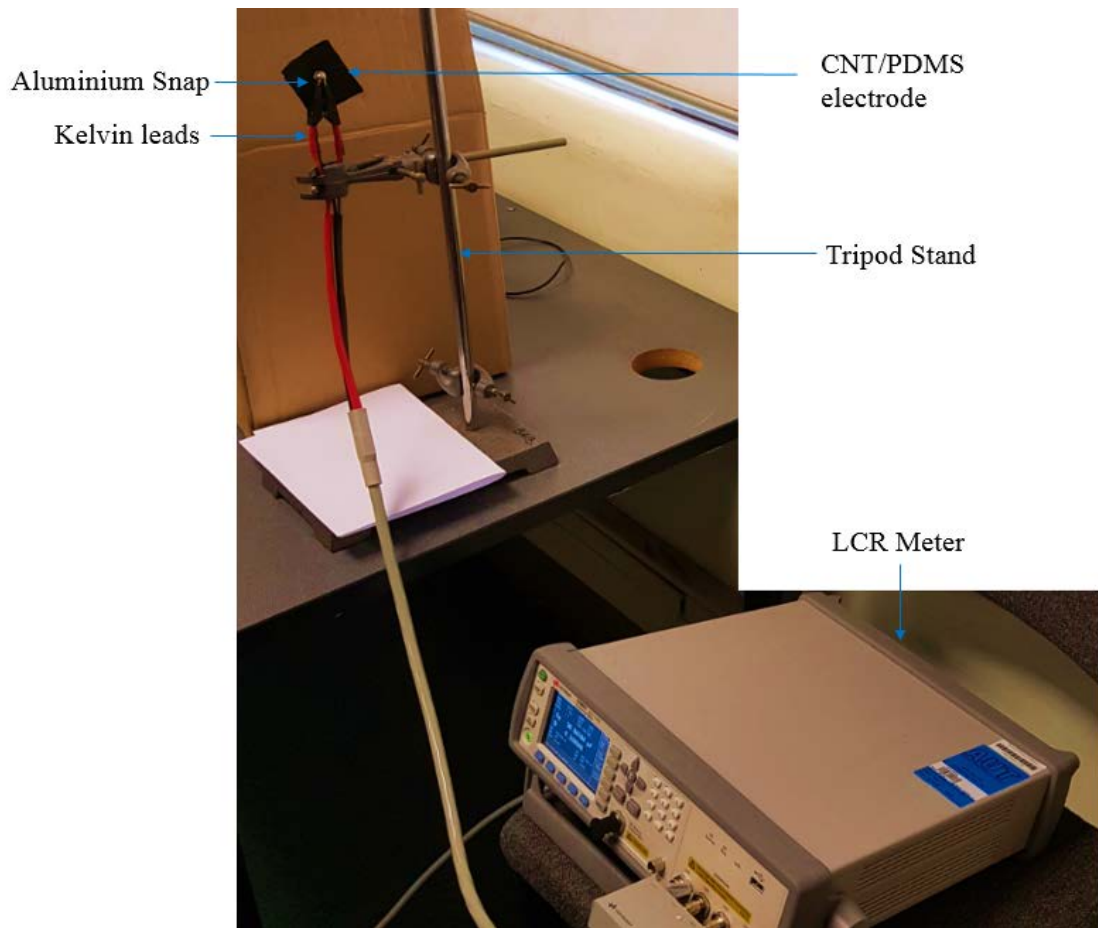


Figure 4.8: Measurement of conductance of CNT/DMF electrodes at different frequencies using LCR meter.

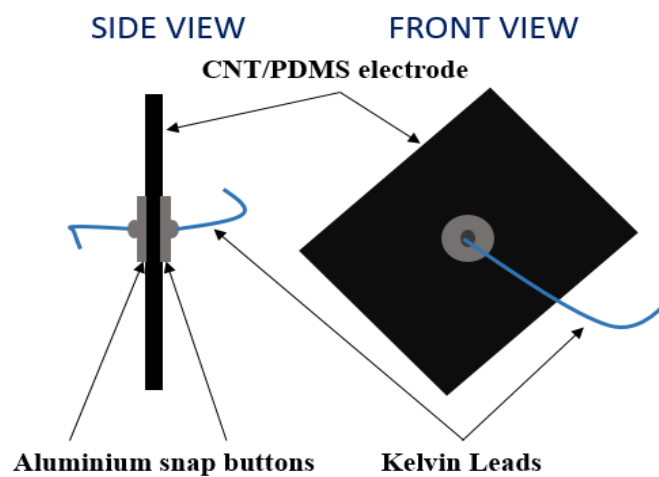


Figure 4.9: Measurement of conductance across the CNT/DMF electrodes.

The conductance values were estimated from obtained impedance magnitudes and phases by using the formula:

$$G = \frac{1}{Z \cos \theta} \quad (4.1)$$

where  $G$  is the estimated conductance in siemens,  $Z$  is the magnitude of impedance in ohms ( $\Omega$ ) and  $\theta$  is the phase angle in radians.

The plot of conductance vs frequency for different electrodes at 100 logarithmically spaced intervals within 10 Hz–10 kHz can be seen in Figure 4.10.

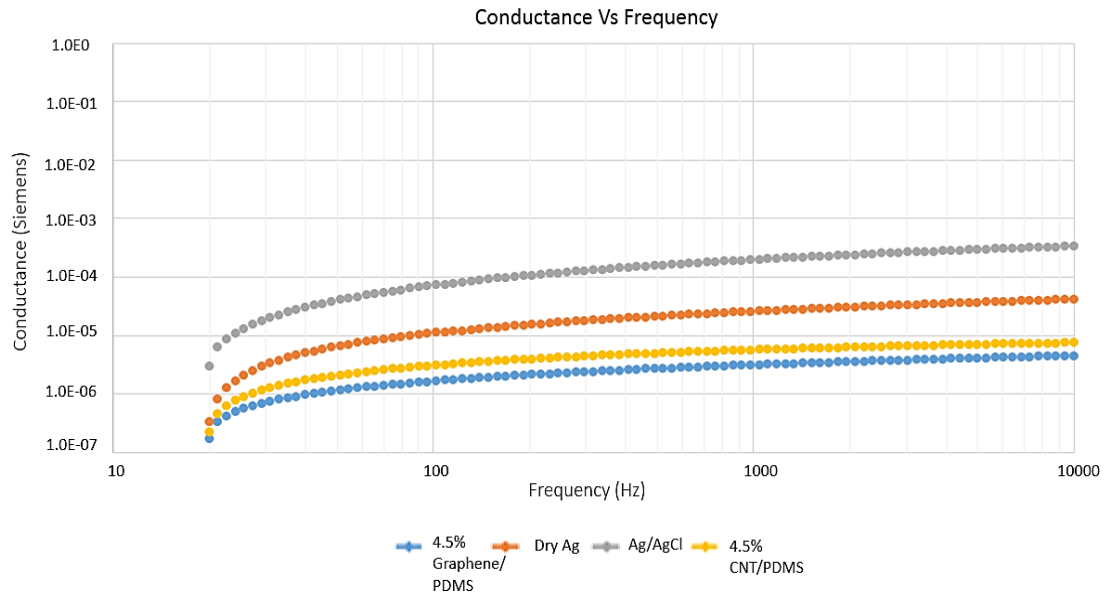
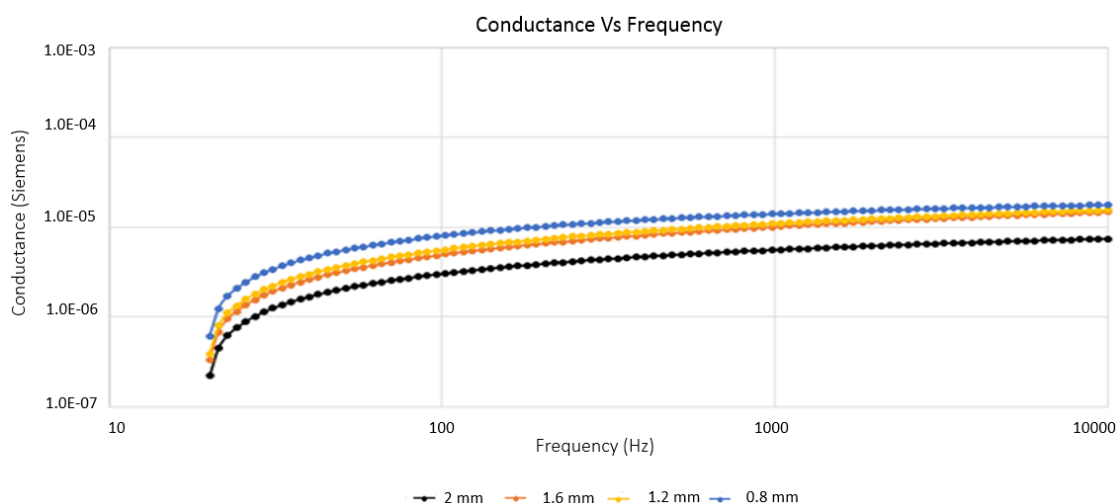


Figure 4.10: Variation in conductance with frequency for different electrodes.

As can be seen in Figure 4.10, the conductance of the standard Ag/AgCl electrodes was the highest. The conductance of 4.5wt% CNT/PDMS electrodes was observed to be higher than the 4.5wt% Graphene/PDMS electrodes and therefore the former was an appropriate choice for ECG sensing. The average conductance offered by CNT/PDMS electrodes in the ECG frequency range (0.01–150 Hz) was approximately 1  $\mu$ S, while the minimum required conductance for ECG measurement is 0.02  $\mu$ S [240]. Although the conductance offered by CNT/PDMS was lower than that of the conventional Ag and Ag/AgCl electrodes, it was acceptable for ECG monitoring.

The variation in conductance was also evaluated for CNT/PDMS samples having different thicknesses. Four samples of thickness – 0.8 mm, 1.2 mm, 1.6 mm and 2 mm – were prepared and their conductance was measured using the method described above. The plot of conductance vs frequency for CNT/PDMS samples of different thicknesses can be seen in Figure 4.11.



*Figure 4.11: Variation in conductance with frequency for CNT/PDMS samples with different thickness.*

As can be seen in Figure 4.11, only a small increase in conductance is observed in the ECG frequency range of 0.05–150 Hz (diagnostic) with decreasing thickness [241]. Therefore, for convenience, the ECG measurements were obtained from subjects using a CNT/PDMS patch electrode of dimensions 30 mm × 30 mm × 2 mm. The ECG signal quality was enhanced by adhering the electrode to the skin using Ten 20 conductive paste.

The main purpose of CNT/PDMS film is to measure ECG signals and skin stretch under the electrode. As the film stretches with the skin it is important to consider the effect of stretching of the film on the ECG signal.

For this purpose, the variation in conductance of the CNT/PDMS film on stretching was measured (see Figure 4.12). The film was stretched up to a maximum strain rate of 50%

using the texture analyser and the conductance across the film was measured using the LCR meter.

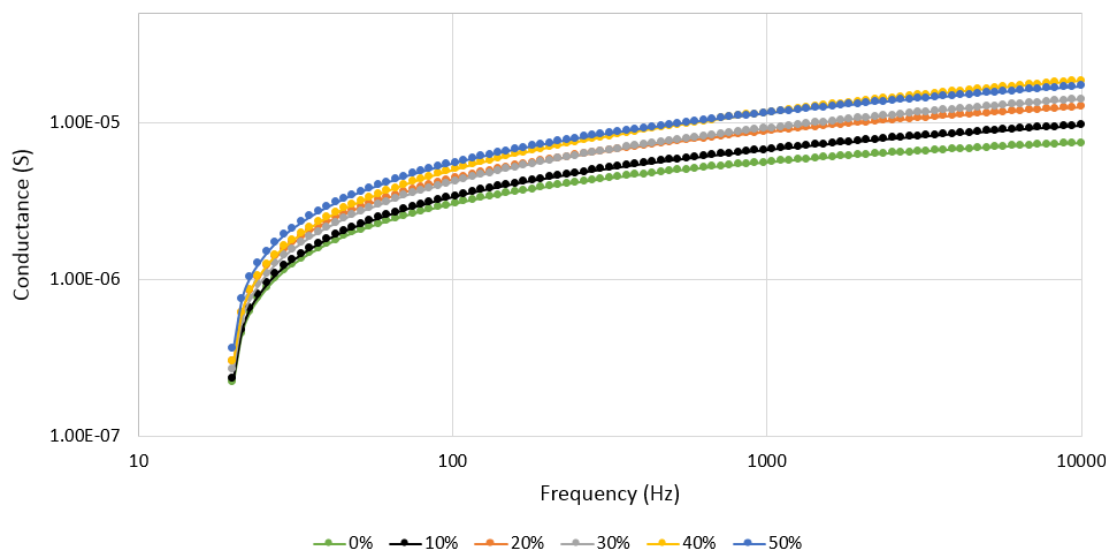


*Figure 4.12: Variation in conductance with frequency for CNT/PDMS samples at different stretch percentages.*

## 4.7 SUMMARY

In this chapter, four PDMS films of dimensions 30mm × 30mm × 2.5 mm were prepared by mixing different ratios of B:CA: 8:1, 10:1, 12:1 and 15:1. The film with a B:CA ratio of 15:1 exhibited the lowest Young's modulus (0.38 MPa), while the highest Young's modulus (1.05 MPa) was exhibited by the film with a B:CA ratio of 8:1. Thus, it can be inferred that increasing the PDMS B concentration in the film makes it more stretchable. However, the Young's modulus of all four films lay within the estimated range of the Young's modulus of human skin (7.2 kPa–17.9 MPa) described in chapter 2. Thus, the PDMS film prepared using the method described in this chapter can be used to emulate skin stretch.

The wet Ag/AgCl electrodes exhibited the maximum conductance within the ECG frequency range, followed by the dry Ag, CNT/PDMS and graphene/PDMS electrodes. A CNT/PDMS patch electrode with dimensions of 30 mm × 30 mm × 2 mm was developed to acquire ECG measurements in this study (see chapter 7). The average

conductance of the film in the ECG frequency range was  $1 \mu\text{S}$ . The Young's modulus of the film was found to be 1.3309 kPa, which is lower than the minimum Young's modulus of skin. Hence, it can be inferred that the addition of CNTs to PDMS makes the film more stretchable, meaning it causes less restriction to skin stretch. The electrode thickness hardly affected the conductance. A slight change in conductance (at ECG frequencies) was observed on stretching the CNT/PDMS film up to a strain rate of 50% using a texture analyser.

## **CHAPTER 5      OPTICAL STRAIN MEASUREMENT SYSTEM**

### **5.1 INTRODUCTION**

This chapter introduces a novel technique to quantify skin stretch in terms of strains by using a video camera and infinitesimal strain theory. The objective of this part of the research was to analyse the strain field distribution due to skin stretch. A PDMS film was used to emulate skin stretch. The effect of PDMS stretching was approximated using a 2D strain analysis over a region of interest. The infinitesimal strain theory has been utilized to quantify stretching in terms of 2D strain distributions using point displacements in PDMS.

The point displacements in PDMS were identified using an optical technique. A checkerboard pattern was printed on a PDMS film which was then stretched using a texture analyser. The movement of the film was video-recorded using a high speed camera. For each video frame, the movement of the corner points of the checkerboard squares from the first frame were identified and tracked. The motion tracking algorithm implemented to obtain the  $x$ - $y$  coordinates of the corners of the checkerboard squares is discussed in detail in section 5.4.

The implementation of this technique was validated with the stretch simulations carried out in SolidWorks (Dassault Systemes, Velizy-Villacoublay, France [242]). The effect of increase in thickness on 2D strain calculation using infinitesimal strain theory was also evaluated. Physical insight into strains can be obtained by decomposing them into normal and shear components. Finite strain theory is used to deal with arbitrarily large (finite) rigid-body displacements and rotations in elastomers, biological tissues and fluids [243]. Rigid-body motion does not contribute to strain field. This study requires the calculation of extensional and shearing deformations, therefore the use of infinitesimal strain theory is appropriate in this case.

### **5.2 MATHEMATICAL APPROACH TO QUANTIFY SKIN STRETCH**

The infinitesimal strain theory is a mathematical approach in which the displacement of the material particles is considered to be smaller than any relevant dimension of the

body [244]. Estimation of the point strains can be achieved by defining a displacement field for a particular body deformation.

Considering a small rectangular body  $PQRS$  with dimensions  $dx$  and  $dy$ , the coordinates of the body will be  $(x, y)$ ,  $(x+dx, y)$ ,  $(x, y+dy)$  and  $(x+dx, y+dy)$ , as shown in Figure 5.1 [245].

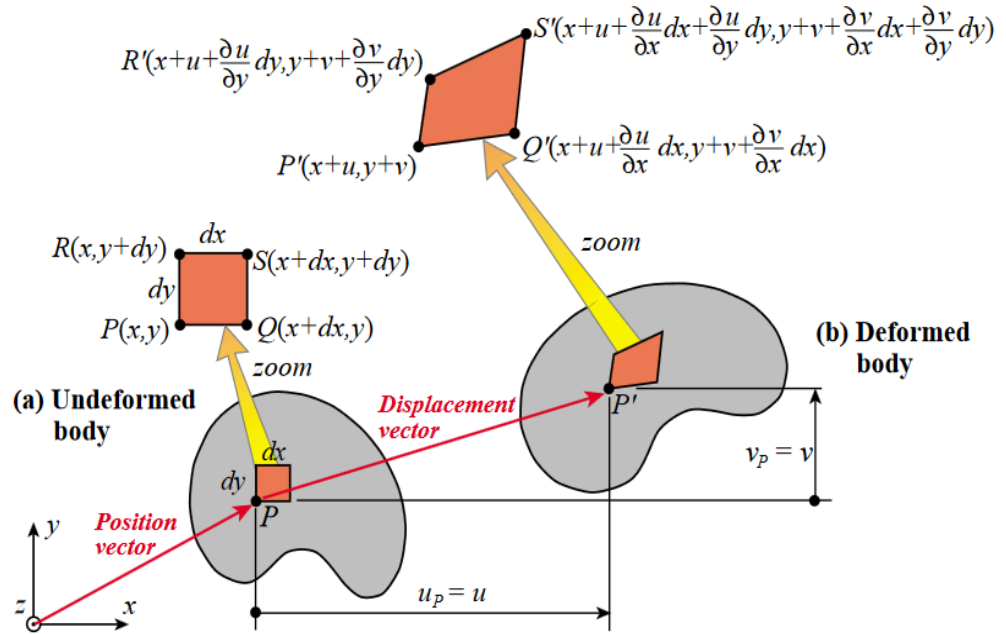


Figure 5.1: A body undergoing infinitesimal deformation [245].

Under the influence of a displacement vector  $PP' = u\hat{x} + v\hat{y}$ , the body  $PQRS$  deforms to  $P'Q'R'S'$  with the following coordinates:

$$P' = (x + u, y + v) \quad (5.1)$$

$$Q' = \left(x + u + \frac{\partial u}{\partial x} dx, y + v + \frac{\partial v}{\partial x} dx\right) \quad (5.2)$$

$$R' = (x + u + \frac{\delta u}{\delta y} dy, y + v + \frac{\delta v}{\delta y} dy) \quad (5.3)$$

$$S' = (x + u + \frac{\delta u}{\delta x} dx + \frac{\delta u}{\delta y} dy, y + v + \frac{\delta v}{\delta x} dx + \frac{\delta v}{\delta y} dy) \quad (5.4)$$

The point strains can be determined from the displacements as:

$$\epsilon_x = \frac{Q'\hat{x} - P'\hat{x}}{dx} = \frac{x + u + \frac{\delta u}{\delta x} dx - (x + u)}{dx} = \frac{\delta u}{\delta x} \quad (5.5)$$

$$\epsilon_y = \frac{R'y - P'\hat{y}}{dy} = \frac{y + v + \frac{\delta v}{\delta y} dy - (y + v)}{dy} = \frac{\delta v}{\delta y} \quad (5.6)$$

$$\epsilon_{xy} = \frac{\delta u}{\delta y} + \frac{\delta v}{\delta x} \quad (5.7)$$

where  $\epsilon_x$  is the normal strain in  $x$ -direction,  $\epsilon_y$  is the normal strain in  $y$ -plane and  $\epsilon_{xy}$  is the shear strain in  $xy$ -plane. The definition of the principal and shear strains for any rotational deformation  $\theta$  can be expressed as [246]:

$$\epsilon_\theta = \frac{\epsilon_x + \epsilon_y}{2} + \frac{\epsilon_x - \epsilon_y}{2} \cos[2\theta] + \frac{1}{2} \epsilon_{xy} \sin[2\theta] \quad (5.7)$$

$$\frac{-1}{2} \gamma_\theta = \frac{\epsilon_x - \epsilon_y}{2} \sin[2\theta] - \frac{1}{2} \epsilon_{xy} \cos[2\theta] \quad (5.8)$$

where

$$\theta = \frac{1}{2} \tan^{-1} \frac{\frac{\epsilon_x - \epsilon_y}{\sqrt{\epsilon_{xy}^2 + (\epsilon_x - \epsilon_y)^2}}}{\frac{\epsilon_{xy}}{\sqrt{\epsilon_{xy}^2 + (\epsilon_x - \epsilon_y)^2}}} \quad (5.9)$$

The principal strains are defined as the maximum and minimum strains for a purely rotational deformation. Thus, they have no shear component and can be expressed as:

$$\epsilon_{1,2} = \frac{\epsilon_x + \epsilon_y}{2} \pm \sqrt{\left(\frac{\epsilon_x - \epsilon_y}{2}\right)^2 + \left(\frac{1}{2}\epsilon_{xy}\right)^2} \quad (5.10)$$

The principal angle  $\theta_p$  associated with principal strains is given by:

$$\theta_p = \frac{1}{2} \tan^{-1} \frac{\epsilon_{xy}}{\epsilon_x - \epsilon_y} \quad (5.11)$$

Also, the maximum shear strain (associated with the 45° angle to the principal strains) can be represented as:

$$\frac{\epsilon_{xy_{max}}}{2} = \sqrt{\left(\frac{\epsilon_x - \epsilon_y}{2}\right)^2 + \left(\frac{\epsilon_{xy}}{2}\right)^2} \quad (5.12)$$

$$\theta_s = -\frac{1}{2} \tan^{-1} \left( \frac{\epsilon_x - \epsilon_y}{\epsilon_{xy}} \right) \quad (5.13)$$

where  $\theta_s$  is the maximum shear angle.

The above terms were used in the analysis of strains in different conditions. They parameterize in the form of a circle called Mohr's circle, which is a widely used representation when performing a stress or strain analysis on a material body. The strain

equations (5.7) and (5.8) describe the locus of Mohr's circle. It is essentially a parametric plot between  $\epsilon_\theta$  and  $\frac{1}{2}\gamma_\theta$  where the principal strains are located diametrically opposite on the horizontal axis, as shown in Figure 5.2

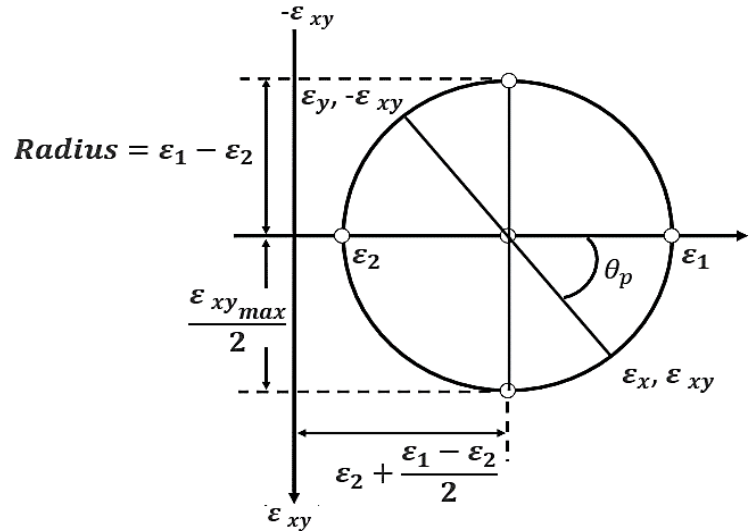


Figure 5.2: Mohr's circle for plane strain

In this research it is desired to estimate the strain field over a region of skin. This can be carried out by assuming that small triangular elements cover the region and estimating the strains based on the displacements of the vertices. Consider a case where some random number of test points/nodes are marked on the skin. They may be triangulated using Delaunay triangulation [247]. Delaunay triangles are well shaped and connect points in the nearest neighbourhood and therefore Delaunay triangulation is useful in scattered data interpolation [248].

Each triangle can be considered as an element that can be represented by a single strain value, as illustrated in Figure 5.3. The overall strain for each element can be calculated at its centroid by applying infinitesimal strain theory [244] for three points (the vertices) undergoing relative displacement.

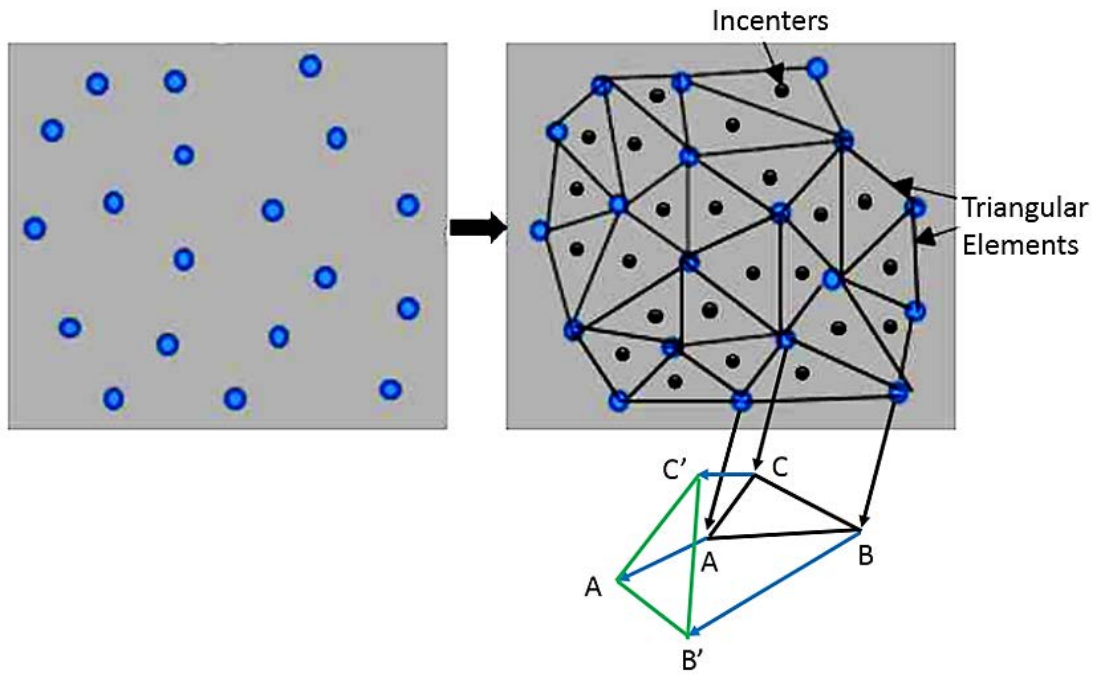


Figure 5.3: Set of points A, B and C on skin undergoing deformation, displaced at A', B' and C'.

Assuming a triangular element ABC deforms to A'B'C', the strain-displacement matrix can be defined using infinite strain theory as:

$$\begin{bmatrix} A_x - B_x & 0 & \frac{(A_y - B_y)}{2} \\ 0 & A_y - B_y & \frac{(A_x - B_x)}{2} \\ B_x - C_x & 0 & \frac{(B_y - C_y)}{2} \\ 0 & B_y - C_y & \frac{(B_x - C_x)}{2} \\ C_x - A_x & 0 & \frac{(C_y - A_y)}{2} \\ 0 & C_y - A_y & \frac{(C_x - A_x)}{2} \end{bmatrix} \begin{bmatrix} \varepsilon_x \\ \varepsilon_y \\ \varepsilon_{xy} \end{bmatrix} = \begin{bmatrix} \Delta A_x - \Delta B_x \\ \Delta A_y - \Delta B_y \\ \Delta B_x - \Delta C_x \\ \Delta B_y - \Delta C_y \\ \Delta C_x - \Delta A_x \\ \Delta C_y - \Delta A_y \end{bmatrix} \quad (5.14)$$

where  $A = (A_x, A_y)$  and likewise  $\varepsilon_x, \varepsilon_y$  &  $\varepsilon_{xy}$  are normal strain components in  $x, y$  and shear  $x$ - $y$  strains respectively.

In order to apply this theory, it is necessary to identify points that move as the skin is stretched, so that the strain of the skin can be calculated. In this work the coordinates

for the initial positions ( $A, B, C \dots$ ) and the final positions ( $A', B', C' \dots$ ) of the points were estimated using an optical device and the strain values ( $\epsilon_x, \epsilon_y$  and  $\epsilon_{xy}$ ) were calculated from equation

(5.14).

Marking a set of points on the skin to measure skin stretch in terms of normal and shear strains would be difficult to implement considering the discomfort caused to the patient. In addition, the points marked on the skin would be covered by the ECG electrode, therefore they can't be used to measure skin stretch under the ECG sensing site. Also, the ink used to mark the points may wash off after some time.

This research circumvented these issues by printing a checkerboard pattern on the PDMS film electrode itself using screen printing. In the screen printing process, the screen, which usually consists of a piece of mesh made of synthetic polymer, is used to transfer ink onto the substrate [249]. In this case, a mesh with an aperture of 0.1 mm was used for fine printing. The mesh was mounted on a frame made of wood. A checkerboard pattern was printed on some part of the mesh using black silicone ink (Print-On, Raw Material Suppliers, California, USA), and the other parts of the mesh were made impermeable to the ink. The ink in the mesh openings was squeezed on the substrate using a blade or a squeegee. The ink was then allowed to dry out for 24 hours. Silicone ink was found to be one of few inks that permanently adhered to the silicone. Other conventional inks (water or oil based) were found to rub off easily. Silicone ink is used for printing on wristbands and swimming caps. It is safe to work with as it does not produce any dangerous fumes on heating. It cures at 121°–204°C in only 2–6 minutes. It is easy to use, provides a robust adhesion and is water resistant and stretchable [250]. The dimensions of each square (black and white) in the checkerboard were 1 mm × 1 mm.

### **5.3 PDMS STRETCH SIMULATION IN SOLIDWORKS®**

After printing, the PDMS stretch simulations were carried out in SolidWorks, where the PDMS was stretched in different directions. The special distributions of plane strain

components  $\epsilon_x$ ,  $\epsilon_y$  and  $\epsilon_{xy}$  in response to the applied force were obtained and the simulations were validated experimentally.

A thin PDMS film was modelled and simulated for strain measurements in SolidWorks. Since the study involved simulating displacement induced strains in a thin elastomer, the SolidWorks platform offered to be an appropriate choice, considering its efficient solver abilities.

A film with dimensions of 30 mm  $\times$  30 mm  $\times$  2.5 mm was modelled, and custom material properties to mimic the mechanical properties of PDMS were assigned to the film, which are listed in Table 5.1 [251].

*Table 5.1: Approximate material properties used to emulate PDMS.*

<b>Material properties</b>	<b>Value</b>
Elastic modulus	1 MPa
Poisson's ratio	0.49
Mass density	0.97 kg/m <sup>3</sup>
Tensile strength	2.24 MPa
Thermal conductivity	0.15 (W/m-K)
Specific heat	1.46 kJ/(kg·K)

The structure was considered to be linearly elastic and isotropic over the range of expected motion. A static study was implemented to respond to small displacements within the elastomer geometry. The construction of any solid geometry in SolidWorks for static analysis requires defining structural restraints as boundary conditions.

A specified translation with respect to a specific plane and axis for a face, edge or vertex can be defined using reference geometry in SolidWorks [252]. The objective of this work was to analyse the strain induced in different parts of the elastomer due to stretching. Two types of fixtures were defined on the designed geometry. The top face of the film was translated by 1 mm in the upward direction (y-axis) by assigning it as reference geometry and the bottom face was fixed using fixed or immovable fixture. Two types of guided clamp pairs – curved and rectangular – were used for PDMS stretch simulation to induce different strain fields in the membrane (see Figure 5.4).

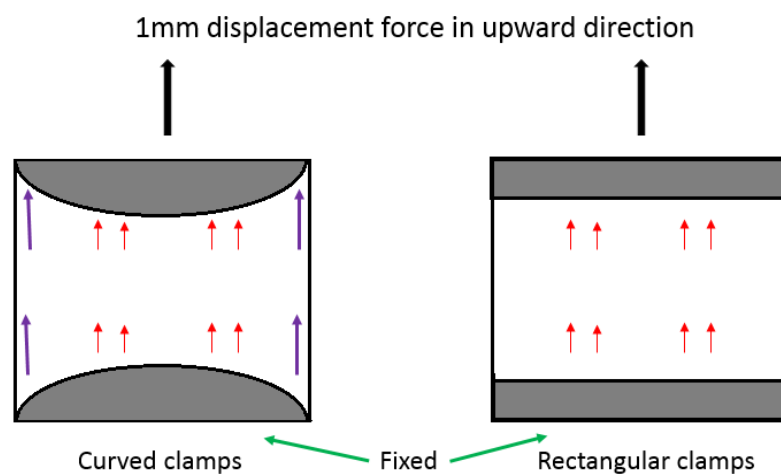


Figure 5.4: Stretch simulation using curved and rectangular clamps.

Finite element analysis (FEA) is a reliable numerical technique for analysing engineering designs. The process starts with the creation of a geometric model. This is followed by subdividing the model into small regions of simple shapes called elements which are connected via common points called nodes. The finite element method (FEM) predicts the behaviour of the model by combining the information obtained from all elements making up the model.

Meshing is a crucial step in design analysis. The automatic mesher in SolidWorks generates a mesh based on a global element size, tolerance, and local mesh control specifications. Mesh control constrains the sizes of elements for components, faces, edges and vertices.

The software estimates a global element size for the model, taking into consideration its volume, surface area and other geometric details. The size of the generated mesh (number of nodes and elements) depends on the geometry and dimensions of the model, element size, mesh tolerance, mesh control and contact specifications. For a more accurate solution, a smaller element size was chosen in this study, as shown in Table 5.2.

Meshing generates 3D tetrahedral solid elements, 2D triangular shell elements and 1D beam elements [253]. A mesh consists of one type of element unless the mixed mesh type is specified. Solid meshes generate linear (draft quality) and parabolic (high quality) tetrahedral geometries, as represented in Figure 5.5.

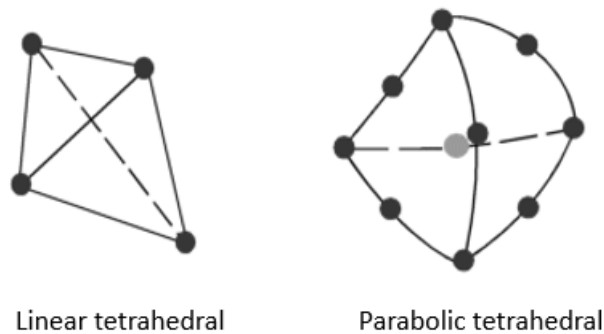


*Figure 5.5: Solid mesh geometries [254].*

Parabolic geometries are superior to linear geometries as they represent curved boundaries more accurately and produce better mathematical approximations. Shell elements are naturally suitable for modelling thin sheet metals, and beams and trusses are suitable for modelling structural membranes [253]. In this case, solid type meshing was performed using high quality geometry, as illustrated in Figure 5.6.

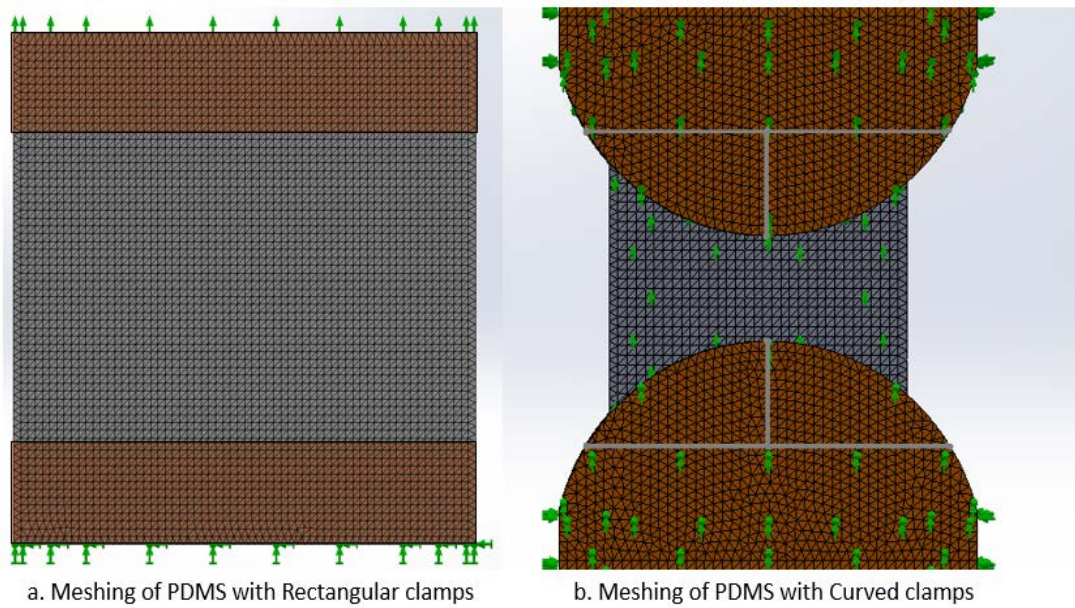


*Figure 5.6: Meshing of PDMS using high quality solid meshing.*

When mesh quality is high, the “Jacobian points” setting controls the number of points to be used in checking the distortion level of high order tetrahedral elements. The tolerance can be adjusted to solve some meshing problems due to free edges. The platform offered two types of meshers: standard and curvature based. The standard mesher involves the use of a Voronoi-Delaunay meshing algorithm while the curvature based mesher is better suited for assigning more elements at the curves, especially in cases of volumetric meshing. The standard mesher option was therefore chosen for this analysis. The details of the generated mesh are listed in Table 5.2.

Table 5.2: Meshing parameters for PDMS stretch simulation.

Mesh parameters	Values
Mesh type	Solid mesh
Mesher used	Standard mesh
Jacobian points	4 points
Element size	2.16 mm
Tolerance	1.067 mm
Mesh quality	High
Total nodes	24, 530
Total elements	14, 103

Once the meshing model was defined, the next step was to run the study using an appropriate modelling solver. Modelling solvers are utilized to solve a large system of simultaneous equations quickly while using minimum time, disk space and memory requirements. The two solver options provided by SolidWorks are:

1. The Direct Sparse solver
2. The FFEPlus solver

The Direct Sparse solver does not use approximations while solving a set of equations, therefore there are no errors associated with the solution process. On the other hand, the FFEPlus solver is an iterative solver that approximates a solution and calculates the associated errors. The iterations continue until the error is reduced to an acceptable level. Discretization errors are present in both iterative and direct solvers [255].

While the answers given by both solvers are similar, speed and performance may differ depending on the type and size of the problem. For large and complex problems, the FFEPlus solver is more efficient than the direct solver [256].

The PDMS stretch simulations in this case were performed for rectangular and curved clamps using the FFEPlus solver. The distribution of plane strain components  $\epsilon_x$ ,  $\epsilon_y$  and  $\epsilon_{xy}$  in response to the applied displacement (1 mm translation in the upward direction) were obtained in this way.

The infinitesimal strain theory equations discussed in section 5.2 are valid for 2D in-plane analysis. This work investigated the effect of skin stretch prevalent through small surface displacements. Therefore, 2D strain analysis is justified by employing surface strain equations and ignoring any significant strain components in the  $z$ -plane. The analyses were subsequently validated by simulating a 3D model, including the effect of increasing PDMS film thickness on overall strain calculations (section 5.4).

To examine the effect of localized perturbations in the film, a bi-axial prescribed displacement force (0.04 mm, 0.001 mm) was applied at the bottom-left corner of a thin PDMS film of dimensions of 30 mm  $\times$  by 30 mm in SolidWorks, as seen in Figure 5.7.

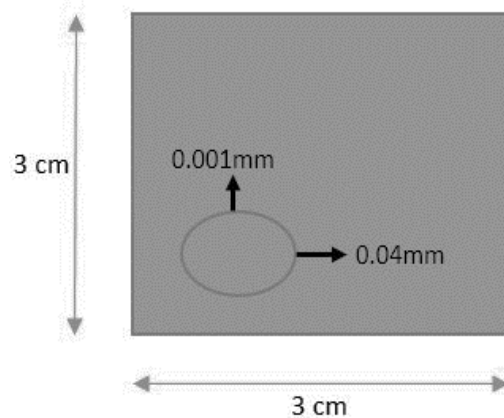


*Figure 5.7: PDMS stretch application on a circular region at the bottom left corner in SolidWorks.*

A set of 500 data points (nodes) from SolidWorks was imported in MATLAB for strain calculation using Delaunay triangulation and the infinitesimal strain theory equations. The simulations were performed for various thickness of the film. The mean values of the strain field distribution ( $\epsilon_x$ ,  $\epsilon_y$  and  $\epsilon_{xy}$ ) were evaluated in SolidWorks and MATLAB for five thicknesses: 1 mm, 5 mm, 10 mm, 15 mm and 20 mm. The error

plots exhibiting the difference between the strain values derived from SolidWorks and MATLAB, computed at different thicknesses of the simulated PDMS film, are shown in section 5.5.

#### 5.4 EXPERIMENTAL VALIDATION

To validate the simulations discussed in section 5.3, experiments were performed on a thin PDMS patch of the same dimensions used in the SolidWorks simulation. A checkerboard pattern was inked on the PDMS patch which was then subjected to tensile testing using a texture analyser. The preparation and printing of the PDMS patch was described in section 5.2. The tensile tests were conducted at a speed of 0.5 mm/s, using rectangular and curved clamps (as shown in Figure 5.8) to mimic the simulation studies in section 5.3.



Rectangular clamps



Curved clamps

*Figure 5.8: Use of rectangular and curved clamps to conduct tensile tests.*

The vertical displacement of the PDMS sample after being subjected to a tension-relaxation test for 13 seconds was recorded using the rear camera of an iPad Air at 720p

HD, 120 fps, with a sensor of 1.12  $\mu\text{m}$  pixel pitch and aperture size of f/2.4. The frames targeted the node points of the checkerboard pattern undergoing stretch and relaxation throughout the test. The pattern selection allowed for a symmetrical analysis of node points. Due to the high video recording rate (120 fps), around 1600 frames were acquired from 13 seconds of test duration. To reduce computational demands, and taking into consideration the slow strain rates, every 25th frame was compared with its corresponding down-sampled value from the texture analyser readings, a more complete description is available in [99].

Initially, all the frames were filtered, sharpened and cropped in Photoshop CC (Adobe, California, USA) [257]. Corner points were identified using the Harris-Stephens algorithm in MATLAB and their movement was tracked over consecutive frames.

Following identification of corner points in each frame, the displacements of points in consecutive frames was estimated by two methods. First, the Point Tracker feature in MATLAB employs the Kanade-Lucas-Tomasi (KLT) algorithm which works well for video stabilization, camera motion estimation and object tracking. However, this tracker works satisfactorily only for short range tracking [258]. It was found that KLT offered effective tracking for small displacements between the points in consecutive frames, but there were some unavoidable errors in the case of medium to large displacements propagated over time. Another confounding factor was the need to re-initialize the tracker periodically. Consequently, an alternative point matching method was developed based on Euclidean distance point mapping. The Euclidean distance method was applied to match points from the initial frame to the next frame by considering the minimum projected distance between them. This was achieved by choosing the least distance between two points in consecutive frames to be a mapped pair [99]. The corners for both black and white squares were tracked for each frame as seen in Figure 5.9.

Changes in ambient lighting conditions proved to be confounding factors in efficient motion tracking of the PDMS. Nevertheless, the displacements of the points from their initial positions were computed and the three components of strain ( $\epsilon_x$ ,  $\epsilon_y$  and  $\epsilon_{xy}$ ) were calculated using the three points on each triangle via equation

(5.14). The strains were attributed to the incentres of the triangles formed by Delaunay triangulation, as shown in Figure 5.10.

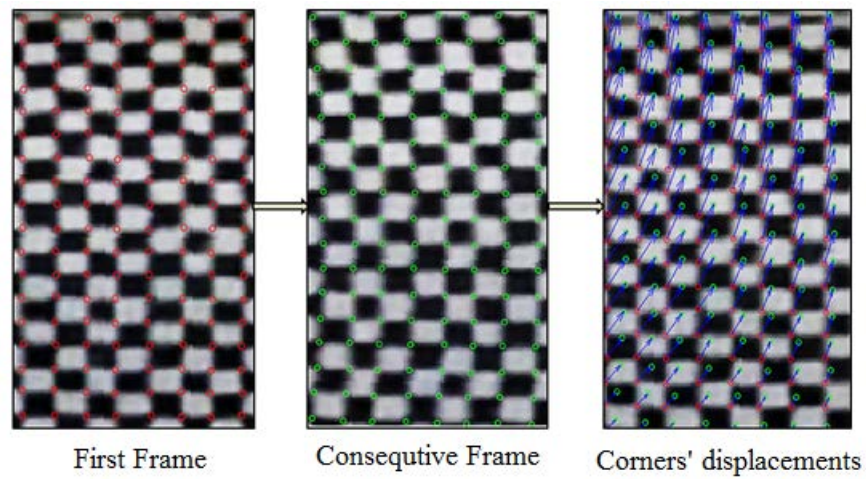


Figure 5.9: Motion tracking from first frame using Euclidean distance mapping.

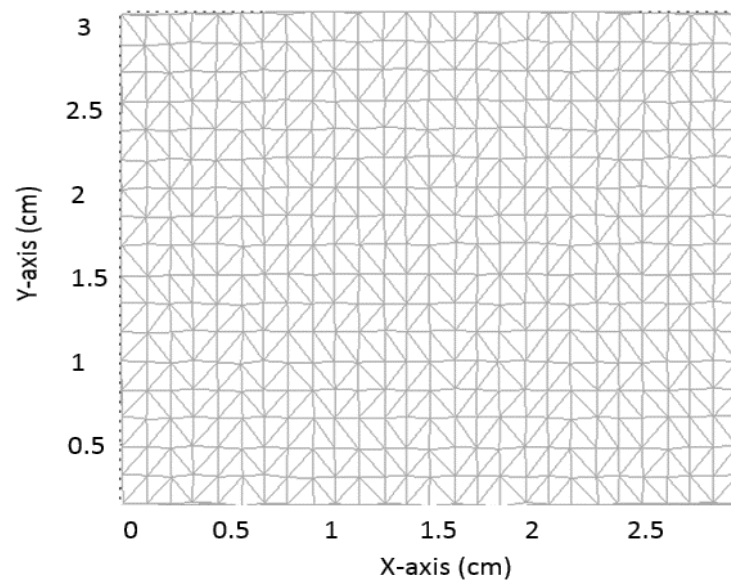


Figure 5.10: Delaunay triangulation using the checkerboard corner points.

## 5.5 RESULTS

The results obtained by interpolating strains due to PDMS translation by texture analyser were found to be in good agreement with the strain distribution ( $\epsilon_x$ ,  $\epsilon_y$  and  $\epsilon_{xy}$ ) over the plane of PDMS in SolidWorks. The strain distributions in the  $x$ ,  $y$  and  $xy$  planes using rectangular clamps are compared in Figures 5.11-5.13 respectively.

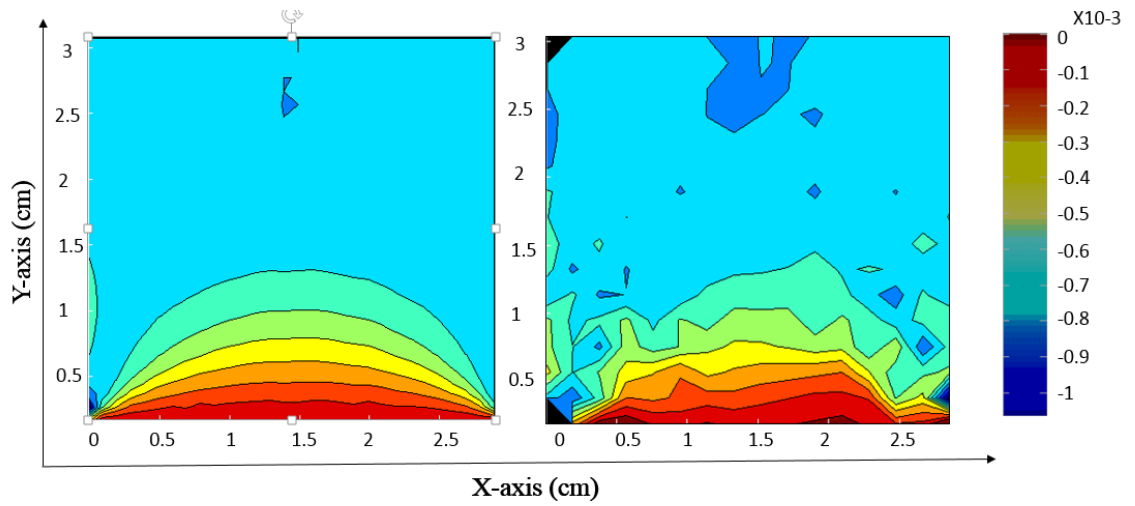


Figure 5.11: Strain distribution in  $\epsilon_x$  for PDMS stretch simulation in SolidWorks (left) and PDMS translation by texture analyser (right) using rectangular clamps

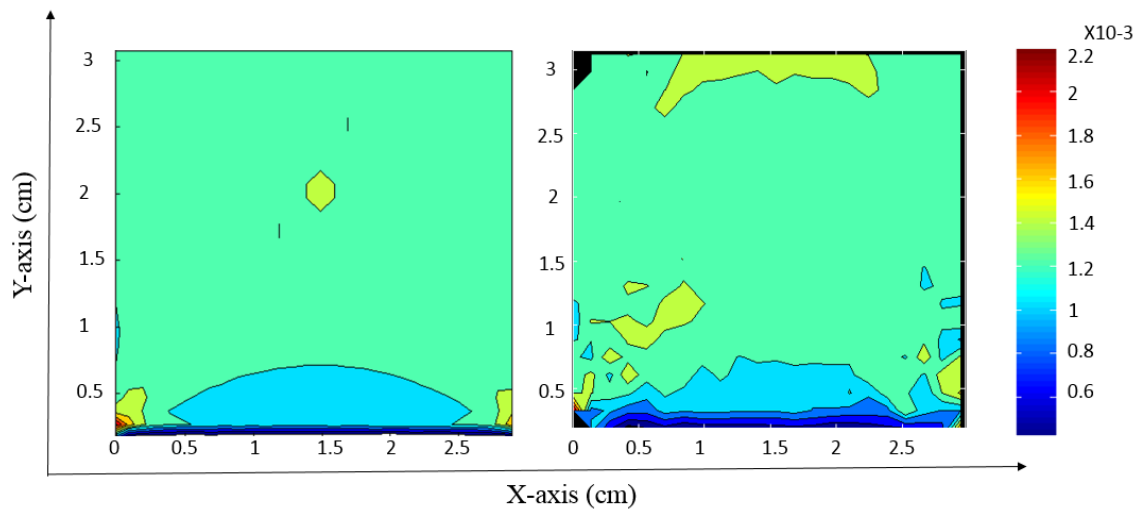


Figure 5.12: Strain distribution in  $\epsilon_y$  for PDMS stretch simulation in SolidWorks (left) and PDMS translation by texture analyser (right) using rectangular clamps

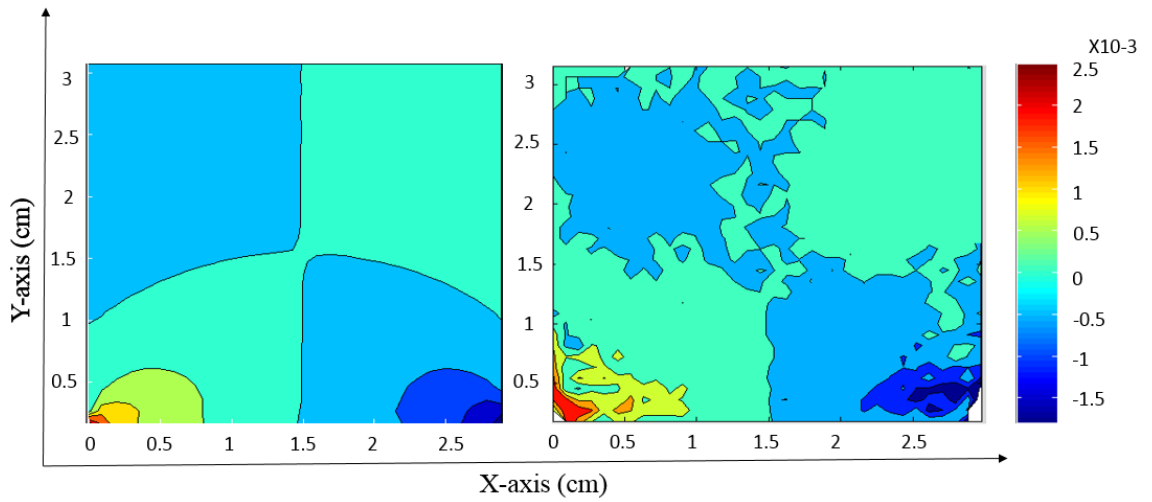


Figure 5.13: Strain distribution in  $\epsilon_{xy}$  for PDMS stretch simulation in SolidWorks (left) and PDMS translation by texture analyser (right) using rectangular clamps

The strain distributions in the  $x$ ,  $y$  and  $xy$  planes using curved or semi-circular clamps are shown in Figures 5.14-5.16 respectively.

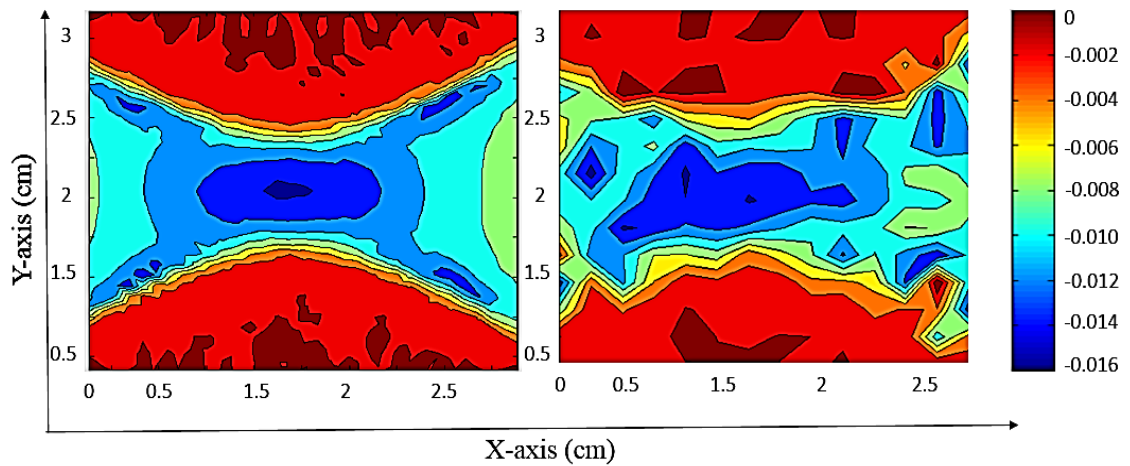


Figure 5.14: Strain distribution in  $\epsilon_x$  for PDMS stretch simulation in SolidWorks (left) and PDMS translation by texture analyser (right) using curved clamps

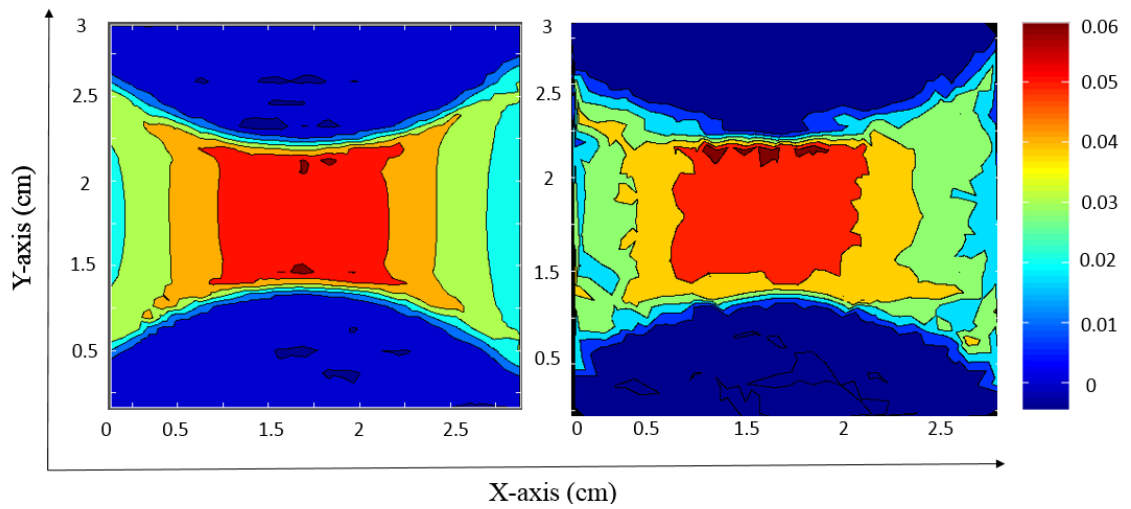


Figure 5.15: Strain distribution in  $\epsilon_y$  for PDMS stretch simulation in SolidWorks (left) and PDMS translation by texture analyser (right) using curved clamps

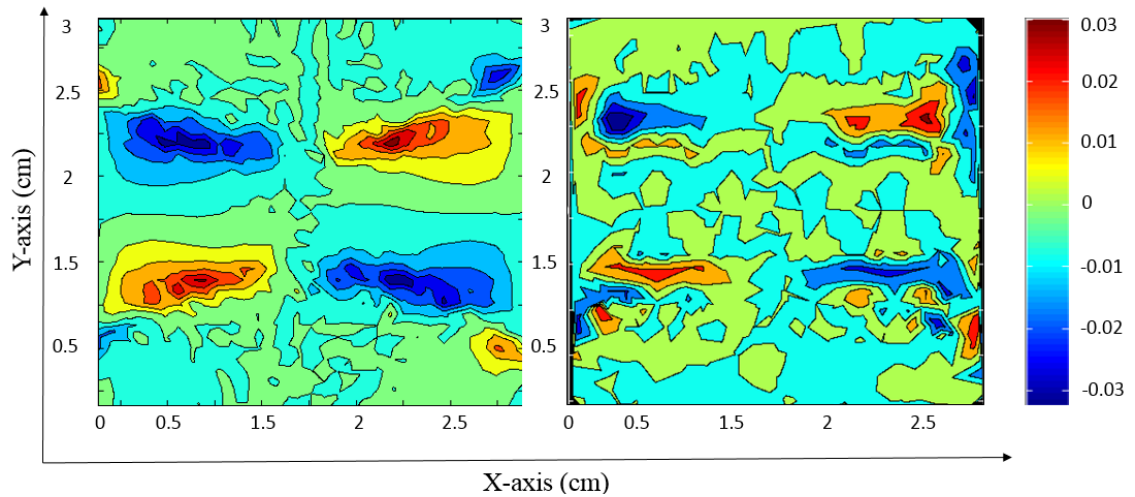


Figure 5.16: Strain distribution in  $\epsilon_{xy}$  for PDMS stretch simulation in SolidWorks (left) and PDMS translation by texture analyser (right) using curved clamps

The difference in mean strains  $\epsilon_x$ ,  $\epsilon_y$  and  $\epsilon_{xy}$  due to the application of a bi-axial displacement force on a PDMS film in SolidWorks and MATLAB (as discussed in section 5.3) for different film thicknesses can be seen in Figure 5.17.

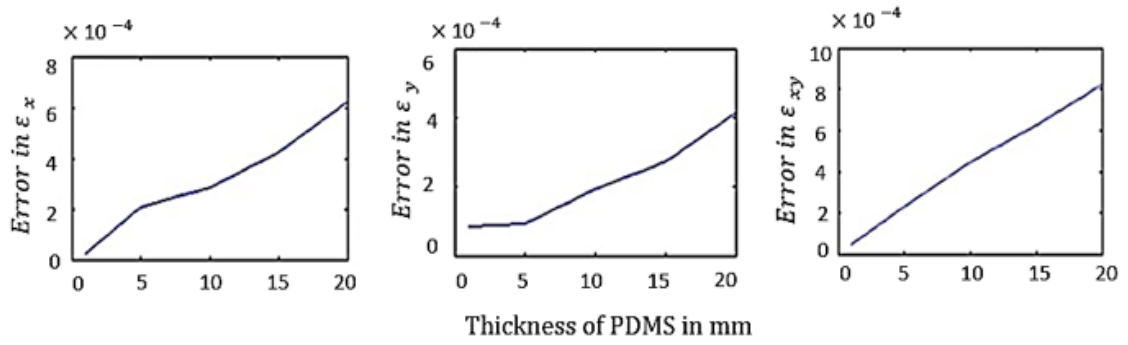


Figure 5.17: Strain differences/errors ( $\epsilon_x$ ,  $\epsilon_y$  &  $\epsilon_{xy}$ ) as a function of thickness

## 5.6 DISCUSSION

The strain distribution for rectangular and circular clamps can be clearly differentiated in the above results. In the strain profiles for rectangular clamps (Figure 5.11–5.13) a uniform distribution of stretch induced strains can be observed for all three strain components. This is due to the equal transmission of stretch along the edge of the clamps with a monotonically increasing displacement as it is transmitted to the bottom fixture. In contrast, the strain distributions for circular clamps (Figure 5.14–5.16) show a radial spread throughout the film’s geometry. In this case, the intensity of induced strain is centralized and decreases uniformly along the edges. The maximum strain is observed in the region with the minimum gap between the clamps and decreases as the gap increases with curvature.

It was expected that the uniformity of strain fields while performing image processing on the measurements obtained from the texture analyser could have been compromised due to errors in fiducial point identification, the interpolation of data using the Delaunay triangulation and mathematical equations. However, the results revealed very similar variations in strain distributions, which confirmed the approach and the parameters used in this study.

The efficacy of 2D strain theory was also tested for different PDMS film thicknesses. The increase in error with thickness was expected since the analysis technique used focused on the 2D strains in the plane of PDMS, considering it to be a planar film. With an increase in thickness, the assumed strain distribution and equations become less appropriate and therefore deviations from the expected values were observed, as shown in Figure 5.17.

## 5.7 SUMMARY

This chapter has investigated the ability of an optical strain measurement system to estimate the strain field resulting from the stretching of PDMS electrodes. This work was motivated by the desire to eliminate skin stretch induced motion artefacts from ECG signals. A novel technique for measuring skin stretch in terms of 2D strains was described which employs an optical sensor and infinitesimal strain theory in MATLAB. A PDMS film with dimensions of 30 mm  $\times$  by 30 mm  $\times$  and a thickness of 2.5 mm was modelled by defining the material properties of PDMS in SolidWorks. The stretch simulations were carried out by clamping the PDMS film between rectangular and curved clamps. In both cases, the PDMS was stretched/translated upwards by 1 mm to analyse the strain distributions  $\epsilon_x$ ,  $\epsilon_y$  and  $\epsilon_{xy}$  under different circumstances.

The results were experimentally validated by stretching a PDMS film of the same dimensions using a texture analyser and by applying similar boundary conditions. Videos capturing the movement of the PDMS film held between rectangular and curved clamps were acquired. Image processing techniques were employed to compute the strain fields due to 1 mm upward translation of the PDMS film using a texture analyser. The experimental results obtained from the tensile testing of PDMS patches were in good agreement with the results obtained from the FEA simulation in SolidWorks. An additional objective of this study was to analyse the effect of increasing thickness of PDMS films on 2D strain calculations. As expected, the accuracy was observed to decrease with increasing the thickness of the film.

## CHAPTER 6      A PILOT STUDY ON ECG MOTION ARTEFACT REJECTION

### 6.1 INTRODUCTION

In chapter 5, a novel technique to estimate motion artefact from ECG signals using a video camera and infinitesimal strain theory equations has been discussed. This chapter describes the use of non-uniform strain field pertaining to skin stretch to reduce motion artefacts from the ECG measurements. Skin stretch was quantified in terms of normal and shear strains ( $\epsilon_x$ ,  $\epsilon_y$  and  $\epsilon_{xy}$ ) and used to remove motion artefacts from ECG signals through Principal Component Analysis (PCA) and Independent Component Analysis (ICA).

Different types of movement artefacts were induced in the left arm of a human subject (age group 18-35 years) by back & forth movement, opening and closing fist and rotating wrist clockwise and anticlockwise. A video camera was used to track the skin stretch under the ECG electrode as a 2-dimensional strain field. The objective of evaluating normal and shear strains was accomplished by mathematically relating them to the displacement of an infinitesimal particle due to skin stretch. The concept behind PCA and ICA has been explained and the results obtained after their implementation on noisy ECG have been illustrated. Although PCA and ICA algorithms are used extensively in the field of biomedical engineering, the main motive of this work is to incorporate the use of strains in the algorithms to remove motion artefacts from ECG. Therefore, a new state-of-the-art algorithm has been devised by implementing PCA and ICA along with skin stretch information.

### 6.2 MATERIALS AND METHODS

An ECG measurement was acquired from a subject for 10 seconds using a PhysioFlow PF05 L1 (Manatec Biomedical, Paris, France) through a National Instruments data acquisition board (NI-DAQ, Texas, USA).

Standard Ag/AgCl electrodes were placed close to the radial artery on the palmar sides of both forearms. The experiments were conducted by generating different kinds of

motion artefacts in the arm. Three types of motion were accounted for in this study: a) continuous back and forth movement of the arm, b) opening hand and closing fist continuously, and c) rotating wrist clockwise and anticlockwise (see Figure 6.1).

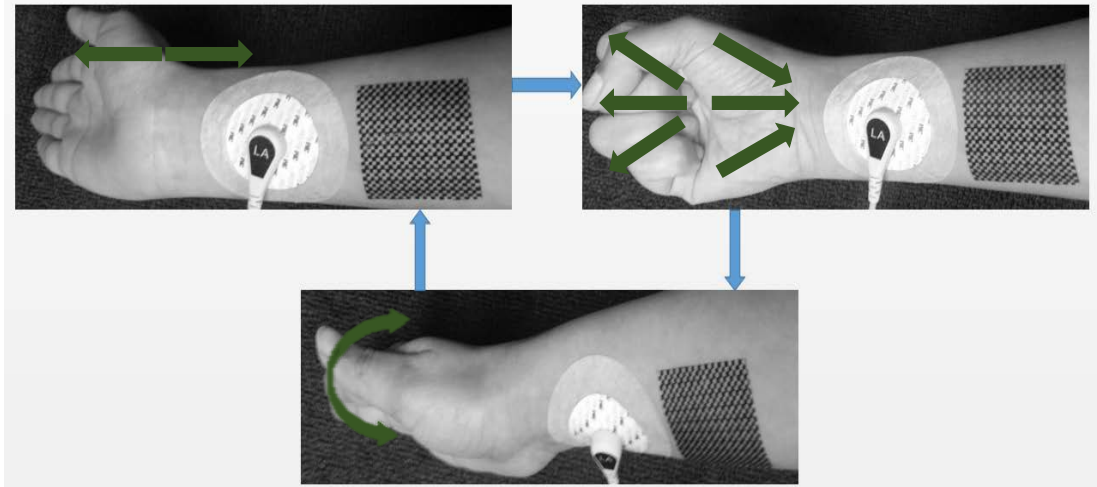


*Figure 6.1: Movements induced in arm by back and forth movement, opening and closing fist and rotating wrist clockwise and anticlockwise*

Motion artefacts were induced in the left forearm of the subject, while the right forearm was kept stable. A PDMS patch of dimensions 30 mm  $\times$  30 mm  $\times$  2.5 mm with similar elasticity to skin was adhered to the arm in the vicinity of the ECG electrode using polyvinyl alcohol (PVA) adhesive. The movement of the patch during the ECG measurement was recorded using a video camera with a resolution of 1920  $\times$  1080 pixels at 25 fps. The PDMS patch had a checkerboard pattern printed on it to identify the corner points of the checker boxes, as shown Figure 6.1. The movement of the patch was quantified by calculating mean values of normal and shear strain components ( $\epsilon_x$ ,  $\epsilon_y$  and  $\epsilon_{xy}$ ) over each frame using infinitesimal strain theory by using the method described in chapter 5 (section 5.4).

A flowchart describing the quantification of motion artefact from an ECG signal is given in Figure 6.2.

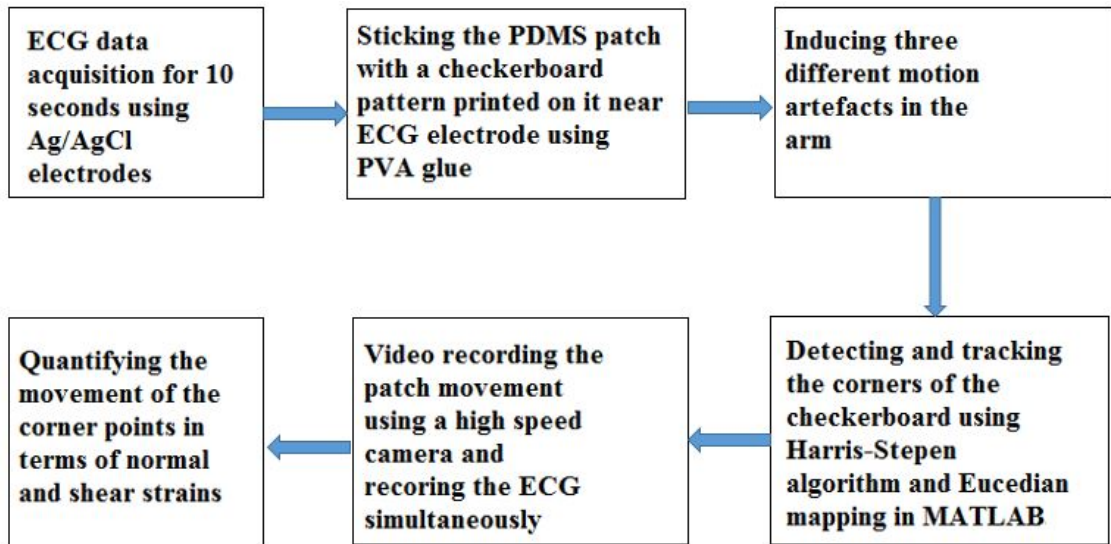


Figure 6.2: Flowchart representing the quantification of ECG motion artefact.

The recorded motion signal was processed using image processing and point tracking. The motion artefacts were calculated using infinitesimal strain equations. The video was recorded for 10 seconds at 25 fps. Plots of normal and shear strains against time can be seen in section 6.5. After the quantification of motion artefacts, the next step involved their elimination from the ECG. The motion artefacts were removed from the ECG signal using PCA and ICA, as discussed in the following sections.

### 6.3 MOTION ARTEFACT REJECTION USING PCA IN MATLAB

PCA is a statistical measure that employs affine transformation to convert a set of correlated values into a set of orthogonal linearly uncorrelated values. PCA is performed by eigenvalue decomposition of the data after mean centring each data element. The first step of PCA involves the calculation of the mean of each element of the data set followed by the evaluation of their deviation from the mean:

$$\bar{X} = X - \hat{X} \quad (6.1)$$

where  $X$  is the input data matrix needed to be filtered.

Baseline wandering of the ECG signal was removed by implementing zero-phase digital filtering in MATLAB [259] using the ‘filtfilt’ function, as seen in Figure 6.3.

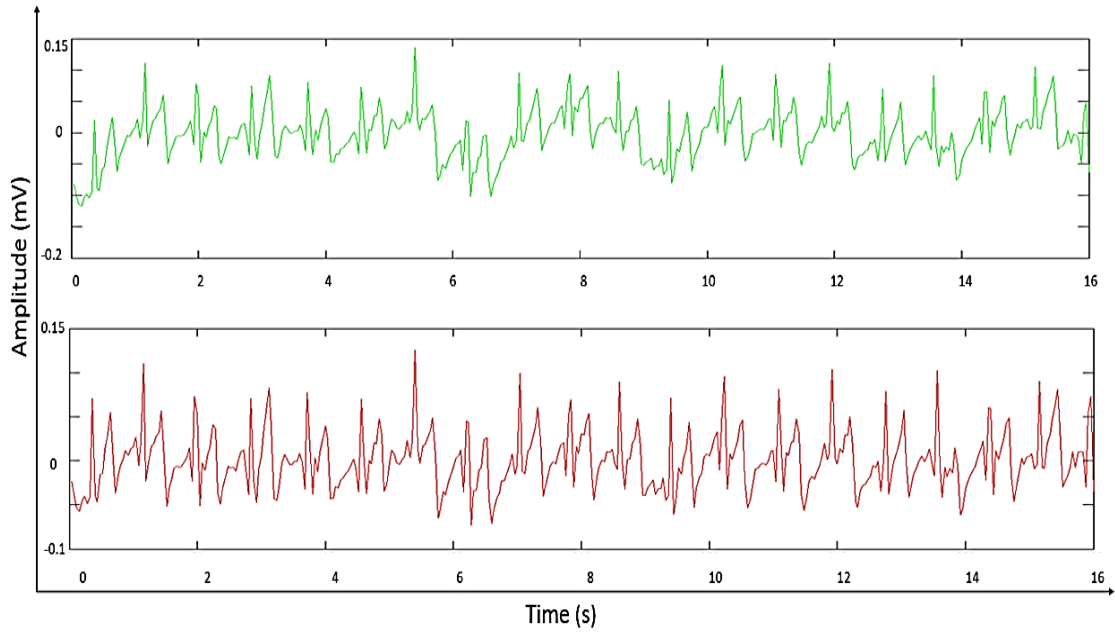


Figure 6.3: Acquired ECG signal (in green) and ECG after baseline removal (in red).

This was achieved by processing the data in both forward and reverse directions [260]. The filter coefficients  $\alpha$  and  $\beta$  were evaluated using the butterworth filter through the following equations [261] [262].

$$\alpha = \frac{(1 - k \times \cos(2\pi f_c) - \sqrt{2 \times k \times (1 - \cos(2\pi f_c) - k^2 \times \sin(2\pi f_c)^2)})}{1 - k} \quad (6.2)$$

$$\beta = 1 - \alpha \quad (6.3)$$

where  $k = 0.707$  for the cut-off frequency and  $f_c$  is the normalized frequency for the power supply interference at 50 Hz.

One method of employing PCA for the elimination of motion artefacts from the ECG involves acquiring multiple ECG measurements through different leads at the same time, and by taking each ECG measurement as an independent data set [263].

In this study, the ECG signals with motion artefacts were acquired using one lead of the ECG measurement system. Each segmented beat of the measured ECG was considered

a separate data vector [264]. A data matrix was formulated using repetitions of a unit beat data set for all the ECG beats, consisting of one column containing the samples from one ECG beat followed by three columns for each of the corresponding strains  $\varepsilon_x$ ,  $\varepsilon_y$  and  $\varepsilon_{xy}$ . For example, if the number of beats in an ECG measurement was 20, then the data set included 20 columns of ECG beats and 20 columns each of  $\varepsilon_x$ ,  $\varepsilon_y$  and  $\varepsilon_{xy}$ , corresponding to the respective ECG beats.

Another case, in which the ECG signal was not segmented into beats, is investigated in chapter 7. In this approach, the data set comprised four columns where the first column contained all the ECG samples and the other three columns for each of the corresponding strains  $\varepsilon_x$ ,  $\varepsilon_y$  and  $\varepsilon_{xy}$ , calculated as the mean strain for all elements in the region.

In order to segment the beats, it is important to find a fiducial point. A fiducial point must be determined so that the exact segment location within the beat can be defined [263]. PCA on the ECG signal was performed here by R peak detection and beat segmentation. Each beat of the ECG signal constituting an R to R interval was segmented and used as an independent vector in the data matrix. Figure 6.4 illustrates a typical ECG with fiducial points identified as R peaks (green dots).

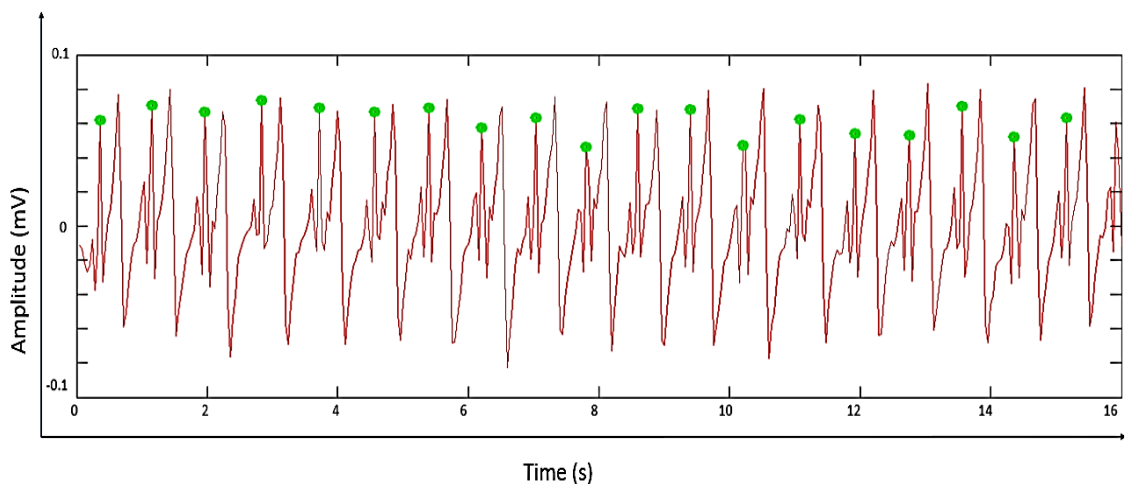


*Figure 6.4: R peak detection and ECG beat segregation.*

The R peak detection was performed in MATLAB *using* a max-min search employed on several windows of the ECG data. Each sample was checked for an absolute maxima or minima in a certain range of a potential window, where the range was approximated using the ECG beat rate. This is similar to the method employed by Sameni et al. (in 2006) [262].

Segmentation was followed by the covariance matrix calculation. Covariance is always measured between two dimensions. Covariance of two sets of data points is a measure of their variance from the mean with respect to each other [265]. The mathematical equation for finding the covariance between two data sets  $X$  and  $Y$ , having  $n$  number of elements is:

$$cov(X, Y) = \frac{\sum_{i=1}^n (X_i - X)(Y_i - Y)}{n - 1} \quad (6.4)$$

In this case, the covariance between the ECG data and the quantified strains (which is assumed to relate to ECG motion artefacts) was calculated.

The next step involves the calculation of the eigenvectors and eigenvalues. Each component of the data set contains new information about the data set. The data set is ordered in a way so that the first few components account for the most variability [263]. An eigenvector is essentially a non-zero vector which does not change its direction on application of a linear transformation. Interestingly, only square matrices can have eigenvectors and not all square matrices have eigenvectors. Eigenvalues and eigenvectors always come in pairs. The eigenvalues and eigenvectors are calculated by solving the equation below.

$$(X - I\lambda).E = 0 \quad (6.5)$$

where  $X$  is the input data matrix,  $\lambda$  contains the eigenvalues,  $I$  is the identity matrix and  $E$  is the eigenvector. The value by which the eigenvector is scaled on multiplication with the transformation matrix is called the eigenvalue. Once the eigenvectors are found, they are ordered with respect to eigenvalue from highest to lowest. In this way, the components are arranged in order of significance. The components of lower significance can then be ignored. The next step is to multiply the significant or chosen eigenvectors with the original data set. The number of eigenvectors is always equal to the number of data sets. Here, the first two most significant eigenvectors were chosen and multiplied with the data set. The mean values were then added back to the data set and the ECG signal was reconstructed as shown below.

$$Y = \lambda_5 X \quad (6.6)$$

$$X_{final} = Y + \hat{X} \quad (6.7)$$

where  $\lambda_s$  constitutes two most significant eigenvectors and  $X_{final}$  is the ECG obtained after PCA filtering.

A flow chart to illustrate the application of PCA is shown in Figure 6.5.

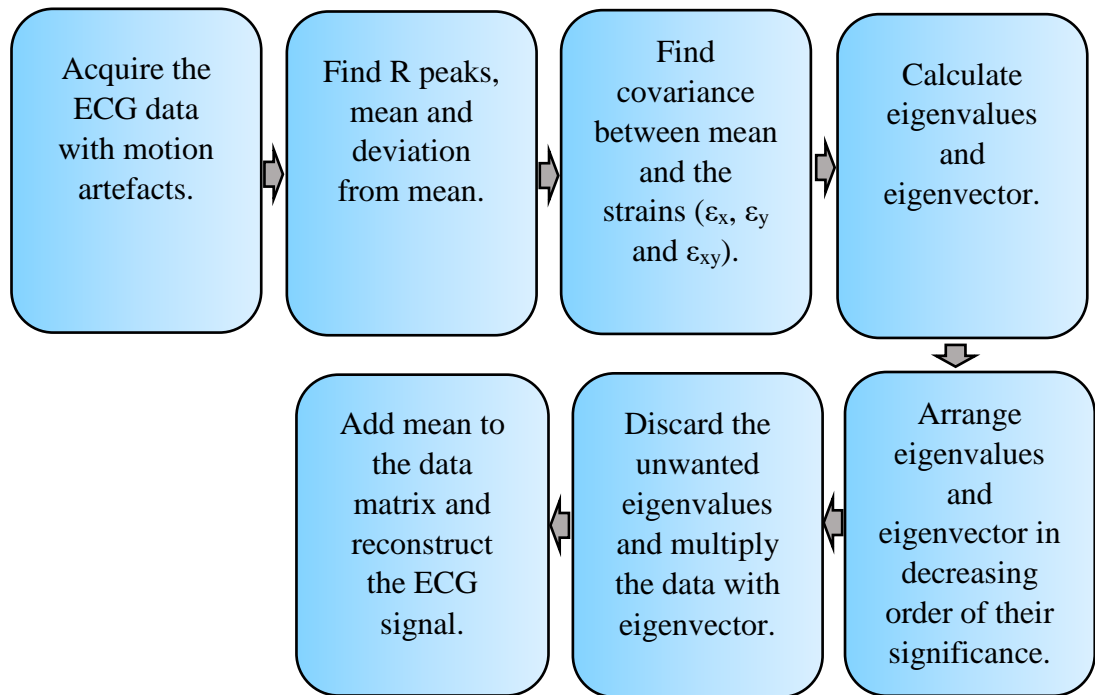


Figure 6.5: Flow chart representing the steps employed in the working of PCA

The number of eigenvectors is always equal to the number of data sets. In Figure 6.6, a comparison between an ECG signal with motion artefacts, an ECG signal with PCA filtering without using strains  $\epsilon_x$ ,  $\epsilon_y$  and  $\epsilon_{xy}$ , and an ECG signal with PCA filtering using those strains can be observed.

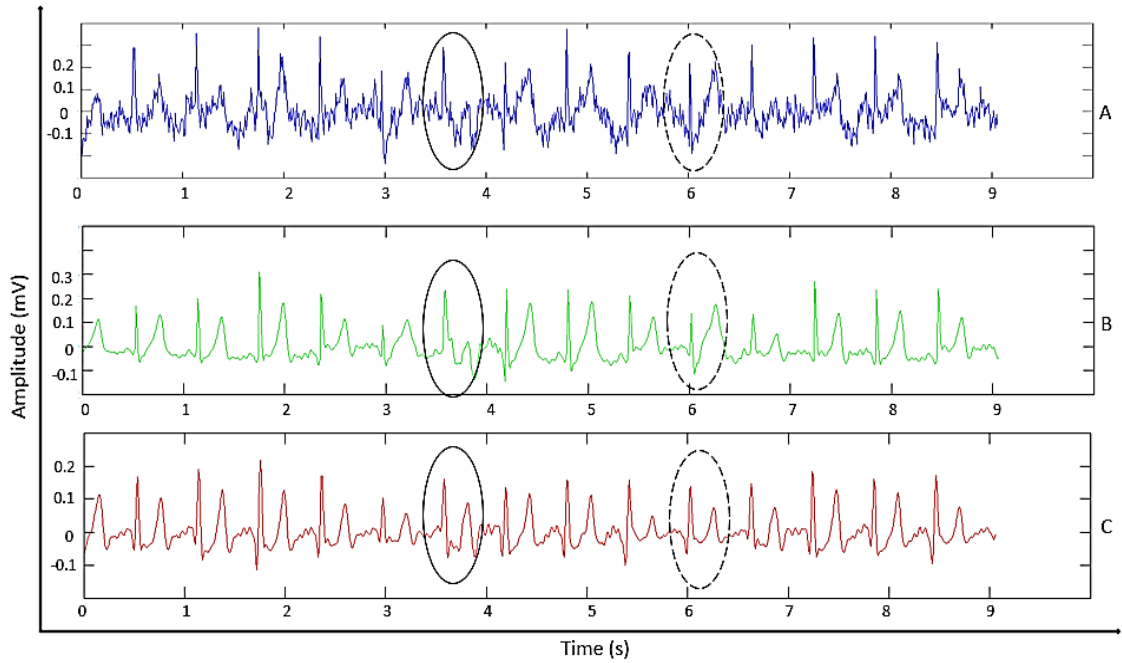


Figure 6.6: (A) Original ECG signal with motion artefacts; (B) PCA filtering of (A) through beat segmentation without using strains; (C) PCA filtering of (A) through beat segmentation by using strains  $\varepsilon_x$ ,  $\varepsilon_y$  and  $\varepsilon_{xy}$  (in red)

The ECG measurements were obtained using the method discussed in section 6.2. From Figure 6.6A, it can be noted that the ECG signal that was affected by arm movement led to an abnormally inverted T wave, highlighted by a solid circle between 3 and 4 seconds. This could lead to the wrong diagnosis of cardiac instability (e.g., ventricular hypertrophy, pulmonary embolism, etc.) [266]. Therefore, it is necessary to filter out the artefacts generated in the signal due to movement of the patient.

On filtering the signal using PCA without strains, the direction of the T wave remained unchanged (see Figure 6.6B). On the other hand, the direction of the T wave was reversed, and was the same as that of the QRS complex, when PCA was performed using strains (see Figure 6.6C). Also, the amplitude of the R peaks was significantly increased (highlighted by a dotted circle between 6 and 7 seconds) on execution of PCA using motion information.

## 6.4 MOTION ARTEFACT REJECTION USING ICA IN MATLAB

ICA is a method through which a multivariate signal can be separated into statistically independent components [267]–[269]. A fundamental feature of ICA is that the independent components are non-Gaussian signals. Like PCA, ICA of ECG signals can be done by either taking segmented beats as independent columns of data sets or by obtaining ECG through different leads at the same time. A flow chart explaining the process involved in ICA appears in Figure 6.7. A statistical ‘latent variables’ method was used to rigorously define ICA [127].

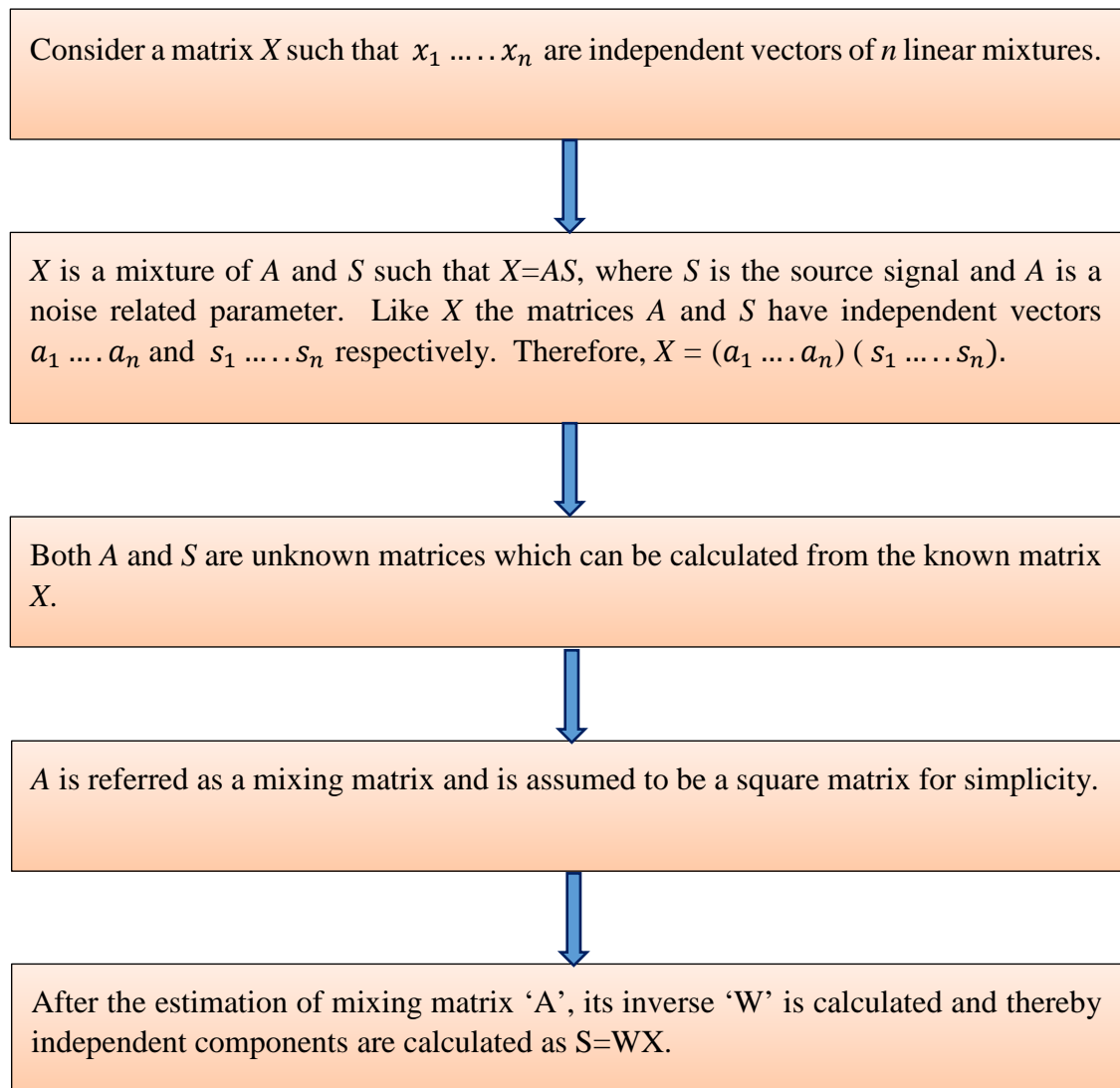


Figure 6.7: Flowchart representing the procedure involved in ICA

For ICA analysis, a linear mixture of  $n$  independent components  $s_1 \dots s_n$  can be defined as:

$$x_j = a_{j1}s_1 + a_{j2}s_2 + \dots a_{jn}s_n \quad (6.8)$$

where  $x_j$  holds for all  $j$ . Here, all the variables are random variables and have a zero mean. In the matrix notation, this can be defined as:

$$X = A.S \quad (6.9)$$

where  $A$  is the matrix of  $a_{j1} \dots a_{jn}$  and  $S$  of  $s_1 \dots s_n$ .  $A$  defines the matrix composed of different mixing weights to the independent signals and is therefore termed the mixing matrix. The independent components can be obtained through processing the inverse of mixing matrix  $A$  with the mixture, as in the following equation:

$$S = W.X \quad (6.10)$$

where  $W$  is estimated with the knowledge of  $A$  and equals its inverse.

The mixing matrix  $A$  can be calculated using different approaches in ICA. Here the JADE algorithm [270]–[272] was used to remove motion artefacts from the ECG signal using beat segmentation and the strains  $\varepsilon_x$ ,  $\varepsilon_y$  and  $\varepsilon_{xy}$ . The first step in the JADE algorithm involves mean centring and whitening of the data using PCA. The data matrix is ordered in the order of decreasing eigenvalues. Before discussing the equations involved in JADE algorithm, it is important to understand the concept of cumulant matrices.

In probability theory, cumulant matrices are used to provide information about the set of possible moments of distribution [273]. JADE can be defined as a blind source separation method involving fourth-order cumulant tensors [127]. The first, second and third order cumulants are the mean, the variance and the central moment respectively. The fourth and higher order cumulants are not equal to central moments [273]. Therefore, in order to make the independent components non-Gaussian, a fourth order cumulant matrix is derived in ICA. The fourth order cumulant [127], also called kurtosis, can be calculated using:

$$kurt(X) = E\{X^4\} - 3(E\{X^2\})^2 \quad (6.11)$$

$X$  corresponds to the data set constituting the ECG beats and their corresponding strains. The JADE algorithm involves the calculation of auto-cumulant and cross-cumulant matrices using equation (6.10). The auto-cumulant is calculated for each independent vector and the cross-cumulant is calculated between at least two independent vectors. If  $x_1$  and  $x_2$  are two independent vectors of data set  $X$ , then the theoretical analysis of kurtosis can be simplified based on its linear additive property, as shown in equation (6.12) [127].

$$kurt(x_1 + x_2) = kurt(x_1) + kurt(x_2) \quad (6.12)$$

After finding the cumulant matrix, a joint diagonalization or orthogonal rotation of the matrix is performed to find the mixing matrix  $A$ . A mathematical implementation of ICA using the JADE algorithm can be explained through the following equations.

First, the data matrix needs to be pre-processed by subtracting its mean value  $\hat{X}$ , as shown in equation (6.13).

$$\bar{X} = X - \hat{X} \quad (6.13)$$

The next step involves data whitened using PCA, which is performed to normalise the data containing ECG and strains, as shown in equation (6.14). Whitening was performed using eigenvalue decomposition of the covariant matrix  $VDV^T$ .  $D$  is a diagonal matrix with the corresponding eigenvalues. The whitening is done by multiplication of  $\bar{X}$  with the transformation matrix  $P$ , as shown in equation (6.15) [274].

$$P = V \cdot D^{-1/2} \cdot V^T \quad (6.14)$$

$$Z = P \cdot \bar{X} \quad (6.15)$$

The fourth order expectation  $E$  of the cumulants of the whitened matrix  $Z$  having four signals  $z_i, z_j, z_k$  &  $z_l$  is calculated by solving equation (6.16) [275].

$$\begin{aligned}
cum(z_i, z_j, z_k, z_l) & \quad (6.16) \\
& = E[z_i, z_j, z_k, z_l] - E[z_i, z_j]E[z_k, z_l] - E[z_i, z_k]E[z_j, z_l] \\
& \quad - E[z_i, z_l]E[z_j, z_k]
\end{aligned}$$

All the fourth order auto-cumulants  $AC$  and cross-cumulants  $CC$  were calculated using mathematical equations in MATLAB, as described in the equations below [276].

$$AC = \sum_{i=1}^m (Z_i^2 \cdot Z \cdot Z^T) / n - I_m - 2 \cdot I_i \cdot I_i^T \quad (6.17)$$

$$CC = \sqrt{2} \times \sum_{j=1}^{i-1} \frac{z_i \cdot z_j \cdot z_j^T}{n} - I_i \cdot I_j^T - I_j \cdot I_i^T \quad (6.18)$$

where  $m$  is the number of data sets,  $n$  is the size of each data set and  $I$  is the identity matrix.

The cumulants were stored in a matrix  $C$  of size  $m \times t$  (as seen in equation (6.19)), where  $t$  is the total number of cumulants  $\left(t = m^2 \times \left(\frac{m+1}{2}\right)\right)$ .

$$C = (C_1, C_2, C_3 \dots \dots C_t) \quad (6.19)$$

The auto-cumulants are the diagonal elements, while the cross-cumulants are the non-diagonal elements of matrix  $C$ .

A joint diagonalization or orthogonal rotation of matrix  $C$  was performed using Given's (or Jacobi's) rotation [125]. A step by step procedure involving the orthogonal diagonalization of the cumulant matrix is explained in the following equations.

Initially, an approximate diagonalization was performed by estimating the eigenvalue  $V$  and by reshaping the cumulant matrix  $C$  as  $CM$  in MATLAB.

$$V = eig(C) \quad (6.20)$$

$$CM = V^T \cdot C \quad (6.21)$$

The Given's rotation matrix  $GM$  was computed by calculating the rotation angle  $\theta$  to make the diagonalized matrix  $CM$  orthogonal.

The Given's rotation parameters  $G$ ,  $q$  and  $r$  were evaluated using the information in the cumulant matrix  $CM$ .

$$G = \sum_{j=1}^{m-1} \sum_{k=j+1}^m \begin{bmatrix} \sum_{l=j+m}^t CM_{jl} - \sum_{l=k+m}^t CM_{kl} \\ \sum_{l=k+m}^t CM_{jl} + \sum_{l=j+m}^t CM_{kl} \end{bmatrix} \quad (6.22)$$

$$q = (G * G^T)(1,2) + (G * G^T)(2,1) \quad (6.23)$$

$$r = (G * G^T)(1,1) + (G * G^T)(2,2) \quad (6.24)$$

The rotation angle  $\theta$  has been calculated using the Given's rotation parameters as:

$$\theta = \frac{q}{r + \sqrt{r^2 + q^2}} \quad (6.25)$$

$GM$  was calculated using  $\theta$  as:

$$GM = \begin{bmatrix} \cos(\theta) & -\sin(\theta) \\ \sin(\theta) & \cos(\theta) \end{bmatrix} \quad (6.26)$$

The orthogonal joint diagonalization was performed by updating the eigen matrix  $V$  from equation (6.27) using  $GM$  as:

$$CM_{diag} = V \cdot GM \quad (6.27)$$

The mixing matrix  $A$  was calculated by multiplying  $CM_{diag}$  with the whitened data  $Z$  in equation (6.28):

$$A = CM_{diag} \cdot Z \quad (6.28)$$

The first column of the mixing matrix  $A$  showed the highest correlation with the ECG signal. Therefore, only the first column of  $A$  was multiplied with the acquired ECG signal in matrix  $X$  to obtain an ECG signal without motion artefacts in matrix  $S$  by using equation (6.9).

The steps involved in the JADE algorithm to calculate the mixing matrix  $A$  and the source signal  $S$  are shown in the flow chart in Figure 6.8.

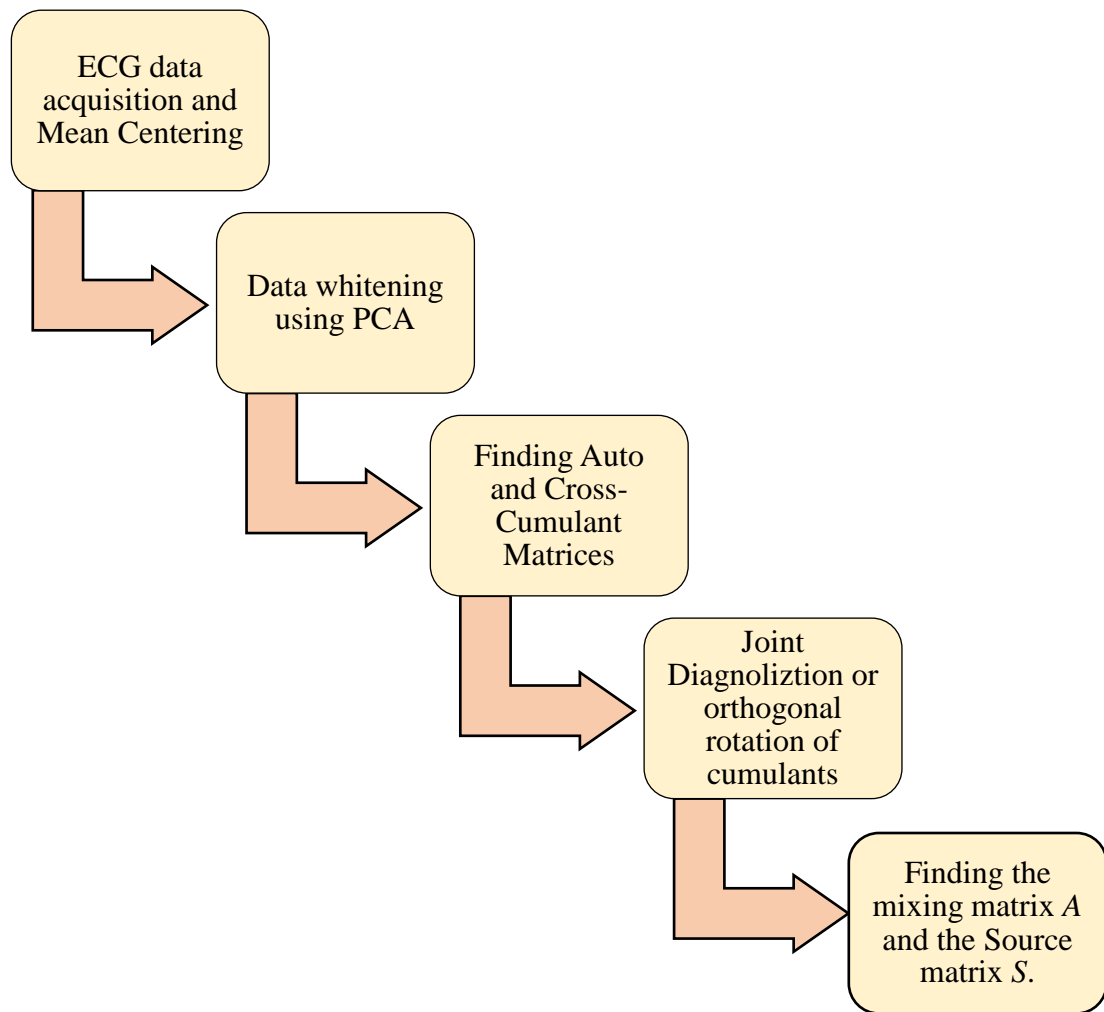


Figure 6.8: Steps involved in the JADE algorithm.

In the following section, a critical analysis of the results obtained after the implementation of PCA and ICA algorithms on the ECG is presented.

## 6.5 RESULTS AND DISCUSSION

As discussed in section 6.2, three different kinds of motion artefacts were induced in the arm by back and forth movement, opening and closing the fist, and rotating the wrist clockwise and anticlockwise. The strain plots obtained by inducing back and forth arm movement are shown in Figure 6.9.

It can be observed that the strain values lie within 0.02 and 0.07, which is a plausible range of strain for skin under these conditions. Signal fluctuations corresponding to the pseudo-periodic motion of the arm can also be observed.

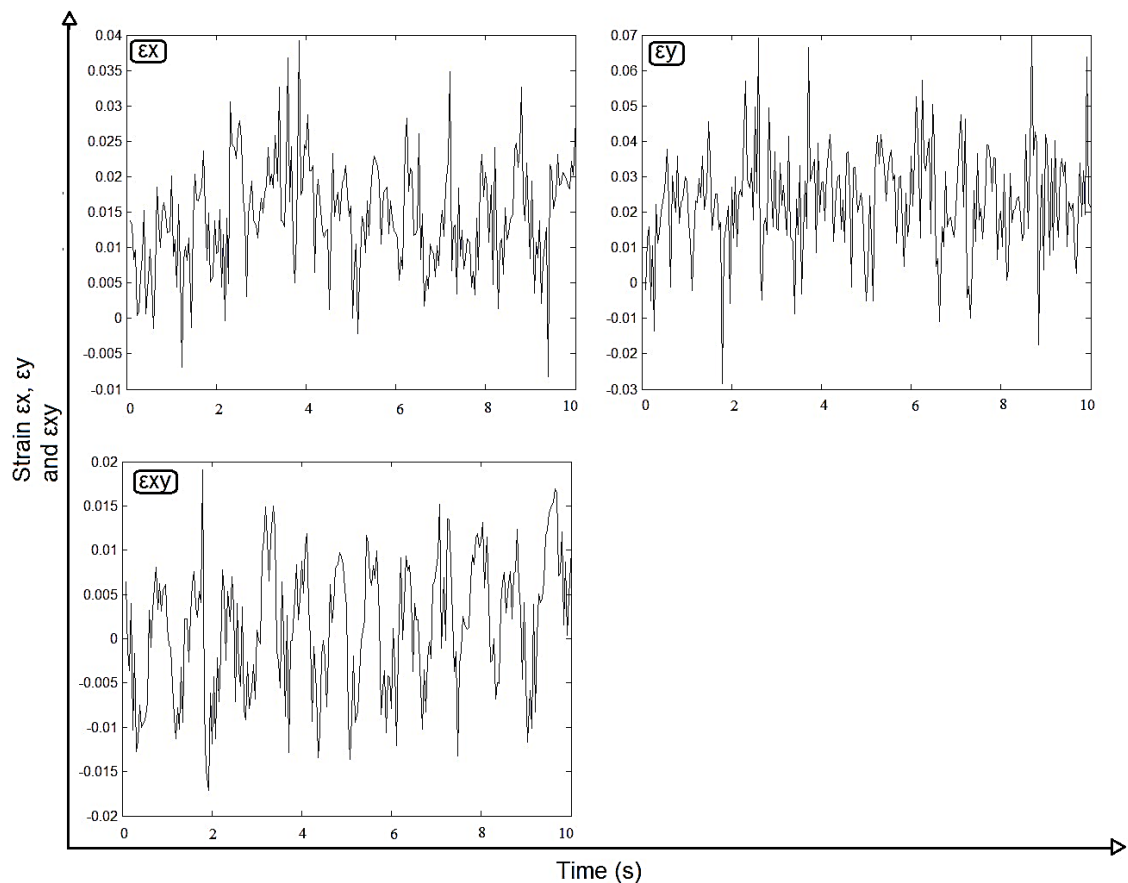


Figure 6.9: Plots of normal and shear strain components against time

The vector plots representing the change in position of the checkerboard corners of the corresponding frame from the first frame of reference can be seen for frames 55, 56 and 57 in Figure 6.10. The direction of the arrows represents the direction in which the points

moved. The strain vectors ( $\epsilon_x$ ,  $\epsilon_y$  and  $\epsilon_{xy}$ ) evaluated from the vector points are mapped onto the incentres of the Delaunay triangles for each frame as described in chapter 5. Strain contour plots of the respective frames corresponding to the vector plots are shown in Figures 6.11 to 6.13.

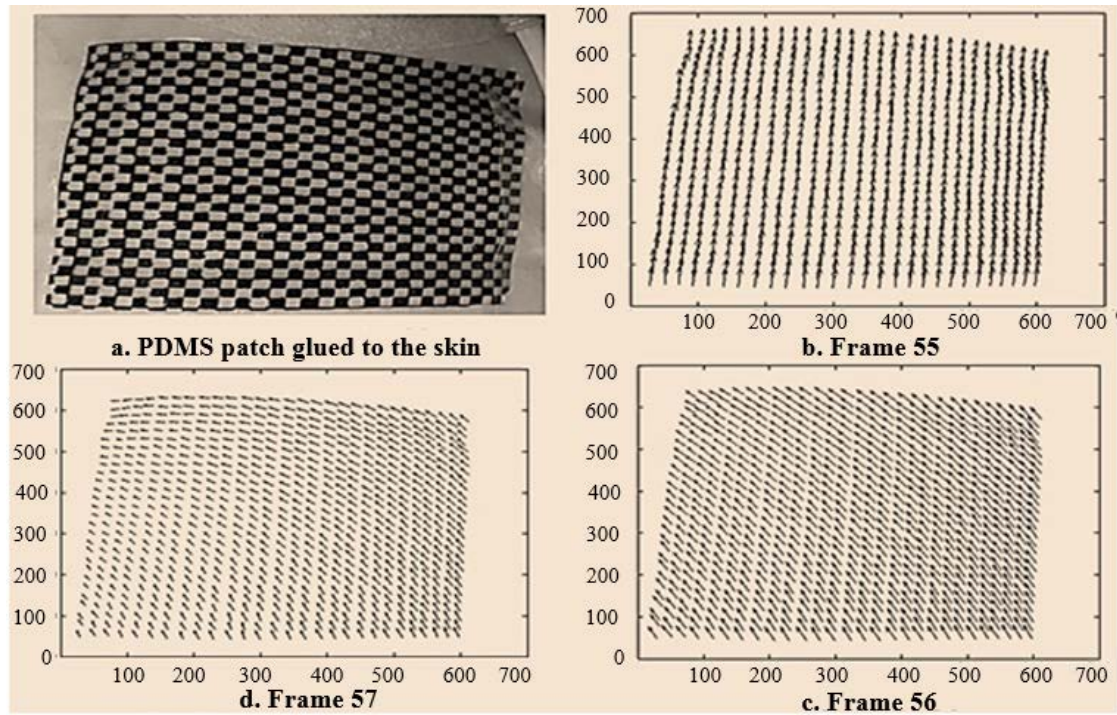


Figure 6.10: PDMS patch adhered to the arm and displacement vectors from the first frame.

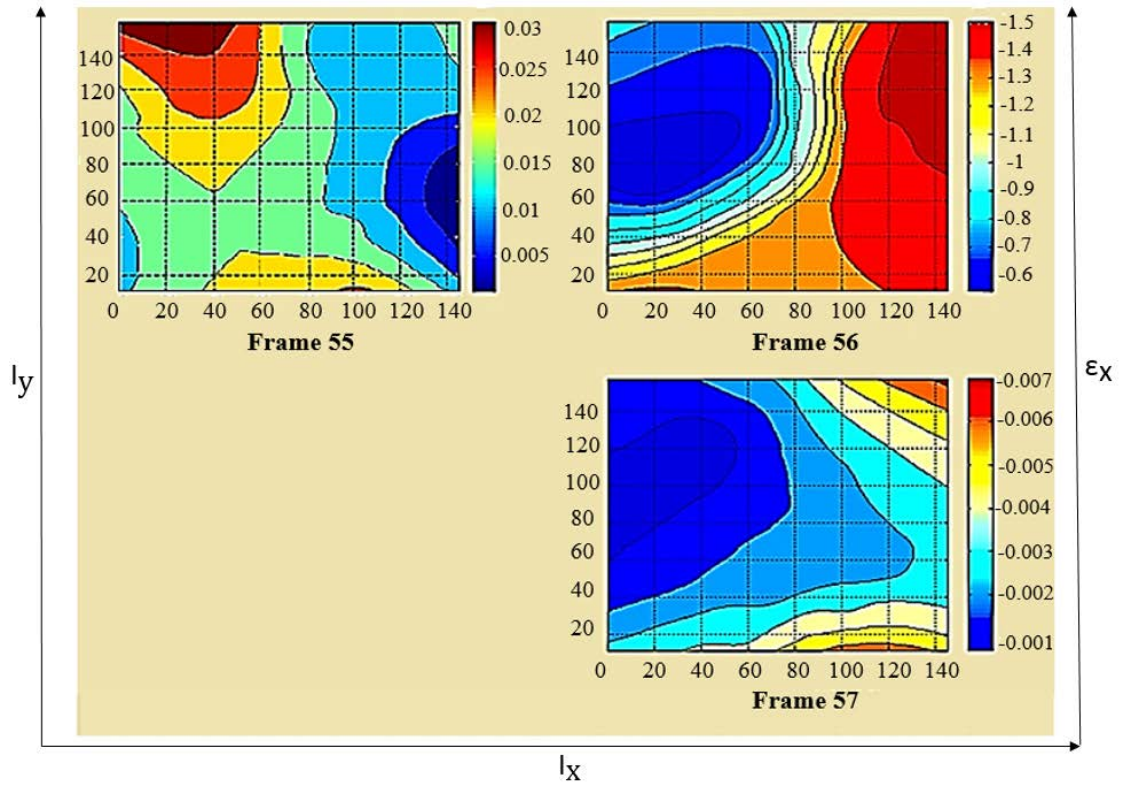


Figure 6.11: Contour plots showing change in normal strain  $\epsilon_x$  with change in displacement

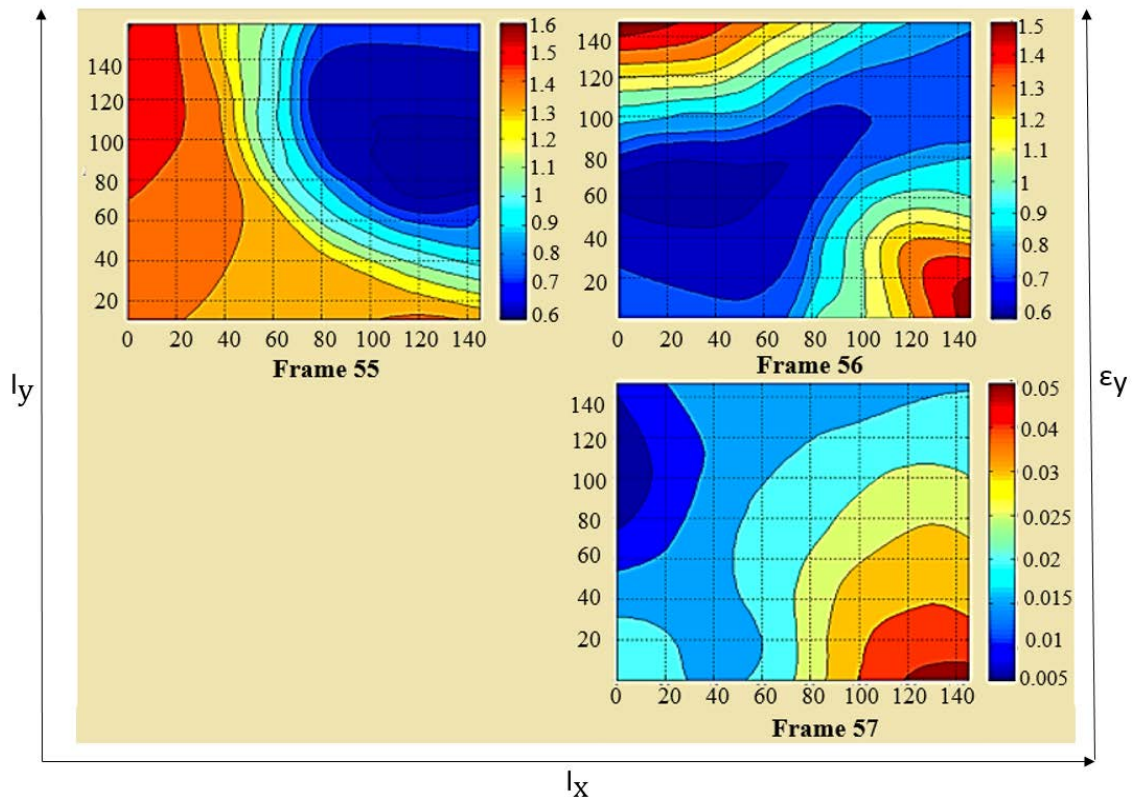


Figure 6.12: Contour plots showing change in normal strain  $\epsilon_y$  with change in displacement

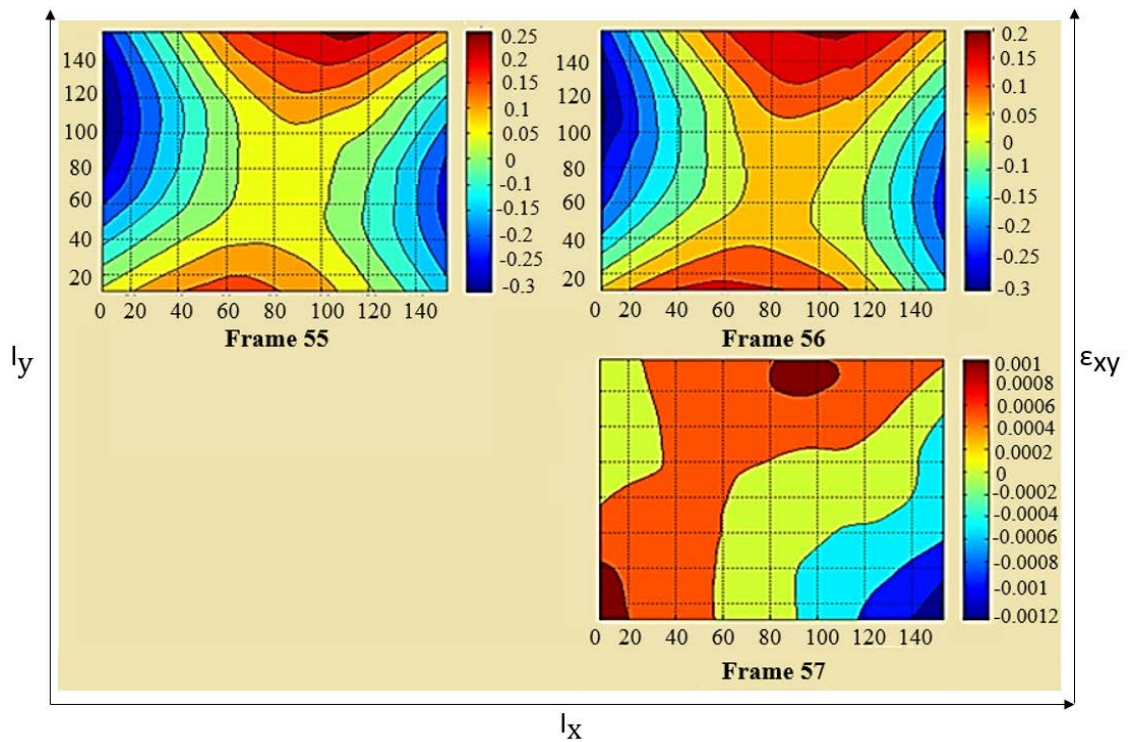


Figure 6.13: Contour plots showing change in shear strain  $\epsilon_{xy}$  with change in displacement

The recorded ECG signal consisted of the true ECG signal, environmental noise and the motion artefact. The environmental noise and the noise due to interference with the mains power line can be filtered by using an instrumentation amplifier and a band pass filter. In this case, hardware filtering was provided by the PhysioFlow PF05 L1 (Manatec Biomedical, Paris, France).

The ECG measurements acquired from the subject with and without movement for 10 seconds are presented in Figure 6.14. It can be observed that the ECG voltage of the subject lies between 1 mV and 1.8 mV. Under the same environmental conditions, a significant change in the ECG pattern can be observed between Figure 6.14A and B due to the effect of motion artefacts induced in the arm by the back and forth movement.

Software processing of the collected raw signal thus becomes necessary to ensure the required signal quality within the required range (of frequency or time). A typical set of algorithms serves to remove noise and the motion artefacts, detect the heartbeats (QRS complex) and compress the data for efficient acquisition [277]. Although the important objective of ECG detection and conditioning is to obtain an accurate QRS pattern, the focus here is to detect the motion artefacts due to skin. A typical procedure for unwanted

jitter and noise removal involves low pass filtering. A low pass butterworth filter with a cut-off frequency of 10 Hz was implemented in MATLAB, as illustrated in Figure 6.14C and D.

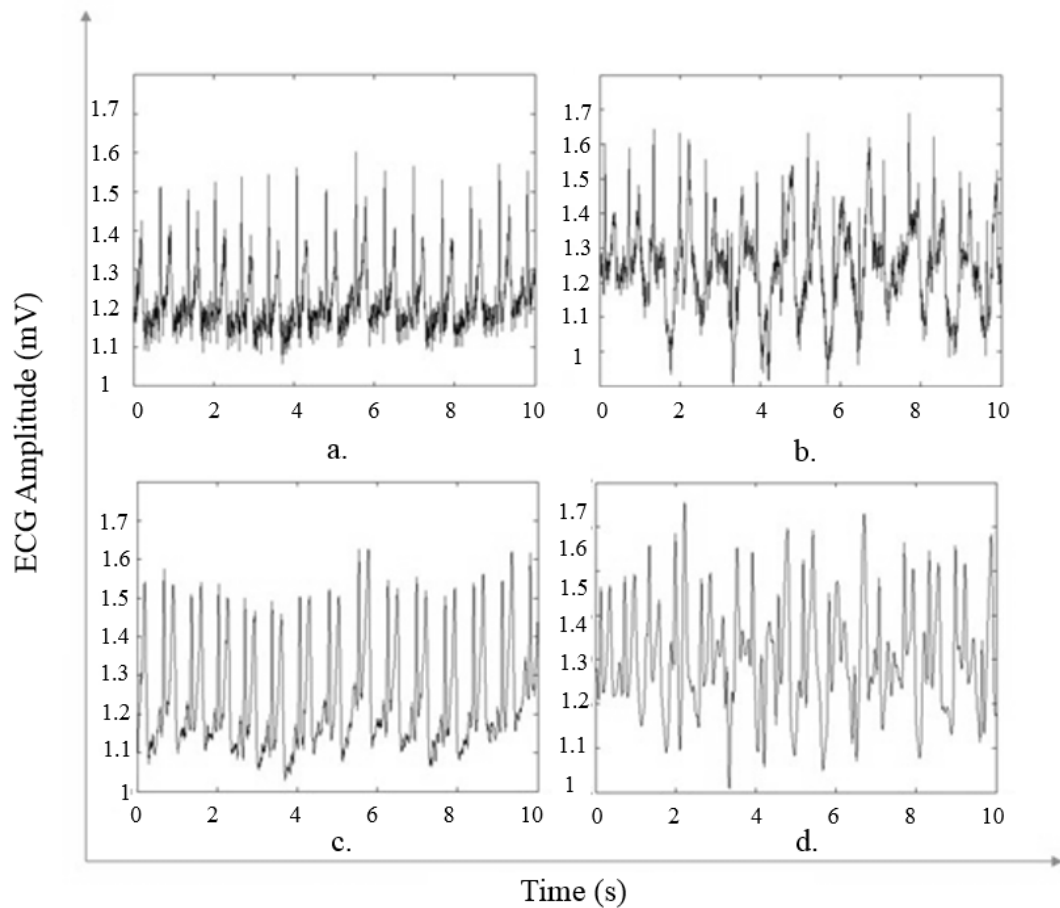


*Figure 6.14: (a) ECG without motion artefacts; (b) ECG with motion artefacts (induced by back and forth movement); (c) bandpass filtering of ECG signal (a); (d) bandpass filtering of ECG signal (b)*

The results obtained by performing PCA and ICA on ECG signals with different kinds of motion artefacts can be seen in Figures 6.15-6.17.

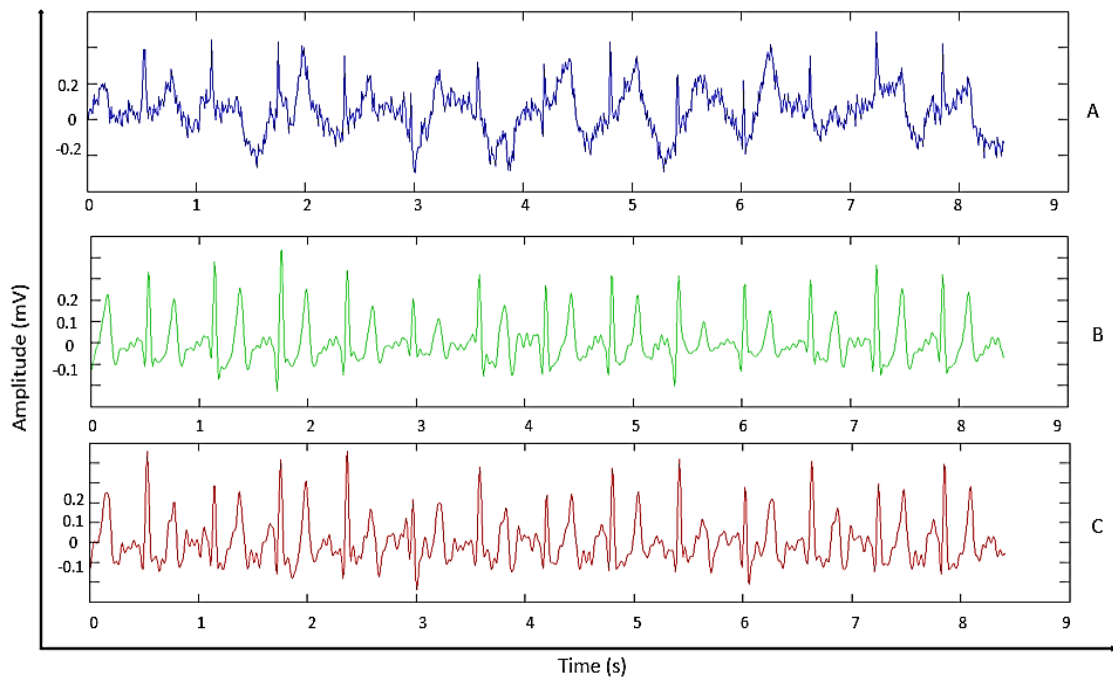


*Figure 6.15: (A) ECG with motion artefacts due to back and forward arm movement; (B) PCA filtering of ECG using beat segmentation; (C) ICA filtering of ECG using the JADE algorithm*

In Figure 6.15 a noticeable improvement can be seen in the signal quality after the implementation of PCA and ICA (in Figure 6.15B and C). However, only a marginal difference between the signals obtained from PCA and ICA can be observed. It should also be noted that the R peaks can be easily identified in Figure 6.15A, thereby implying that there are not many motion artefacts present in the signal. Importantly, the direction of the negative T waves due to the presence of motion artefacts has been successfully reversed using PCA and ICA. It can also be established that the R peaks in Figure 6.15B and C are more distinguishable and easier to identify than in Figure 6.15A.

Another case where motion artefacts were introduced – this time by closing the fist and opening hand continuously – can be seen in Figure 6.16.

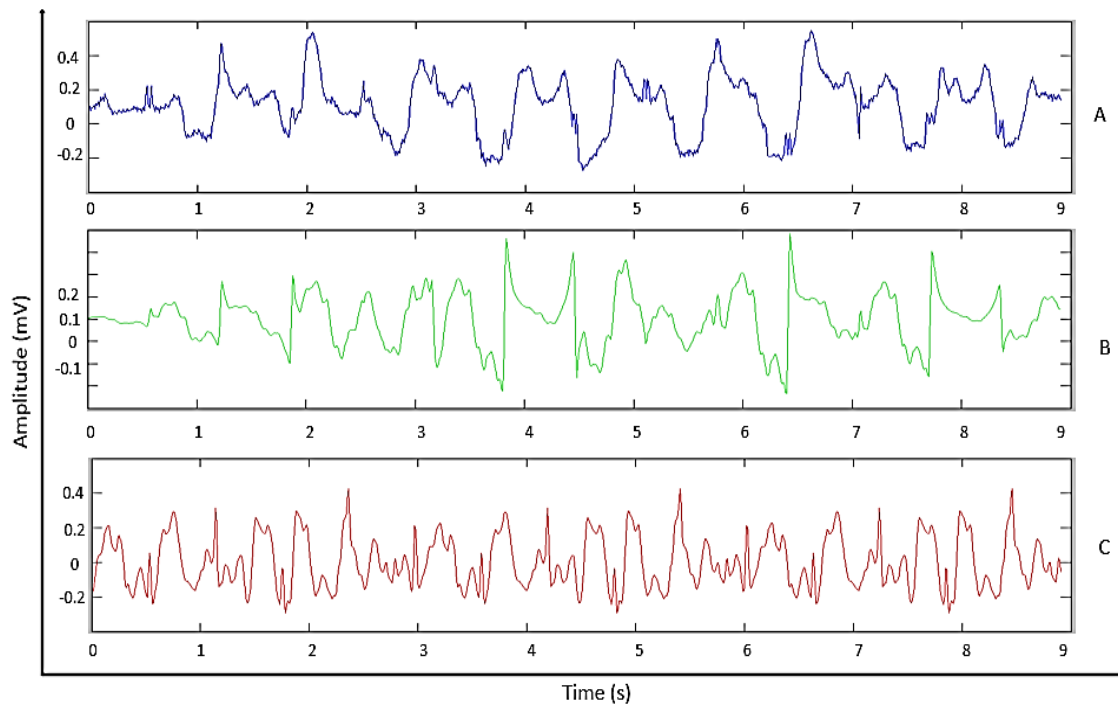


*Figure 6.16: (A) ECG with motion artefacts caused by closing fist and opening hand continuously, B. PCA filtering of ECG using beat segmentation, C. ICA filtering of ECG using JADE algorithm*

It is evident from Figure 6.16A that the ECG signal is greatly corrupted by motion artefacts, making it difficult to distinguish the ECG beats. There was no significant improvement in signal quality after the execution of PCA. However, on implementing ICA on the ECG with motion artefact, a remarkable transformation in the shape of the signal can be seen (Figure 6.16C). Even though the application of ICA makes the appearance of the R peaks in ECG more distinguishable, it is still hard to interpret the P and T waves. It should also be noted that no form of pre- or post-filtering (high pass or low pass) was performed on the signal other than PCA and ICA.

The third kind of motion artefacts were generated by rotating the left wrist in clockwise and anticlockwise directions; the results of which are shown in Figure 6.17.

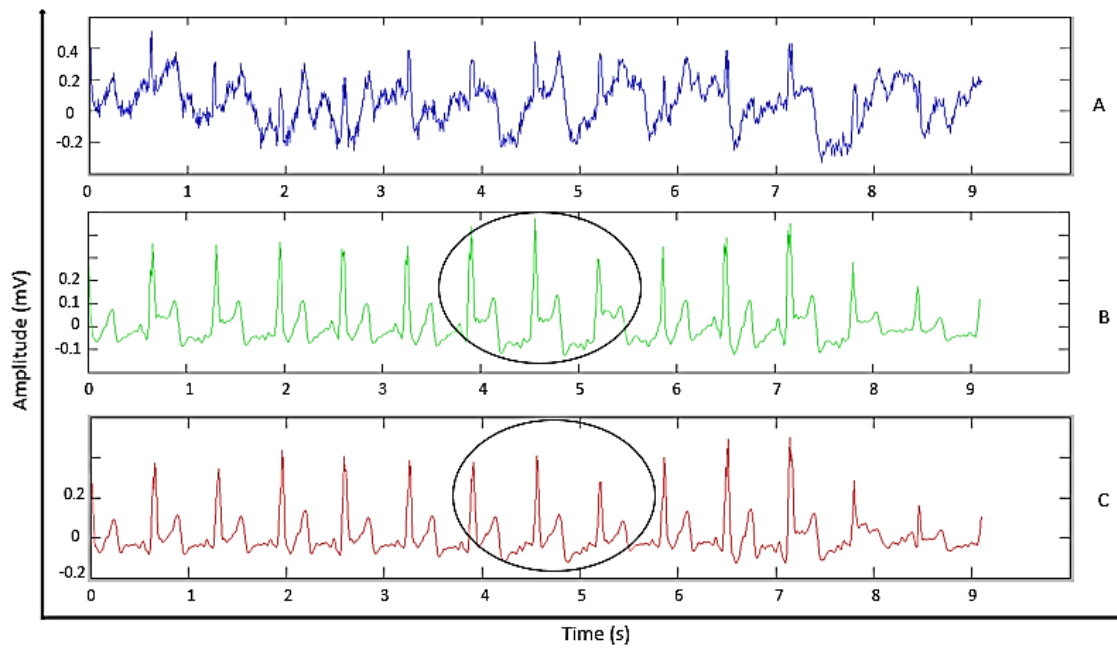


*Figure 6.17: (A) ECG with motion due to clockwise and anticlockwise rotation of the wrist; (B) PCA filtering of ECG using beat segmentation; (C) ICA filtering of ECG using the JADE algorithm*

The presence of motion artefacts in the ECG due to wrist rotation can be observed from Figure 6.17A. The QRS complex in the ECG can be easily detected after filtering the signal using PCA and ICA, as seen in Figure 6.17B and C respectively. An abnormal ST elevation in the signal could be observed after the execution of PCA in Figure 6.17B, between 4 and 6 seconds (highlighted by a solid circle). This could lead to the misdiagnosis of cardiac abnormalities such as acute myocardial infarction, coronary vasospasm (Prinzmetal's angina), left ventricular hypertrophy, etc. [278]. The ST elevation was successfully removed by using ICA (Figure 6.17C). It is also possible that some heart arrhythmias are filtered out as motion artefacts by PCA or ICA. However, in this case the ECG recording was obtained from a healthy subject.

After analysing the results demonstrated in Figure 6.15 and Figure 6.17, it can be inferred that the performance of PCA and ICA is similar in eliminating motion related artefacts from ECG signals if the signal is not corrupted by a large amount of motion artefacts. When motion artefacts in the ECG signal are more significant, as in Figure 6.16, then ICA performs better than PCA.

In PCA, the data matrix is decomposed into a set of orthogonal components arranged in order of importance. In other words, if the first component of PCA is the best

representation of the data set, the second component will be the second best representation (and orthogonal to the first component). In ICA, by contrast, statistically independent and uncorrelated components of the data are generated. Romero (2011) [114] performed PCA and ICA on artificially generated ECGs with motion artefacts, and ICA outperformed PCA by providing a better signal-to-noise ratio and positive predictivity.

Although ICA has been shown to be a more effective method in removing motion artefacts from ECG than PCA, there are a few ambiguities involved in the calculation of ICA. With reference to Figure 6.7, both source  $S$  and noise related parameter  $A$  are unknown matrices in ICA, and therefore any scalar multiple in one of the sources in matrix  $S$  can be cancelled by dividing the corresponding vector  $A$  [127]. Thus, the independent components obtained after the multiplication of  $X$  (ECG signal with motion artefacts) with  $W$  (inverse of mixing matrix  $A$ ) are sometimes required to be scaled in amplitude. There is another ambiguity of change in sign due to scaling, which can be addressed by multiplying the independent components by -1 if needed. Another disadvantage of using ICA is that we cannot directly determine the order of significance of the independent components [127]. Therefore, this research has used the approach of disregarding the independent components which show high correlation with the measured strains.

## 6.6 SUMMARY

This chapter has addressed the quantification of skin stretch using an optical technique and the elimination of motion artefacts from ECG signals by implementing PCA and ICA. The simulation of strain values reflecting skin stretch was accomplished by acquiring a video recording of a moving PDMS patch glued to the subject's arm during an ECG measurement. This was followed by the superposition of the strain vectors  $\varepsilon_x$ ,  $\varepsilon_y$  and  $\varepsilon_{xy}$  pertaining to skin stretch. To measure deformation, a predetermined checkerboard pattern was marked on the PDMS patch to aid in video-based motion tracking. The quality of image frames was improved using Adobe Photoshop CC and the region of interest was cropped in MATLAB. Vector plots representing the displacements of corner points of the checkerboard from the first frame were obtained

over a period of 10 seconds. A simple yet effective method of point tracking was employed and no corner points were lost while tracking.

The objective of evaluating normal and shear strains was accomplished by mathematically relating them to the displacement of an infinitesimal particle due to skin stretch. A strain field pertaining to the movement of the arm was obtained over a period of 10 seconds.

This motion information and was used to remove motion artefact the measured ECG using PCA and ICA. A step by step procedure for implementing PCA using baseline wander removal and ECG beat segregation was presented in section 6.3. In section 6.4, the ICA approach involving the use of the JADE algorithm was detailed. It was concluded that the application of both PCA and ICA resulted in a significant improvement in the morphology of the ECG. However, ICA proved to be more efficient than PCA in the case where the ECG was highly degraded by motion artefacts (Figure 6.16). There are some constraints involved in this study regarding analysis of the signal after using PCA and ICA algorithms. It is possible that these algorithms discard some important ECG information as motion artefacts. Therefore, it is important to statistically determine the enhancement in the signal quality on the application of these algorithms. In this chapter, all the ECG measurements were taken from one subject by inducing different kinds of motion artefacts due to arm movement. Although a useful proof of concept study, it would be better to obtain the measurements from more than one subject as one person may only move his/her arm in a certain way. Another limitation of this study was that the ECG signal was only acquired for 10 seconds, and no reference ECG signal was collected, which makes it hard to investigate the performance of PCA and ICA algorithms objectively and for longer durations. All these limitations are further addressed in the following chapter.

# CHAPTER 7      VALIDATION OF ARTEFACT REJECTION SYSTEM

## 7.1 INTRODUCTION

This chapter describes experiments to validate removal of motion artefacts from skin strain information. Statistical methods employing the calculation of SNR and infinity norms ( $\infty$ -norms) were used to determine the performance of PCA and ICA algorithms, using strains as motion information. The statistical significance of the algorithms implementing PCA and ICA was determined by performing Student's t-tests. The Young's modulus of the skin varies with age, therefore the effect of skin stretch induced artefacts on an ECG was measured in people from different age groups. The study was performed on 7 healthy subjects across the following age groups: 18–35 years (3 subjects), 36–55 years (2 subjects), and 56 years and above (2 subjects) for a time period of 60 seconds. Approval for this study was obtained from the Auckland University of Technology Ethics Committee (Application number: 17/170).

The materials used and methods employed to measure the ECG using wet Ag/AgCl, dry Ag and CNT/PDMS electrodes are discussed in section 7.2. The various attributes of the system, such as intra-test repeatability, EMG artefact rejection (AR) efficiency, performance of PCA with and without beat segmentation, and the effect of Langer's lines were assessed. The use of strains for providing motion information in terms of skin stretch is also described.

The results obtained by implementing the PCA and ICA algorithms on ECG measurements were compared across the experiments and with other related studies. In addition, the performance of CNT/PDMS electrodes was compared with dry Ag electrodes. Finally, the benefits and limitations of this work are discussed in detail.

A flow chart describing the experimental validation of the system performed in this chapter can be seen in Figure 7.1.

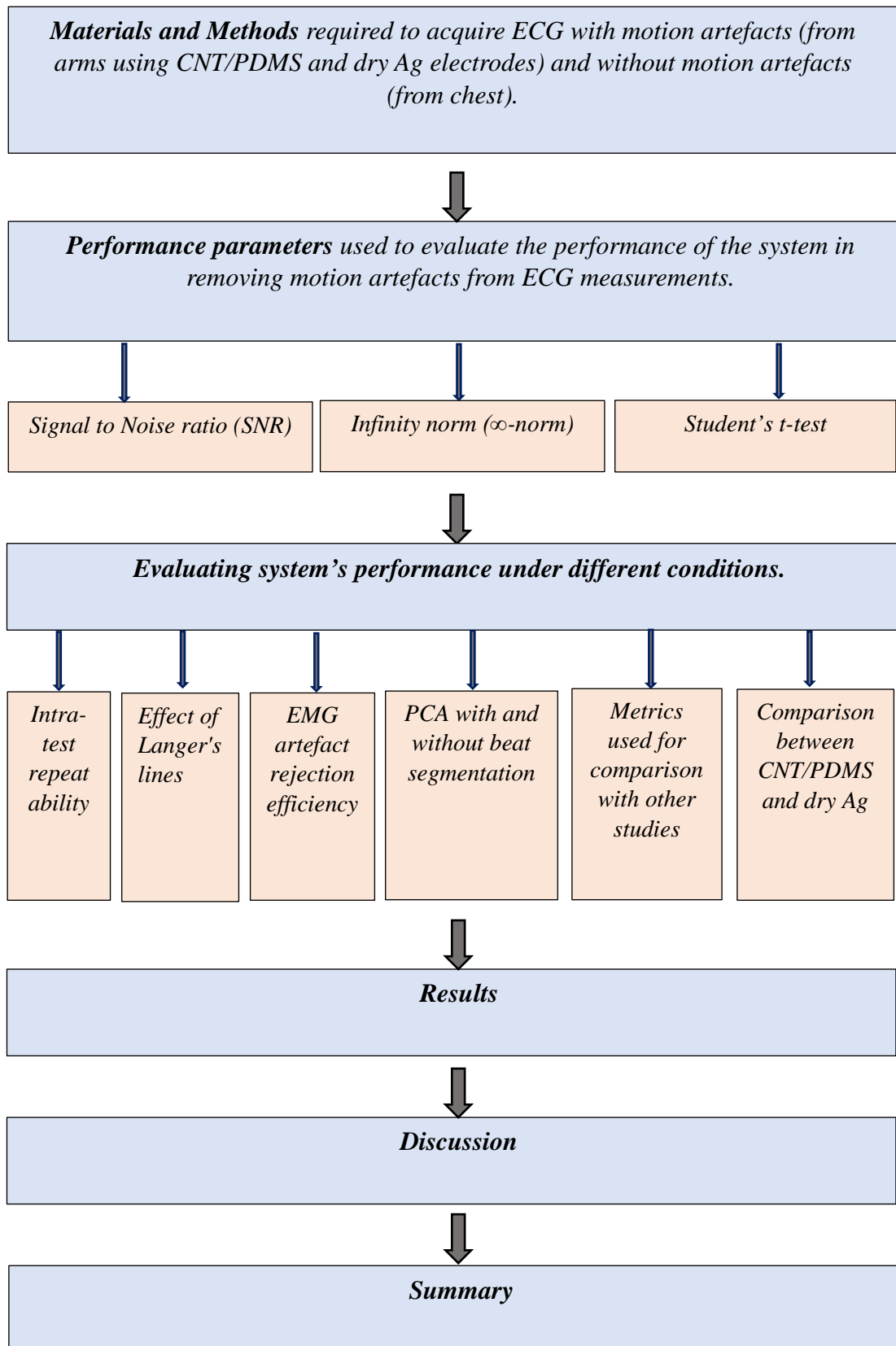


Figure 7.1: Flow chart describing the layout of the experimental validation of the system.

## 7.2 MATERIALS AND METHODS

A simple 1-lead configuration was used to obtain a reference ECG through standard Ag/AgCl electrodes. This was implemented by placing one electrode on each shoulder of the subjects, as shown in Figure 7.2. The subjects were asked to sit still to avoid any shoulder movement during the ECG monitoring so that the reference ECG was free from motion artefacts. However, as part of the experiments, different types of movements were induced in one of the forearms of the subject and the ECG with motion artefacts was measured using electrodes prepared from CNTs and PDMS, with dimensions of 30 mm × 30 mm × 2 mm, as discussed in chapter 4. ECG measurements were also obtained using dry Ag electrodes on each forearm, as seen in Figure 7.2.

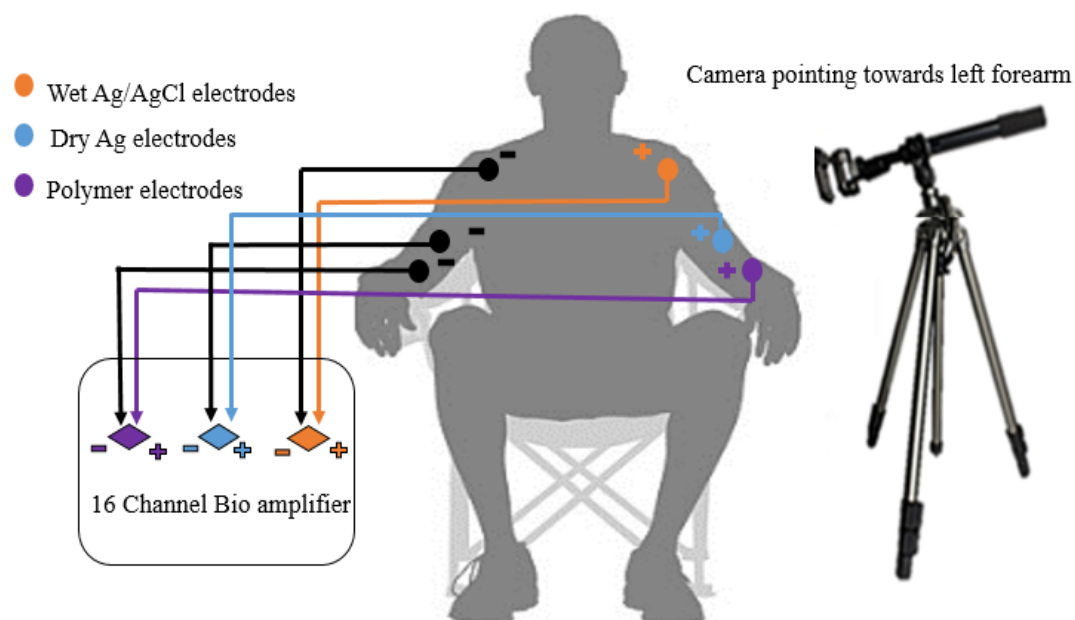


Figure 7.2: ECG measurement set up

As shown in Figure 7.2, three ECG measurements were obtained simultaneously from a subject over a period of 60 seconds using wet Ag/AgCl electrodes, dry Ag electrodes or CNT/PDMS electrodes. The ECG measurements were taken using a 16-channel bio-amplifier (g-USBamp 3.0, G.TEC Medical Engineering GmbH, Austria) at 1256 Hz through a National Instruments Data Acquisition board (NI-DAQ, Texas, USA).

The g.USBamp employs wide-range, DC-coupled amplifier along with 24-bit sampling generating an input voltage range of  $\pm 250\text{mV}$  with a resolution of  $<30\text{nV}$  [279]. The

ECG pre-processing was performed by implementing a low pass fourth order Butterworth filter in LabVIEW followed by bandpass filtering in MATLAB within normalized cut-off frequencies of 0.001 to 0.038.

A checkered pattern was printed on the CNT/PDMS electrodes and a video camera attached on a tripod was used to capture the electrode's movement on the left forearm while the right forearm was kept at rest. The resolution of the video camera was 1920 pixels  $\times$  1080 pixels and the frames were recorded at a frame rate of 25 fps.

Motion artefacts were generated in the 7 subjects by stretching and releasing their skin on the left forearm in the vicinity of the CNT/PDMS electrode using a plastic tube, as illustrated in Figure 7.3. The plastic tube was used to avoid any interference in the ECG recordings due to electrical charges arising from another person.

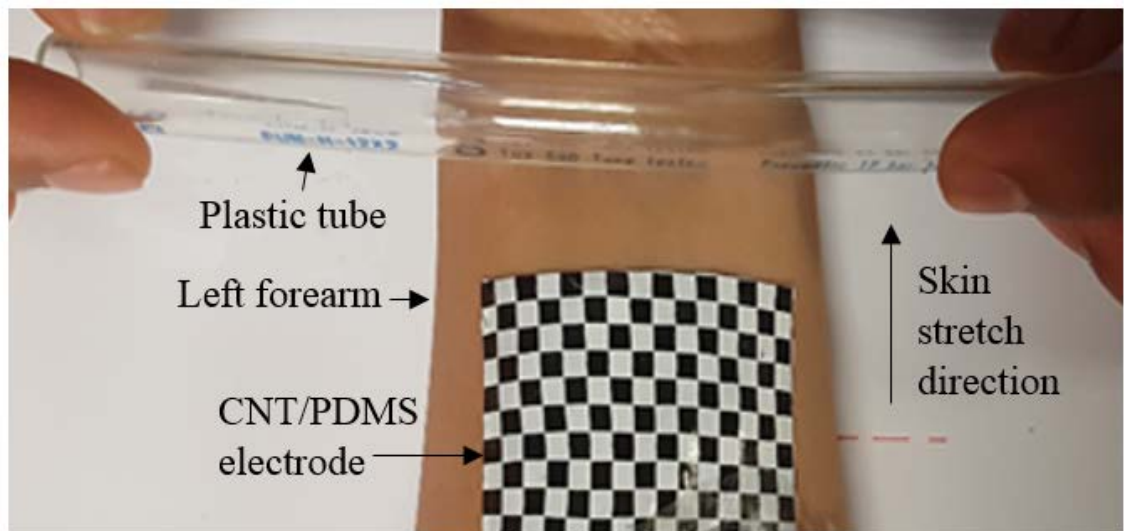


*Figure 7.3: Generating motion artefact by stretching forearm using a plastic tube*

### **7.3 PERFORMANCE PARAMETERS**

The following parameters were used to evaluate the performance of the artefact rejection system in this study.

### 7.3.1 Improvement in SNRs

In order to statistically measure the improvement in signal quality, the signal to noise ratio (SNR) for the signals filtered using PCA and ICA was calculated. SNR was used as a measure of signal strength relative to the motion artefact with respect to the reference signal. The ratio was calculated in decibels (dB) by using the formulas shown in equations (7.1) and (7.2).

$$SNR_{noisy\ ECG} = 10\log_{10} \left\{ \frac{\text{variance}(\text{reference ECG})}{\text{variance}(\text{reference ECG} - \text{noisy ECG})} \right\} \quad (7.1)$$

$$SNR_{filtered\ ECG} = 10\log_{10} \left\{ \frac{\text{variance}(\text{reference ECG})}{\text{variance} \left( \text{reference ECG} - \text{ECG after PCA/ICA} \right)} \right\} \quad (7.2)$$

The improvement in SNR on application of PCA and ICA was measured using equation (7.3):

$$SNR\ Improvement = SNR\ of\ filtered\ ECG - SNR\ of\ noisy\ ECG \quad (7.3)$$

### 7.3.2 Infinity norm ( $\infty$ -norm)

Another method adopted to analyse the effectiveness of signal filtering using PCA and ICA involved the calculation of the  $\infty$ -norms of the ECG with motion artefacts, filtered ECG, and ECG without motion artefacts. The  $\infty$ -norm or max norm is the maximum absolute value of a vector [280]. This can be useful for calculating the maximum deviation of the noisy signal from the reference ECG. The  $\infty$ -norm was calculated for the acquired ECG with motion artefacts and the filtered ECG by finding the absolute maximum of their differences from the reference ECG. The maximum deviation of the signal from the reference ECG was calculated by using equation (7.4).

$$\infty\ norm = \max(\text{abs}(\text{Reference ECG} - \text{Noisy ECG}/\text{Filtered ECG})) \quad (7.4)$$

### 7.3.3 Student's t-test

Student's t-tests were performed (assuming unequal variances) between the filtered signal (using PCA and ICA) and the measured signal (ECG with motion artefacts) to establish that the results had not occurred by random chance. The residuals between the filtered and measured data were calculated and  $T$  and  $P$  values were derived. The  $T$  value is used for calculation of the size of the difference relative to the variation in the sample data. The greater the value of  $T$ , the greater the evidence against the null hypothesis (of no difference). Two-tailed t-tests were performed in this study, as they are more conservative than one-tailed t-tests [281].  $P$  values are used to estimate the probability of null hypothesis. The significance level of the test is set by assigning the value of  $\alpha=0.05$ . If the value of  $P$  is less than  $\alpha$ , then the null hypothesis is rejected. The paired t-test was used in this case, where each observation in one group is paired with a related observation in the other group.

## 7.4 EVALUATING SYSTEM PERFORMANCE UNDER DIFFERENT CONDITIONS

The following aspects were investigated in 2 subjects, one from the 18–35 age group and one from the 36–55 age group. This section (from 7.4.1 to 7.4.7) describes the evaluations performed and the corresponding results are presented in section 7.5.

### 7.4.1 EMG induced artefact rejection efficiency

Muscle movement artefacts were introduced by asking the subjects to repeatedly close and open one fist, as illustrated in Figure 6.1. This was done to test the performance of the PCA and ICA algorithms in eliminating artefacts generated that include EMG signals.

### 7.4.2 Intra-test repeatability

The performance of both PCA and ICA algorithms was evaluated at epochs of 15 seconds over a period of 60 seconds. This allows comparison of intra-test repeatability.

### 7.4.3 PCA with and without beat segmentation

The performance of PCA with and without beat segmentation was also evaluated. In the first case, the data samples of each of the segmented ECG beats were arranged in an independent column vector of the data set followed by three corresponding strains ( $\varepsilon_x$ ,  $\varepsilon_y$  and  $\varepsilon_{xy}$ ). In the second case, the data set consisted of four columns where the first column was composed of the entire ECG signal with motion artefacts and the remaining columns contained motion information in the form of the corresponding strains. In the work reported in this chapter, PCA was performed without using beat segmentation.

### 7.4.4 Effect of Langer's lines

As discussed in section 2.6, the Young's modulus of the skin in directions parallel to Langer's lines is much higher (almost double) than that in directions perpendicular to them. On the other hand, the Young's modulus of the skin at  $45^\circ$  to Langer's lines is lower than that at parallel and perpendicular directions. The direction of Langer's lines on the human forearm is shown in Figure 7.4.

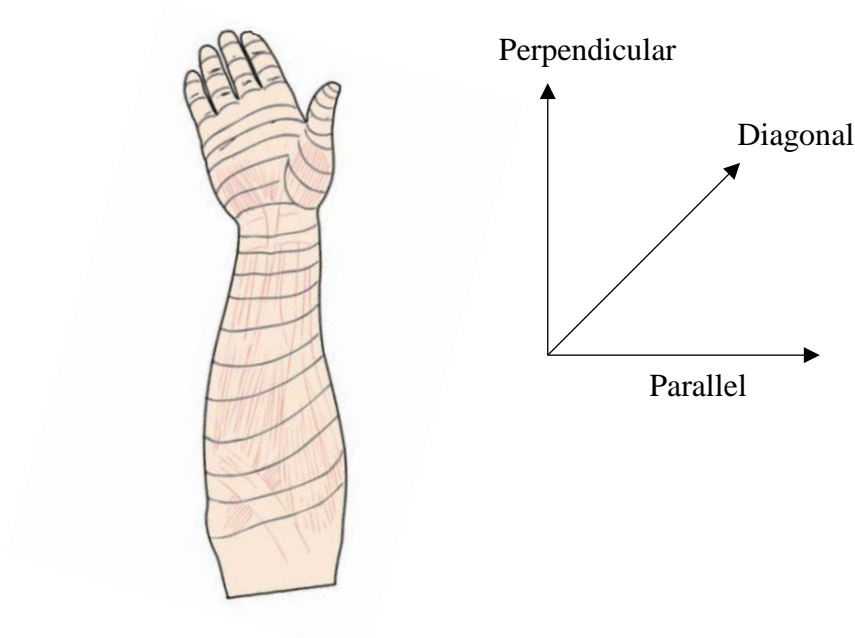


Figure 7.4: Orientation of Langer's lines on human forearm

To observe any significant changes in the magnitude and morphology of motion artefacts, the skin of the subjects was stretched and released in directions perpendicular, parallel and diagonal to Langer's lines in following ways.

#### *7.4.4.1 Effect of stretching the skin perpendicular to Langer's lines*

As shown in Figure 7.3, the skin on the left forearm of the subjects was stretched and released in direction perpendicular to Langer's lines using a plastic tube.

#### *7.4.4.2 Effect of stretching the skin parallel to Langer's lines*

Since the edges of the forearms are curved, the skin on the left forearm of the subjects was pulled and released along Langer's lines by an assistant using his thumbs to get a better grip, as seen in Figure 7.5. In order to avoid any electrical interference in the ECG recordings, Latex gloves were worn by the assistant stretching the skin.



*Figure 7.5: Introducing motion artefacts by stretching the skin parallel to Langer's lines*

#### *7.4.4.3 Effect of stretching the skin diagonal to Langer's lines*

The skin was stretched diagonal to Langer's lines as shown in Figure 7.6.



*Figure 7.6: Introducing motion artefacts by stretching the skin diagonal to Langer's lines*

The ECG signals acquired from the subjects while stretching their skin in different directions were filtered using PCA and ICA algorithms. The motion AR efficacies using the two algorithms were then compared.

#### **7.4.5 Alternative methods of calculating strain signals**

As mentioned in section 7.2, a video camera was used to record the movement of the CNT/PDMS patch during the skin stretches. The video frames obtained from the camera were filtered, sharpened and cropped in Photoshop CC (Adobe, California, USA). The four corner points of the patch's boundary were detected in each frame using the boundary detection feature in MATLAB (Figure 7.7).

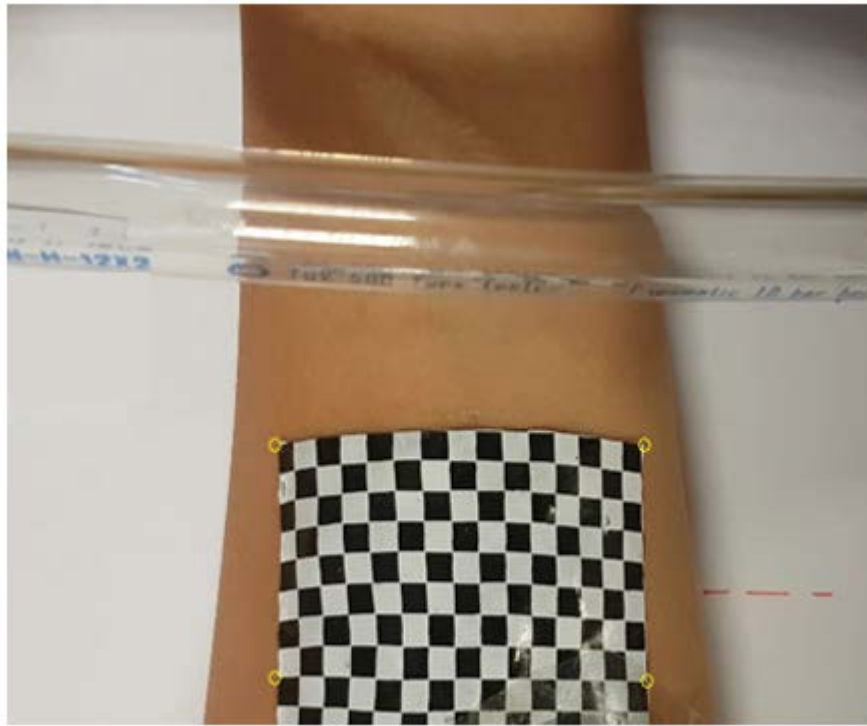


*Figure 7.7: Detecting the patch's boundary in each frame*

The corner points of the checker boxes within the patch's boundary were detected and tracked over each frame using the Harris-Stephens algorithm and Euclidian distance mapping (Figure 7.8), as discussed in section 6.2.

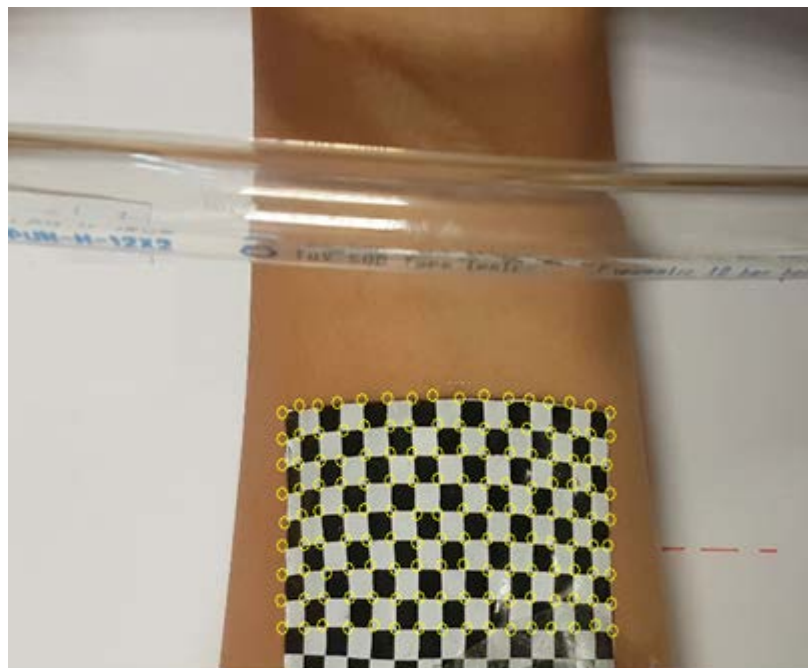


*Figure 7.8: Detecting and tracking the corner points of the checker boxes within the patch*

The strains at the incentres of each triangle formed by performing Delaunay triangulation were computed in all video frames (Figure 5.10). Mean and median values of the normal, shear ( $\varepsilon_x, \varepsilon_y$  and  $\varepsilon_{xy}$ ) and principal strains ( $\varepsilon_1, \varepsilon_2$ ) were calculated for each frame. The ECG measurements along with the corresponding strains were used as the data set to be filtered by PCA and ICA.

Strains in different regions of the CNT/PDMS patch were evaluated (Figure 7.9) and used as motion information when the skin was stretched and released using a plastic tube on one subject in the 18–35 year age group.

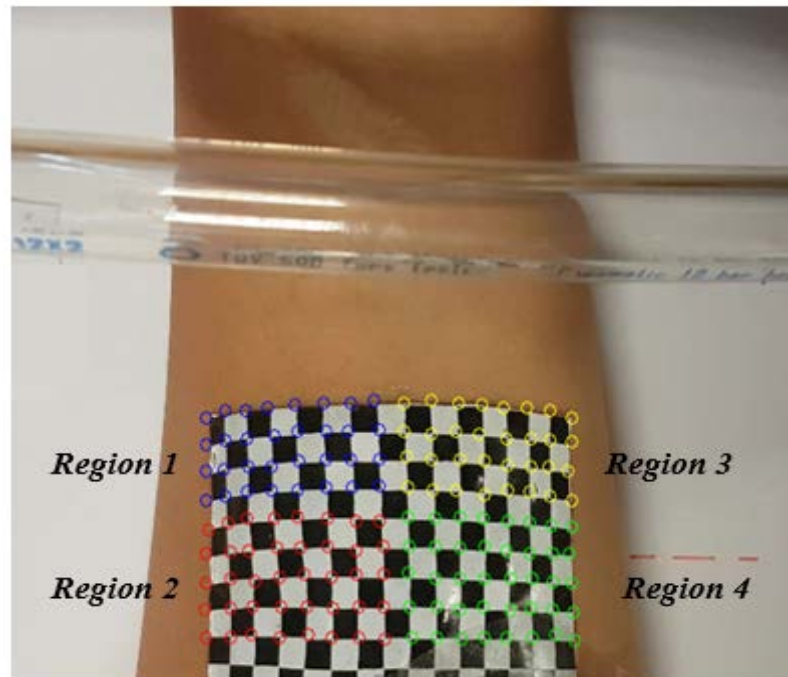


Figure 7.9: Strains obtained from different regions of the CNT/PDMS patch.

PCA was performed without using beat segmentation wherein the data set comprised of only 4 columns (ECG with motion artefacts, normal strain in  $x$ -direction ( $\varepsilon_x$ ), normal strain in  $y$ -direction ( $\varepsilon_y$ ) and shear strain ( $\varepsilon_{xy}$ )). In contrast, ICA was performed using beat segmentation where the data set contained each column of the ECG beat as well as 3 columns for the corresponding strains ( $\varepsilon_x, \varepsilon_y$  and  $\varepsilon_{xy}$ ), as shown in Figure 7.10. The reason for not segmenting the ECG beats while performing PCA is explained in section 7.9. The performance of both PCA and ICA was evaluated with and without using motion information. The motion information was acquired by taking mean and median values of the following strains for each video frame:

- normal and shear strains ( $\varepsilon_x, \varepsilon_y$  and  $\varepsilon_{xy}$ ).

- maximum and minimum principal strains ( $\varepsilon_1, \varepsilon_2$ ).
- maximum principal strain ( $\varepsilon_1$ ).
- minimum principal strain ( $\varepsilon_2$ ).
- average Euclidian displacements.

The column vectors of the data set matrix were arranged in different ways, as shown in Figure 7.10 – 7.14.

<b>Case 1: Taking normal and shear strains as motion information</b>	
<b>PCA</b>	<b>ICA (Total number of R peaks = n)</b>
(Total number columns = 4)	(Total number columns = 4n)
Column 1: ECG signal	Column 1: ECG beat 1 (from R to R peak)
Column 2: $\varepsilon_x$ corresponding to ECG	Column 2: $\varepsilon_x$ corresponding to ECG beat 1
Column 3: $\varepsilon_y$ corresponding to ECG	Column 3: $\varepsilon_y$ corresponding to ECG beat 1
Column 4: $\varepsilon_{xy}$ corresponding to ECG	Column 4: $\varepsilon_{xy}$ corresponding to ECG beat 1
	⋮
	Column 4n-3: ECG beat n (from R to R peak)
	Column 4n-2: $\varepsilon_x$ corresponding to ECG beat n
	Column 4n-1: $\varepsilon_y$ corresponding to ECG beat n
	Column 4n: $\varepsilon_{xy}$ corresponding to ECG beat n

Figure 7.10: Arrangement of data matrix by taking normal and shear strains ( $\varepsilon_x, \varepsilon_y$  and  $\varepsilon_{xy}$ ) as motion information in PCA and ICA

<b>Case 2: Taking principal strains as motion information</b>	
<b>PCA</b>	<b>ICA (Total number of R peaks = n)</b>
(Total number columns = 3)	(Total number columns = 3n)
Column 1: ECG signal	Column 1: ECG beat 1 (from R to R peak)
Column 2: $\varepsilon_1$ corresponding to ECG	Column 2: $\varepsilon_1$ corresponding to ECG beat 1
Column 3: $\varepsilon_2$ corresponding to ECG	Column 3: $\varepsilon_2$ corresponding to ECG beat 1
	⋮
	Column 3n-2: ECG beat n (from R to R peak)
	Column 3n-1: $\varepsilon_1$ corresponding to ECG beat n
	Column 3n: $\varepsilon_2$ corresponding to ECG beat n

Figure 7.11: Arrangement of data matrix by taking principal strains ( $\varepsilon_1, \varepsilon_2$ ) as motion information in PCA and ICA.

<b>Case 3: Taking maximum principal strain as motion information</b>	
<b>PCA</b>	<b>ICA (Total number of R peaks = 2n)</b>
(Total number columns = 3)	(Total number columns = n+1)
Column 1: ECG signal	Column 1: ECG beat 1 (from R to R peak)
Column 2: $\varepsilon_1$ corresponding to ECG	Column 2: $\varepsilon_1$ corresponding to ECG beat 1
	⋮
	Column 2n-1: ECG beat n (from R to R peak)
	Column 2n: $\varepsilon_1$ corresponding to ECG beat n

Figure 7.12: Arrangement of data matrix by taking maximum principal strain ( $\varepsilon_1$ ) as motion information in PCA and ICA.

<b>Case 4: Taking minimum principal strain as motion information</b>	
<b>PCA</b>	<b>ICA (Total number of R peaks = 2n)</b>
(Total number columns = 3)	(Total number columns = n+1)
Column 1: ECG signal	Column 1: ECG beat 1 (from R to R peak)
Column 2: $\varepsilon_2$ corresponding to ECG	Column 2: $\varepsilon_2$ corresponding to ECG beat 1
	⋮
	Column 2n-1: ECG beat n (from R to R peak)
	Column 2n: $\varepsilon_2$ corresponding to ECG beat n

Figure 7.13: Arrangement of data matrix by taking minimum principal strain ( $\varepsilon_2$ ) as motion information in PCA and ICA.

<b>Case 5: Taking normal and shear strains from 4 checkerboard regions as motion information</b>	
<b>PCA</b>	<b>ICA (Total number of R peaks= n)</b>
(Total number columns =13)	(Total number columns = 13n)
Column 1: ECG signal	Column 1: ECG beat 1 (from R to R peak)
Columns 2, 3, 4: $\epsilon_x$ , $\epsilon_y$ & $\epsilon_{xy}$ (from checkerboard region 1) corresponding to ECG signal	Columns 2, 3,4: $\epsilon_x$ , $\epsilon_y$ & $\epsilon_{xy}$ (from checkerboard region 1) corresponding to ECG beat 1
Columns 5, 6,7: $\epsilon_x$ , $\epsilon_y$ & $\epsilon_{xy}$ (from checkerboard region 2) corresponding to ECG signal	Columns 5, 6,7: $\epsilon_x$ , $\epsilon_y$ & $\epsilon_{xy}$ (from checkerboard region 2) corresponding to ECG beat 1
Columns 8, 9,10: $\epsilon_x$ , $\epsilon_y$ & $\epsilon_{xy}$ (from checkerboard region 3) corresponding to ECG signal	Columns 8, 9,10: $\epsilon_x$ , $\epsilon_y$ & $\epsilon_{xy}$ (from checkerboard region 3) corresponding to ECG beat 1
Columns 11, 12,13: $\epsilon_x$ , $\epsilon_y$ & $\epsilon_{xy}$ (from checkerboard region 4) corresponding to ECG signal	Columns 11, 12,13: $\epsilon_x$ , $\epsilon_y$ & $\epsilon_{xy}$ (from checkerboard region 4) corresponding to ECG beat 1
	⋮
	Column 13n-12: ECG beat n (from R to R peak)
	Column 13n-11, 13n-10, 13n-9: $\epsilon_x$ , $\epsilon_y$ & $\epsilon_{xy}$ (from checkerboard region 1) corresponding to ECG beat n
	Column 13n-8, 13n-7, 13n-6: $\epsilon_x$ , $\epsilon_y$ & $\epsilon_{xy}$ (from checkerboard region 2) corresponding to ECG beat n
	Column 13n-5, 13n-4, 13n-3: $\epsilon_x$ , $\epsilon_y$ & $\epsilon_{xy}$ (from checkerboard region 3) corresponding to ECG beat n
	Column 13n-2, 13n-1, 13n: $\epsilon_x$ , $\epsilon_y$ & $\epsilon_{xy}$ (from checkerboard region 4) corresponding to ECG beat n

Figure 7.14: Arrangement of data matrix by taking normal and shear strains ( $\epsilon_x$ ,  $\epsilon_y$  and  $\epsilon_{xy}$ ) from 4 checkerboard regions as motion information in PCA and ICA.

#### 7.4.6 Metrics used for comparison with other research

Section 7.5.4 compares the results achieved in this study with those of similar studies. In 2007 an optical sensor was used by Liu [108] to quantify motion artefacts in terms of uniaxial displacement of the skin in one subject. ECG signals were measured from the subject's chest using Ag/AgCl electrodes and an optical sensor was attached near the ECG sensing site. The reference ECG was obtained from the wrist before introducing motion artefacts.

In this study, the optical sensing technique was employed to measure skin stretch directly under the ECG electrode in 7 subjects within different age groups. The reference ECG signals were measured simultaneously (from the chest) with the ECG with motion artefacts (from the forearm). Two-dimensional strains instead of uniaxial displacements were measured using CNT/PDMS electrodes. The motion artefacts from the ECG were filtered using PCA and ICA instead of the adaptive filtering performed by Liu [108].

The AR percentage was calculated using equation (7.5):

$$AR \% = \frac{L_2 \text{ norm}_{noisy \text{ signal}} - L_2 \text{ norm}_{filtered \text{ signal}}}{L_2 \text{ norm}_{noisy \text{ signal}} - L_2 \text{ norm}_{reference \text{ signal}}} \quad (7.5)$$

The  $L_2$  norm or Euclidean norm of a vector can be defined as the square root of the sum of the absolute values squared, as seen in equation (7.6):

$$\|x\|_2 = \sqrt{\sum_i x_i^2} \quad (7.6)$$

where  $i$  is the length of vector  $x$ .

The AR ratio calculated by Liu [108] on introducing different types of motions (slightly stretching the upper chest, horizontally waving the left arm, vertically raising the left arm, walking and running) in one subject was 85% [108].

In this study, motion artefacts were generated in 7 subjects by stretching the skin on their forearm and the motion AR percentage was evaluated using equation (7.5).

#### **7.4.7 Comparison between CNT/PDMS and dry Ag electrodes**

A comparison of the SNRs achieved using CNT/PDMS and dry Ag electrodes with that achieved using the standard Ag/AgCl electrodes was also performed. ECG measurements were obtained at rest for 10 seconds using Ag/AgCl electrodes (on the chest), dry Ag and CNT/PDMS electrodes (on the forearm), as seen in Figure 7.3. Conventionally, an ECG is measured using a 12-lead measurement system with 10 electrodes placed on the patient's limbs and on the surface of the chest [282]. However, an ECG in ambulatory conditions is typically measured using a 1-lead or a 2-lead measurement system with electrodes placed on the chest or wrist. Although the signal

quality of the ECG obtained from chest is superior to that obtained from wrist, it can be more convenient to measure the signal from wrist, especially for longer periods of time. In research by Chaiwisood et al. [283], the signal quality of the ECG obtained using a 3-lead measurement system from both the chest and wrist was investigated. It was found that the ECG obtained from both chest and the wrist using wet Ag/AgCl electrodes exhibited similar morphology and power spectrum in time and frequency domains respectively. However, the SNR for the signal obtained from chest was 9 dB higher than that obtained from wrists. In this study, a 1-lead ECG measurement system was used and the pre-processing of the signals was done in LabVIEW and MATLAB. The ECG measurements obtained from the wrist using dry Ag and CNT/PDMS electrodes with the subject at rest for 10 seconds were compared with those obtained from the chest using wet Ag/AgCl electrodes (3M Red Dot, Minnesota, USA).

## 7.5 RESULTS

The results of the tests described above are presented below.

### 7.5.1 *Skin stretch induced artefact rejection*

Table 7.1 compares the improvement in SNRs (dB) and  $\infty$ -norms and P values (from Student's t-tests) obtained using PCA and ICA on ECG signals measured from 7 subjects by stretching the skin on their forearm for 60 seconds. Both PCA and ICA utilized normal and shear strains ( $\varepsilon_x, \varepsilon_y, \varepsilon_{xy}$ ) to eliminate motion artefacts from ECG signals.

Table 7.1: Comparison of various performance parameters for ECG with motion artefacts (MA) and ECG filtered using PCA and ICA for 60 seconds.

Age groups and subjects	Subjects within various age groups	Average SNR improvement for 60 seconds (dB)		$\infty$ -norms			P values	
		PCA	ICA	MA	PCA	ICA	PCA	ICA
<b>18-35 years</b>	Subject 1	3.193	9.679	0.12	0.1	0.064	<0.05	<0.05
	Subject 2	2.816	7.8	0.093	0.0811	0.0519	<0.05	<0.05
	Subject 3	4.708	10.377	0.075	0.0682	0.0365	<0.05	<0.05
<b>36-55 years</b>	Subject 4	3.153	9.034	0.06	0.055	0.041	<0.05	<0.05
	Subject 5	4.065	8.702	0.14	0.095	0.0547	<0.05	<0.05
<b>Above 56 years</b>	Subject 6	5.891	11.461	0.0519	0.05	0.0318	<0.05	<0.05
	Subject 7	5.915	10.05	0.0507	0.0421	0.0296	<0.05	<0.05
<b>Average</b>	All subjects	4.249	9.586	0.0843	0.0702	0.0442	<0.05	<0.05

Figures 7.15 and 7.16 show the cases with the least and most improvement in SNRs using PCA, while Figures 7.17 and 7.18 show the cases with the least and most improvement in SNRs using ICA.

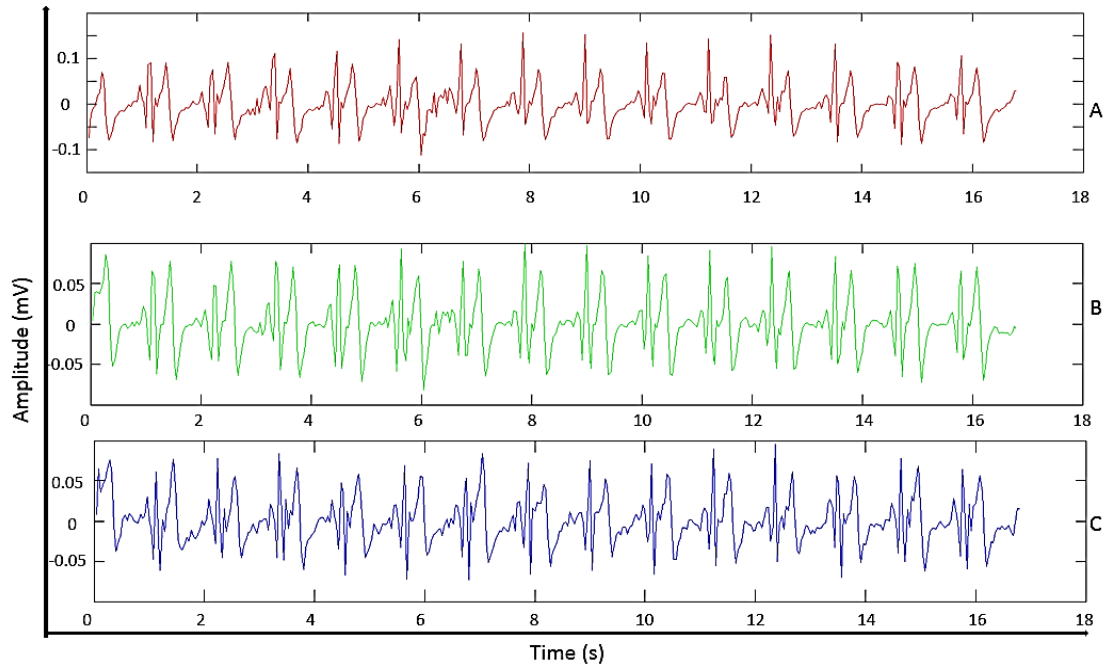


Figure 7.15: Case with least improvement in SNR (2.816 dB) using PCA.  
 A: ECG with motion artefact induced in Subject 2 by opening hand and closing fist continuously (in red); B: Signal filtered using PCA (in green); C: Reference signal (in blue).

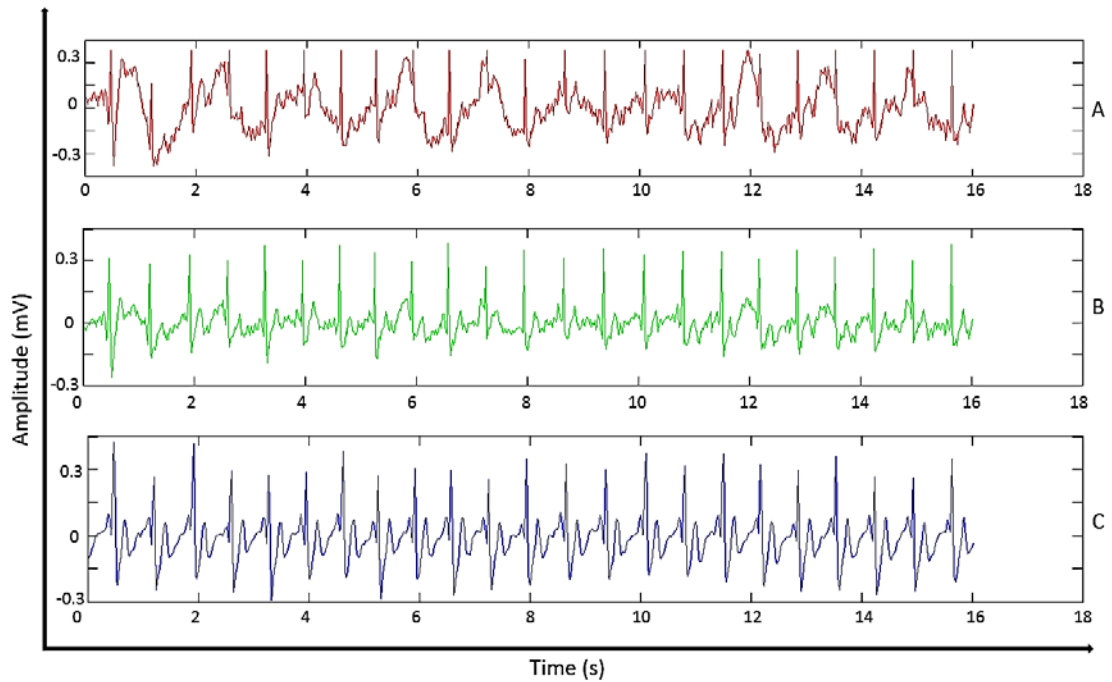


Figure 7.16: Case with most improvement in SNR (5.915 dB) using PCA.  
 A: ECG with motion artefact induced in Subject 7, by opening hand and closing fist continuously (in red); B: Signal filtered using PCA (in green); C: Reference signal (in blue).

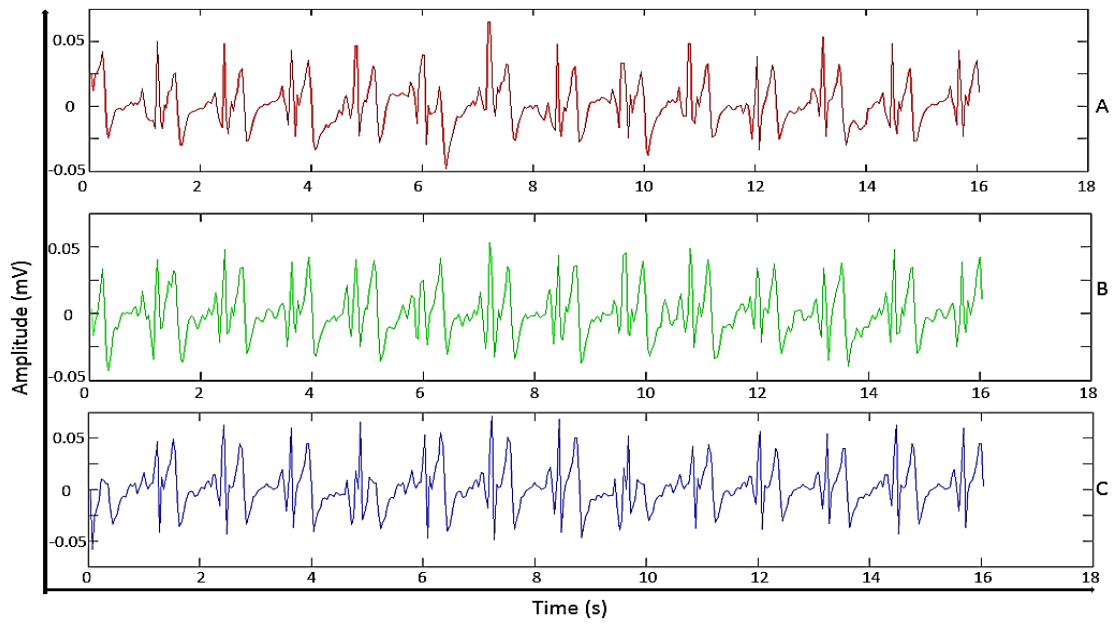


Figure 7.17: Case with least improvement in SNR (7.8 dB) using ICA. A: ECG with motion artefact induced in Subject 2, by stretching the forearm skin using a glass slide (in red), B: Signal filtered using ICA (in green), C: Reference signal (in blue).

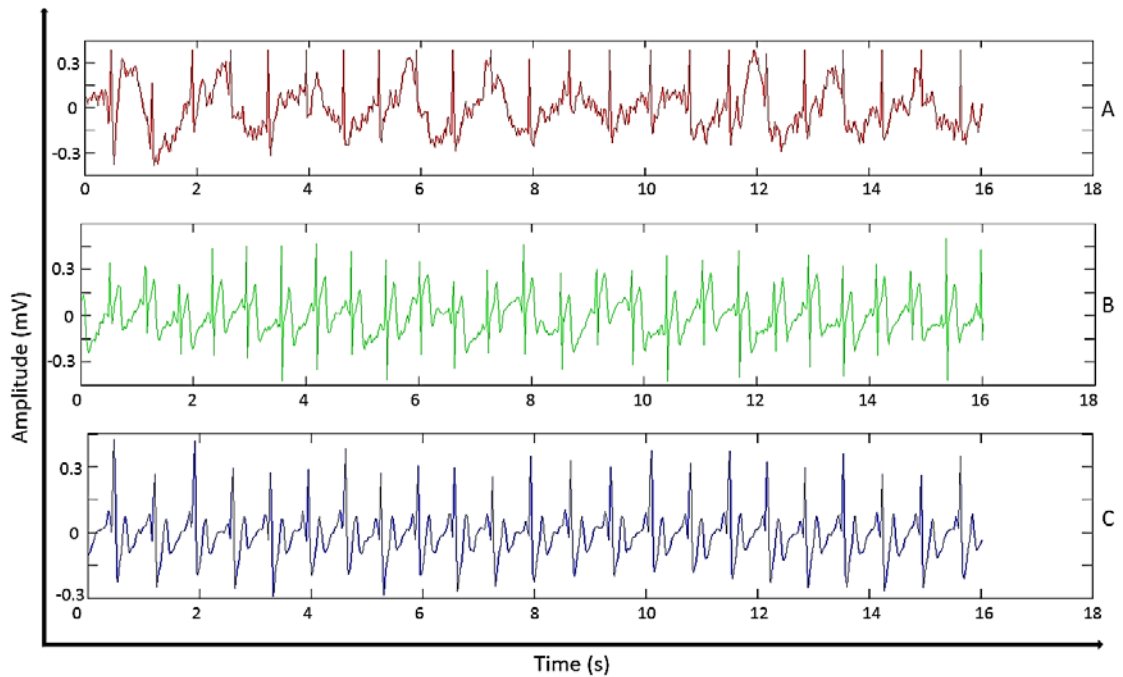


Figure 7.18: Case with most improvement in SNR (11.461 dB) using ICA. A: ECG with motion artefact induced in Subject 6, by stretching the forearm skin using a glass slide (in red), B: Signal filtered using ICA (in green), C: Reference signal (in blue).

The morphology of the ECG with motion artefacts and corresponding strains on stretching the skin of a subject (Subject 4, 18–35 years) at different time sequences can be seen in Figure 7.19-7.22.

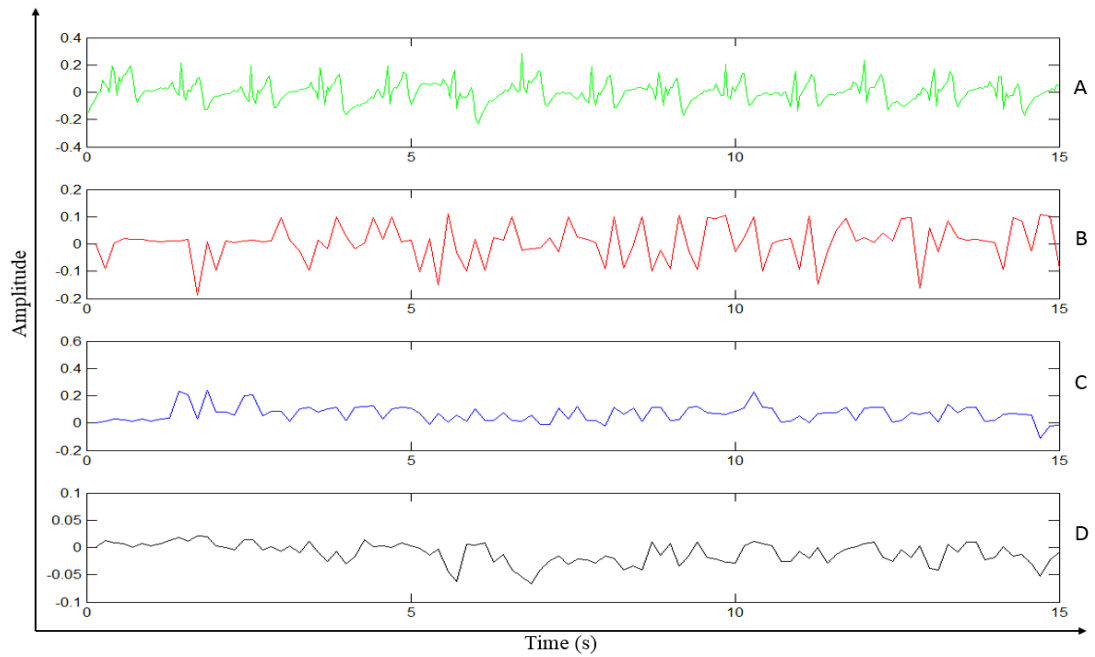


Figure 7.19 : A: ECG (in mV) with motion artefact induced in Subject 4 for the first time sequence (0–15 seconds), SNR= 3.5171(in green); B: Corresponding strain  $\epsilon_x$  (in red); C: Corresponding strain  $\epsilon_y$  (in blue); D: Corresponding strain  $\epsilon_{xy}$  (in black)

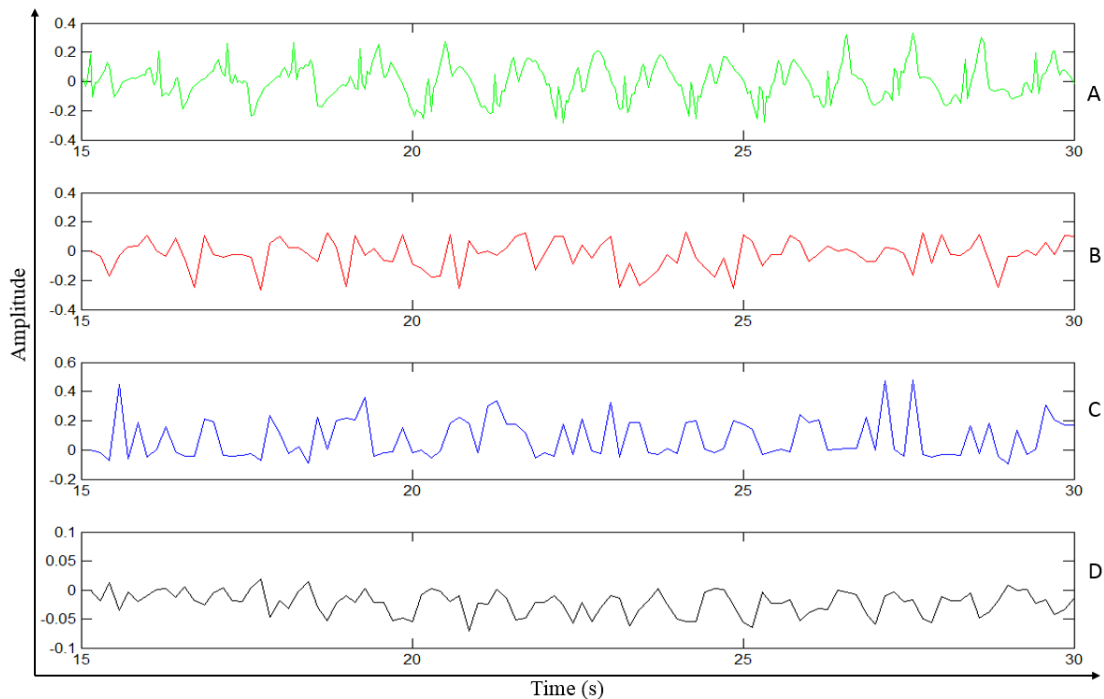


Figure 7.20: A: ECG (in mV) with motion artefact induced in Subject 4 for the second time sequence (15–30 seconds), SNR= -3.4925 (in green); B: Corresponding strain  $\epsilon_x$  (in red); C: Corresponding strain  $\epsilon_y$  (in blue); D: Corresponding strain  $\epsilon_{xy}$  (in black)

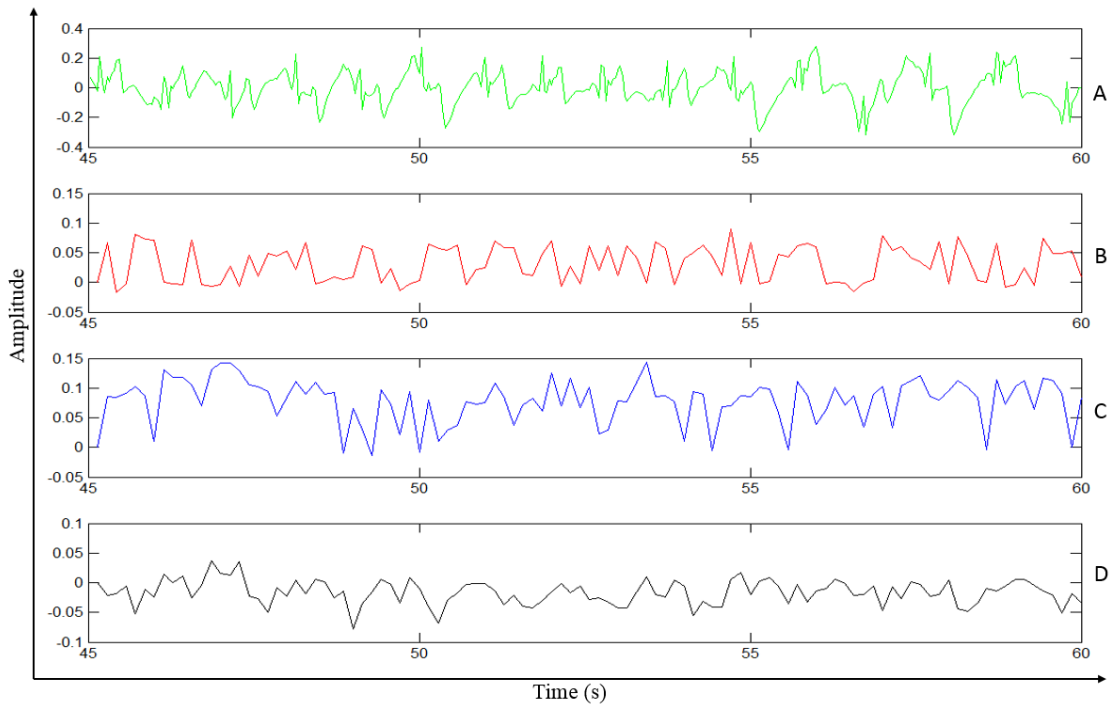


Figure 7.22: A: ECG (in mV) with motion artefact induced in Subject 4 for the third time sequence (30–45 seconds), SNR= -0.8761(in green); B: Corresponding strain  $\epsilon_x$  (in red); C: Corresponding strain  $\epsilon_y$  (in blue); D: Corresponding strain  $\epsilon_{xy}$  (in black)

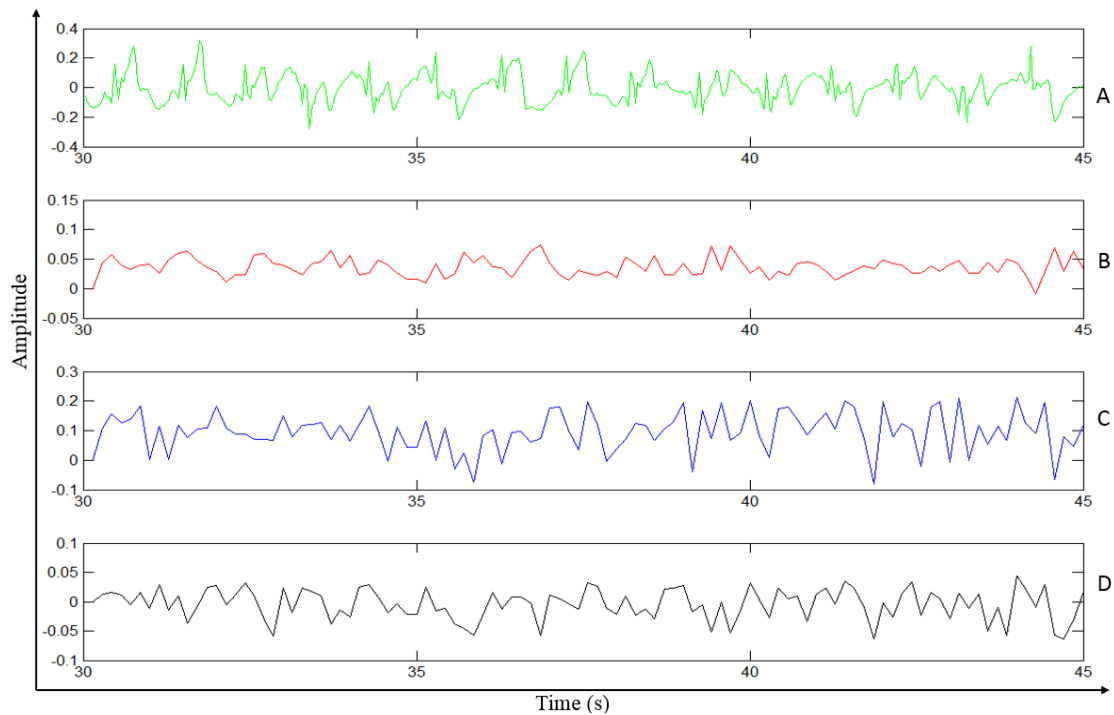


Figure 7.21: A: ECG (in mV) with motion artefact induced in Subject 4 for the fourth time sequence (45-60 seconds), SNR= -0.3916 (in green); B: Corresponding strain  $\epsilon_x$  (in red); C: Corresponding strain  $\epsilon_y$  (in blue); D: Corresponding strain  $\epsilon_{xy}$  (in black).

## 7.5.2 Evaluating system performance under different conditions

### 7.5.2.1 EMG induced artefact rejection efficiency

The performance of PCA and ICA upon introducing voluntary muscle movements (EMG induced artefacts) in 2 subjects by asking them to repeatedly close and open one fist can be seen in Table 7.2.

Table 7.2: Performance of PCA and ICA in eliminating EMG induced artefacts

Subjects	Time interval (seconds)	SNR improvement (dB)		$\infty$ -norms			P values	
		PCA	ICA	MA	PCA	ICA	PCA	ICA
Subject 1 (18-35 years)	0-15	1.7835	9.551	0.093	0.092	0.057	<0.05	<0.05
	16-30	2.1399	10.20	0.102	0.109	0.053	<0.05	<0.05
	31-45	2.6377	8.244	0.103	0.062	0.065	0.112	<0.05
	46-60	2.03	8.137	0.076	0.063	0.046	<0.05	<0.05
Average: Subject 1	60	2.14	9.034	0.093	0.082	0.055	<0.05	<0.05
Subject 2 (36-55 years)	0-15	2.6558	6.914	0.115	0.108	0.033	<0.05	<0.05
	16-30	1.8131	6.545	0.088	0.084	0.053	<0.05	<0.05
	31-45	4.0525	8.339	0.110	0.095	0.041	<0.05	<0.05
	46-60	1.7337	6.189	0.097	0.093	0.068	<0.05	<0.05
Average Subject 2	60	2.5637	6.997	0.103	0.095	0.049	<0.05	<0.05
Overall average performance	120	2.35	8.015	0.098	0.088	0.052	<0.05	<0.05

### 7.5.2.2 *Intra-test repeatability*

In Figures 7.23 and 7.24, the SNRs and  $\infty$ -norms of ECGs with motion artefacts (MA) and ECGs filtered using PCA and ICA are compared across epochs of 15 seconds.

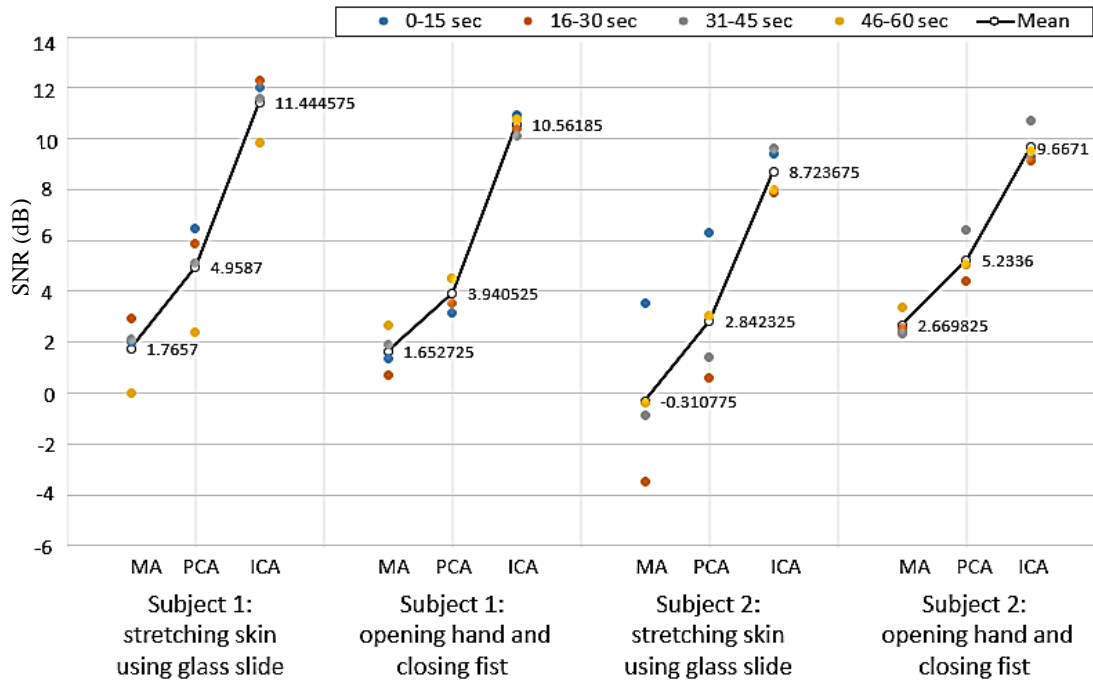


Figure 7.23: Comparison of SNRs calculated for ECG with motion artefact and ECG filtered using PCA and ICA (represented by MA, PCA and ICA respectively) by inducing motion artefacts in 2 subjects, at different time intervals

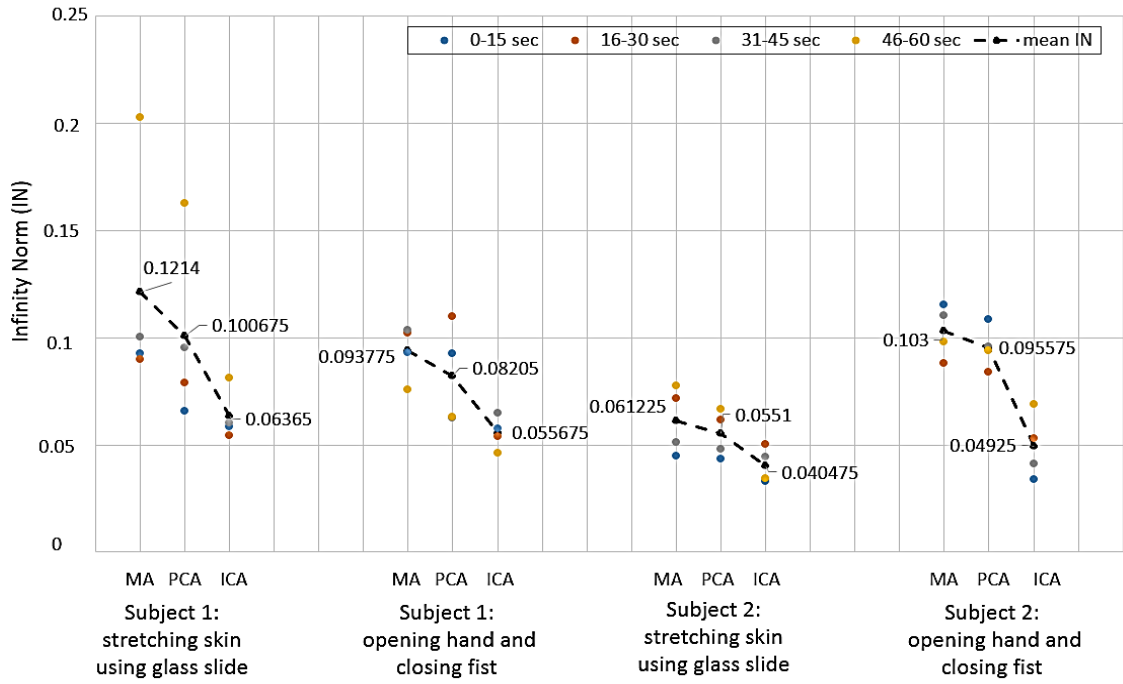


Figure 7.24: Comparison of  $\infty$ -norms (represented by MA, PCA and ICA respectively) by inducing motion artefacts in 2 subjects, at different time intervals

The mean values of SNRs and  $\infty$ -norms for 60 seconds are shown in the above figures.

### 7.5.2.3 PCA with and without beat segmentation

A comparison of SNRs obtained after implementing PCA with and without beat segmentation is shown in Figure 7.25 (mean values shown with dashed line).

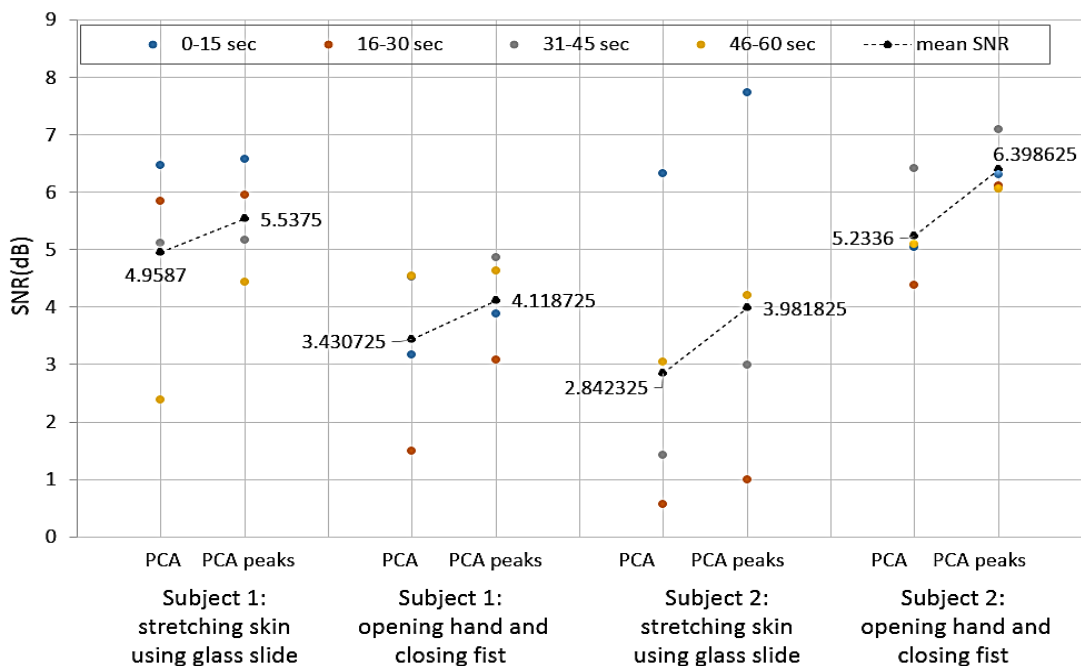


Figure 7.25: Comparison of SNRs on application of PCA with and without peak detection/beat segmentation (represented as PCA peaks and PCA respectively)

An example signal showing the difference in ECG waveform on the implementation of PCA with and without ECG segmentation is shown in Figure 7.26. The SNR for the acquired ECG with induced motion artefact (in Figure 7.26A) with respect to the reference signal (in Figure 7.26D) was -3.49 dB. A negative SNR implies that the signal noise, or motion artefact in this case, has a greater impact on the acquired signal compared to the ECG. On performing PCA on the measured ECG signal in Figure 7.26A without beat segmentation, the SNR was improved by 4.06 dB, as shown in Figure 7.26B. On the other hand, the improvement in SNR on application of PCA with beat segmentation was 4.48 dB, which is slightly better than the figure without beat segmentation, as shown in Figure 7.26C.

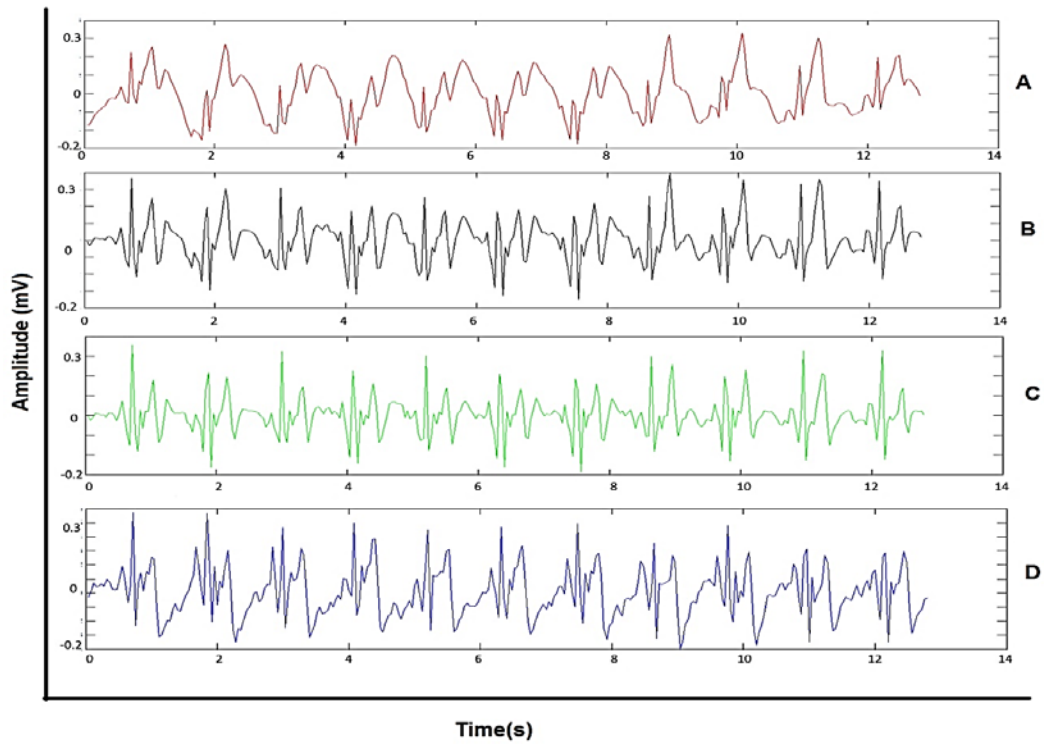


Figure 7.26: A: Recorded ECG signal with motion artefact (in Subject 2 by stretching the skin using a plastic tube); B: PCA filtering on ECG without beat segmentation; C: PCA filtering on ECG with beat segmentation; D: Reference ECG signal

#### 7.5.2.4 Effect of Langer's lines

A comparison between SNRs obtained on stretching the skin parallel, diagonal and perpendicular to the Langer's lines (in 2 subjects) is shown in Figure 7.27.

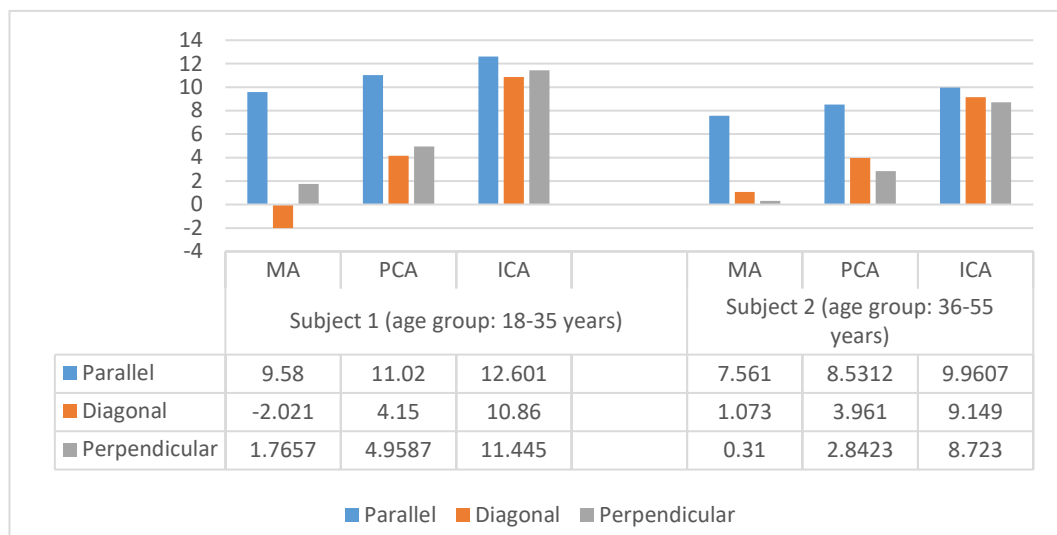


Figure 7.27: Comparison of SNRs calculated for ECG with motion artefact and ECG filtered using PCA and ICA (represented by MA, PCA and ICA respectively) by stretching the skin parallel, diagonal and perpendicular to Langer's lines

The following plots show a comparison between ECG with motion artefact, PCA-ICA filtered ECG and reference ECG at different orientations of Langer's lines. The 2D strains obtained by stretching the skin in different directions can be seen in Figure 7.31.

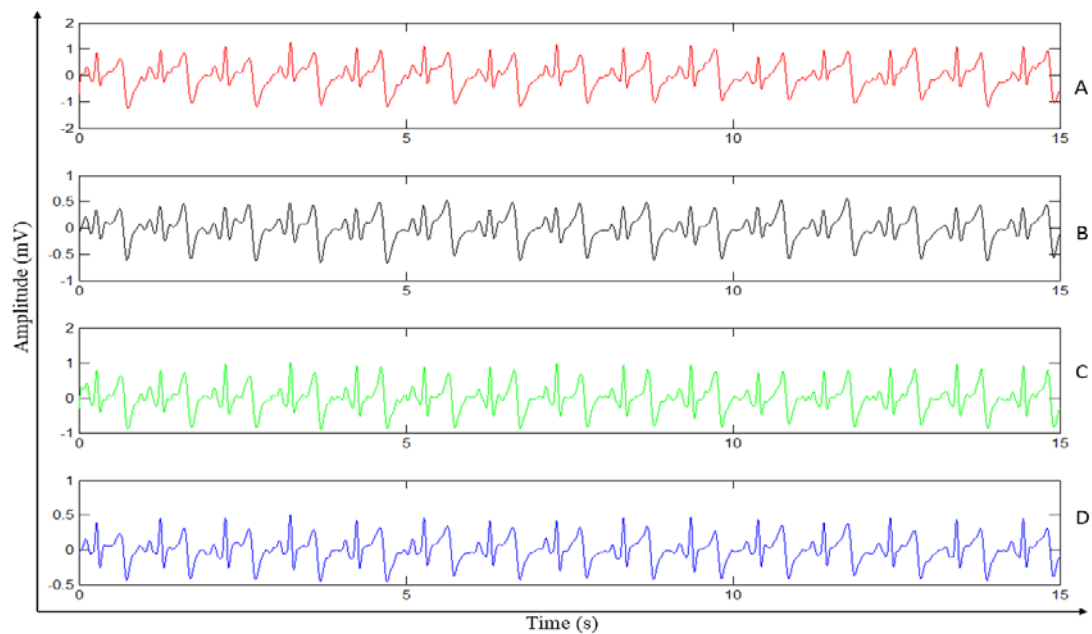


Figure 7.28: A: ECG with motion artefact in Subject 1 on stretching the skin parallel to Langer's lines, SNR= 9.58 dB (in red); B: ECG after PCA filtering, SNR= 11.02 dB (in black); C: ICA after ICA filtering, SNR=12.601 dB (in green); D: Reference ECG signal (in blue)

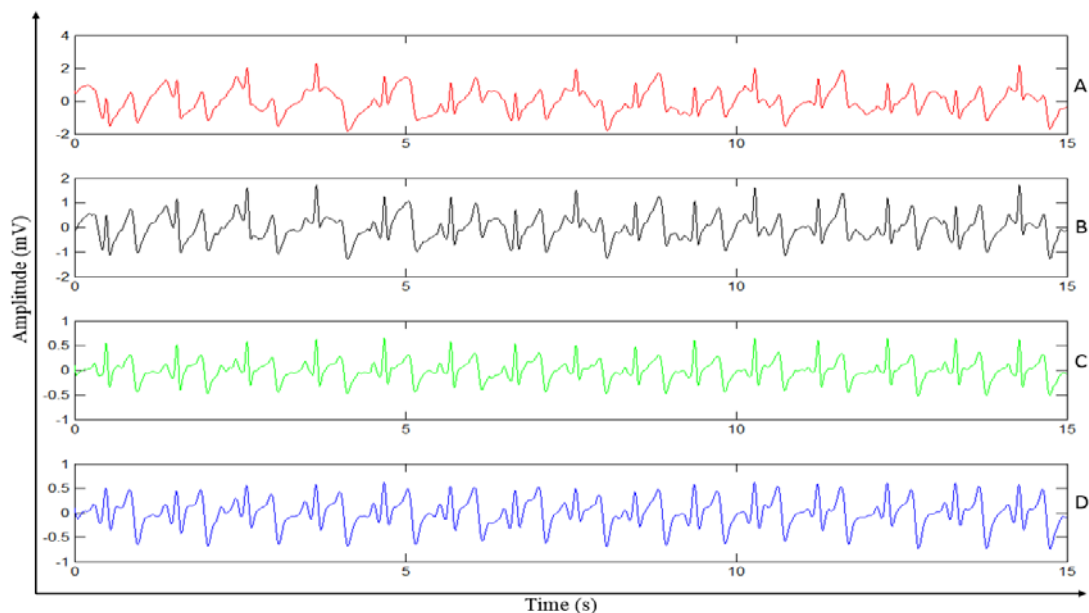


Figure 7.29: A: ECG with motion artefact in Subject 1 on stretching the skin diagonal to Langer's lines, SNR= -2.021 dB (in red); B: ECG after PCA filtering, SNR= 4.15 dB (in black); C: ICA after ICA filtering, SNR=10.86 dB (in green); D: Reference ECG signal (in blue)

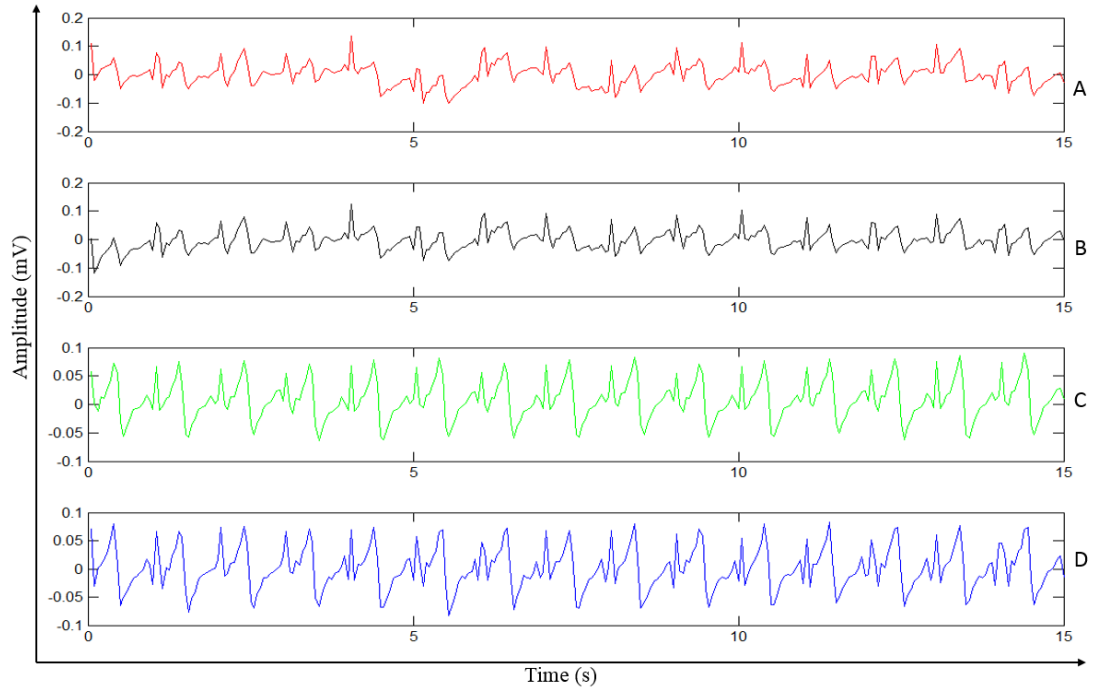


Figure 7.30: A: ECG with motion artefact in Subject 1 on stretching the skin perpendicular to Langer's lines, SNR=1.7657 dB (in red); B: ECG after PCA filtering, SNR= 4.9587 dB (in black); C: ECG after ICA filtering, SNR=11.445 dB (in green); D: Reference ECG signal (in blue)

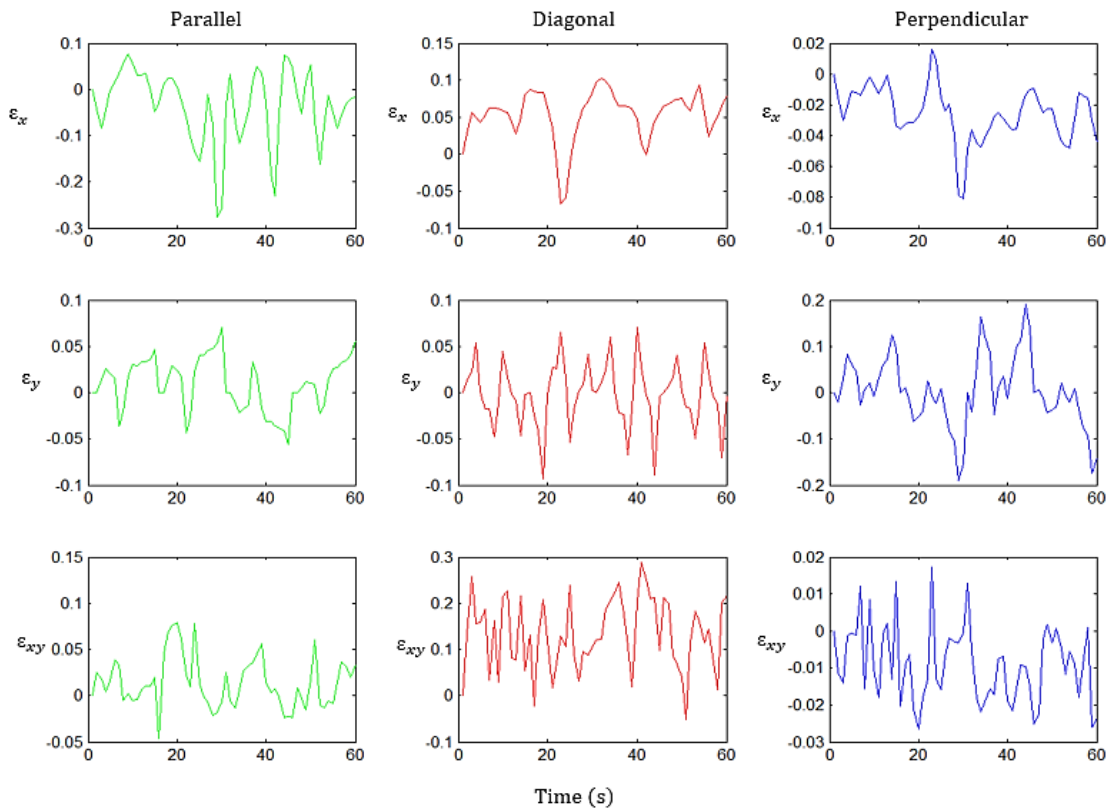


Figure 7.31: Strain plots ( $\epsilon_x, \epsilon_y, \epsilon_{xy}$ ) corresponding to ECG signals acquired by stretching the skin parallel (in green), diagonal (in red) and perpendicular (in blue) to Langer's lines

### **7.5.3 Strain contribution in skin stretch quantification**

The performance of PCA and ICA using data set arrangements shown in Cases 1, 2, 3 and 4 in section 7.4.5 can be seen in Figure 7.32 – 7.35.

The motion noise was quantified in terms of normal and shear strains ( $\varepsilon_x, \varepsilon_y, \varepsilon_{xy}$ ) in Case 1, principal strains ( $\varepsilon_1, \varepsilon_2$ ) in Case 2, maximum principal strain ( $\varepsilon_1$ ) in Case 3 and minimum principal strain ( $\varepsilon_2$ ) in Case 4. The mean and median amplitudes of the normal ( $\varepsilon_x, \varepsilon_y$ ), shear ( $\varepsilon_{xy}$ ) and principal strains ( $\varepsilon_1$  and  $\varepsilon_2$ ) computed from all points, 4 corner points, and regional points of the checkerboard (see section 7.4.5) can be seen in Figures 7.36-7.39.

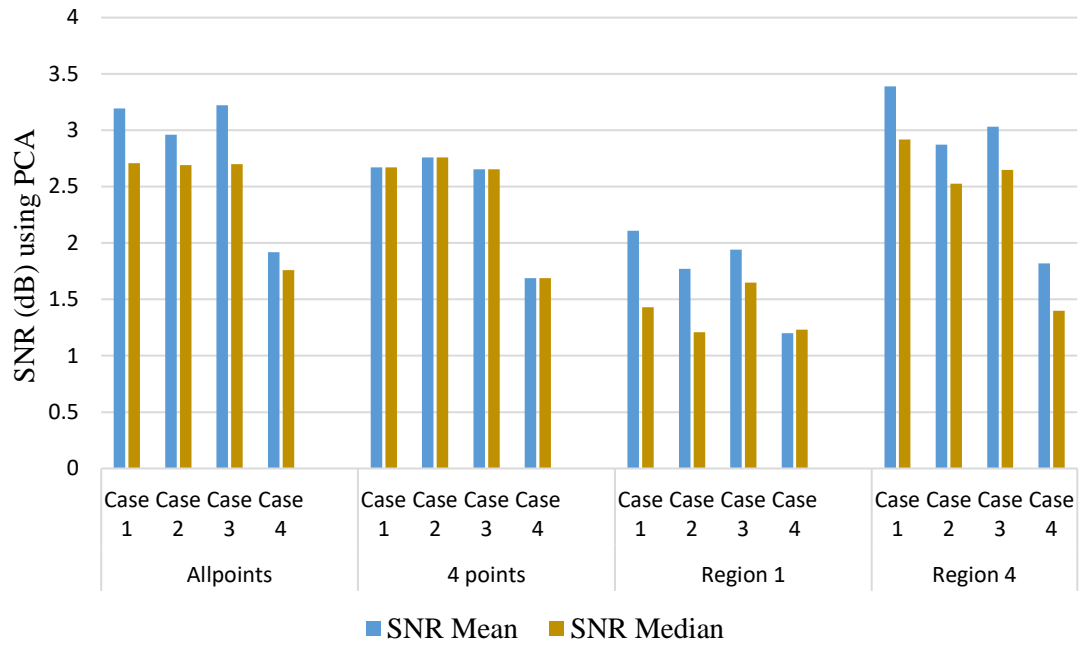


Figure 7.32: Evaluation of SNRs using PCA and taking mean and median values of strains as motion information

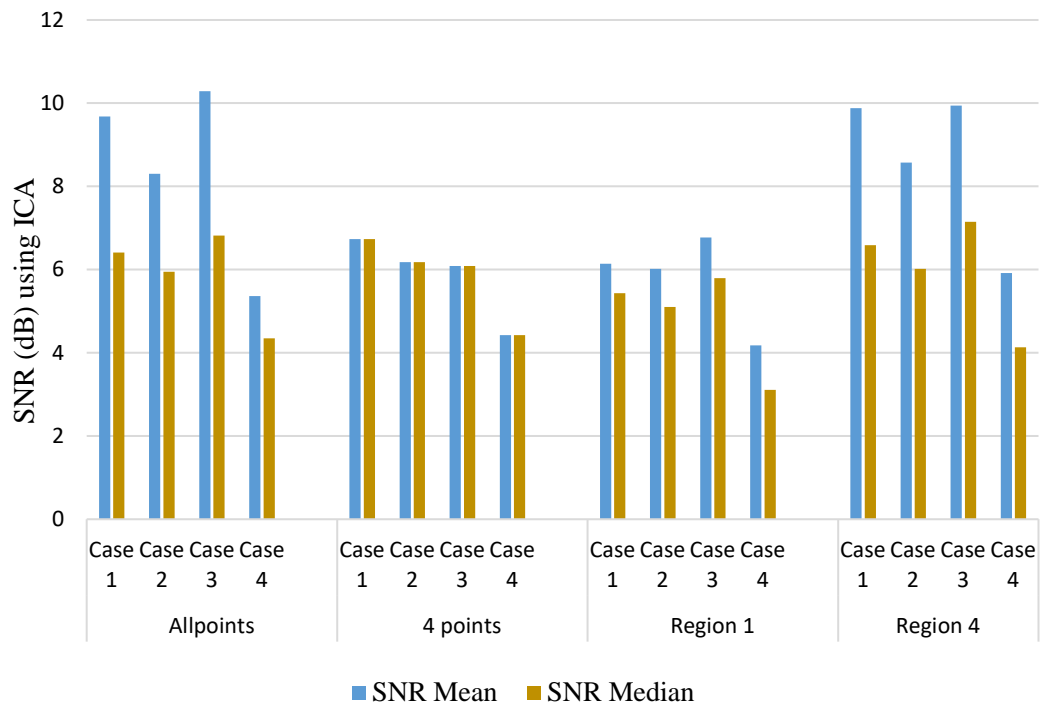


Figure 7.33: Evaluation of SNRs using ICA and taking mean and median values of strains as motion information

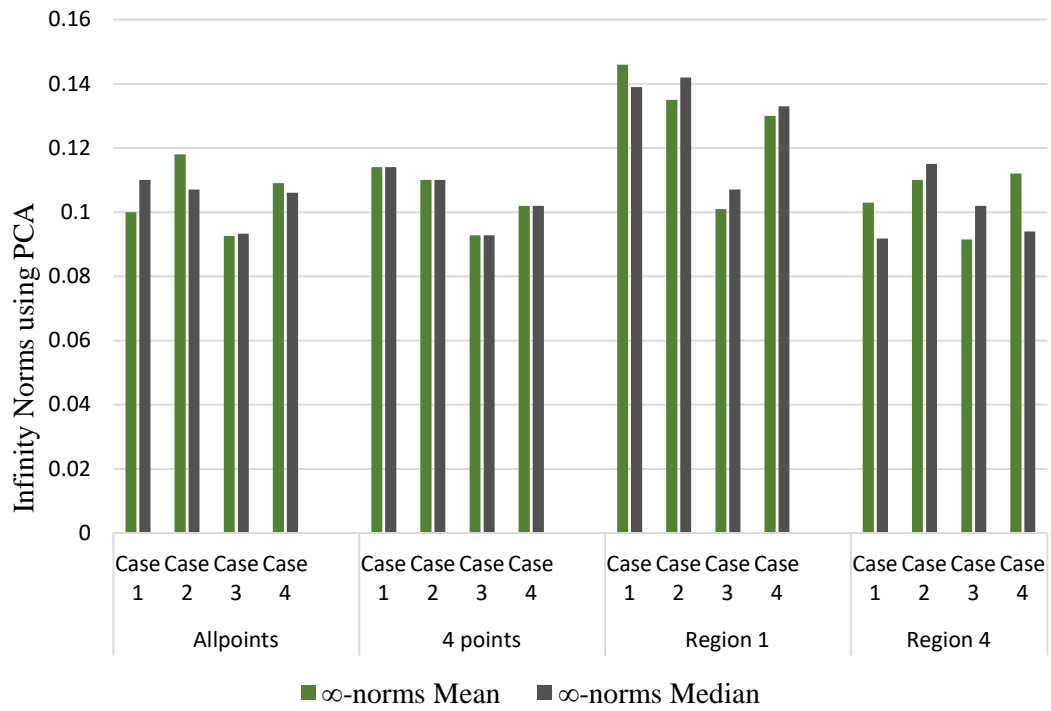


Figure 7.34: Evaluation of  $\infty$ -norm using PCA and taking mean and median values of strains as motion information.

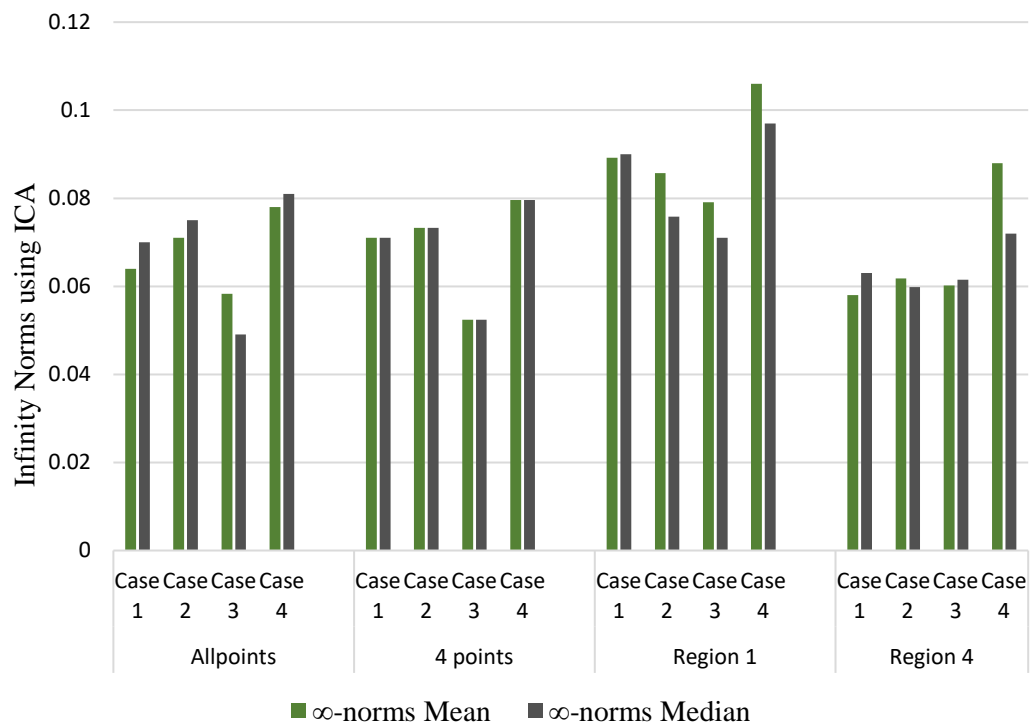


Figure 7.35: Evaluation of  $\infty$ -norm using ICA and taking mean and median values of strains as motion information.

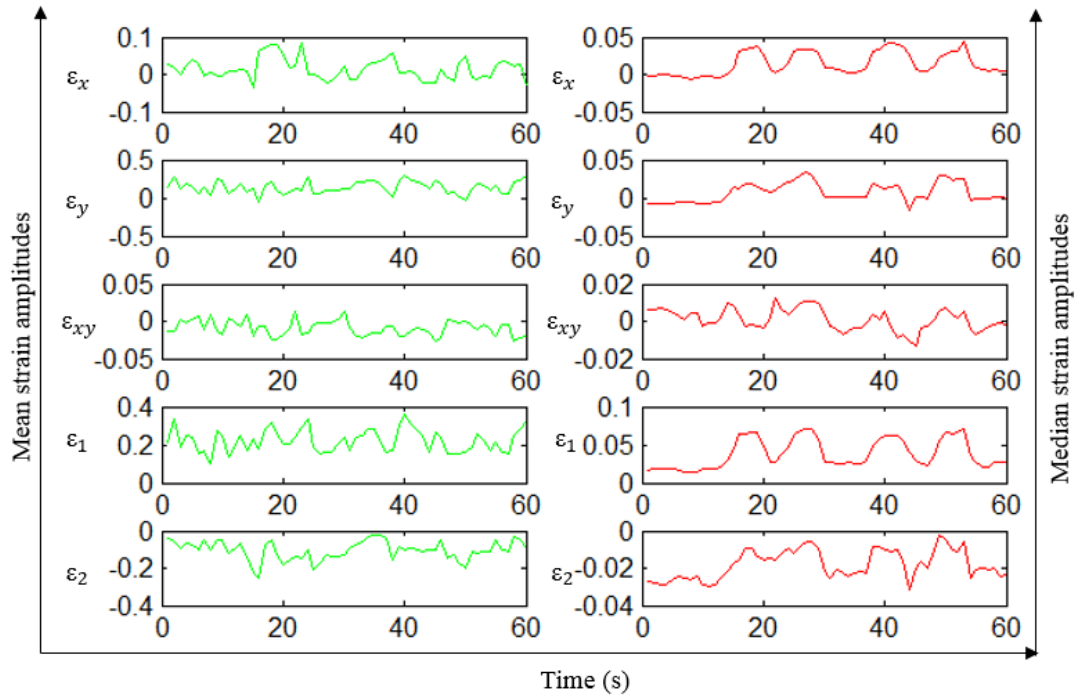


Figure 7.36: Mean and median strains (for all points in Figure 7.8) corresponding to ECG measurement in Subject 1 (age group: 18–35 years) for 60 seconds

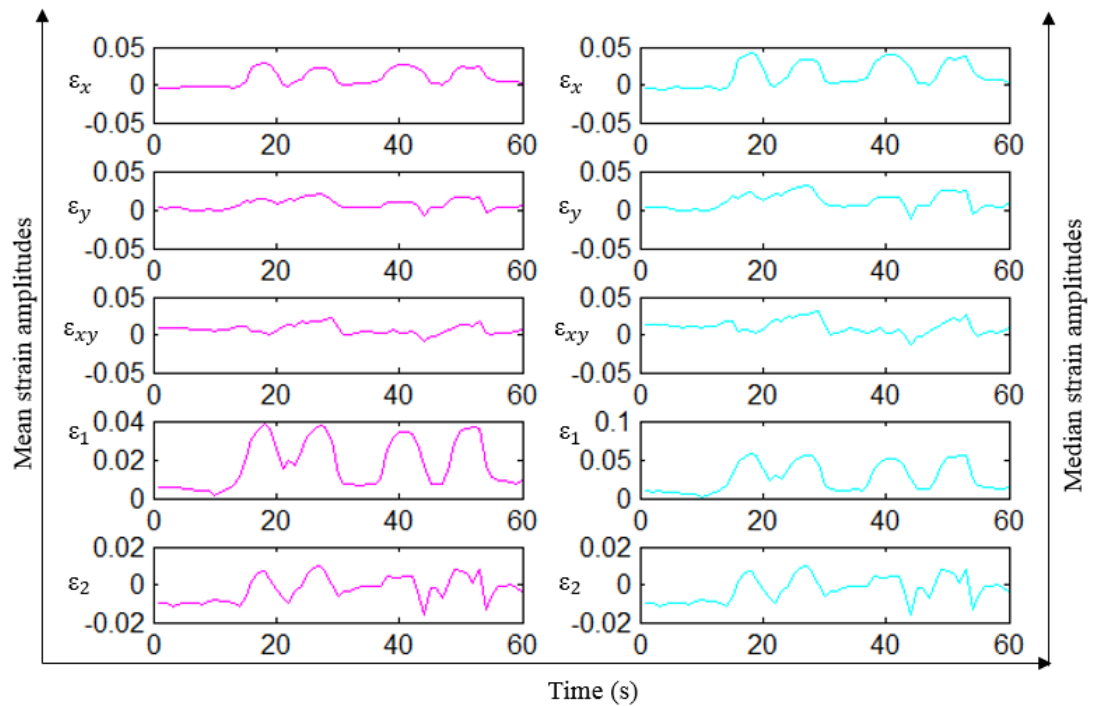


Figure 7.37: Mean and median strains (for corner points in Figure 7.7) corresponding to ECG measurement in Subject 1 (age group: 18–35 years) for 60 seconds

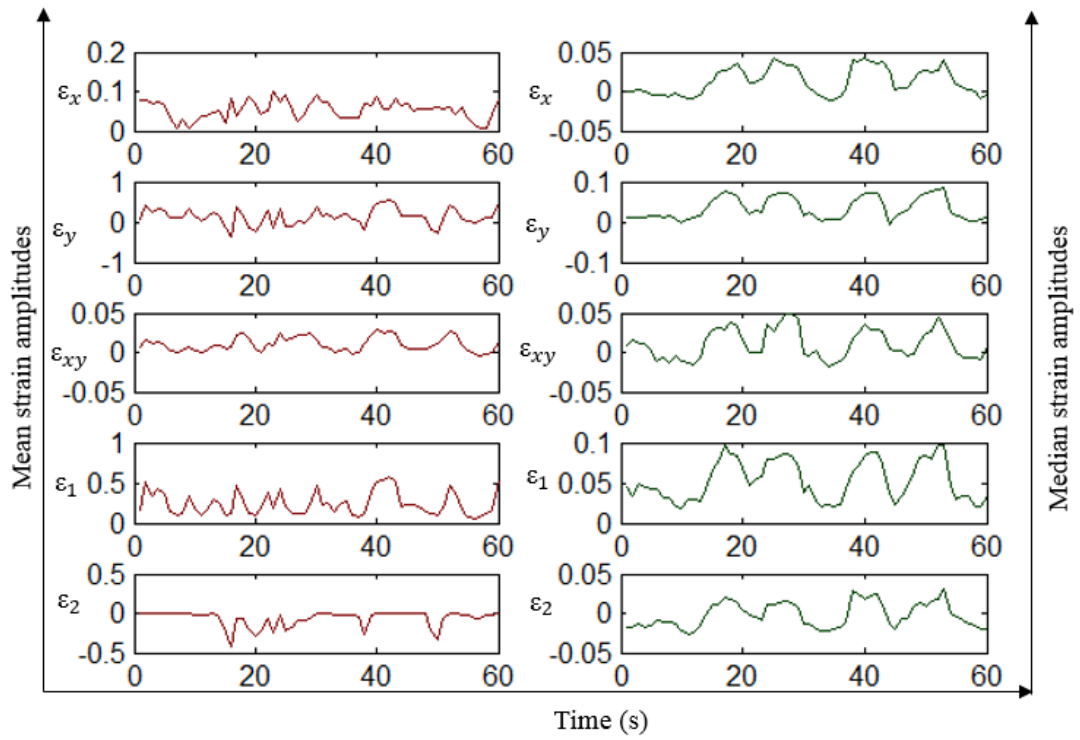


Figure 7.38: Mean and median strains (for points in region 1 in Figure 7.9) corresponding to ECG measurement in Subject 1 (age group: 18–35 years) for 60 seconds

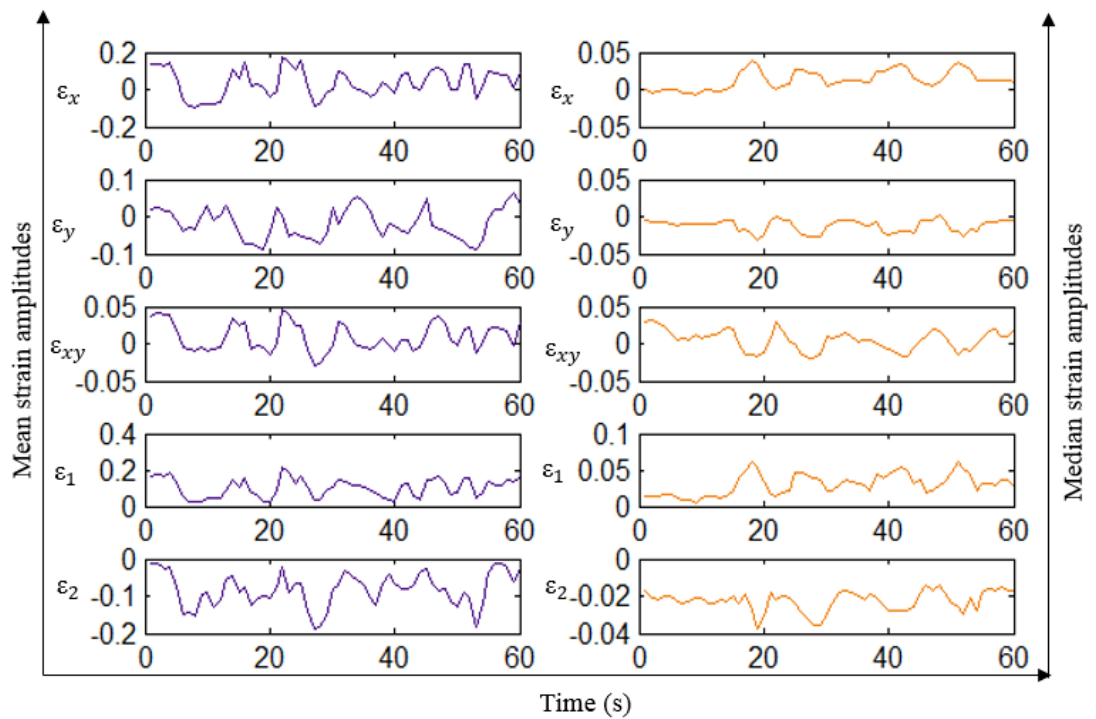
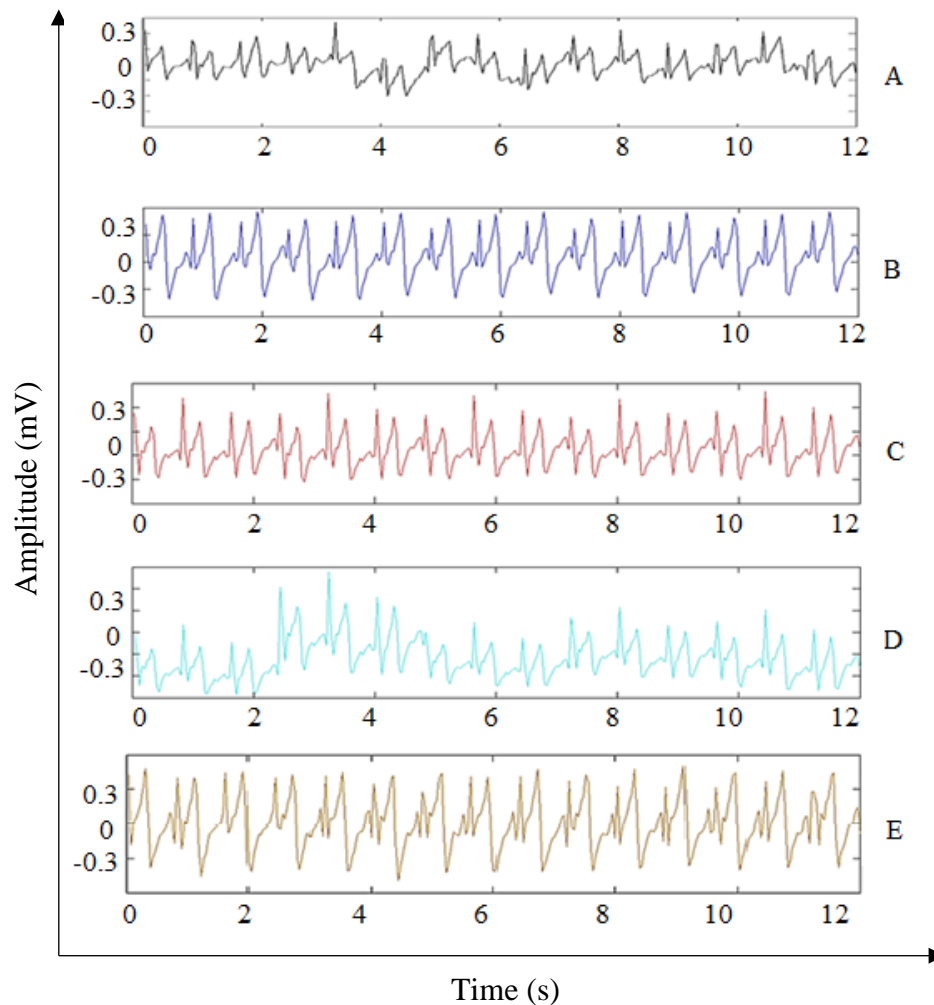


Figure 7.39: Mean and median strains (for points in region 4 in Figure 7.9) corresponding to ECG measurement in Subject 1 (age group: 18–35 years) for 60 seconds

The ECG waveforms obtained using some of the above mentioned cases can be seen in Figure 7.40.



*Figure 7.40: A: ECG with motion artefact, filtered using ICA with data set arrangement in Case 1 (Figure 7.10); B: On taking motion information from all points (Figure 7.8); C: On taking motion information from corner points (Figure 7.7); D: On taking motion information from points in region 4 (Figure 7.9)  
E: Reference ECG from shoulders*

The performance of PCA and ICA using data set arrangement in Case 5 (Figure 7.14), using average displacements and without using motion information, was evaluated for 60 seconds in one subject (age group 18–35 years). A comparative tabulation of these values against Case 1 is shown in Table 7.3.

*Table 7.3: Comparison of PCA and ICA performance for Case 5, average displacements and without motion information against Case 1*

Cases	SNR improvements (dB)		Infinity norms ( $\infty$ -norms)			P values	
	PCA	ICA	MA	PCA	ICA	PCA	ICA
Case1	3.193	9.679	0.12	0.100	0.064	<0.05	<0.05
Case 5	3.24	9.46	0.12	0.094	0.0589	<0.05	<0.05
Average displacements	1.71	5.264	0.12	0.113	0.0625	<0.05	<0.05
Without using motion information	1.38	4.417	0.12	0.124	0.1195	<0.05	<0.05

#### **7.5.4 Comparison of this study with other research**

The motion AR efficiencies of the PCA and ICA algorithms were calculated from equation (7.5) using the  $L_2$  norms of the ECG measurements obtained by inducing skin stretch in the 7 subjects. The average AR percentages using PCA and ICA were found to be 48% and 91% respectively. The average improvement in SNR using PCA and ICA were 4.249 dB and 9.586 dB respectively (see Table 7.1). A comparison of this study with other related research is shown in Table 7.4.

*Table 7.4: Comparison between performances in related research with those in the current study*

<b>Type of filtering</b>	<b>Performance parameters</b>	<b>Current study</b>
ICA [115]	SNR Improvement (Fast ICA) =0.394 dB	SNR improvement (JADE) =9.586 dB
PCA [113]	SNR improvement= 1.44 dB	SNR improvement = 4.249 dB
ICA [117]	P value of corrupted vs reconstructed signal < 0.01	Mean of P value for all ICA (JADE) cases = 0.00678
ICA [118]	SNR improvement (Fast ICA) =1.26 dB	SNR improvement (JADE) = 9.586 dB
PCA [112]	SNR improvement for most corrupted signal= 8.88 dB  SNR improvement for least corrupted signal = 2.92 dB	SNR improvement for most corrupted signal=6.0291 dB  SNR improvement for least corrupted signal =1.337 dB

### **7.5.5 Comparison between CNT/PDMS and dry Ag electrodes**

The SNRs for the dry Ag and CNT/PDMS electrodes were found to be 9.029 and 15.27 dB respectively; corresponding signals are shown in Figure 7.41.

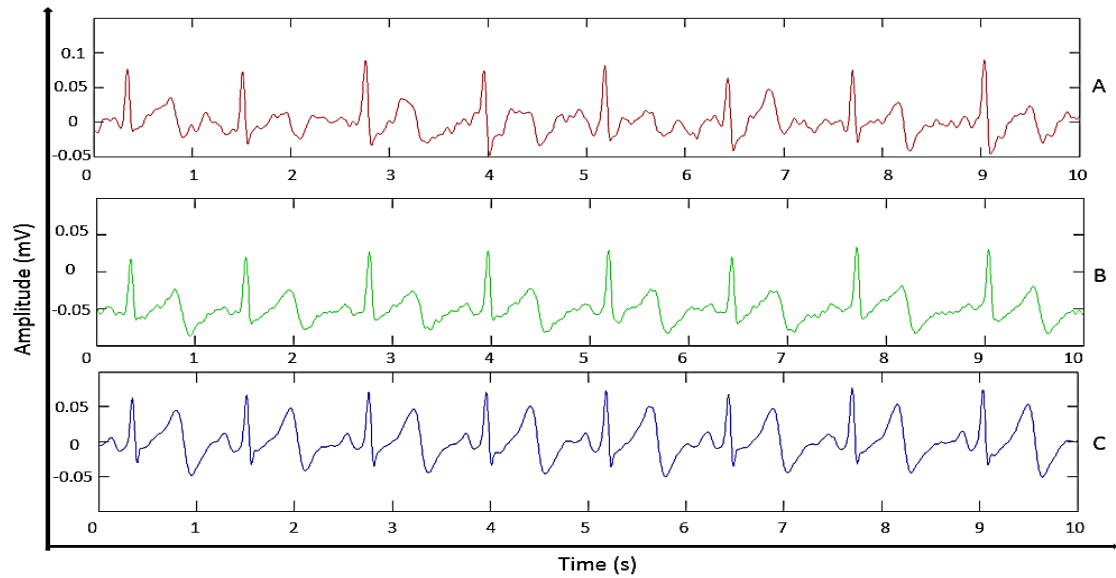


*Figure 7.41: ECG measurement for 10 seconds at rest using:  
A: Dry Ag electrodes on wrist with SNR= 9.029 dB; B: CNT/PDMS electrodes on wrist with SNR= 15.27 dB; C: Ag/AgCl electrodes on chest*

## 7.6 DISCUSSION

In this study, three ECG measurements were taken from 7 healthy subjects from three age groups (18–35 years, 36–55 years and 56 and above) simultaneously using CNT/PDMS, dry Ag and Ag/AgCl electrodes. During the experiments, the forearm skin of the subjects was stretched by another person using a plastic tube. The CNT/PDMS and dry Ag electrodes were used to measure ECG with motion artefacts from the wrist, while the rest (reference) ECG was measured across the chest using conventional Ag/AgCl electrodes. The CNT/PDMS electrodes were employed to measure the ECG and to emulate skin stretch. An optical sensor was used to capture the forearm movement, and 2D strains corresponding to the skin stretch were evaluated.

An altered cardiac action potential may lead to changes in ECG characteristics with time, even when the patient is at rest. Therefore, in this work, the ECG at rest and with motion artefacts were measured simultaneously, as opposed to the studies performed by Liu [108] and Romero [113], where they were measured separately. The SNRs of the filtered and the corrupted signals (ECGs with motion artefacts) were calculated by considering the ECG obtained from chest as the rest/reference ECG. A difference in the signal qualities obtained from the chest (using Ag/AgCl electrodes) and the wrist (using CNT/PDMS electrodes) was expected, and therefore the improvements in SNRs (from

equation (7.3)) were measured to estimate the performances of the algorithms. In some cases, the reference signal was degraded due to the shoulder movement of the subjects, an example of which is seen in Figure 7.26.

The average improvements in SNR using PCA and ICA were 4.249 dB and 9.586 dB respectively. The  $\infty$ -norms of the signals were found to be in the order ICA<PCA<MA for all cases, as shown in Table 7.1. Although PCA filtering led to a significant increase in SNR, the efficacy of ICA on motion AR was greater. Student's T-tests were carried out to determine statistical significance of noise reduction using the PCA and ICA algorithms. The P values were always less than the threshold  $\alpha=0.05$  (confidence level 95%) for ICA, thereby rejecting the null hypothesis. The average P value for ICA was lower than that for PCA, thus showing greater statistical significance.

The best and the worst performances exhibited by PCA and ICA were illustrated in Figures 7.15–7.18. It can be deduced from the results that both PCA and ICA perform better in cases where the motion artefact is large. Even though the amplitudes of ECG and strains due to skin stretch varied from person to person, both PCA and ICA algorithms exhibited higher SNRs and lower  $\infty$ -norms in all subjects, as shown in Table 7.1.

Different 15 second epochs of motion artefacts in ECGs in the same subject were compared when the skin was stretched and relaxed continuously using a plastic tube, as observed in Figures 7.19-7.22. The higher resultant strain due to stretching led to more degradation in the ECG in Figure 7.20 compared to that in Figure 7.21. On the other hand, when the resultant strain due to stretching was similar (in Figure 7.19 and Figure 7.22), the ECG signal in Figure 7.22 was more affected. Therefore, it can be inferred that skin stretch doesn't necessarily introduce similar effects on the ECG signal at different time sequences.

These observations are supported by a 2007 study performed by Liu [109], in which a subject's skin stretch induced artefacts were found to be larger than the ECG signal for a certain period of time, and then disappear over another time frame. Odman [152] found a non-linear relationship between the size of potential variations in the skin and the mechanical stress, which was found to vary amongst individuals.

The proposed technique in this study involving the implementation of JADE (in ICA) was effective in removing considerable motion artefacts from ECG signals. Unlike an

extended Kalman filter (EKF), ICA does not require any assumptions or prior information related to the model describing the data. This is beneficial as it makes ICA general in its application [126]. In principle, ICA alone could have been used on the ECG signal. However, it is useful to use some prior information with ICA to remove artefacts from heavily corrupted signals. In this work, motion information in terms of 2D strains was employed to improve the motion AR from ECG using PCA and ICA.

Artefacts due to EMG interference were also generated in 2 subjects by asking them to repeatedly close and open one fist. The intra-test repeatability of the system was tested by applying PCA and ICA algorithms to the acquired ECG measurements at different time sequences. No significant variation in the performance of PCA and ICA was observed for four epochs of 15 seconds, as seen in Figures 7.23 and 7.24.

PCA was performed on the ECG signals with and without beat segmentation. From Figure 7.25, it can be inferred that the SNRs were slightly higher when PCA was performed by segmenting the ECG signal into beats. An explanation for this is that an adaptive averaging of the segmented ECG beats was performed in the former case. Therefore, the ECG beats that deteriorated due to motion artefacts were averaged out by clean ECG beats. The signal is then decomposed into orthogonal components and the contribution of the components to the signal is measured through eigenvalues. Even though the SNR achieved by applying PCA with beat segmentation was higher, it is more appropriate to not segment beats from the ECG signal in this application. This is because the main objective of this study is to remove motion artefacts from the ECG using quantified motion information in the form of strains. In applying PCA after beat segmentation, an intermediate or average of the beats is taken which might lead to loss of some clinically significant information. If the ECG beats are averaged over a longer period of time, infrequently occurring abnormalities could go undiagnosed. In contrast, if the signal is not segmented, only strain information is utilized to remove motion artefacts, without averaging individual beats. However, in case of ICA, the ECG signal is decomposed into independent components and the components which are most correlated with the noise are removed, therefore, ICA does not produce the same “averaging” effect as PCA.

The SNRs of the acquired ECGs were significantly lower when the skin was stretched perpendicular (in the  $y$ -direction, SNR= -1.7657 dB) and diagonal (in the  $xy$ -direction,

SNR= -2.021 dB) as compared to parallel (in the  $z$ -direction, SNR=9.58 dB) to Langer's lines, as seen in Figure 7.30.

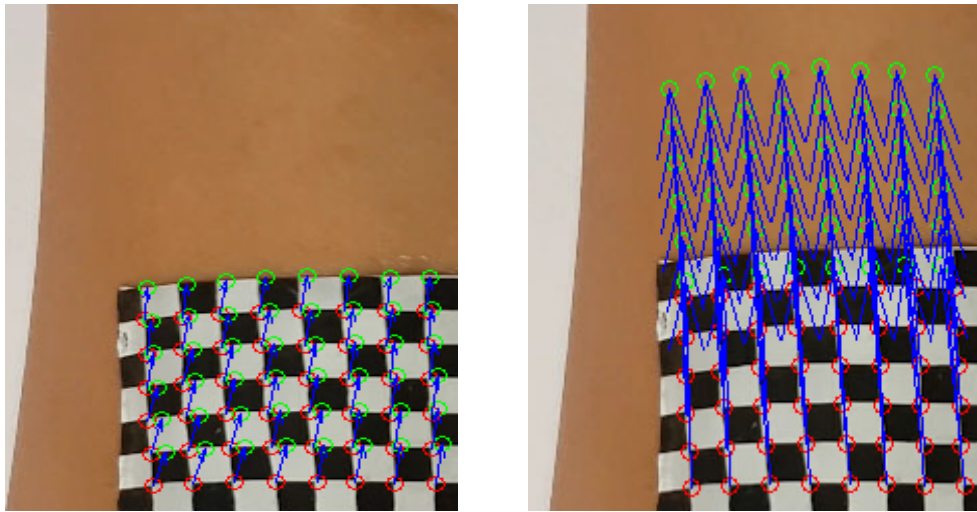


Figure 7.42: Small and large displacements (blue arrows) of checkerboard corner points (in green circles) from the points in initial frame (in red circles)

This can be due to two causes. Firstly, stretching the skin parallel to Langer's lines doesn't generate enough injury current to contribute motion artefacts to the acquired ECG measurements. Secondly, as depicted in Figure 2.5, the Young's modulus of the skin lowers as the direction changes from parallel to perpendicular to Langer's lines, which may affect the amount of motion artefacts due to lesser skin stretch. The former possibility is the more likely explanation in this case as the 2D strains due to stretching in all directions were similar (within -0.3–0.3), with highest strain amplitudes  $\epsilon_x$ ,  $\epsilon_{xy}$  and  $\epsilon_y$  in the parallel, diagonal and perpendicular directions respectively, as seen in Figure 7.31.

Data sets having different arrangements of ECG signals with corresponding mean and median strains ( $\epsilon_x$ ,  $\epsilon_y$ ,  $\epsilon_{xy}$ ,  $\epsilon_1$  and  $\epsilon_2$ ) were taken for filtering using PCA and ICA, as seen from Figures 7.10-7.14.

Mean and median values of strains for each frame corresponding to each ECG sample were calculated. The strain amplitudes due to stretching were as high as 0.5 and as low as 0.001. Figure 7.42 shows small and large displacements of the checkerboard points in consecutive frames from the initial frame.

It can be inferred from Figure 7.36 that the mean strain amplitudes were significantly higher than the median strain amplitudes when computed from the movement of all checkerboard points and points in Regions 1 and 4 for each frame. This was due to larger displacements of some points in certain areas of the checkerboard. It can be observed from Figure 7.43 that the resultant displacement of the checkerboard corners due to stretching is higher in the  $y$ - and  $xy$ -directions in Region B compared to that in Region A; therefore, the mean strain amplitudes  $\varepsilon_y$  and  $\varepsilon_{xy}$  are higher than the median strain amplitudes.

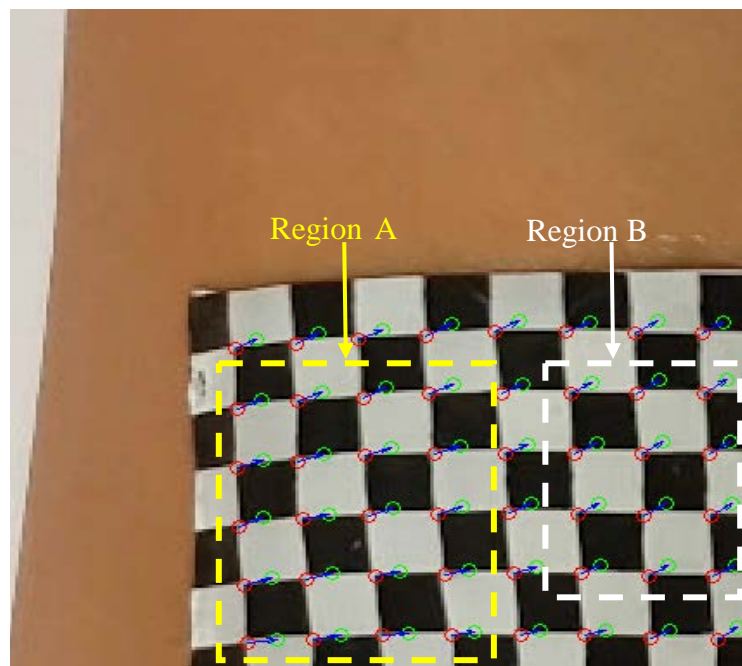


*Figure 7.43: Displacements (blue arrows) of checkerboard corner points (in green circles) in Regions A and B from the points in the initial frame (in red circles)*

In contrast, the mean and median strain amplitudes computed by tracking the four corner points for each frame were similar. The SNRs achieved using mean strain amplitudes as motion information in PCA and ICA were higher than those using median strain amplitudes, as seen from Figures 7.32 and 7.33. The performance of PCA and ICA using data set arrangements in Cases 1, 2, 3 and 5 (section 7.4.5) can be seen in Figures 7.32-7.35. When motion information was evaluated by taking strains from all points (see Figures 7.32 and 7.33), the lowest SNR was obtained in Case 4 for both PCA and ICA. On the other hand, Cases 1 and 3 showed a similar improvement in SNR, whereas Case 2 showed a slightly lower improvement. Therefore, the PCA and ICA algorithms can be simplified by taking  $\varepsilon_1$  in place of  $\varepsilon_x$ ,  $\varepsilon_y$  and  $\varepsilon_{xy}$  as motion information.

The AR system performed best when strains were obtained from all points and from points in Region 4, as seen in Figures 7.32-7.35, the performance of the system was worst when strains were evaluated from Region 1 and the four corner points of the checkerboard. This is because Region 4 is the closest and Region 1 is the farthest from the ECG lead site, as shown in Figure 7.44. It appears that the strains due the displacements of 4 corner points (as opposed to using the entire strain field) are not sufficient to quantify motion information in terms of skin stretch.

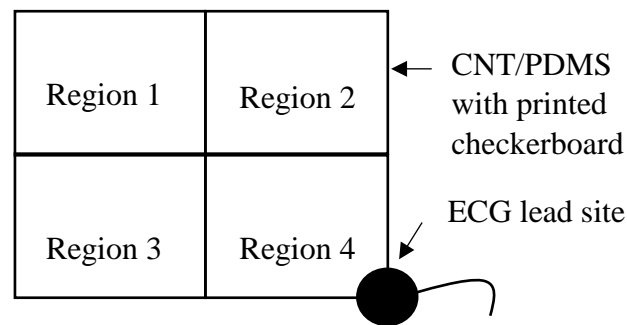


Figure 7.44: Representation of position of each region of the checkerboard from the ECG sensing site

No significant change in SNRs using PCA and ICA was observed on taking individual strains from all four regions of the checkerboard (Case 5, Figure 7.14) as motion information as seen in Table 7.3. On the contrary, the SNR dropped considerably when the algorithms were performed without taking any motion information or by taking average displacements as motion information.

The performance of this system was found to be better than other systems employing PCA and ICA for motion artefact removal from ECGs (Table 7.4). The average AR percentages evaluated using  $L_2$  norms (from equation (7.5)) were higher for ICA than for PCA. A greater SNR was achieved using CNT/PDMS electrodes compared to dry Ag electrodes on the forearm.

The method adopted to identify skin stretch did not lead to a wrong diagnosis when no motion artefacts were introduced. This is because the overall strain at rest was zero.

The efficacy of the ICA algorithm depends on the accurate detection of R-peaks. The window length in the peak detection algorithm (discussed in section 6.3) was optimized manually for the ECG measurement obtained from each subject due to a difference in

their heart rate. Accurate detection of R-peaks can be challenging in cases where the ECG signal is heavily corrupted with motion artefacts.

In this study, the skin was only stretched in two dimension along the planar surface of the arm using a plastic tube. The effect on ECG signals due to stretching the skin along the curved edges of the arm, inflating the skin in form of a dome (in section 2.5.3) and twisting the skin (in section 2.5.4) were not considered.

The experiments were carried out in only seven subjects within different age groups and the changes in magnitude and morphology of skin stretch induced artefacts with change in skin's thickness, gender and skin's hydration were neglected.

The ECG was measured from arms instead of the chest and the efficacy of the AR system was not tested in conditions where the subjects were actively moving, walking, jumping, or running. Offline instead of real time signal processing was performed on the ECG signals using PCA and ICA.

Another downside of this study was the discomfort experienced by the subjects due to the application of conductive paste on their skin to hold the electrodes in place. Therefore, people having a history of skin lesions, skin allergies or sensitivities to cosmetics and lotions were not allowed to participate in this study.

The study was only conducted in healthy subjects and did not involve people with a history of heart arrhythmia.

## **7.7 SUMMARY**

Overall, a novel method to eliminate motion artefacts from ECG signals was developed and validated in 7 healthy individuals. The strains were normalized and PCA and ICA was used to remove the motion artefacts from the ECG using various schemes for calculating strain signals.

The AR system employing PCA and ICA efficiently removed motion artefacts from the ECG measurements of all seven subjects. A significantly higher improvement in SNR was attained when mean strain amplitudes were used rather than median strain amplitudes as motion information in PCA and ICA. The AR system performed best when mean strains  $\varepsilon_x$ ,  $\varepsilon_y$ ,  $\varepsilon_{xy}$  or  $\varepsilon_1$  evaluated from all points and from points in Region 4 of the checkerboard were used as motion information in ICA (Figures 7.32-7.35). The average improvement in SNRs obtained on employing ICA in the AR system was almost

two times higher than that obtained using PCA. The performance of the AR system under different conditions has been compared in Figure 7.45.

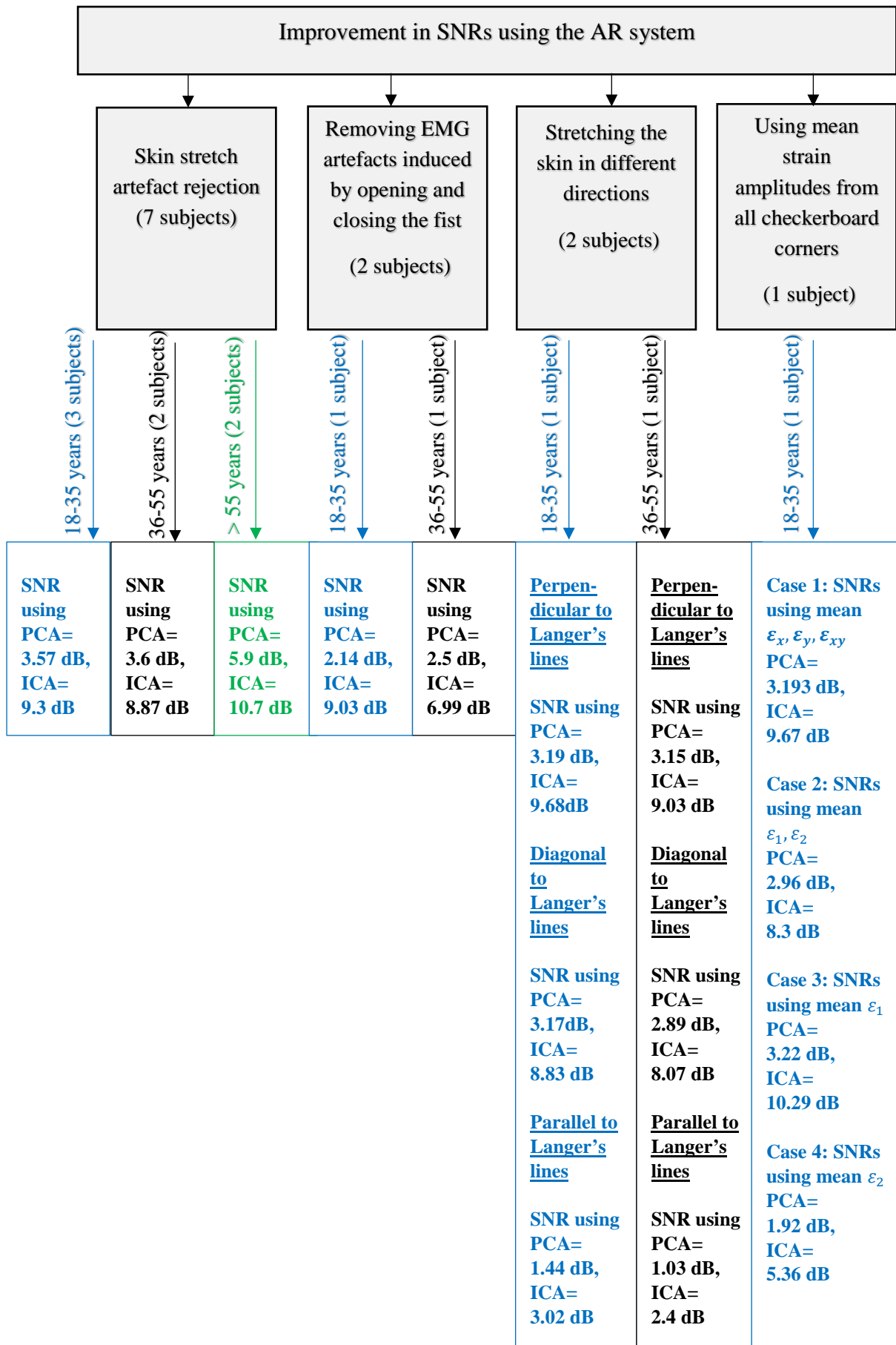


Figure 7.43: A comparison of performance of the AR system under different conditions

## CHAPTER 8 CONCLUSIONS AND FUTURE WORKS

### 8.1 CONCLUSIONS

A novel non-invasive technique to remove motion artefacts from ECG signals has been developed and demonstrated. In this study, skin stretch has been used to quantify motion artefact from ECG, as opposed to other studies employing rigid body displacements for motion artefact quantification, such as in accelerometers, LVDTs, gradiometers and optical sensors. The use of infinitesimal strain theory for skin stretch measurements in removing motion artefacts from ECG has not been previously reported in the literature. The following conclusions and contributions have resulted from this study:

1. An Artefact Rejection (AR) system employing 2D strain analysis can effectively remove motion artefacts due to externally imposed skin-stretch and voluntary motion. Although both PCA and ICA have been extensively used in previous studies, this study emphasises using 2D strains corresponding to skin stretch during ECG measurements in mitigating motion artefacts using PCA and ICA. Taking motion information in the form of 2D strains rather than Euclidian displacements of the points within the electrode resulted in better AR. These results support physiological evidence that the injury current caused by skin stretch is an important contributor to ECG motion artefact.
2. Greater improvements in SNRs and lower  $\infty$ -norms were obtained using ICA than PCA in all the cases. As the ICA algorithm decomposes the signal into independent and uncorrelated components, this supports the presumption that noise due to motion is independent from the ECG.
3. The system performed better when PCA and ICA were applied using 2D strains than without using them. The best performance (SNR improvement = 11.461 dB in subject 6) was achieved when normal and shear strains ( $\epsilon_x, \epsilon_y, \epsilon_{xy}$ ) due to skin stretch were used as motion information in ICA. The results indicate that more detailed information of the 2D strain distribution within the electrode is necessary and this information cannot be directly estimated from the corners of the electrode (i.e. using strain information with a lower spatial resolution).

4. The AR system performed better when mean rather than median strains were considered, for both PCA and ICA. This seems to indicate that ECG noise is affected by “outliers” that are filtered out when using median strains.
5. In this study a thin, conductive and biocompatible prototype electrode was developed using CNTs and PDMS to both measure ECGs and emulate skin stretch. Even though CNT/PDMS electrodes are quite commonly employed in bio signal acquisition, in this study, they have been shown to be suitable for measuring ECG and skin strain measurements simultaneously.
6. This study demonstrated a technique and algorithms for measuring a skin strain field by optically tracking the corner points of checkerboard squares printed on the electrode. Although the technique needs to be further developed to be practical, it may nevertheless find use in a variety of applications.
7. The motion artefacts induced on stretching the skin perpendicular and diagonal to the Langer’s lines were significantly higher than those induced by stretching the skin parallel to them. This provides evidence that the injury current and susceptibility of the ECG to motion artefacts is dependent on the directionality of skin stretch. This may aid in designing electrodes and choosing appropriate electrode placement for motion artefact minimization.

## **8.2 FUTURE DIRECTIONS**

The following investigations related to this study can be performed in future:

### ***8.2.1 Future sensor development***

One of the major limitations of this study is that the camera focus and the light conditions easily obstructed the strain measurements in cases of vigorous motion. Therefore, an alternate approach for measuring skin displacement, such as piezoresistive sensing, could be used in subsequent studies.

The integration of ECG circuitry into compact CNT/PDMS polymer patch electrodes could be implemented for long-term ECG monitoring.

It was found that strong forces of attraction between the CNTs leading to CNT clumping could be mitigated using DMF as a wetting agent, thereby ensuring their homogeneous dispersion in PDMS. Both DMF and NMP solvents can be used to detangle CNTs, however, DMF was used in this study as it is easily available, cheaper and safer to handle. Future work may direct towards using and comparing NMP as a wetting agent against DMF in terms of analysing Young's modulus, homogeneity of the composite and change in conductance with stretching.

### **8.2.2 Further development of algorithms**

In this study, a singular mean strain amplitude corresponding to each ECG sample was used as motion information in PCA and ICA. However, further use of the distribution of 2D strains in the plane of the electrode instead of a singular representative can be employed in future studies. The AR system in this study could also be augmented by other sensor systems to quantify motion artefacts. Such an implementation could then be assessed against the current system's performance to provide the best solution for motion artefact rejection from ECG signals.

### **8.2.3 Further validation**

The current study has only been validated in 7 healthy subjects. In order to evaluate the true efficacy of the PCA and ICA algorithms used in this study, they should be tested in patients with heart arrhythmias to ensure that clinically important information isn't filtered out. It should be noted that even though the average AR percentages achieved using PCA and ICA are 40% and 93% respectively, the amount of motion artefact under the conditions of vigorous exercises like running could be much higher. Therefore, the algorithm needs to be tested for motion artefacts under ambulatory conditions like running, walking and jumping.

This research has shown that if limitations of the current approach (robust and compact wear-ability, and validation in real-world conditions) can be achieved, the technique of directly utilising measurements of skin-strain field under ECG electrodes may become a viable and highly effective means of removing motion artefact from ECG signals, and consequently making ambulatory ECG measurements much more clinically useful.

## REFERENCES

- [1] C. Bowden and J. Masters, *Veterinary nursing medical textbook*. Oxford: Butterworth-Heinemann, 2001.
- [2] S. Korsakas *et al.*, “Electrocardiosignals and motion signals telemonitoring and analysis system for sportsmen,” in *Computers in Cardiology, 2005*, 2005, pp. 363–366.
- [3] C. Matteucci, “Sur le courant électrique ou propre de la grenouille,” *Bibl. Univ. Genève*, vol. 15, pp. 157–168, 1838.
- [4] A. D. Waller, “A demonstration on man of electromotive changes accompanying the heart’s beat,” *The Journal of physiology*, vol. 8, no. 5, pp. 229–234, 1887.
- [5] W. Einthoven, *Un nouveau galvanometre*. Soc. Holl. des Sciences, 1901.
- [6] W. Einthoven, “THE DIFFERENT FORMS OF THE HUMAN ELECTROCARDIOGRAM AND THEIR SIGNIFICATION.,” *The Lancet*, vol. 179, no. 4622, pp. 853–861, 1912.
- [7] “Quantitative Physiology: Organ Transport Systems,” *MIT OpenCourseWare*. [Online]. Available: <http://ocw.mit.edu/courses/health-sciences-and-technology/hst-542j-quantitative-physiology-organ-transport-systems-spring-2004/>. [Accessed: 22-Jul-2014].
- [8] “Excitable Cells.” [Online]. Available: <http://users.rcn.com/jkimball.ma.ultranet/BiologyPages/E/ExcitableCells.html>. [Accessed: 15-Jul-2014].
- [9] “Cardiac action potential,” *Wikipedia*. 25-Mar-2017.
- [10] “Electrocardiogram (ECG or EKG).” [Online]. Available: [http://www.heart.org/HEARTORG/Conditions/HeartAttack/DiagnosingaHeartAttack/Electrocardiogram-ECG-or-EKG\\_UCM\\_309050\\_Article.jsp#.WO3QrGslGpo](http://www.heart.org/HEARTORG/Conditions/HeartAttack/DiagnosingaHeartAttack/Electrocardiogram-ECG-or-EKG_UCM_309050_Article.jsp#.WO3QrGslGpo). [Accessed: 12-Apr-2017].
- [11] “Academic paper (PDF): Bioelectromagnetism - Principles and Applications of Bioelectric and Biomagnetic Fields,” *ResearchGate*. [Online]. Available: [https://www.researchgate.net/publication/258884491\\_Bioelectromagnetism\\_-\\_Principles\\_and\\_Applications\\_of\\_Bioelectric\\_and\\_Biomagnetic\\_Fields](https://www.researchgate.net/publication/258884491_Bioelectromagnetism_-_Principles_and_Applications_of_Bioelectric_and_Biomagnetic_Fields). [Accessed: 12-Apr-2017].
- [12] H. J. Wellens and A. P. M. Gorgels, “How Important Is the Electrocardiogram in Protecting and Guiding the Athlete?,” *Circulation*, vol. 124, no. 6, pp. 669–671, Aug. 2011.
- [13] K. G. Harmon, I. M. Asif, D. Klossner, and J. A. Drezner, “Incidence of Sudden Cardiac Death in National Collegiate Athletic Association Athletes: Clinical Perspective,” *Circulation*, vol. 123, no. 15, pp. 1594–1600, 2011.
- [14] A. Uberoi *et al.*, “Interpretation of the electrocardiogram of young athletes,” *Circulation*, vol. 124, no. 6, pp. 746–757, 2011.
- [15] E.-M. Fong and W.-Y. Chung, “Mobile Cloud-Computing-Based Healthcare Service by Noncontact ECG Monitoring,” *Sensors*, vol. 13, no. 12, pp. 16451–16473, 2013.
- [16] Y. Liu, V. Evely, and M. Pecht, “Non-invasive electrocardiogram and blood pressure monitors for cardiovascular disease,” in *38th International Symposium on Microelectronics, Sensor and MEMS Packaging*, 2005, pp. 66–74.
- [17] “Cardiovascular Medical Device Series: Introduction and Technical Trends in the Cardiac Monitoring Industry | ochis.org.” [Online]. Available: <http://ochis.org/CMreport>. [Accessed: 29-Apr-2017].

- [18] H. Boudoulas, S. F. Schaal, R. P. Lewis, J. L. Robinson, and R. S. Goodwin, "Superiority of 24-hour outpatient monitoring over multi-stage exercise testing for the evaluation of syncope," *Journal of electrocardiology*, vol. 12, no. 1, pp. 103–108, 1979.
- [19] P. F. Poblete, H. L. Kennedy, and D. G. Caralis, "Detection of ventricular ectopy in patients with coronary heart disease and normal subjects by exercise testing and ambulatory electrocardiography," *Chest*, vol. 74, no. 4, pp. 402–407, 1978.
- [20] "Ambulatory ECG Monitoring and Related Investigations AECG. Patient." [Online]. Available: <https://patient.info/doctor/ambulatory-ecg-monitoring-and-related-investigations>. [Accessed: 29-Mar-2017].
- [21] "Norman Holter," *Wikipedia*. 16-Feb-2016.
- [22] "Holter Monitor." [Online]. Available: [http://www.heart.org/HEARTORG/Conditions/HeartAttack/DiagnosingaHeartAttack/Holter-Monitor\\_UCM\\_446437\\_Article.jsp#.WNuT5mW9qpo](http://www.heart.org/HEARTORG/Conditions/HeartAttack/DiagnosingaHeartAttack/Holter-Monitor_UCM_446437_Article.jsp#.WNuT5mW9qpo). [Accessed: 29-Mar-2017].
- [23] B. Surawicz and R. P. Pinto, "Symptoms in hospital patients and outpatients with ventricular arrhythmias during ambulatory ECG monitoring," *J Ambul Monit*, vol. 4, p. 83, 1991.
- [24] S. M. Zeldis, B. J. Levine, E. L. Michelson, and J. Morganroth, "Cardiovascular complaints: correlation with cardiac arrhythmias on 24-hour electrocardiographic monitoring," *Chest*, vol. 78, no. 3, pp. 456–462, 1980.
- [25] T. Drake, "Diagnostic efficacy of 24-hour electrocardiographic monitoring for syncope: Gibson TC, Heitzman MR. *Am J Cardiol* 1984; 53: 1013–1017," *The Journal of Emergency Medicine*, vol. 2, no. 1, p. 65, 1984.
- [26] E. B. Bass *et al.*, "The duration of Holter monitoring in patients with syncope: is 24 hours enough?," *Archives of Internal Medicine*, vol. 150, no. 5, pp. 1073–1078, 1990.
- [27] "Ambulatory ECG monitoring - UpToDate." [Online]. Available: <https://www.uptodate.com/contents/ambulatory-ecg-monitoring#H1>. [Accessed: 30-Mar-2017].
- [28] A. K. Joshi *et al.*, "First experience with a Mobile Cardiac Outpatient Telemetry (MCOT) system for the diagnosis and management of cardiac arrhythmia," *The American journal of cardiology*, vol. 95, no. 7, pp. 878–881, 2005.
- [29] J. A. Olson, A. M. Fouts, B. J. Padanilam, and E. N. Prystowsky, "Utility of mobile cardiac outpatient telemetry for the diagnosis of palpitations, presyncope, syncope, and the assessment of therapy efficacy," *Journal of cardiovascular electrophysiology*, vol. 18, no. 5, pp. 473–477, 2007.
- [30] nate, "Product Guidelines | Monitor Hookups | SAVI Air," *Medicomp Inc.* [Online]. Available: <https://medicompinc.com/product-guides/>. [Accessed: 28-Apr-2017].
- [31] F. Giada *et al.*, "Recurrent unexplained palpitations (RUP) study: comparison of implantable loop recorder versus conventional diagnostic strategy," *Journal of the American College of Cardiology*, vol. 49, no. 19, pp. 1951–1956, 2007.
- [32] T. Furukawa, R. Maggi, C. Bertolone, D. Fontana, and M. Brignole, "Additional diagnostic value of very prolonged observation by implantable loop recorder in patients with unexplained syncope," *Journal of cardiovascular electrophysiology*, vol. 23, no. 1, pp. 67–71, 2012.
- [33] M. P. Turakhia *et al.*, "Diagnostic utility of a novel leadless arrhythmia monitoring device," *The American journal of cardiology*, vol. 112, no. 4, pp. 520–524, 2013.

- [34] P. M. Barrett *et al.*, “Comparison of 24-hour Holter monitoring with 14-day novel adhesive patch electrocardiographic monitoring,” *The American journal of medicine*, vol. 127, no. 1, pp. 95–e11, 2014.
- [35] “SEEQ Mobile Cardiac Telemetry System | Diagnostics & Monitoring.” [Online]. Available: <http://www.medtronicdiagnostics.com/us/cardiac-monitors/seeq-mct-system/index.htm>. [Accessed: 29-Apr-2017].
- [36] C. V. Pollack Jr, “Wireless cardiac event alert monitoring is feasible and effective in the emergency department and adjacent waiting areas,” *Critical pathways in cardiology*, vol. 8, no. 1, pp. 7–11, 2009.
- [37] “Intelesens | Responsive Healthcare - V-Patch.” [Online]. Available: <http://www.intelesens.com/inhomedmonitoring/vpatch.html>. [Accessed: 30-Jul-2014].
- [38] “Solutions Library | Engineering for Change.” [Online]. Available: <https://www.engineeringforchange.org/solution/library/viewAll/Health>. [Accessed: 15-Jul-2014].
- [39] I. Romero *et al.*, “Motion artifact reduction in ambulatory ECG monitoring: an integrated system approach,” in *Proceedings of the 2nd Conference on Wireless Health*, 2011, p. 11.
- [40] E. Fung *et al.*, “Electrocardiographic patch devices and contemporary wireless cardiac monitoring,” *Front Physiol*, vol. 6, May 2015.
- [41] J. S. Shinbane, M. Merkert, R. Fogoros, V. Mehta, M. Cao, and L. A. Saxon, “Wearable wireless arrhythmia detection patches: diagnostic arrhythmia yield, time to first arrhythmia, and patient compliance,” *Heart Rhythm*, vol. 10, p. 5S–S305, 2013.
- [42] M. A. Rosenberg, M. Samuel, A. Thosani, and P. J. Zimetbaum, “Use of a noninvasive continuous monitoring device in the management of atrial fibrillation: a pilot study,” *Pacing and Clinical Electrophysiology*, vol. 36, no. 3, pp. 328–333, 2013.
- [43] “Atrial Fibrillation and Cryptogenic Stroke: Is There a Link? Rhea C. Pimentel, MD Associate Professor of Medicine Fellowship Program Director, Clinical. - Documents,” *Documents.tips*. [Online]. Available: <http://documents.tips/documents/atrial-fibrillation-and-cryptogenic-stroke-is-there-a-link-rhea-c-pimentel.html>. [Accessed: 28-Apr-2017].
- [44] C. C. Cheung, C. R. Kerr, and A. D. Krahn, “Comparing 14-day adhesive patch with 24-h Holter monitoring,” *Future cardiology*, vol. 10, no. 3, pp. 319–322, 2014.
- [45] Plessey Semiconductors, “Application Note # 291566 Non-contact ECG measurement using EPIC.” 26-Mar-2012.
- [46] C. J. Harland, T. D. Clark, N. S. Peters, M. J. Everitt, and P. B. Stiffell, “A compact electric potential sensor array for the acquisition and reconstruction of the 7-lead electrocardiogram without electrical charge contact with the skin,” *Physiological Measurement*, vol. 26, no. 6, pp. 939–950, Dec. 2005.
- [47] “The bumps have it when it comes to CardioWare | Cardiovascular content from Medical Design.” [Online]. Available: <http://medicaldesign.com/cardiovascular/bumps-have-it-when-it-comes-cardioware>. [Accessed: 15-Jul-2014].
- [48] “Maxim ‘Fit’ shirt,” *EDN*. [Online]. Available: <http://www.edn.com/design/medical/4397635/Maxim--Fit--shirt>. [Accessed: 15-Jul-2014].
- [49] M. K. Delano, “A long term wearable electrocardiogram (ecg) measurement system,” Massachusetts Institute of Technology, 2012.

- [50] M. R. Neuman, "Biopotential amplifiers," *Medical instrumentation: application and design*, pp. 292–296, 1998.
- [51] J. Webster, *Medical instrumentation: application and design*. John Wiley & Sons, 2009.
- [52] "ECG Circuit Analysis and Design « Engineers Labs." .
- [53] Y. M. Chi, S. R. Deiss, and G. Cauwenberghs, "Non-contact Low Power EEG/ECG Electrode for High Density Wearable Biopotential Sensor Networks," 2009, pp. 246–250.
- [54] A. C. M. van Rijn, A. Peper, and C. A. Grimbergen, "High-quality recording of bioelectric events," *Med. Biol. Eng. Comput.*, vol. 29, no. 4, pp. 433–440, Jul. 1991.
- [55] A. Metting van Rijn, A. Peper, and C. . Grimbergen, "The isolation mode rejection ratio in bioelectric amplifiers," *IEEE Transactions on Biomedical Engineering*, vol. 38, no. 11, pp. 1154–1157, Nov. 1991.
- [56] J. C. Huhta and J. G. Webster, "60-Hz Interference in Electrocardiography," *IEEE Transactions on Biomedical Engineering*, vol. BME-20, no. 2, pp. 91–101, Mar. 1973.
- [57] N. V. Thakor and J. G. Webster, "Ground-Free ECG Recording with Two Electrodes," *IEEE Transactions on Biomedical Engineering*, vol. BME-27, no. 12, pp. 699–704, Dec. 1980.
- [58] I. C. Forster, "Measurement of patient body capacitance and a method of patient isolation in mains environments," *Medical and Biological Engineering and Computing*, vol. 12, no. 5, pp. 730–732, 1974.
- [59] "IEC 60601," *Wikipedia*. 29-Mar-2017.
- [60] A. M. Van Rijn, A. Peper, and C. A. Grimbergen, "High-quality recording of bioelectric events," *Medical and Biological Engineering and Computing*, vol. 28, no. 5, pp. 389–397, 1990.
- [61] Y. M. Chi, "Non-contact biopotential sensing," 2011.
- [62] T.-H. Kang, "Textile-embedded sensors for wearable physiological monitoring systems," 2007.
- [63] Z. Ping, L. Zhoucheng, W. Feng, and J. Hongyu, "Non-contact ECG Monitoring Based on Capacitive Electrodes," in *World Congress on Medical Physics and Biomedical Engineering May 26-31, 2012, Beijing, China*, 2013, pp. 1506–1509.
- [64] Y. M. Chi, Tzyy-Ping Jung, and G. Cauwenberghs, "Dry-Contact and Noncontact Biopotential Electrodes: Methodological Review," *IEEE Reviews in Biomedical Engineering*, vol. 3, pp. 106–119, 2010.
- [65] L. A. Geddes, L. E. Baker, and A. G. Moore, "Optimum electrolytic chloriding of silver electrodes," *Med. & Biol. Engng.*, vol. 7, no. 1, pp. 49–56, Jan. 1969.
- [66] M. Catrysse, R. Puers, C. Hertleer, L. Van Langenhove, H. van Egmond, and D. Matthys, "Towards the integration of textile sensors in a wireless monitoring suit," *Sensors and Actuators A: Physical*, vol. 114, no. 2–3, pp. 302–311, Sep. 2004.
- [67] F. Carpi and D. De-Rossi, "Electroactive polymer-based devices for e-textiles in biomedicine," *IEEE Transactions on Information Technology in Biomedicine*, vol. 9, no. 3, pp. 295–318, Sep. 2005.
- [68] M. Coyle, "Ambulatory cardiopulmonary data capture," in *Microtechnologies in Medicine amp; Biology 2nd Annual International IEEE-EMB Special Topic Conference on*, 2002, pp. 297–300.
- [69] D. Marculescu *et al.*, "Electronic textiles: A platform for pervasive computing," *Proceedings of the IEEE*, vol. 91, no. 12, pp. 1995–2018, Dec. 2003.

- [70] E. Jovanov, A. O'Donnell Lords, D. Raskovic, P. G. Cox, R. Adhami, and F. Andrasik, "Stress monitoring using a distributed wireless intelligent sensor system," *IEEE Engineering in Medicine and Biology Magazine*, vol. 22, no. 3, pp. 49–55, May 2003.
- [71] S. Ghosh and O. Inganäs, "Conducting polymer hydrogels as 3D electrodes: applications for supercapacitors," *Advanced Materials*, vol. 11, no. 14, pp. 1214–1218, 1999.
- [72] S. M. Lee *et al.*, "Self-adhesive epidermal carbon nanotube electronics for tether-free long-term continuous recording of biosignals," *Scientific Reports*, vol. 4, p. 6074, Aug. 2014.
- [73] "Carbon nanotube," *ScienceDaily*. [Online]. Available: [https://www.sciencedaily.com/terms/carbon\\_nanotube.htm](https://www.sciencedaily.com/terms/carbon_nanotube.htm). [Accessed: 16-Feb-2017].
- [74] L. Cai *et al.*, "Super-stretchable, Transparent Carbon Nanotube-Based Capacitive Strain Sensors for Human Motion Detection," *Scientific Reports*, vol. 3, p. 3048, Oct. 2013.
- [75] H. C. Jung *et al.*, "CNT/PDMS Composite Flexible Dry Electrodes for Long-Term ECG Monitoring," *IEEE Transactions on Biomedical Engineering*, vol. 59, no. 5, pp. 1472–1479, May 2012.
- [76] J. Wang *et al.*, "Development of CNT/Graphene/PDMS Stretchable and Conductive Electrode for Wearable ECG Monitoring."
- [77] J. H. Lee, Y. W. Nam, H.-C. Jung, D.-H. Baek, S.-H. Lee, and J. S. Hong, "Shear induced CNT/PDMS conducting thin film for electrode cardiogram (ECG) electrode," *BioChip Journal*, vol. 6, no. 1, pp. 91–98, Mar. 2012.
- [78] L. Kutějová, J. Vilčáková, R. Moučka, E. NATALIA, and V. BABAYAN, "A solvent dispersion method for the preparation of silicone composites filled with carbon nanotubes," *Chem. Listy*, vol. 108, pp. s78–s85, 2014.
- [79] J. Liu *et al.*, "Controlled deposition of individual single-walled carbon nanotubes on chemically functionalized templates," *Chemical Physics Letters*, vol. 303, no. 1, pp. 125–129, 1999.
- [80] C. A. Furtado, U. J. Kim, H. R. Gutierrez, L. Pan, E. C. Dickey, and P. C. Eklund, "Debundling and dissolution of single-walled carbon nanotubes in amide solvents," *J. Am. Chem. Soc.*, vol. 126, no. 19, pp. 6095–6105, May 2004.
- [81] B. J. Landi, H. J. Ruf, J. J. Worman, and R. P. Raffaele, "Effects of Alkyl Amide Solvents on the Dispersion of Single-Wall Carbon Nanotubes," *The Journal of Physical Chemistry B*, vol. 108, no. 44, pp. 17089–17095, Nov. 2004.
- [82] M. M. Rahman, H. Younes, N. Subramanian, and A. Al Ghaferi, "Optimizing the Dispersion Conditions of SWCNTs in Aqueous Solution of Surfactants and Organic Solvents," *Journal of Nanomaterials*, vol. 2014, Oct. 2014.
- [83] D. M. Kernan and W. J. Blau, "Exploring the mechanisms of carbon-nanotube dispersion aggregation in a highly polar solvent," *EPL*, vol. 83, no. 6, p. 66009, Sep. 2008.
- [84] "c3cp55530e1.pdf." [Online]. Available: <http://www.rsc.org/suppdata/cp/c3/c3cp55530e/c3cp55530e1.pdf>. [Accessed: 16-Feb-2017].
- [85] "Solvents for Solid Phase Peptide Synthesis Contents." [Online]. Available: <http://www.aapptec.com/solvents-solid-phase-peptide-synthesis-i-240.html>. [Accessed: 16-Feb-2017].

- [86] J. G. Webster, "Reducing Motion Artifacts and Interference in Biopotential Recording," *IEEE Transactions on Biomedical Engineering*, vol. BME-31, no. 12, pp. 823–826, Dec. 1984.
- [87] N. V. Thakor and J. G. Webster, "Electrode studies for the long-term ambulatory ECG," *Med. Biol. Eng. Comput.*, vol. 23, no. 2, pp. 116–121, Mar. 1985.
- [88] J. a. J. Klijn and M. J. G. M. Klopogge, "Movement artefact suppressor during ECG monitoring," *Cardiovasc Res*, vol. 8, no. 1, pp. 149–152, Jan. 1974.
- [89] M. H. Limaye and M. V. Deshmukh, "ECG Noise Sources and Various Noise Removal Techniques: A Survey."
- [90] "Artefact - Types and Causes of Interferencen - Cardiology Teaching Package - Practice Learning - Division of Nursing - The University of Nottingham." [Online]. Available: <http://www.nottingham.ac.uk/nursing/practice/resources/cardiology/interference/artefact.php>. [Accessed: 29-Mar-2017].
- [91] D. Vala, T. Pawar, and V. K. Thakar, "Motion Artifact removal in Ambulatory ECG Signal using ICA."
- [92] N. V. Thakor and Y.-S. Zhu, "Applications of adaptive filtering to ECG analysis: noise cancellation and arrhythmia detection," *IEEE Transactions on Biomedical Engineering*, vol. 38, no. 8, pp. 785–794, Aug. 1991.
- [93] K. A. L. A. and A.-J. Am, "Quantifying Skin Stretch induced Motion Artifact from an Electrocardiogram signal-A Pilot Study," *Journal of Biosensors & Bioelectronics*, vol. 7, no. 2, pp. 1–7, Apr. 2016.
- [94] A. Lanata, A. Guidi, P. Baragli, G. Valenza, and E. P. Scilingo, "A Novel Algorithm for Movement Artifact Removal in ECG Signals Acquired from Wearable Systems Applied to Horses," *PLOS ONE*, vol. 10, no. 10, p. e0140783, Oct. 2015.
- [95] F. Strasser, M. Muma, and A. M. Zoubir, "Motion artifact removal in ECG signals using multi-resolution thresholding," in *Signal Processing Conference (EUSIPCO), 2012 Proceedings of the 20th European*, 2012, pp. 899–903.
- [96] Q. Xue, Y. H. Hu, and W. J. Tompkins, "Neural-network-based adaptive matched filtering for QRS detection," *IEEE Transactions on Biomedical Engineering*, vol. 39, no. 4, pp. 317–329, Apr. 1992.
- [97] T. Kiryu, H. Kaneko, and Y. Saitoh, "Motion Artifact Elimination Using Fuzzy Rule Based Adaptive Nonlinear Filter," *IEICE TRANSACTIONS on Fundamentals of Electronics, Communications and Computer Sciences*, vol. E77–A, no. 5, pp. 833–838, May 1994.
- [98] "Motion capture - Wikipedia, the free encyclopedia." [Online]. Available: [about:reader?url=https%3A%2F%2Fen.wikipedia.org%2Fwiki%2FMotion\\_capture](https://en.wikipedia.org/wiki/Motion_capture). [Accessed: 09-Oct-2015].
- [99] A. Kalra, A. Lowe, and A. Al-Jumaily, "Point Tracking on a thin elastomer to emulate Skin-stretch induced motion artifacts in Electrocardiogram measurements," in *Image and Vision Computing New Zealand (IVCNZ), 2015 International Conference on*, 2015, pp. 1–6.
- [100] S. W. Yoon, S. D. Min, Y. H. Yun, S. Lee, and M. Lee, "Adaptive Motion Artifacts Reduction Using 3-axis Accelerometer in E-textile ECG Measurement System," *Journal of Medical Systems*, vol. 32, no. 2, pp. 101–106, Apr. 2008.
- [101] Y. Kishimoto, Y. Kutsuna, and K. Oguri, "Detecting Motion Artifact ECG Noise During Sleeping by Means of a Tri-axis Accelerometer," in *2007 29th Annual International Conference of the IEEE Engineering in Medicine and Biology Society*, 2007, pp. 2669–2672.

- [102] S.-H. Liu, "Motion artifact reduction in electrocardiogram using adaptive filter," *Journal of Medical and Biological Engineering*, vol. 31, no. 1, pp. 67–72, 2011.
- [103] M. A. Raya and L. G. Sison, "Adaptive noise cancelling of motion artifact in stress ECG signals using accelerometer," in *Engineering in Medicine and Biology, 2002. 24th Annual Conference and the Annual Fall Meeting of the Biomedical Engineering Society EMBS/BMES Conference, 2002. Proceedings of the Second Joint*, 2002, vol. 2, pp. 1756–1757 vol.2.
- [104] G. Peng, "A non-contact, low-noise electrocardiogram sensor ASIC employing motion artifact reduction," 2014.
- [105] A. Yilmaz, O. Javed, and M. Shah, "Object Tracking: A Survey," *ACM Comput. Surv.*, vol. 38, no. 4, Dec. 2006.
- [106] H. Matsumura, N. Yoshizawa, K. Watanabe, and N. B. Vedder, "Preconditioning of the distal portion of a rat random-pattern skin flap," *British journal of plastic surgery*, vol. 54, no. 1, pp. 58–61, 2001.
- [107] "Kanade–Lucas–Tomasi feature tracker," *Wikipedia*. 22-Sep-2014.
- [108] Y. Liu, "Reduction of skin stretch induced motion artifacts in electrocardiogram monitoring using adaptive filtering," 2007.
- [109] B. Widrow and M. E. Hoff, "Adaptive switching circuits," STANFORD UNIV CA STANFORD ELECTRONICS LABS, 1960.
- [110] "Expected value," *Wikipedia*. 03-Oct-2017.
- [111] A. Cichocki and S. Amari, *Adaptive blind signal and image processing: learning algorithms and applications*, vol. 1. John Wiley & Sons, 2002.
- [112] P. Ramaswamy, "Uni-channel PCA for noise reduction from ECG signals."
- [113] I. Romero, "PCA-based noise reduction in ambulatory ECGs," in *2010 Computing in Cardiology*, 2010, pp. 677–680.
- [114] I. Romero, "PCA and ICA applied to noise reduction in multi-lead ECG," in *2011 Computing in Cardiology*, 2011, pp. 613–616.
- [115] T. Alkhidir, A. Sluzek, and M. K. Yapici, "Simple method for adaptive filtering of motion artifacts in E-textile wearable ECG sensors," in *2015 37th Annual International Conference of the IEEE Engineering in Medicine and Biology Society (EMBC)*, 2015, pp. 3807–3810.
- [116] A. u Rehman, F. Khan, and B. K. Jadoon, "Analysis of adaptive filter and ICA for noise cancellation from a video frame," in *2016 International Conference on Intelligent Systems Engineering (ICISE)*, 2016, pp. 250–255.
- [117] M. Granegger, T. Werther, and H. Gilly, "Use of independent component analysis for reducing CPR artefacts in human emergency ECGs," *Resuscitation*, vol. 82, no. 1, pp. 79–84, Jan. 2011.
- [118] N. Jain and D. K. Shakya, "Denoising baseline wander noise from electrocardiogram signal using fast ICA with multiple adjustments," *International Journal of Computer Applications*, vol. 99, no. 2, pp. 34–39, 2014.
- [119] B. S. Kim and S. K. Yoo, "Motion artifact reduction in photoplethysmography using independent component analysis," *IEEE Transactions on Biomedical Engineering*, vol. 53, no. 3, pp. 566–568, Mar. 2006.
- [120] J. Y. . Foo, "Use of Independent Component Analysis to Reduce Motion Artifact in Pulse Transit Time Measurement," *IEEE Signal Processing Letters*, vol. 15, pp. 124–126, 2008.
- [121] S. Parmar and B. Unhelkar, "Performance Comparisons of ICA Algorithms to DS-CDMA Detection," *arXiv preprint arXiv:1002.3332*, 2010.
- [122] C. G. Puntonet and A. Prieto, *Independent Component Analysis and Blind Signal Separation: Fifth International Conference, ICA 2004, Granada, Spain, September 22-24, 2004, Proceedings*. Springer, 2004.

- [123] V. Matic, W. Deburchgraeve, and S. Van Huffel, "Comparison of ICA algorithms for ECG artifact removal from EEG signals," in *Proc. of the 4th Annual symposium of the IEEE-EMBS Benelux Chapter.(IEEE-EMBS)*, 2009, pp. 137–140.
- [124] C. J. James and C. W. Hesse, "Independent component analysis for biomedical signals," *Physiological Measurement*, vol. 26, no. 1, pp. R15–R39, Feb. 2005.
- [125] J. Miettinen, K. Nordhausen, and S. Taskinen, "Blind source separation based on joint diagonalization in R: the packages JADE and BSSasyp," *Conditional accepted for publication in the Journal of Statistical Software*, 2015.
- [126] T. He, G. Clifford, and L. Tarassenko, "Application of independent component analysis in removing artefacts from the electrocardiogram," *Neural Computing & Applications*, vol. 15, no. 2, pp. 105–116, 2006.
- [127] A. Hyvarinen, *Independent component analysis*. New York: J. Wiley, 2001.
- [128] J. M. A. Tanskanen and J. J. Viik, "Independent Component Analysis in ECG Signal Processing," 2012.
- [129] A. S. Barhatte, R. Ghongade, and S. V. Tekale, "Noise analysis of ECG signal using fast ICA," in *2016 Conference on Advances in Signal Processing (CASP)*, 2016, pp. 118–122.
- [130] V. Monasterio, G. D. Clifford, and J. P. Martínez, "Comparison of source separation techniques for multilead T-wave alternans detection in the ECG," in *Engineering in Medicine and Biology Society (EMBC), 2010 Annual International Conference of the IEEE*, 2010, pp. 5367–5370.
- [131] C. K. Chui, *An introduction to wavelets*. Boston: Academic Press, 1992.
- [132] A. N. Akansu, W. A. Serdijn, and I. W. Selesnick, "Emerging applications of wavelets: A review," *Physical Communication*, vol. 3, no. 1, pp. 1–18, Mar. 2010.
- [133] Ho Tatt Wei and V. Jeoti, "A wavelet footprints-based compression scheme for ECG signals," 2004, vol. A, pp. 283–286.
- [134] M. Alfaouri and K. Daqrouq, "ECG Signal Denoising By Wavelet Transform Thresholding," *American Journal of Applied Sciences*, vol. 5, no. 3, pp. 276–281, Mar. 2008.
- [135] M. Raghuram, K. V. Madhav, E. H. Krishna, and K. . Reddy, "On the Performance of Wavelets in Reducing Motion Artifacts from Photoplethysmographic Signals," in *2010 4th International Conference on Bioinformatics and Biomedical Engineering (iCBBE)*, 2010, pp. 1–4.
- [136] J. Y. A. Foo, "Comparison of wavelet transformation and adaptive filtering in restoring artefact-induced time-related measurement," *Biomedical Signal Processing and Control*, vol. 1, no. 1, pp. 93–98, Jan. 2006.
- [137] S. Abbaspour, H. Gholamhosseini, and M. Linden, "Evaluation of Wavelet Based Methods in Removing Motion Artifact from ECG Signal," *SpringerLink*, pp. 1–4, 2015.
- [138] D. Hayn, B. Jammerbund, and G. Schreier, "QRS detection based ECG quality assessment," *Physiol Meas*, vol. 33, no. 9, pp. 1449–1461, Sep. 2012.
- [139] Y. Kigawa and K. Oguri, "Support Vector Machine Based Error Filtering for Holter Electrocardiogram Analysis," in *2005 IEEE Engineering in Medicine and Biology 27th Annual Conference*, 2005, pp. 3872–3875.
- [140] M. M. Khambalkar, "Simulating Motion Artifact In ECG Using Wiener And Adaptive Filter Structures."
- [141] R. Sameni, "Extraction of fetal cardiac signals from an array of maternal abdominal recordings," Sharif University of Technology, Tehran, Iran, 2008.
- [142] K. T. Sweeney, T. E. Ward, and S. F. McLoone, "Artifact Removal in Physiological Signals #x2014;Practices and Possibilities," *IEEE Transactions*

- on Information Technology in Biomedicine*, vol. 16, no. 3, pp. 488–500, May 2012.
- [143] E. P. Scilingo, A. Gemignani, R. Paradiso, N. Taccini, B. Ghelarducci, and D. De Rossi, “Performance evaluation of sensing fabrics for monitoring physiological and biomechanical variables,” *IEEE Transactions on information technology in biomedicine*, vol. 9, no. 3, pp. 345–352, 2005.
- [144] A. T. Vehkaoja, J. A. Verho, and J. O. Lekkala, “Miniature wireless measurement node for ECG signal transmission in home area network,” in *Engineering in Medicine and Biology Society, 2006. EMBS’06. 28th Annual International Conference of the IEEE*, 2006, pp. 2049–2052.
- [145] L. Beckmann *et al.*, “Characterization of textile electrodes for bioimpedance spectroscopy,” in *Proceedings of Ambience 2008: International Scientific Conference Smart Textile—Technology and Design*, 2008, pp. 79–83.
- [146] S. Kim *et al.*, “Influence of contact pressure and moisture on the signal quality of a newly developed textile ECG sensor shirt,” in *Medical Devices and Biosensors, 2008. ISSS-MDBS 2008. 5th International Summer School and Symposium on*, 2008, pp. 256–259.
- [147] A. Cömert, M. Honkala, and J. Hyttinen, “Effect of pressure and padding on motion artifact of textile electrodes,” *Biomedical engineering online*, vol. 12, no. 1, p. 26, 2013.
- [148] “Ambulatory Electrocardiogram.” [Online]. Available: <https://www.cardiosmart.org/healthwise/aa10/253/aa10253>. [Accessed: 29-Apr-2017].
- [149] A. C. Glatz *et al.*, “Long-term Noninvasive Arrhythmia Assessment after Surgical Repair of Sinus Venosus Atrial Septal Defect,” *Congenital heart disease*, vol. 5, no. 2, pp. 141–148, 2010.
- [150] R. J. Czosek, J. Anderson, P. R. Khoury, T. K. Knilans, D. S. Spar, and B. S. Marino, “Utility of ambulatory monitoring in patients with congenital heart disease,” *The American journal of cardiology*, vol. 111, no. 5, pp. 723–730, 2013.
- [151] M. Hoffman and MD, “The Skin (Human Anatomy): Picture, Definition, Function, and Skin Conditions,” *WebMD*. [Online]. Available: <http://www.webmd.com/skin-problems-and-treatments/picture-of-the-skin>. [Accessed: 15-Apr-2017].
- [152] S. Ödman, “Potential and impedance variations following skin deformation,” *Med. Biol. Eng. Comput.*, vol. 19, no. 3, pp. 271–278, May 1981.
- [153] S. Odman, “On the spread of deformation potentials in the skin,” *Med Biol Eng Comput*, vol. 20, no. 4, pp. 451–456, Jul. 1982.
- [154] S. Ödman and P. \AAke Öberg, “Movement-induced potentials in surface electrodes,” *Medical and Biological Engineering and Computing*, vol. 20, no. 2, pp. 159–166, 1982.
- [155] H. de Talhouet and J. G. Webster, “The origin of skin-stretch-caused motion artifacts under electrodes,” *Physiological Measurement*, vol. 17, no. 2, p. 81, 1996.
- [156] S. Ödman, “Changes in skin potentials induced by skin compression,” *Medical and Biological Engineering and Computing*, vol. 27, no. 4, p. 390, 1989.
- [157] R. Groves, “Quantifying the mechanical properties of skin in vivo and ex vivo to optimise microneedle device design,” Cardiff University, 2012.
- [158] “E-QURE - The Science of Bioelectricity.” [Online]. Available: <http://www.e-quire.com/the-science-of-bioelectricity/the-science-of-bioelectricity>. [Accessed: 02-Apr-2017].

- [159] N. Thakor and J. Webster, "The origin of skin potential and its variations," in *Proc. Ann. Conf. Eng. Biol. Med.*, 1978, vol. 20, p. 212.
- [160] H. Tam and J. G. Webster, "Minimizing Electrode Motion Artifact by Skin Abrasion," *IEEE Transactions on Biomedical Engineering*, vol. BME-24, no. 2, pp. 134–139, Mar. 1977.
- [161] D. P. Burbank and J. G. Webster, "Reducing skin potential motion artefact by skin abrasion," *Med. Biol. Eng. Comput.*, vol. 16, no. 1, pp. 31–38, Jan. 1978.
- [162] B. P. Pereira, P. W. Lucas, and T. Swee-Hin, "Ranking the fracture toughness of thin mammalian soft tissues using the scissors cutting test," *Journal of Biomechanics*, vol. 30, no. 1, pp. 91–94, 1997.
- [163] H. Oxlund, J. Manschot, and A. Viidik, "The role of elastin in the mechanical properties of skin," *Journal of biomechanics*, vol. 21, no. 3, pp. 213–218, 1988.
- [164] G. A. Holzapfel, "Biomechanics of soft tissue," *The handbook of materials behavior models*, vol. 3, pp. 1049–1063, 2001.
- [165] F. H. Silver, J. W. Freeman, and D. DeVore, "Viscoelastic properties of human skin and processed dermis," *Skin Research and Technology*, vol. 7, no. 1, pp. 18–23, 2001.
- [166] K. A and L. A, "Mechanical Behaviour of Skin: A Review," *Journal of Material Science & Engineering*, vol. 5, no. 4, 2016.
- [167] D. C. Vlasblom, *Skin Elasticity*. Bronder-Offset, 1967.
- [168] P. G. Agache, P. Agache, and P. Humbert, *Measuring the Skin*. Springer Science & Business Media, 2004.
- [169] A. Oba and C. Edwards, "Relationships between changes in mechanical properties of the skin, wrinkling, and destruction of dermal collagen fiber bundles caused by photoaging," *Skin Res Technol*, vol. 12, no. 4, pp. 283–288, Nov. 2006.
- [170] Y. Kuwahara *et al.*, "Quantification of hardness, elasticity and viscosity of the skin of patients with systemic sclerosis using a novel sensing device (Vesmeter): a proposal for a new outcome measurement procedure," *Rheumatology*, vol. 47, no. 7, pp. 1018–1024, Jul. 2008.
- [171] F. M. Hendriks, D. Brokken, J. T. W. M. Van Eemeren, C. W. J. Oomens, F. P. T. Baaijens, and J. B. a. M. Horsten, "A numerical-experimental method to characterize the non-linear mechanical behaviour of human skin," *Skin Research and Technology*, vol. 9, no. 3, pp. 274–283, Aug. 2003.
- [172] A. N. Annaidh, K. Bruyère, M. Destrade, M. D. Gilchrist, and M. Otténio, "Characterization of the anisotropic mechanical properties of excised human skin," *Journal of the mechanical behavior of biomedical materials*, vol. 5, no. 1, pp. 139–148, 2012.
- [173] J. F. M. Manschot and A. J. M. Brakkee, "The measurement and modelling of the mechanical properties of human skin in vivo—I. The measurement," *Journal of Biomechanics*, vol. 19, no. 7, pp. 511–515, 1986.
- [174] R. Meijer, L. F. A. Douven, and C. W. J. Oomens, "Characterisation of anisotropic and non-linear behaviour of human skin in vivo," *Computer methods in biomechanics and biomedical engineering*, vol. 2, no. 1, pp. 13–27, 1999.
- [175] Y. Lanir, "Constitutive equations for fibrous connective tissues," *Journal of biomechanics*, vol. 16, no. 1, pp. 1–12, 1983.
- [176] A. N. Annaidh, M. Destrade, M. Ottenio, K. Bruyere, and M. D. Gilchrist, "Strain rate effects on the failure characteristics of excised human skin."
- [177] C. Jacquemoud, K. Bruyere-Garnier, and M. Coret, "Methodology to determine failure characteristics of planar soft tissues using a dynamic tensile test," *Journal of biomechanics*, vol. 40, no. 2, pp. 468–475, 2007.

- [178] A. J. Gallagher, A. Ní Annaidh, K. Bruyère, and others, “Dynamic tensile properties of human skin,” in *2012 IRCOBI Conference Proceedings*, 2012.
- [179] J. Ankersen, A. E. Birkbeck, R. D. Thomson, and P. Vanezis, “Puncture resistance and tensile strength of skin simulants,” *Proceedings of the Institution of Mechanical Engineers, Part H: Journal of Engineering in Medicine*, vol. 213, no. 6, pp. 493–501, 1999.
- [180] M. Ottenio, D. Tran, A. N. Annaidh, M. D. Gilchrist, and K. Bruyère, “Strain rate and anisotropy effects on the tensile failure characteristics of human skin,” *Journal of the mechanical behavior of biomedical materials*, vol. 41, pp. 241–250, 2015.
- [181] A. Delalleau, G. Josse, J.-M. Lagarde, H. Zahouani, and J.-M. Bergheau, “Characterization of the mechanical properties of skin by inverse analysis combined with the indentation test,” *Journal of biomechanics*, vol. 39, no. 9, pp. 1603–1610, 2006.
- [182] C. Pailler-Mattei, S. Bec, and H. Zahouani, “In vivo measurements of the elastic mechanical properties of human skin by indentation tests,” *Medical Engineering & Physics*, vol. 30, no. 5, pp. 599–606, Jun. 2008.
- [183] D. L. Bader and P. Bowker, “Mechanical characteristics of skin and underlying tissues in vivo,” *Biomaterials*, vol. 4, no. 4, pp. 305–308, 1983.
- [184] V. Falanga and B. Bucalo, “Use of a durometer to assess skin hardness,” *Journal of the American Academy of Dermatology*, vol. 29, no. 1, pp. 47–51, 1993.
- [185] P. A. Choi, “Estimation of Young’s modulus and Poisson’s ratio of soft tissue using indentation,” The Hong Kong Polytechnic University, 2009.
- [186] M. Jia, “Nonlinear Finite Element Analysis of Static and Dynamic Tissue Indentation,” University of Toronto, 2009.
- [187] G. Boyer, C. Pailler Mattei, J. Molimard, M. Pericoi, S. Laquieze, and H. Zahouani, “Non contact method for in vivo assessment of skin mechanical properties for assessing effect of ageing,” *Medical Engineering & Physics*, vol. 34, no. 2, pp. 172–178, Mar. 2012.
- [188] K. Khaothong, “In vivo measurements of the mechanical properties of human skin and muscle by inverse finite element method combined with the indentation test,” in *6th World Congress of Biomechanics (WCB 2010). August 1-6, 2010 Singapore*, 2010, pp. 1467–1470.
- [189] Y. Zheng and A. F. Mak, “Effective elastic properties for lower limb soft tissues from manual indentation experiment,” *Rehabilitation Engineering, IEEE Transactions on*, vol. 7, no. 3, pp. 257–267, 1999.
- [190] P. J. Burnett and D. S. Rickerby, “The mechanical properties of wear-resistant coatings: II: Experimental studies and interpretation of hardness,” *Thin Solid Films*, vol. 148, no. 1, pp. 51–65, 1987.
- [191] D. L. Joslin and W. C. Oliver, “A new method for analyzing data from continuous depth-sensing microindentation tests,” *Journal of Materials Research*, vol. 5, no. 01, pp. 123–126, 1990.
- [192] A. M. Korsunsky, M. R. McGurk, S. J. Bull, and T. F. Page, “On the hardness of coated systems,” *Surface and Coatings Technology*, vol. 99, no. 1–2, pp. 171–183, 1998.
- [193] J. Menčík, D. Munz, E. Quandt, E. R. Weppelmann, and M. V. Swain, “Determination of elastic modulus of thin layers using nanoindentation,” *Journal of Materials Research*, vol. 12, no. 09, pp. 2475–2484, 1997.
- [194] T. Y. Tsui and G. M. Pharr, “Substrate effects on nanoindentation mechanical property measurement of soft films on hard substrates,” *Journal of Materials Research*, vol. 14, no. 01, pp. 292–301, 1999.

- [195] J. van Kuilenburg, M. A. Masen, and E. van der Heide, "Contact modelling of human skin: What value to use for the modulus of elasticity?," *Proceedings of the Institution of Mechanical Engineers, Part J: Journal of Engineering Tribology*, vol. 227, no. 4, pp. 349–361, Apr. 2013.
- [196] R. Grahame, "A method for measuring human skin elasticity in vivo with observations on the effects of age, sex and pregnancy," *Clin Sci*, vol. 39, no. 2, pp. 223–229, 1970.
- [197] H. Alexander and T. H. Cook, "Accounting for natural tension in the mechanical testing of human skin," *Journal of Investigative Dermatology*, vol. 69, no. 3, pp. 310–314, 1977.
- [198] F. Hendriks, "Mechanical behaviour of human skin in vivo," *Bio-medical Engineering*, vol. 4, pp. 322–327, 1969.
- [199] M. G. Gregor B. E. Jemec, "Measurement of skin mechanics," *Skin Research and Technology*, vol. 2, no. 4, pp. 164–166, 2006.
- [200] Monika Gniadecka and J?rgen Serup, "Suction Chamber Method for Measuring Skin Mechanical Properties," in *Handbook of Non-Invasive Methods and the Skin, Second Edition*, 0 vols., CRC Press, 2006, pp. 571–577.
- [201] Y. Li and D. X.-Q. Dai, *Biomechanical Engineering of Textiles and Clothing*. Woodhead Publishing, 2006.
- [202] A. O. Barel, W. Courage, and P. Clarys, "Suction chamber method for measurement of skin mechanics: the new digital version of the cutometer," *Handbook of Noninvasive Methods and the Skin*, pp. 583–591, 2006.
- [203] S. Diridollou *et al.*, "An In Vivo Method for Measuring the Mechanical Properties of the Skin Using Ultrasound," *Ultrasound in Medicine and Biology*, vol. 24, no. 2, pp. 215–224, Feb. 1998.
- [204] C. Siqueira, "Développement d'un essai biaxial sur plaques composites et utilisation pour la modélisation du comportement d'un matériau SMC," *Doctorat d'Université, Université de Franche-Comté*, 1993.
- [205] S. P. Timoshenko and S. Woinowsky-Krieger, "Théorie des plaques et coques," 1961.
- [206] X. Liang and S. A. Boppart, "Biomechanical Properties of In Vivo Human Skin From Dynamic Optical Coherence Elastography," *IEEE Transactions on Biomedical Engineering*, vol. 57, no. 4, pp. 953–959, Apr. 2010.
- [207] C. Escoffier, J. de Rigal, A. Rochefort, R. Vasselet, J.-L. Lévêque, and P. G. Agache, "Age-Related Mechanical Properties of Human Skin: An In Vivo Study," *J Investig Dermatol*, vol. 93, no. 3, pp. 353–357, Sep. 1989.
- [208] J. Serup, G. B. E. Jemec, and G. L. Grove, *Handbook of Non-Invasive Methods and the Skin, Second Edition*. CRC Press, 2006.
- [209] R. Sanders, "Torsional elasticity of human skin in vivo," *Pflugers Arch.*, vol. 342, no. 3, pp. 255–260, Sep. 1973.
- [210] D. C. Vlasblom, "Skin elasticity," Bronder-Offset, 1967.
- [211] P. G. Agache, C. Monneur, J. L. Leveque, and J. D. Rigal, "Mechanical properties and Young's modulus of human skin in vivo," *Arch Dermatol Res*, vol. 269, no. 3, pp. 221–232, Dec. 1980.
- [212] L. A. Grebenyuk and A. A. Uten'kin, "Mechanical properties of the human skin. Communication I," *Human Physiology*, vol. 20, no. 2, p. 149, 1994.
- [213] A. Kalra, A. Lowe, and A. A. Jumaily, "An Overview of Factors Affecting the Skins Youngs Modulus," *Journal of Aging Science*, Aug. 2016.
- [214] Boundless, "Structure of the Skin: Dermis," *Boundless*, Dec. 2016.
- [215] "Understanding Human Structure and Function by Valerie C. Scanlon, Tina Sanders | Waterstones.com." [Online]. Available: <https://www.waterstones.com/book/understanding-human-structure-and->

- function/valerie-c-scanlon/tina-sanders/9780803602366. [Accessed: 19-May-2015].
- [216] I. A. BROWN, "A scanning electron microscope study of the effects of uniaxial tension on human skin," *British Journal of Dermatology*, vol. 89, no. 4, pp. 383–393, 1973.
- [217] "Langer's lines," *Wikipedia*. 27-May-2016.
- [218] "Langer's lines of the skin." [Online]. Available: <http://www.med-ars.it/galleries/langer.htm>. [Accessed: 23-May-2015].
- [219] M. D. Ridge and V. Wright, "The directional effects of skin," *Journal of Investigative Dermatology*, vol. 46, no. 4, pp. 341–346, 1966.
- [220] S. Diridollou *et al.*, "In vivo model of the mechanical properties of the human skin under suction," *Skin Research and Technology*, vol. 6, no. 4, pp. 214–221, Nov. 2000.
- [221] H. Alexander and T. Cook, "Variations with age in the mechanical properties of human skin in vivo," *J Tissue Viability*, vol. 16, no. 3, pp. 6–11, Aug. 2006.
- [222] G. Boyer, L. Laquière, A. Le Bot, S. Laquière, and H. Zahouani, "Dynamic indentation on human skin in vivo: ageing effects," *Skin Research and Technology*, vol. 15, no. 1, pp. 55–67, 2009.
- [223] R. Sanders, "Torsional elasticity of human skin in vivo," *Pflügers Archiv*, vol. 342, no. 3, pp. 255–260, 1973.
- [224] Y. Hara, Y. Masuda, T. Hirao, and N. Yoshikawa, "The relationship between the Young's modulus of the stratum corneum and age: a pilot study," *Skin Res Technol*, vol. 19, no. 3, pp. 339–345, Aug. 2013.
- [225] I. T, I. O, and M. Y, "Measurement of skin elastic properties with a new suction device (I): Relationship to age, sex and the degree of obesity in normal individuals.," *J Dermatol*, vol. 22, no. 10, pp. 713–717, Oct. 1995.
- [226] I. H. Blank, "Factors Which Influence the Water Content of the Stratum Corneum1," *The Journal of Investigative Dermatology*, vol. 18, no. 6, pp. 433–440, Jun. 1952.
- [227] A. C. Park and C. B. Baddiel, "Rheology of stratum corneum-I: A molecular interpretation of the stress-strain curve," *J. Soc. Cosmet. Chem*, vol. 23, no. 1, pp. 3–12, 1972.
- [228] R. H. Wildnauer, J. W. Bothwell, and A. B. Douglass, "STRATUM CORNEUM BIOMECHANICAL PROPERTIES I. Influence of Relative Humidity on Normal and Extracted Human Stratum Corneum," *J Investig Dermatol*, vol. 56, no. 1, pp. 72–78, Jan. 1971.
- [229] Y. S. Papir, K.-H. Hsu, and R. H. Wildnauer, "The mechanical properties of stratum corneum: I. The effect of water and ambient temperature on the tensile properties of newborn rat stratum corneum," *Biochimica et Biophysica Acta (BBA) - General Subjects*, vol. 399, no. 1, pp. 170–180, Jul. 1975.
- [230] "Polydimethylsiloxane - Wikipedia." [Online]. Available: <https://en.wikipedia.org/wiki/Polydimethylsiloxane>. [Accessed: 25-Feb-2017].
- [231] "PDMS: A review," *Elveflow*. .
- [232] K. E. Herold and A. Rasooly, *Lab on a Chip Technology: Biomolecular separation and analysis*. Horizon Scientific Press, 2009.
- [233] "Spin coating," *Wikipedia*. 23-Oct-2015.
- [234] "PDMS softlithography," *Elveflow*. .
- [235] J. Weeks, "What causes hysteresis loop during the stretching of materials?," 21-Mar-2000. [Online]. Available: <http://www.madsci.org/posts/archives/2000-03/953739237.Ph.r.html>. [Accessed: 25-Feb-2017].
- [236] "Carbon nanotube," *Wikipedia*. 24-Apr-2008.

- [237] “Multiwall Carbon Nanotubes (MWCNT): Production, Analysis and Application,” *AZoNano.com*, 23-May-2013. [Online]. Available: <http://www.azonano.com/article.aspx?ArticleID=3469>. [Accessed: 17-Feb-2017].
- [238] P. R. Bandaru, “Electrical Properties and Applications of Carbon Nanotube Structures,” *Journal of Nanoscience and Nanotechnology*, vol. 7, no. 4, pp. 1239–1267, Apr. 2007.
- [239] R. Atif and F. Inam, “Reasons and remedies for the agglomeration of multilayered graphene and carbon nanotubes in polymers,” *Beilstein J Nanotechnol*, vol. 7, pp. 1174–1196, Aug. 2016.
- [240] “SC\_explained.” [Online]. Available: [http://www.psychlab.com/SC\\_explained.html](http://www.psychlab.com/SC_explained.html). [Accessed: 20-Apr-2017].
- [241] R. F. Yazicioglu, C. van Hoof, and R. Puers, *Biopotential Readout Circuits for Portable Acquisition Systems*. Springer Science & Business Media, 2008.
- [242] “Home.” [Online]. Available: <https://www.3ds.com/>. [Accessed: 04-May-2017].
- [243] “Deformation (mechanics),” *Wikipedia*. 07-Dec-2016.
- [244] “Infinitesimal strain theory - Wikipedia.” [Online]. Available: [https://en.wikipedia.org/wiki/Infinitesimal\\_strain\\_theory](https://en.wikipedia.org/wiki/Infinitesimal_strain_theory). [Accessed: 22-Feb-2017].
- [245] “Introduction to Aerospace Structures (ASEN 3112) Course Material.” [Online]. Available: <http://www.colorado.edu/engineering/CAS/courses.d/Structures.d/>. [Accessed: 23-Feb-2017].
- [246] “Teaching - AB Zavatsky.” [Online]. Available: [http://users.ox.ac.uk/~kneabz/seh\\_first\\_year.htm](http://users.ox.ac.uk/~kneabz/seh_first_year.htm). [Accessed: 24-Feb-2017].
- [247] “Delaunay triangulation - Wikipedia.” [Online]. Available: [https://en.wikipedia.org/wiki/Delaunay\\_triangulation](https://en.wikipedia.org/wiki/Delaunay_triangulation). [Accessed: 24-Feb-2017].
- [248] “Delaunay Triangulation - MATLAB & Simulink - MathWorks Australia.” [Online]. Available: <https://au.mathworks.com/help/matlab/math/delaunay-triangulation.html>. [Accessed: 05-Mar-2017].
- [249] “Screen printing - Wikipedia.” [Online]. Available: [https://en.wikipedia.org/wiki/Screen\\_printing](https://en.wikipedia.org/wiki/Screen_printing). [Accessed: 26-Feb-2017].
- [250] “Silicone Ink Information,” *Raw Material Suppliers*. .
- [251] J. E. Mark, *Polymer Data Handbook*. Oxford University Press, 1999.
- [252] J. E. Akin, *Finite element analysis concepts: via SolidWorks*. World Scientific Publishing Co Inc, 2010.
- [253] “2016 SOLIDWORKS Help - Meshing.” [Online]. Available: [http://help.solidworks.com/2016/English/SolidWorks/cworks/c\\_Background\\_on\\_Meshing.htm?id=2558d14e96c54a9b846c4cdf6bae5e89](http://help.solidworks.com/2016/English/SolidWorks/cworks/c_Background_on_Meshing.htm?id=2558d14e96c54a9b846c4cdf6bae5e89). [Accessed: 02-Mar-2017].
- [254] “2016 SOLIDWORKS Help - Solid Mesh.” [Online]. Available: [http://help.solidworks.com/2016/English/SolidWorks/cworks/c\\_Solid\\_Mesh.htm](http://help.solidworks.com/2016/English/SolidWorks/cworks/c_Solid_Mesh.htm). [Accessed: 02-Mar-2017].
- [255] W. S. Ffep. vs D. S.-P. 2says, “Which Solver? FFEPlus vs. Direct Sparse - PART 1,” *SOLIDWORKS Tech Tips, Videos & Tutorials from Javelin*, 15-Jan-2013. .
- [256] “2016 SOLIDWORKS Help - Running Studies.” [Online]. Available: [http://help.solidworks.com/2016/English/SolidWorks/cworks/c\\_Running\\_Studies.htm?id=34aadf3be9d944fb937a291c219764cc#Pg0&ProductType=&ProductName=](http://help.solidworks.com/2016/English/SolidWorks/cworks/c_Running_Studies.htm?id=34aadf3be9d944fb937a291c219764cc#Pg0&ProductType=&ProductName=). [Accessed: 02-Mar-2017].
- [257] “Finite strain theory,” *Wikipedia, the free encyclopedia*. 08-Sep-2015.

- [258] J. Graham, “Target tracking with Lucas-Kanade optical flow and particle filters through affine transforms and occlusion,” 2011.
- [259] *Discrete-time Signal Processing*. .
- [260] A. Irimia, “A Modular Computer Program for the Acquisition and Analysis of Biomagnetic Signals Using SQUID Magnetometers,” Vanderbilt University, 2004.
- [261] G. D. Clifford, “Signal processing methods for heart rate variability,” Department of Engineering Science, University of Oxford, 2002.
- [262] R. Sameni, *Open source ecg toolbox (oset)*. 2006.
- [263] F. Castells, P. Laguna, L. Sörnmo, A. Bollmann, and J. M. Roig, “Principal Component Analysis in ECG Signal Processing,” *EURASIP Journal on Advances in Signal Processing*, vol. 2007, no. 1, p. 074580, Feb. 2007.
- [264] R. J. Martis, U. R. Acharya, K. M. Mandana, A. K. Ray, and C. Chakraborty, “Application of principal component analysis to ECG signals for automated diagnosis of cardiac health,” *Expert Systems with Applications*, vol. 39, no. 14, pp. 11792–11800, Oct. 2012.
- [265] H. Anton, *Elementary linear algebra*. New York: Wiley, 1987.
- [266] “T wave ECG Basics LITFL ECG Library,” *LITFL: Life in the Fast Lane Medical Blog*, 11-Nov-2010. [Online]. Available: <http://lifeinthefastlane.com/ecg-library/basics/t-wave/>. [Accessed: 26-Jan-2017].
- [267] T.-W. Lee, *Independent component analysis: theory and applications*. Boston: Kluwer Academic Publishers, 1998.
- [268] P. Comon, “Independent component analysis, A new concept?,” *Signal Processing*, vol. 36, no. 3, pp. 287–314, Apr. 1994.
- [269] “Independent component analysis,” *Wikipedia*. 03-Dec-2016.
- [270] J. Miettinen, K. Nordhausen, H. Oja, and S. Taskinen, “Fast equivariant JADE,” in *Acoustics, Speech and Signal Processing (ICASSP), 2013 IEEE International Conference on*, 2013, pp. 6153–6157.
- [271] Y. Li, D. Powers, and J. Peach, “Comparison of blind source separation algorithms,” *Advances in neural networks and applications*, pp. 18–21, 2000.
- [272] B. Afsari, “Gradient flow based matrix joint diagonalization for independent component analysis,” DTIC Document, 2004.
- [273] “Cumulant,” *Wikipedia*. 12-Jan-2017.
- [274] V. Krishnaveni, S. Jayaraman, P. M. Kumar, K. Shivakumar, and K. Ramadoss, “Comparison of independent component analysis algorithms for removal of ocular artifacts from electroencephalogram,” *Measurement Science Review*, vol. 5, no. 2, pp. 67–78, 2005.
- [275] “Blind source separation based on JADE algorithm and application,” in *ResearchGate*.
- [276] J.-F. Cardoso, “High-order contrasts for independent component analysis,” *Neural computation*, vol. 11, no. 1, pp. 157–192, 1999.
- [277] L. Sörnmo and P. Laguna, “Electrocardiogram (ECG) signal processing,” *Wiley Encyclopedia of Biomedical Engineering*, 2006.
- [278] “The ST segment - Life in the Fast Lane ECG Library,” *LITFL: Life in the Fast Lane Medical Blog*, 17-Jan-2012. [Online]. Available: <http://lifeinthefastlane.com/ecg-library/st-segment/>. [Accessed: 29-Jan-2017].
- [279] g.tec, “g.tec medical engineering.” [Online]. Available: <http://www.gtec.at/Company>. [Accessed: 08-Mar-2017].
- [280] “Norm (mathematics),” *Wikipedia*. 24-Nov-2016.
- [281] “What is a critical value?” [Online]. Available: <http://support.minitab.com/en-us/minitab/17/topic-library/basic-statistics-and-graphs/hypothesis-tests/basics/what-is-a-critical-value/>. [Accessed: 19-Mar-2017].

- [282] “Electrocardiography,” *Wikipedia*. 22-Mar-2017.
- [283] S. Chaiwisood, B. Wongkittisuksa, and P. Phukpattaranont, “Comparison of Signal Quality between Electrocardiograms Measured from the Chest and the Wrist,” in *Proceedings of PSU-Engineering Conference (IPEC-10)*, 2012, pp. 14–15.

## APPENDICES

### APPENDIX A: LIST OF PUBLICATIONS

- Kalra A, Lowe A, Al-Jumaily A.M., “Quantifying Skin Stretch induced Motion Artifact from an Electrocardiogram signal-A Pilot Study”, Journal of Biosensors and Bioelectronics, 2016.
- Kalra A, Lowe A, Al-Jumaily A.M., “Mechanical behaviour of skin: a review”, Journal of Material Sciences and Engineering, 2016.
- Kalra A, Lowe A, Al-Jumaily A.M., “An Overview of factors affecting the Skin’s Young’s Modulus”, “Journal of Aging Science, 2016.
- Anubha Kalra, Andrew Lowe, Ahmed Al-Jumaily, “A Novel Technique for Motion Artefact Removal from ECG signals”, 38<sup>th</sup> Annual International Conference of IEEE Engineering in Medicine and Biology Society, 2016.
- Anubha Kalra, Andrew Lowe, Ahmed Al-Jumaily, “Point Tracking on a thin elastomer to emulate skin-stretch induced motion artefacts in Electrocardiogram measurements”, International Conference on Image and Vision Computing New Zealand (IVCNZ), 2015.

## APPENDIX B: APPLICATIONS FROM ETHICS COMMITTEE AT AUCKLAND UNIVERSITY OF TECHNOLOGY FOR ECG DATA COLLECTION

### Approved Application

#### AUTEC Secretariat

Auckland University of Technology  
D-88, WU406 Level 4 WU Building City Campus  
T: +64 9 921 9999 ext. 8316  
E: [ethics@aut.ac.nz](mailto:ethics@aut.ac.nz)  
[www.aut.ac.nz/researchethics](http://www.aut.ac.nz/researchethics)



16 June 2017

Andrew Lowe  
Faculty of Design and Creative Technologies

Dear Andrew

Re Ethics Application: **17/170 Collection of ECG signals along with induced skin stretch.**

Thank you for providing evidence as requested, which satisfies the points raised by the Auckland University of Technology Ethics Committee (AUTEC).

Your ethics application has been approved for three years until 15 June 2020.

**Standard Conditions of Approval**

1. A progress report is due annually on the anniversary of the approval date, using form EA2, which is available online through <http://www.aut.ac.nz/researchethics>.
2. A final report is due at the expiration of the approval period, or, upon completion of project, using form EA3, which is available online through <http://www.aut.ac.nz/researchethics>.
3. Any amendments to the project must be approved by AUTEC prior to being implemented. Amendments can be requested using the EA2 form: <http://www.aut.ac.nz/researchethics>.
4. Any serious or unexpected adverse events must be reported to AUTEC Secretariat as a matter of priority.
5. Any unforeseen events that might affect continued ethical acceptability of the project should also be reported to the AUTEC Secretariat as a matter of priority.

Please quote the application number and title on all future correspondence related to this project.

AUTEC grants ethical approval only. If you require management approval for access for your research from another institution or organisation then you are responsible for obtaining it. You are reminded that it is your responsibility to ensure that the spelling and grammar of documents being provided to participants or external organisations is of a high standard.

For any enquiries, please contact [ethics@aut.ac.nz](mailto:ethics@aut.ac.nz)

Yours sincerely,



Kate O'Connor  
Executive Manager  
**Auckland University of Technology Ethics Committee**

Cc: [anubha.kalra@aut.ac.nz](mailto:anubha.kalra@aut.ac.nz); Ahmed Al Jumaily

## Participant Information Sheet



### Participant Information Sheet

**Date Information Sheet Produced:**

15 May 2017

**Project Title**

Collection of ECG signals (representing the heart's electrical activity) along with induced skin stretch

**An Invitation**

I am Anubha Kalra, a PhD candidate at the Institute of Biomedical Technologies, AUT. I would like to invite you to participate in my research study involving the measurement of electrocardiographic (ECG) signals from the chest and forearms. The research study will be conducted at the following address during business hours.

Institute of Biomedical Technologies, Auckland University of Technology  
Room WD-301E, Level 3, WD Building  
19 St. Paul Street,  
Auckland 1010

**What is the purpose of this research?**

This research aims to develop a technique to eliminate skin stretched induced artefacts (noise) from ECG signals for their use in health, rehabilitation and sports science application. This will help to make ECG more useful in situations where people are moving, such as when they need to be recorded for a long time, and in health and sports applications.

The data collected through this research will be used in my PhD work to eliminate skin stretch induced artefacts from the acquired ECG measurements.

**How was I identified and why am I being invited to participate in this research?**

As an adult, you have been invited to be part of this research via advertisements posted around AUT city campus and have responded by making contact with me. You will need to be able to communicate freely in written and spoken English and you will be required to attend the testing session at WD-301, Institute of biomedical technologies, AUT. You are not able to participate in the study if you have a history of broken skin (blisters, rashes etc.) or if you have an irregular heartbeat.

**How do I agree to participate in this research?**

Your participation in this research is voluntary (it is your choice) and whether or not you choose to participate will neither advantage nor disadvantage you. You are able to withdraw from the study at any time. If you choose to withdraw from the study, then you will be offered the choice between having any data that is identifiable as belonging to you removed or allowing it to continue to be used. However, once the findings have been produced, removal of your data may not be possible.

**What will happen in this research?**

You will be asked to sit comfortably while three pairs of ECG electrodes (sticky wet circular patches) will be applied to your shoulders and forearms. The skin near the electrode site on your left forearm will be lightly stretched without causing any discomfort. The ECG measurements will be acquired from the forearms and the shoulders for 3-4 minutes. Please wear or bring a loose short-sleeve or sleeveless shirt or t-shirt with you so that it is easy to place electrodes on your forearms and shoulders. You may choose to apply the shoulder electrodes yourself. If you have any personal or cultural issues regarding the above procedures please let me know prior to the assessment. In addition, prior to the session, you will be asked to complete and bring the consent form with you to your appointment.

**What are the discomforts and risks?**

The ECG electrodes would normally not cause any skin irritation as they have been tested and approved for the use up to 5 days as per the primary recommendations for facility wide electrode standardization. The ECG measurement procedure would only last for 3-4 minutes. However, you are not advised to participate in the study if you have a history of broken skin. A new pair of electrodes will be used for each participant.

**How will these discomforts and risks be alleviated?**

The electrode sites will be cleaned before and after the measurements using a disposable wet cloth.

**What are the benefits?**

Your own ECG measurements can be made available to you on your request.

A selection of light refreshments will be offered to participants.

If successful, this research will be useful in establishing a technique to eliminate skin stretched induced artefacts from ECG measurements for their use in health, rehabilitation and sports science application.

**How will my privacy be protected?**

All the data obtained during this study that can be linked to you will be kept confidential. Only I and my PhD supervisor (Dr. Andrew Lowe) will have access to your data.

If the data is published in the public domain your name as a subject will not be revealed and your data will be de-identified.

**What are the costs of participating in this research?**

Participating in this study will require your time to fill in the consent form, and about 30 minutes of your time for setting up the ECG measurement system and recording the ECG measurements.

**What opportunity do I have to consider this invitation?**

You can choose to participate in this research within 7 days of receiving this Information Sheet.

**Will I receive feedback on the results of this research?**

Yes, you will be provided with a summary of the results of this research on request (a snapshot of your ECG). This summary will be emailed to you.

**What do I do if I have concerns about this research?**

You may withdraw any time before and during the data collection process. Any concerns regarding the nature of this project should be notified in the first instance to the Project Supervisor:

Name: Andrew Lowe,

Email ID: [andrew.lowe@aut.ac.nz](mailto:andrew.lowe@aut.ac.nz),

Phone: +64-9-921-9999 ext 6303

Concerns regarding the conduct of the research should be notified to the Executive Secretary of AUTEK, Kate O'Connor, [ethics@aut.ac.nz](mailto:ethics@aut.ac.nz), 921 9999 ext 6038.

**Whom do I contact for further information about this research?**

Please keep this Information Sheet and a copy of the Consent Form for your future reference. You are also able to contact the research team as follows:

***Researcher Contact Details:***

Name: Anubha Kalra,

Email ID: [anubha.kalra@aut.ac.nz](mailto:anubha.kalra@aut.ac.nz),

Phone: +64-9-921-9999 ext 8617

***Project Supervisor Contact Details:***

Andrew Lowe, [andrew.lowe@aut.ac.nz](mailto:andrew.lowe@aut.ac.nz), +64-9-921-9999 ext 6303

Approved by the Auckland University of Technology Ethics Committee on *type the date final ethics approval was granted*, AUTEK Reference number *type the reference number*.

## Consent Form



### Consent Form

*Project title:* COLLECTION OF ECG SIGNALS ALONG WITH INDUCED SKIN STRETCH.

*Project Supervisor:* **Dr. Andrew Lowe**

*Researcher:* **Anubha Kalra**

- I have read and understood the information provided about this research project in the Information Sheet dated 01 June 2017.
- I have had an opportunity to ask questions and to have them answered.
- I understand that taking part in this study is voluntary (my choice) and that I may withdraw from the study at any time without being disadvantaged in any way.
- I am not suffering from an irregular heart rhythm, skin lesions, any illness or injury that impairs my physical performance, or any infection.
- I understand that my data obtained during this study that can be linked to me will only be available to the named researchers and supervisor involved and will be kept confidential, and that my data will be de-identified prior to use.
- I agree to take part in this research.
- I wish to receive my ECG snapshots (please tick one): Yes  No
- I agree to allow the use of my collected data to be used for research into the elimination of motion artefacts from ambulatory ECG recordings.

Participant's signature: .....

Participant's name: .....

Participant's phone number .....

Participant's email address .....

Date: .....

**Approved by the Auckland University of Technology Ethics Committee on *type the date on which the final approval was granted* AUTEK Reference number *type the AUTEK reference number***

*Note: The Participant should retain a copy of this form.*

# APPENDIX C: SAFETY DATA SHEET OF MATERIALS USED IN THIS STUDY

## Sylgard® 184

<b>SAFETY DATA SHEET</b>	
according to Regulation (EC) No. 1907/2006 Version 5.3 Revision Date 07.06.2017 Print Date 26.06.2017	
GENERIC EU MSDS - NO COUNTRY SPECIFIC DATA - NO OEL DATA	
<b>SECTION 1: Identification of the substance/mixture and of the company/undertaking</b>	
<b>1.1 Product identifiers</b>	
Product name	: SYLGARD® 184
Product Number	: 761036
Brand	: Aldrich
REACH No.	: A registration number is not available for this substance as the substance or its uses are exempted from registration, the annual tonnage does not require a registration or the registration is envisaged for a later registration deadline.
<b>1.2 Relevant identified uses of the substance or mixture and uses advised against</b>	
Identified uses	: Laboratory chemicals, Manufacture of substances
<b>1.3 Details of the supplier of the safety data sheet</b>	
Company	: Sigma-Aldrich New Zealand Co. PO BOX 106-406 1030 AUCKLAND NEW ZEALAND
Telephone	: 0800 936 666
<b>1.4 Emergency telephone number</b>	
Emergency Phone #	0800 928 888 (NZ) +64 9 801 0034 (Int'l CHEMTREC)
This is a summary MSDS for a kit, for the full MSDS for each of the components listed in section 16 please visit our website.	
<b>SECTION 2: Hazards identification</b>	
<b>2.1 Classification of the substance or mixture</b>	
<b>Classification according to Regulation (EC) No 1272/2008</b>	
Skin irritation (Category 2), H315	
Eye irritation (Category 2), H319	
Specific target organ toxicity - single exposure (Category 3), H335	
For the full text of the H-Statements mentioned in this Section, see Section 16.	
<b>2.2 Label elements</b>	
<b>Labelling according Regulation (EC) No 1272/2008</b>	
Pictogram	
Signal word	Warning
Hazard statement(s)	
H315	Causes skin irritation.
H319	Causes serious eye irritation.

**Ten 20 ® conductive paste**

**Safety Data Sheet**

(according to European Directive 2006/1907/EC and OSHA 29CFR 1910.1200)

**for Ten20® Conductive Paste**

revised January 9, 2014  
supersedes March 26, 2013

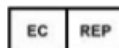
**1. IDENTIFICATION OR THE SUBSTANCE/PREPARATION AND OF THE COMPANY/UNDERTAKING**

- 1.1. Identification of the Substance/Preparation: Ten20® Conductive Paste
- 1.2. Use of Substance/Preparation: conductive and adhesive paste for use in neuromonitoring procedures in conjunction with non-gelled neurodiagnostic electrodes to improve test results

1.3. Company Identification:



Weaver and Company  
565 Nucla Way, Unit B  
Aurora, CO 80011-9319  
USA  
Tel +1 800 525 2130  
Fax +1 303 367 5118  
Email: nlee@weaverandcompany.com  
Website: www.weaverandcompany.com



Emergo Europe  
Molenstraat 15  
2513 The Hague, The Netherlands  
Tel +31 70 345 8570  
Fax +31 70 346 7299

- 1.4. Emergency Telephone: +1 800 525 2130  
Available during normal business hours only:  
Monday – Thursday: 8:00 – 16:30 Mountain Time (GMT-7:00)  
Friday: 8:00 – 15:00 Mountain Time (GMT-7:00)

**2. HAZARD IDENTIFICATION**

- 2.1. Health hazards beyond those associated with drying and chapping of skin or minor skin sensitivity have not been demonstrated. Ten20 Conductive Paste is to be used to adhere electrodes topically on healthy, intact skin only.

Multi walled carbon nanotubes



**Safety Data Sheet**

Prepared on 04/07/2016  
This form is subject to changes

**1. Identification of substance:**

**Product Name:** Multi Walled Carbon Nanotubes

**Product Number(s):** MWNT-100G

CAS-No. 308068-56-6

**Manufacturer/Supplier:**

**Graphene Supermarket**

[www.graphene-supermarket.com](http://www.graphene-supermarket.com)

Graphene Laboratories, Inc.

4603 Middle Country Rd. Unit 125

Calverton, NY11933

[info@graphenelab.com](mailto:info@graphenelab.com)

Phone: (516) 382-8649

Fax: (781) 287-1248

**2. Hazards identification**

**2.1 Classification of the substance or mixture**

**GHS Classification in accordance with 29 CFR 1910 (OSHA HCS)**

Eye irritation (Category 2A), H319

Carcinogenicity (Category 2), H351

Specific target organ toxicity - single exposure (Category 3), Respiratory system, H335

For the full text of the H-Statements mentioned in this Section, see Section 16.

**2.2 GHS Label elements, including precautionary statements**

Pictogram



Signal word (s): Warning

Hazard statement(s)

H319: Causes serious eye irritation.

H335: May cause respiratory irritation.

H351: Suspected of causing cancer.

Precautionary statement(s)

P201: Obtain special instructions before use.

P202: Do not handle until all safety precautions have been read and understood.

P261: Avoid breathing dust/ fume/ gas/ mist/ vapours/ spray.

## APPENDIX D: DEVICE SPECIFICATIONS

### TA.XT Plus

## TECHNICAL SPECIFICATIONS

	<b>TA.XT<sub>plus</sub></b>	<b>TA.HD<sub>plus</sub></b>
Force Capacity	50kg.f (500N)	750kg.f (7.5kN)
Force Resolution	0.1g	0.1g
Loadcells	1, 30, 50kg.f	5, 30, 50, 100, 250, 500, 750kg.f
Speed Range	0.01 – 40mm/s(20mm/s @ 30–50kg.f)	0.01 – 20mm/s (13mm/s @ 500–750kg.f)
Speed Accuracy	Better than 0.1%	Better than 0.1%
Range Setting	1 - 295mm	1 – 524mm
Extended Range Setting	1 - 545mm	-
Range Resolution	0.001mm	0.001mm
Net weight	16.2 kg	37kg
Dimensions	665x440x280mm	980x390x300mm
Width Between Columns	-	300mm
Loadcells	Directly interchangeable by the user. Loadcells store Factory calibration and identification information in 'onboard' non-volatile memory	
Loadcell Accuracy	0.5% of reading down to 1% of Loadcell capacity	
Data Channels	Filtered force at 20bit	
	Distance at 24 bit	
	Unfiltered force at 16 bit	
	Two linear analogue inputs: (range +/- 4.5v @ 16 bit) or PT100 temperature probe inputs (range -50°C to +250°C)	
	Bi-phase digital encoder input at 24 bit suitable for any compatible linear or rotary extensometer	
Data Acquisition Rate	Up to 500 points per second (PPS) for each data channel	
Filtered Force	Oversampled at 8000 samples per second and digitally filtered to 500pps. at 20 bit resolution	
External Instrumentation Channels	Four channels of RS485	
	Each channel logs at one sample per ten seconds at 16 bit and is suitable for external sensing of temperature, humidity etc.	
Operating Temperature	0 – 40°C	
Operating Environment	Laboratory conditions. Dust and splash resistant	
PC Interface	Interface to PC through a standard RS232 serial port	
Power supply	Universal mains input voltage	
Firmware updates	FLASH update of firmware via PC	



#### RECOMMENDED PC SPECIFICATION FOR EXPONENT SOFTWARE

- 1 GHz CPU
- 1Gb RAM
- 1024 x 768 x 24 bit graphics
- 500Mb of free hard disc space (2Gb if video clips installed)
- DVD/CD-ROM
- Windows 95, 98, NT4, ME, 2000 or XP Home / XP Professional
- RS 232 @ 115,200 Baud port (if connected to TA.XT<sub>plus</sub>)
- Mouse
- Sound card (optional)
- Internet access for updating purposes (optional)
- Printer (optional)

**EXPONENT**  
Stable Micro Systems

## LCR meter E4980A

### General Specifications

Table 48. Power source

Voltage	90 VAC - 264 VAC
Frequency	47 Hz - 63 Hz
Power consumption	Max. 150 VA

Table 49. Operating environment

Temperature	0 - 55 °C
Humidity ( $\leq 40$ °C, no condensation)	15% - 85% RH
Altitude	0 m - 2000 m

Table 50. Storage environment

Temperature	-20 - 70 °C
Humidity ( $\leq 60$ °C, no condensation)	0% - 90% RH
Altitude	0 m - 4572 m

Outer dimensions: 375 (width) x 105 (height) x 390 (depth) mm (nominal)

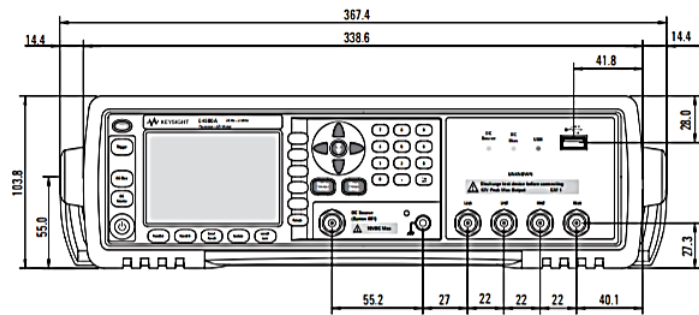


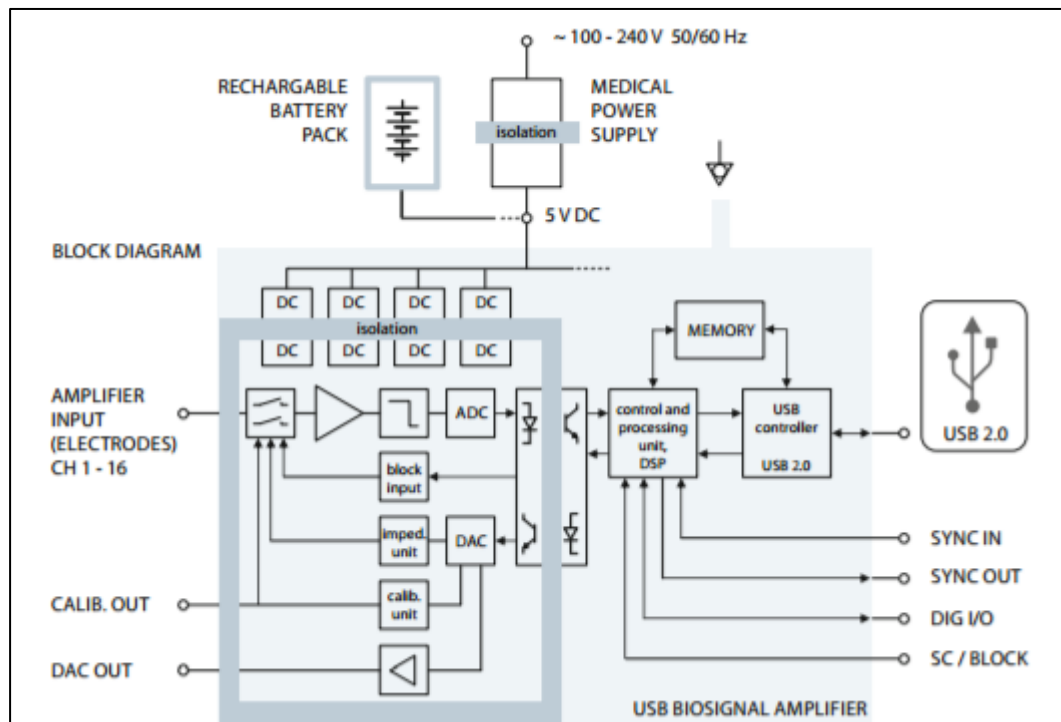
Figure 2. Dimensions (front view, with handle and bumper, in millimeters, nominal)



**Appendix B: Specifications**

<b>General</b>	
Dimension	343 x 260 x 84 mm
Weight	4.0 Kg
Protection	Full EMI protection, (Metallic enclosure with special EMC shielding)
Power supply	100-240 VAC 50/60 Hz
Fuses	1A/250V only
Power input	50 VA
Galvanic insulation of patient, and optical coupling	Device of BF type
Electrodes	6 Ag/AgCl pregelled adhesive electrodes per examination Recommended : Agilent HP40493E
<b>Connectors</b>	
Back panel	Female SUB-D9 (serial link to PC) Switcher-filter-fuses module Schaffner
Front panel	Specific patient connector (6 leads + ground) Gilded contacts
Measurement current	Intensity of 3.6 mA peak to peak Sinus frequency : 75 KHz
Operating temperature	5°C - 55°C
Patient cable	6 leads, EMCD shielded Length 3.5 meters (ref. SP090) or 10 meters (ref SP090-10M) Gilded contacts
Specific RS232 serial link	Null modem type wiring (1,8 Meters) SUB-D9M/SUBD9F connectors Optical cable available, (for connection with a desktop computer).
Power supply cable	2P+T/CEE 22 (computer type) (3 meters)
<b>Computer environment</b>	
Minimal computer configuration	PC Pentium compatible Desktop or Laptop 200 MHz, 32Mb RAM, HD 50 Mb free, screen 800x600, 65536 colours Microsoft Windows 95 / 98 / Me / NT / 2000 operating system. 1 available serial link (RS 232)

*g-USBamp 3.0*



- Sensitivity: < 30 nV (LSB) -  $\pm 250$  mV
- Amplifier type: real DC coupled
- 16 x ADC: 24 bit (38.4 kHz internal sampling per channel)
- 2 x DAC: 12 bit
- Input channels: 16 mono- / 8 bi-polar (per device, software-selectable)
- Noise level: < 0.4  $\mu$ V RMS (0.1 - 10 Hz)
- Input impedance: > 100 MOhm
- Input connectors: standard safety connectors and system connectors
- Weight: 1000 g
- Size: 197 x 155 x 40 mm
- Applied part: type CF
- Safety class: II
- Directive of medical products: 93/42/EWG
- Standards: EN60601-1 (+A1 +A2 +A12 +A13)  
EN60601-2-26  
EN60601-1-2  
EN60601-2-25 +A1  
EN60601-2-40